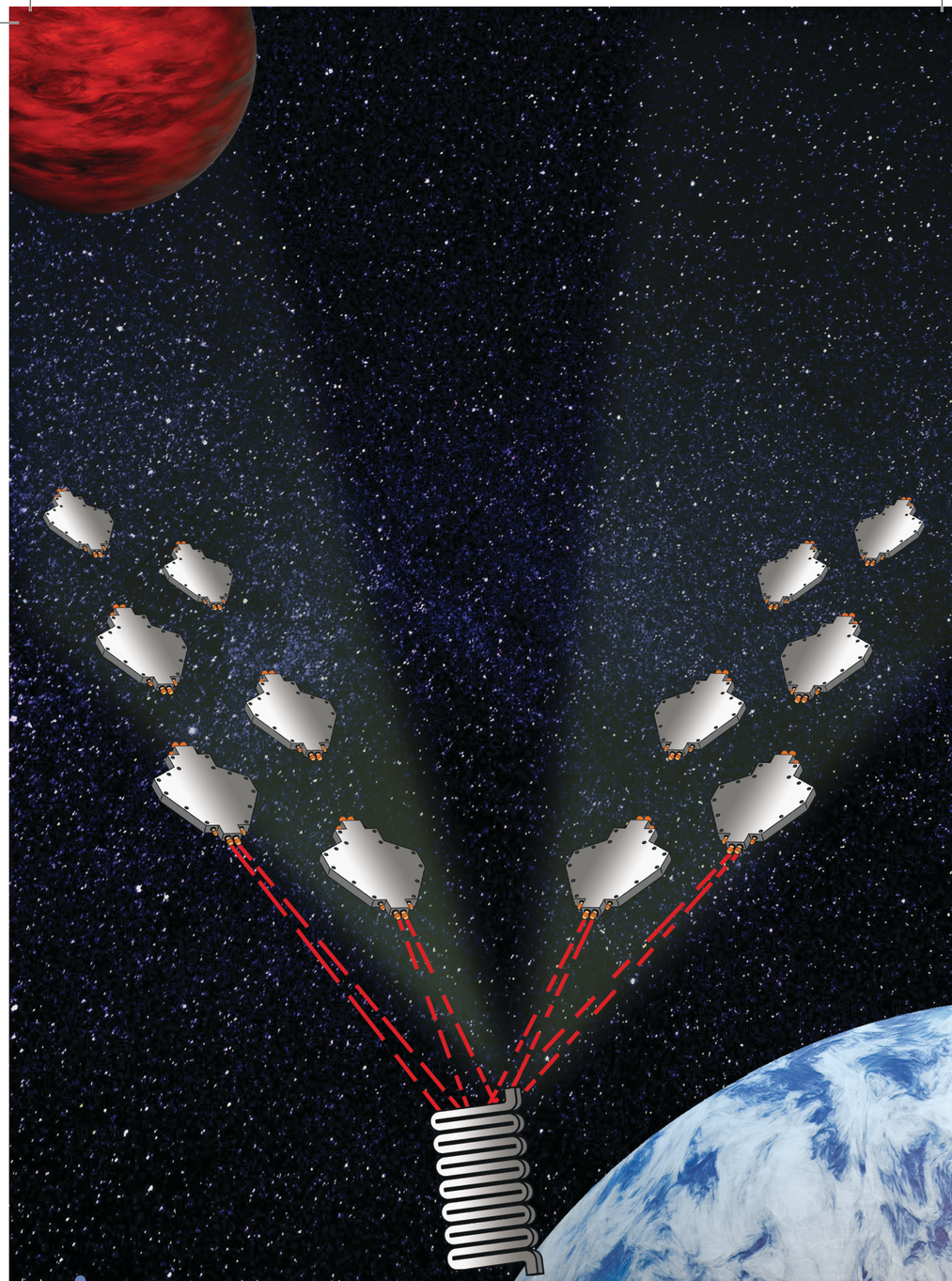

Selective particle control in suspensions using multi-wavelength resonators

M. H. Kandemir

2021

SELECTIVE PARTICLE CONTROL IN SUSPENSIONS USING MULTI-WAVELENGTH RESONATORS

Towards acoustophoresis on centimeter scale

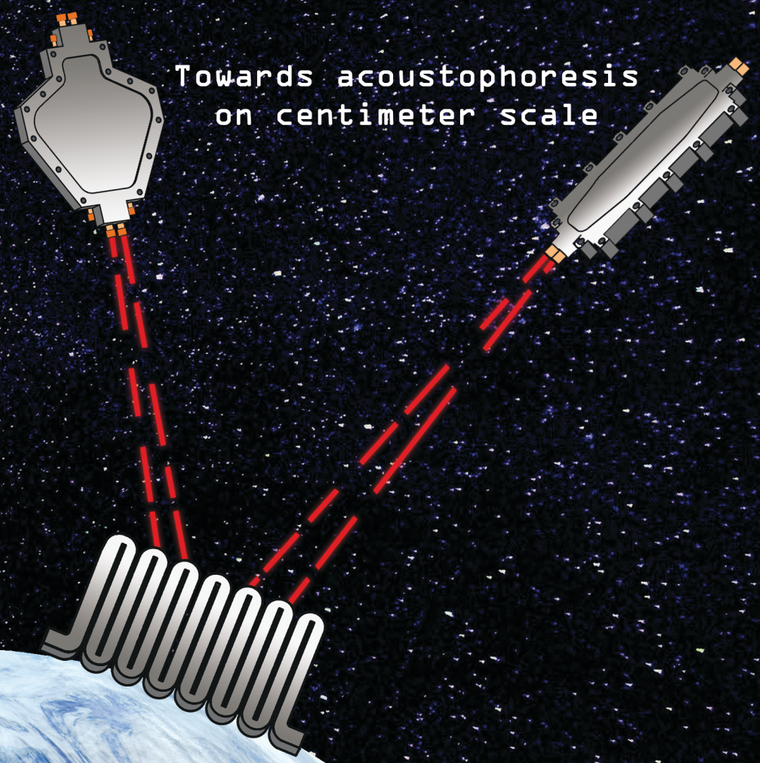

M. Hakan Kandemir

INVITATION

It is my great pleasure to invite you to the public defense of my PhD thesis titled

Selective particle control in suspensions using multi-wavelength resonators

Friday 23 April 2021
at 13:30
in Wetsus*
Leeuwarden

*:to be broadcasted online
enquire for the link

Mehmet Hakan Kandemir
hakan@f1grid.com

Paranymphs
Maarten van de Griend
Shuyana Heredia Deba

PROPOSITIONS

1. For scaling up acoustophoresis to centimeter scale, multi-wavelength resonators are a better solution than half-wavelength resonators. (this thesis)

2. In multi-wavelength acoustophoretic devices, selectivity is exploited by creative design of flow patterns and/or dynamic acoustic fields. (this thesis)

3. Gaining and founding sufficient theoretical base before conducting an experiment is essential to correctly explicate the results.

4. Science is similar to casting magic; it has to be done responsibly.

5. Laziness, when practiced in moderation, is very good fuel for action, innovation and creativity.

6. The way a phenomenon is presented is mostly not how it actually is.

Propositions belonging to the thesis, titled:

"Selective particle control in suspensions using multi-wavelength resonators: Towards acoustophoresis on centimeter scale"

M. H. Kandemir

Leeuwarden, 23 April 2021

SELECTIVE PARTICLE CONTROL IN SUSPENSIONS USING MULTI-WAVELENGTH RESONATORS

TOWARDS ACOUSTOPHORESIS ON CENTIMETER SCALE

MEHMET HAKAN KANDEMIR

Thesis committee

Promotor

Prof. Dr K. J. Keesman
Personal Chair at Mathematical and Statistical Methods - Biometris
Wageningen University & Research

Co-promotors

Dr D. R. Yntema
Scientific Project Manager, Wetsus, European Centre of Excellence for Sustainable Water Technology, Leeuwarden

Dr R. M. Wagterveld
Scientific Project Manager, Wetsus, European Centre of Excellence for Sustainable Water Technology, Leeuwarden

Other members

Prof. Dr C. Buisman, Wageningen University & Research
Prof. Dr H. Bruus, Technical University of Denmark, Denmark
Prof. Dr H. Offerhaus, University of Twente
Dr H. Cappon, HZ University of Applied Sciences, Vlissingen

This research was conducted under the auspices of the Graduate School for Socio-Economic and Natural Sciences of the Environment (SENSE)

SELECTIVE PARTICLE CONTROL IN SUSPENSIONS USING MULTI-WAVELENGTH RESONATORS

TOWARDS ACOUSTOPHORESIS ON CENTIMETER SCALE

Mehmet Hakan Kandemir

Thesis

submitted in fulfilment of the requirements for the degree of doctor
at Wageningen University
by the authority of the Rector Magnificus,
Prof. Dr A. P. J. Mol,
in the presence of the
Thesis Committee appointed by the Academic Board
to be defended in public
on Friday 23 April 2021
at 1:30 p.m. in Wetsus, Leeuwarden

Mehmet Hakan Kandemir

Selective particle control in suspensions using multi-wavelength resonators: Towards acoustophoresis on centimeter scale.
204 pages

PhD thesis, Wageningen University, Wageningen, the Netherlands (2021)
With references, with summary in English

ISBN 978-94-6395-761-8
DOI https://doi.org/10.18174/544213

Table of Contents

1 INTRODUCTION

1.1 Motivation

Particles are everywhere. By definition, a particle refers to a relatively small discrete portion of matter. In this definition of being “relatively small”, a human being can be referred to as a particle relative to the cosmos [1]. While this is more of philosophical interest [1-3], particles that are relatively small with respect to humans attract more scientific interest, as they can be hazardous and must be removed or they can be precious and must be recovered or concentrated. Industries such as food, biomedical, pharmaceutical and petrochemical industries are examples where particle separation is of crucial importance [4-8].

Many technologies exist to either separate particles from a mixture or retain particles in the mixture [9-20]. For example, sedimentation can be used to separate particles from suspensions owing to the density difference between the particles and the medium. Depending on the relative density to the medium, particles can either float or sink. While this technique allows the treatment of large volumes, it relies only on gravity and buoyancy forces, which usually makes it a slow process [13]. Acceleration and gravity are equivalent [21]; hence, the sinking phenomenon can be made faster by rotating the mixture with the cost of increased energy consumption, known as centrifugation [12]. Another way to accelerate sedimentation is called enhanced sedimentation, in which particles are agglomerated by virtue of external forces and thus settle quicker [18, 22-26]. Both sedimentation and centrifugation are able to selectively separate particles from suspensions based on differences in particle densities. Filtration using membranes is also utilized in suspension separation [9-11]. By adjusting the pore size, selective separation or retention is possible based on particle size. However, filtration is susceptible to fouling and clogging, and cleaning of the membranes requires additional operations. Based on the particle’s charge or magnetic properties, electric and magnetic fields can also be used to separate particles from suspensions [19]. Without requiring such properties, inertial focusing methods allow to separate particles using the forces due to flow and inertia [16, 20]. A relatively recent technology, acoustic separation, is the focus of this thesis.

Acoustic separation is based on the principle of acoustophoresis. Acoustophoresis, or acoustic levitation, is defined as manipulating particles by virtue of acoustic radiation force. For practical applications, it is important to note that an acoustic separation system does not contain internal parts that may be clogged or damaged during the operation [5]. Furthermore, standing wave fields exert larger acoustic radiation forces on particles than traveling wave fields [27]. Acoustic separation can

be used in combination with other methods or separately. For example, by concentrating particles in the pressure nodes of a standing wave pattern, acoustics can be used to enhance sedimentation and flocculation [18, 22-26]. However, it is more common that for particle separation acoustics are used alone. The acoustic radiation force on particle depends on particle size, density and compressibility [28-33]. It is therefore possible to selectively separate particles based on such property differences. On microscale, there are a number of successful applications of acoustophoresis for selective separation, for example, in cell separation or harvesting and in microparticle separation [34-56]. On cm-scale, examples of applications are enhanced sedimentation and particle filtering/enhancement, allowing larger volumes to be treated [22-26, 57-66]. Also, utilizing dynamic standing wave fields opens up new possibilities of selectively manipulating the particles [67-78].

Even though selective separation on microscale by acoustophoresis has been demonstrated [34-35, 37-42, 46, 47, 49, 50, 52], the throughput is usually very low for industrial applications [5]. Simply scaling up the dimensions and input power is not suitable [28-33], thus higher throughput requires new designs and procedures [57, 66]. This thesis investigates the selective separation of particles in suspensions using acoustics on cm-scale.

1.2 Principle of Acoustic Separation

1.2.1 Acoustics and Standing Waves

When a perturbance occurs in an elastic body or medium it does not stay local. It travels within the material without permanently changing the material properties while carrying energy as it propagates. For example, the perturbance can be a local impulse on a metallic rod, causing stress waves among the material. A stone dropped in water creates waves on the surface. In air, a loudspeaker creates a disturbance and the pressure waves travel in air. The behavior of such disturbances is modelled with the well-known wave equation. Acoustics is the branch of science that deals with wave propagation in elastic media.

Two main types of acoustic waves are the so-called spherical waves and plane waves. Spherical waves propagate in multiple directions (stone dropped in water is a perfect example for this), the amplitude of wave decreases as the wave travels

away from the source and eventually completely decays. For the loudspeaker example, this decrease is the reason it becomes harder to hear somebody as one gets farther. Sufficiently away from the source, the wave front tends to become a plane. Plane waves propagate in one direction and the amplitude does not decay in space. In addition, if a source is radiating sound at one frequency and the source is much larger than the wavelength, the radiated sound can be considered as plane wave. Due to the dimensions and high frequencies used in acoustophoresis devices, acoustic waves are modelled as plane waves. Figure 1.1 illustrates a typical spherical wave and a plane wave.

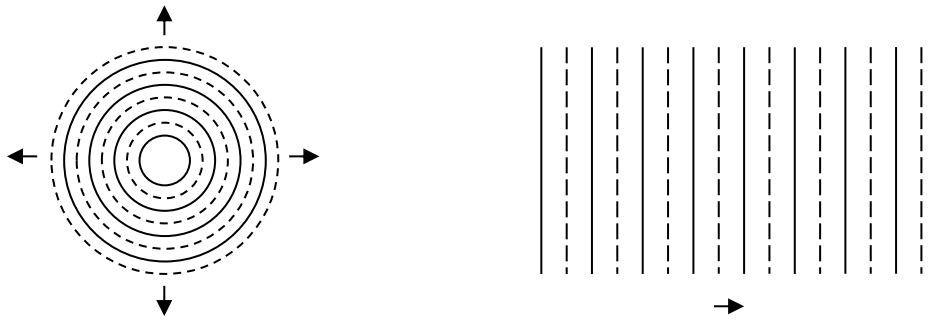

(a) (b)

Figure 1.1 - A spherical wave propagating in every direction. (b) A plane wave propagating in the indicated direction. The solid and dashed lines represent the peaks and valleys in the wave pattern, respectively.

Plane waves are the simplest type of wave motion in a medium. In the one dimensional plane wave equation, where t denotes time and x denotes the position, $p \coloneqq p(x,t)$ is the acoustic pressure (or local pressure variation) and the total pressure is the sum of equilibrium pressure (p_0) and p, as $p_{tot} \coloneqq p_0 + p$. Similarly $\rho \coloneqq \rho(x,t)$ is the local density fluctuation in the medium while the total density is the sum of the equilibrium density (ρ_0) and ρ, as $\rho_{tot} \coloneqq \rho_0 + \rho$. c_0 is the speed of sound in the medium. Finally, the one-dimensional wave equation is given by

$$\frac{1}{c_0^2}\frac{\partial^2 p}{\partial t^2} = \frac{\partial^2 p}{\partial x^2} \tag{1.1}$$

The harmonic solutions for the wave equation are of the form: $p_1(x,t) = f(x - c_0 t) = P^* e^{i(\omega t - kx)}$ for a positive traveling plane wave and $p_2(x,t) = f(x + c_0 t) = P^* e^{i(\omega t + kx)}$ for a negative traveling plane wave. Here, P^* is the complex pressure amplitude, $\omega = 2\pi f$ is the angular frequency and $k = \omega / c_0$ is the wavenumber. There is also a standing wave solution for the wave equation, which is of the form: $p(x,t) = f(x - c_0 t) + g(x + c_0 t)$, indicating that when two harmonic waves with the same frequency and amplitude are traveling in opposite direction, their interaction creates a standing wave. Figure 1.2 illustrates two similar waves, with period T, traveling opposite to each other and resulting in a standing wave, where $p_1(x,t) = Re\left(P^* e^{i(\omega t - kx)}\right)$ and $p_2(x,t) = Re\left(P^* e^{i(\omega t + kx)}\right)$.

The equation for a standing wave can be obtained by summation of two similar opposite traveling waves.

$$p(x,t) = P\cos(\omega t - kx) + P\cos(\omega t + kx) = 2P\cos(\omega t)\cos(kx) \qquad (1.2)$$

Figure 1.2 and Equation (1.2) indicate the following:

- In a traveling wave the pressure is a combined function of time and position, that is $p(x,t) = f(x,t)$ while in a standing wave $p(x,t) = g(t)h(x)$, indicating that the effects of time and space are uncoupled.
- In a traveling wave the pressure maxima, also known as antinodes, and the pressure minima, also known as nodes, travel in the propagation direction with the speed of sound in the medium. In a standing wave, however, nodes and antinodes are stationary. The shape of the wave scales with time only.
- In a standing wave, the pressure amplitude is doubled in the antinodes, whereas in the nodes the waves cancel each other. In Figure 1.2c, the wave pattern is not shown at $t = 0.25T$ and $t = 0.75T$ due to the waves cancelling each other and causing a zero acoustic pressure.

In order to obtain a standing wave, two similar waves traveling opposite to each other are needed. The simplest way to obtain a standing wave is with a sound source and a reflector. If the source is radiating plane waves and the reflector is placed parallel to the sound source, a standing wave occurs between the sound source and reflector. Another way to obtain a standing wave is replacing the

reflector by an active sound source, both operated at the same frequency [66, 79].

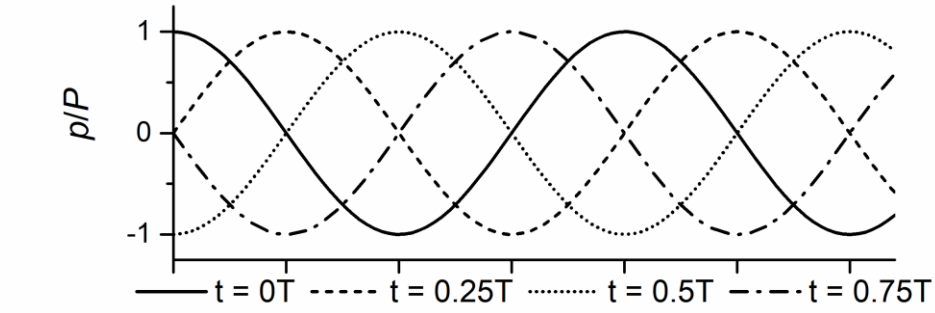

(a) $p_1(x,t) = P\cos(\omega t - kx)$

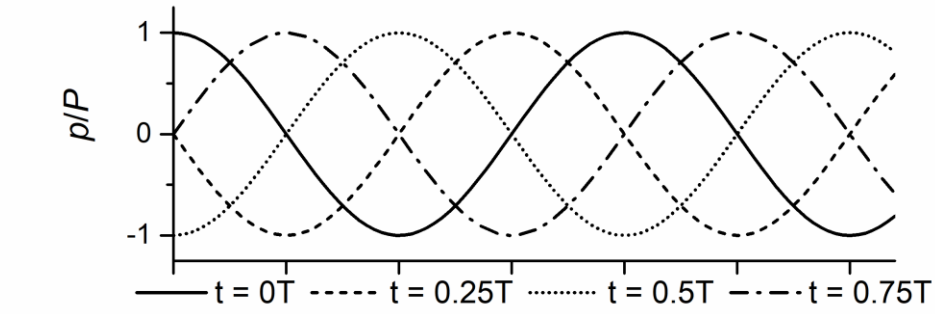

(b) $p_2(x,t) = P\cos(\omega t + kx)$

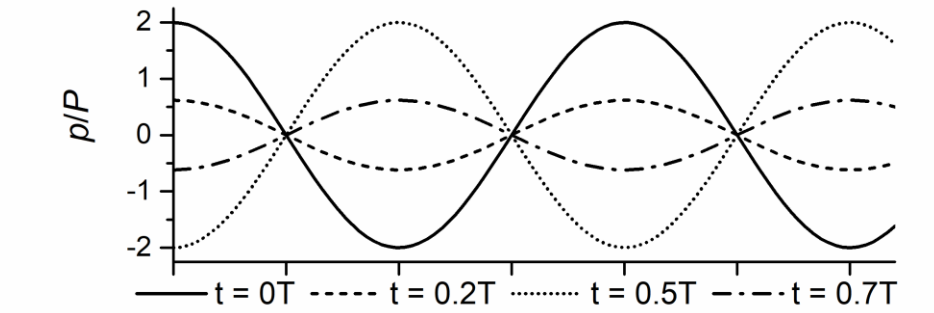

(c) $p(x,t) = p_1(x,t) + p_2(x,t)$

Figure 1.2 - (a) Positive traveling wave, (b) negative traveling wave and (c) standing wave

Figure 1.2 illustrates a standing wave field that has multiple pressure nodes. At microscale, however, the separators typically utilize a single pressure node. The separator can be a half-wavelength resonator with the pressure node in the middle of the channel, if the width of the channel is half of the wavelength in the host medium at the excitation frequency [28]. The separator can also be a quarter-wavelength resonator, if the width of the channel is a quarter of the wavelength. In such a case, a pressure node is obtained at the edge of the channel [80].

A configuration that generates a standing wave field can also generate a dynamic acoustic wave field. In case of a single sound source and a reflector, the sound source can be operated at a changing frequency, effectively making a frequency sweep [68-70]. Such a field shows the characteristics of a standing wave field, but the pressure nodes move towards the reflector with increasing frequency. Another way to generate a dynamic acoustic wave field is to use two separate sound sources, operating at slightly different frequencies [71--78]. The resulting field has the characteristics of a standing wave field, while the pressure nodes move from the low-frequency source to the high-frequency source with a speed proportional to the frequency difference between the sources.

1.2.2 Acoustic Radiation Force

As the acoustic waves carry energy, the interaction between an object and the surrounding sound field results in a net force acting on the object. Mostly, the acoustic radiation force is weak. When the object size is in the range from μm to cm and the acoustic waves are concentrated, the forces can become significant. In that case, standing wave fields are capable of concentrating and manipulating particles.

The acoustic radiation force on a spherical rigid particle was calculated first by King [32], and then for an elastic particle by Yosioka and Kawasima [33]. Later, Gor'kov formulated the acoustic radiation force acting on a small particle in an ideal fluid [29]. The expression of Gor'kov is applicable for an elastic spherical particle in any sound field, and therefore widely used in the literature.

For a spherical particle in an ideal fluid, the acoustic radiation force expression can be derived from the radiation potential U^{rad}, that is

$$U^{rad} = V\left(\Phi_1 \frac{1}{2}\rho_0 c_0^2 \langle p_{in}^2\rangle - \Phi_2 \frac{3}{4}\rho_0 \langle v_{in}^2\rangle\right) \tag{1.3}$$

Where V is the particle volume, $\langle p_{in}\rangle$ and $\langle v_{in}\rangle$ are time-averaged incident pressure and velocity fields at the location of the particle center, ρ_0 and c_0 are the density and speed of sound of the host medium and ϕ_1 and ϕ_2 are the monopole and dipole scattering coefficients. The combination of the scattering coefficients forms the acoustic contrast factor, which is given by

$$\Phi(\rho, c) = \frac{1}{3}\Phi_1 + \frac{1}{2}\Phi_2 = \frac{\rho + \frac{2}{3}(\rho - \rho_0)}{2\rho + \rho_0} - \frac{1}{3}\frac{\rho_0 c_0^2}{\rho c^2} \tag{1.4}$$

Where ρ and c are the density and the speed of sound in the particle material, respectively.

The acoustic radiation force on an elastic spherical particle in a standing wave field, in only one direction (x), can be calculated from

$$F_x^{ac} = \frac{\partial U^{rad}}{\partial x} = 4\pi k r^3 \mathrm{E_{ac}} \Phi(\rho, c)\sin(2kx) \tag{1.5}$$

Where $E_{ac} = \left(\frac{P_D^2}{4\rho_0 c_0^2}\right)$ is the acoustic energy density, with P_D is the amplitude of the standing wave field.

The acoustic radiation force on a spherical particle thus depends on the particle volume (Equation (1.5)); larger particles experience larger force thus they will be trapped easier. The amplitude of the force scales linearly with the frequency through $k = \omega/c$, and the square of the pressure amplitude through $E_{ac} = \left(\frac{P_D^2}{4\rho_0 c_0^2}\right)$. The acoustic contrast factor is a multiplier in the expression. For example, it indicates that a water particle in water will not experience any acoustic radiation force as the acoustic contrast factor is zero. The acoustic contrast factor can either be positive or negative. Figure 1.3 illustrates the force distribution on a spherical particle with a positive contrast factor in a standing wave field.

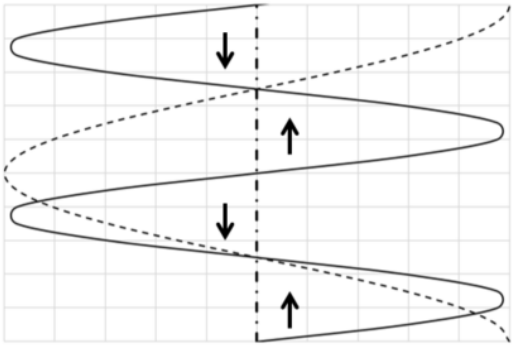

Figure 1.3 - Force distribution on a particle in a standing wave field. Dashed line indicates the harmonic pressure distribution, solid line indicates the force distribution on the particle. Arrows indicate the direction of the force

Under the effect of the acoustic radiation force only, Figure 1.3 indicates that a spherical particle with positive contrast factor experiences a net zero force in either pressure nodes or antinodes. When slightly disturbed, however, the particle will be repelled from the pressure antinodes and attracted towards the pressure nodes. Thus, a particle with a positive contrast factor can have a stable equilibrium in the pressure nodes. Similarly, a particle with negative contrast factor will be stabilized in the pressure antinodes. This property has been successfully exploited for selective cell separation on microscale [56, 80].

Exploiting the acoustic contrast factor is not the only way to selectively filter or separate particles using acoustophoresis. Whenever the particle has a relative motion with respect to the surrounding liquid there is drag force acting on the particle. Figure 1.4 illustrates a generic picture of forces acting on a particle in an acoustic field, where the acoustic field acts in y direction and the flow is in x direction.

In acoustophoresis applications commonly the flow has a low Reynolds number, hence laminar. On a spherical particle, therefore, the drag force is modeled as Stokes drag: $F_x^D = 6\pi\mu r(u_x(y) - \dot{x})$ in x direction and $F_y^D = 6\pi\mu r(u_y(x) - \dot{y})$ in y direction. The equation of motion for a spherical particle in a two-dimensional acoustic field and a laminar flow field, with velocities $u_x(y)$ and $u_y(x)$, is therefore given by

$$m\ddot{x} + 6\pi\mu r(u_x(y) - \dot{x}) + F_x^{ac}(x,t) = 0$$
$$m\ddot{y} + 6\pi\mu r\left(u_y(x) - \dot{y}\right) + F_y^{ac}(x,t) = 0 \quad (1.6)$$

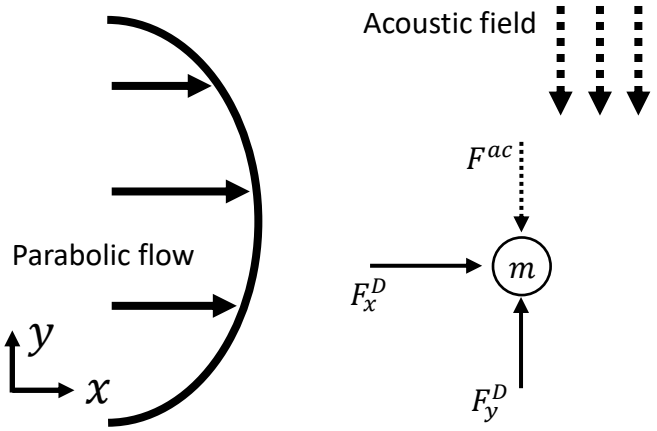

Figure 1.4 – Forces acting on a particle moving in an acoustic field

Investigation of Equations (1.5) and (1.6) together shows that while the acoustic radiation force scales with particle volume, the drag force scales with particle radius. Furthermore, the acoustic contrast factor depends on the particle's elastic modulus and speed of sound. The interplay of such parameters offers the following selectivity possibilities;

1- Depending on the acoustic contrast factor, particles are attracted towards either nodes or antinodes. This possibility has been exploited on microscale, for example, in [56, 80].
2- Depending on the acoustic contrast factor, some particles are attracted faster towards either nodes or antinodes.
3- Depending on the particle size, some particles are attracted faster towards the corresponding locations. This possibility has been exploited on microscale, for example, in [34].
4- The flow and the acoustic field can be in the same direction, making the flow, for example, push the particles selectively against the acoustic field. This possibility is very suitable for applications at macroscale and demonstrated in Chapter 3, using different particle sizes.
5- Similar to case 4, a dynamic acoustic field can actively push the particles selectively against the flow.

6- Similar to a case in Figure 1.4, a dynamic acoustic field can push the particles selectively perpendicular to the flow direction. This possibility is very suitable at macroscale and demonstrated in Chapters 5 and 6 using different particle sizes.

1.2.3 Piezoelectric Effect

To create an acoustic field in an acoustophoresis device piezoelectric transducers are utilized, making use of the converse piezoelectric effect. The converse piezoelectric effect is realized through an electric field across certain opposite faces of the material and results in deformation. The opposite, the direct piezoelectric effect is more commonly used in sensing, as the deformation in the material results in an electric field across certain opposite faces of the material. Materials that show this effect are called piezo-electric materials, where 'piezin' means 'to press' in Greek.

The constitutive modeling of linear piezoelectric materials uses relationships for linear elasticity and electrostatic charge equations. The relation between an applied electric field and corresponding free strain in the piezoelectric material is given by

$$\varepsilon_{33} = d_{33}\frac{V}{t_p}$$
$$\varepsilon_{31} = d_{31}\frac{V}{t_p} \tag{1.7}$$

Here, V is the voltage applied in the polarization direction and t_p is the thickness of the material in the polarization direction. The polarization direction is denoted by direction 3 in piezoelectric elements, thus ε_{33} is the strain in the third direction and d_{33} is the piezoelectric modulus in the corresponding direction. Similarly, ε_{31} is the strain in the first direction and d_{31} is the corresponding modulus. Equation (1.8) introduces the 1D model of piezoelectric behavior [81]

$$\begin{bmatrix} S \\ D \end{bmatrix} = \begin{bmatrix} s & d \\ d & \epsilon \end{bmatrix} \begin{bmatrix} T \\ E \end{bmatrix} \tag{1.8}$$

Top row of Equation (1.8) governs the converse piezoelectric effect while bottom row governs the direct piezoelectric effect. Diagonal terms of the matrix contain the mechanical and electrical constitutive relations while off-diagonal terms govern

the electromechanical coupling. S is the mechanical strain, D is the electrical displacement, T is the mechanical stress and E is the electric field. Furthermore, s is the mechanical compliance, ϵ is the dielectric permittivity and d is the piezoelectric strain coefficient. Equation (1.8) can also be rewritten as given by Equation (1.9).

$$\begin{bmatrix} T \\ E \end{bmatrix} = \frac{1}{1-\kappa^2} \begin{bmatrix} s^{-1} & d^{-1}\kappa^2 \\ d^{-1}\kappa^2 & \epsilon^{-1} \end{bmatrix} \begin{bmatrix} S \\ D \end{bmatrix} \tag{1.9}$$

Where $\kappa = \frac{d}{\sqrt{s\epsilon}}$ is the piezoelectric coupling coefficient. κ is bounded between 0 and 1 and is related to the energy conversion properties of the piezoelectric material. The bounds already indicate that only a fraction of energy is converted. For multiple directions, multiple coupling coefficients exist.

The 1D model for piezoelectric behavior can be extended to 3D using a similar approach. In case of a 3D material Equation (1.8) holds while S is the mechanical strain vector, D is the electrical displacement vector, T is the stress vector and E is the electric field vector (6×1). Furthermore, s is the elastic modulus matrix (6×6) under constant electric field boundary condition, ϵ is the dielectric permittivity matrix (3×3) under constant stress boundary condition and d is the piezoelectric coupling matrix (6×3). Assuming the 3D material is orthotropic and there is symmetry between the first and second directions, the top rows of Equation (1.8) can be expanded and simplified as [81]

$$\begin{bmatrix} S_1 \\ S_2 \\ S_3 \\ S_4 \\ S_5 \\ S_6 \end{bmatrix} = \begin{bmatrix} \frac{1}{Y_1^E} & -\frac{\nu_{12}}{Y_1^E} & -\frac{\nu_{13}}{Y_1^E} & 0 & 0 & 0 \\ -\frac{\nu_{12}}{Y_1^E} & \frac{1}{Y_1^E} & -\frac{\nu_{23}}{Y_1^E} & 0 & 0 & 0 \\ -\frac{\nu_{31}}{Y_3^E} & -\frac{\nu_{32}}{Y_3^E} & \frac{1}{Y_3^E} & 0 & 0 & 0 \\ 0 & 0 & 0 & \frac{1}{G_{23}^E} & 0 & 0 \\ 0 & 0 & 0 & 0 & \frac{1}{G_{13}^E} & 0 \\ 0 & 0 & 0 & 0 & 0 & \frac{1}{G_{12}^E} \end{bmatrix} \begin{bmatrix} T_1 \\ T_2 \\ T_3 \\ T_4 \\ T_5 \\ T_6 \end{bmatrix} + \begin{bmatrix} 0 & 0 & d_{13} \\ 0 & 0 & d_{23} \\ 0 & 0 & d_{33} \\ 0 & d_{24} & 0 \\ d_{15} & 0 & 0 \\ 0 & 0 & 0 \end{bmatrix} \begin{bmatrix} E_1 \\ E_2 \\ E_3 \end{bmatrix} \tag{1.10}$$

Similarly, the bottom rows of Equation (1.8) can be expanded as

$$\begin{bmatrix} D_1 \\ D_2 \\ D_3 \end{bmatrix} = \begin{bmatrix} 0 & 0 & 0 & 0 & d_{15} & 0 \\ 0 & 0 & 0 & d_{24} & 0 & 0 \\ d_{13} & d_{23} & d_{33} & 0 & 0 & 0 \end{bmatrix} \begin{bmatrix} T_1 \\ T_2 \\ T_3 \\ T_4 \\ T_5 \\ T_6 \end{bmatrix} + \begin{bmatrix} \epsilon_{11}^T & 0 & 0 \\ 0 & \epsilon_{22}^T & 0 \\ 0 & 0 & \epsilon_{33}^T \end{bmatrix} \begin{bmatrix} E_1 \\ E_2 \\ E_3 \end{bmatrix} \tag{1.11}$$

Where Y_i^E is the elastic modulus in the i direction, ν_{ij} is the Poisson's ratio governing the ratio of transverse strain in j direction to the axial strain in i direction and G_{ij}^E are the shear moduli. The superscript E indicates that the property is measured under short circuit condition, when there is no electric field to affect the mechanical behavior. Similarly, superscript T indicates that the property is measured under stress-free condition, when there are no mechanical constraints on the material to generate electric field. In 3D, multiple coupling coefficients exist for different directions as $\kappa_{ij} = \frac{d_{ij}}{\sqrt{\epsilon_{ii}^T s_{jj}^E}}$.

In order to generate the acoustic field in the acoustophoresis devices the transducers are mostly used in 33 mode. In 33 mode the voltage is applied in the 3 direction and the mechanical response is generated in the 3 direction. Hence, Equations (1.10) and (1.11) reduce to [81]

$$S_3 = \frac{1}{Y_3^E} T_3 + d_{33} E_3 \tag{1.12}$$

$$D_3 = d_{33} T_3 + \epsilon_{33}^T E_3 \tag{1.13}$$

With the assumption of uniform strain, stress, electric field and electric displacement, the strain in the 3 direction becomes $S_3 = u_3/t_p$. Similarly, the stress becomes $T_3 = f_3/A_p$, the electric field becomes $E_3 = V/t_p$ and the electric displacement becomes $D_3 = q/A_p$. In this expressions f_3 is the force applied to the transducer, u_3 is the displacement in 3 direction, V is the voltage applied, q is the charge and A_p is the cross-sectional area of the transducer. Inserting these expressions and defining the stiffness of the transducer as $k_p = \frac{Y_3^E A_p}{t_p}$, Equation (1.12) becomes

$$u_3 = \frac{1}{k_p} f + d_{33} V \tag{1.14}$$

The maximum stress can develop in the transducer when the transducer is completely restrained and therefore $u_3 = 0$. The force applied on the transducer (and hence applied by the transducer) is defined as the blocked force, and expressed as

$$f_b = d_{33} Y_3^E \frac{A_p}{t_p} V \tag{1.15}$$

Similarly, the maximum displacement is obtained when there is no force acting on the transducer. The free displacement, δ_0, is expressed as

$$\delta_0 = d_{33}V \tag{1.16}$$

Furthermore, the excited medium has its own elastic and mechanical properties. In order to represent such a condition, consider a piezoelectric device exciting a single degree of freedom mass-spring system axially in the third direction, illustrated in Figure 1.5, where the stiffness of the connection between the mass and the ground is k_s, the stiffness of the piezoelectric material is k_p and the mass is m. The transducer and the mass remain in contact; hence, the deformation of the transducer is equal to the displacement of the mass. Under these conditions, the equation of motion of the mass is given by

$$f + m\frac{d^2u(t)}{dt^2} + k_s u(t) = 0 \tag{1.17}$$

Inserting Equation (1.17) into Equation (1.14) yields the following relation

$$u_3(t) = \frac{1}{k_p}\left(-m\frac{d^2u_3(t)}{dt^2} - k_s u_3(t)\right) + u_0 V(t) \tag{1.18}$$

In Equation (1.18), u_0 is the free displacement of the transducer for unit voltage input, $u_3(t)$ is the displacement of the transducer equal to the displacement of the mass and $V(t)$ is the voltage input to the transducer. Assuming a harmonic excitation $V(t) = V_0 e^{i\omega t}$, similarly $u_3(t) = U_3 e^{i\omega t}$, where V_0 and U_3 are the amplitudes of the input and output, respectively. The natural frequency of the mass-spring system is $\omega_n = \sqrt{k_s/m}$. The ratio of the displacement response to the voltage input is given by

$$\frac{U_3}{u_o V_0} = \frac{1}{1 + \left(\frac{k_s}{k_p}\right) - \left(\frac{\omega}{\omega_n}\right)^2} \tag{1.19}$$

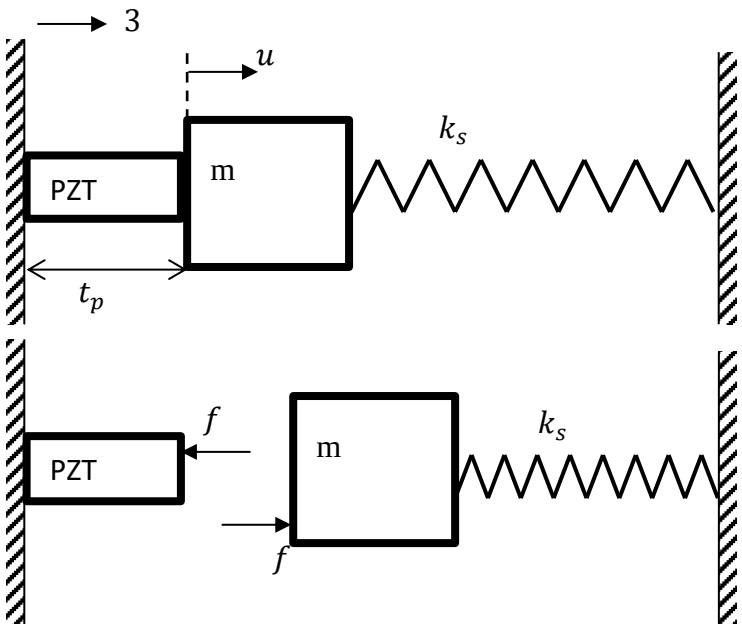

Figure 1.5 - An elastic structure excited by a piezoelectric transducer. Voltage applied to the transducer is deforming the transducer, whereas the presence of the elastic structure is resisting this deformation by applying a force on the transducer.

Equation (1.19) indicates that the ratio of the response of the mass to the voltage input is maximized when $\omega = \omega_n$. Hence, exciting the acoustophoresis devices in the resonant frequencies is the most effective way of using the transducer.

1.3 Research Aim

Acoustic separation is a promising method for selectively separating and/or filtering of particulate matter in suspensions. This thesis investigates the possibilities on cm-scale, where the following research questions were formulated:

1- How do the particles behave under an acoustic standing wave field? Which parameters affect the particle behavior and in which ways?

2- What is needed to scale up microscale applications to applications on a cm-scale using an ultrasonic resonator?

3- How can multi-wavelength standing wave fields be used for selective separation on cm-scale?
4- What are the possibilities offered by dynamic standing wave fields on cm-scale? How do particles behave under such conditions?

The approach, while investigating the issues as formulated in the research questions, is as follows. First, a mathematical model that is able to represent the conditions affecting the particle was proposed and analyzed in order to understand the particle behavior. Second, to gain more detailed insight and to better represent the real conditions, computer models were created using Mathcad, MATLAB and COMSOL Multiphysics. Especially the simulations in COMSOL Multiphysics supported the development of prototypes. Third, prototypes were created in a CAD environment using Kubotek KeyCreator and subsequently manufactured by 3D printing. Fourth, assessment of the filtering was done by using a DIPA2000 particle size & shape analyzer in Chapters 3 and 5, and by using a Mastersizer 3000 Particle size analyzer in Chapter 6. The responses of the piezoelectric transducers were measured by using a Polytec OFV 5000 single point laser Doppler vibrometer. Its responses were used to improve the computer models in Chapters 5 and 6.

1.4 Thesis Outline

This thesis consists of seven Chapters.

Chapter 2 revisits the theory of acoustophoretic particle manipulation, by focusing on a half-wavelength resonator on microscale. A linearized single degree-of freedom was introduced to investigate the effects of the excitation parameters on particle behavior, illuminating the path towards selectivity of acoustophoresis.

Chapter 3 presents a selective separation application, using a combination of a multi-wavelength acoustic standing wave field and a special serpentine flow field.

Chapter 4 introduces in-depth investigations of dynamic acoustic fields as another way to enhance the interplay between acoustic radiation force and drag force in multi-wavelength resonators, laying the foundation for Chapters 5 and 6.

Chapter 5 demonstrates selective particle separation on centimeter scale by frequency sweep type of dynamic acoustic field, using an X-shaped prototype with two inlets and two outlets.

Similar to Chapter 5, Chapter 6 demonstrates selective particle separation on centimeter scale by dual frequency type dynamic acoustic field, using an X-shaped prototype specially designed to minimize reflections.

Chapter 7 presents a general discussion on the topics presented in the previous chapters. Some explorative studies related to the chapters were also included here. Finally, an outlook was provided for possible future studies.

References

[1] Sagan, C., Tyson, N.D., Druyan, A., 2013. Cosmos. Ballantine, New York.

[2] Lem, S., 1986. One human minute. Harcourt Brace Jovanovich, San Diego [Calif.

[3] Kundera, M., 2020. The Festival of Insignificance. Faber and Faber.

[4] Luo, Y., Guo, W., Ngo, H.H., Nghiem, L.D., Hai, F.I., Zhang, J., Liang, S., Wang, X.C., 2014. A review on the occurrence of micropollutants in the aquatic environment and their fate and removal during wastewater treatment. Science of The Total Environment 473–474, 619–641. doi:10.1016/j.scitotenv.2013.12.065

[5] Cappon, H.J., 2014. Numerical and experimental design of ultrasonic particle filters for water treatment.

[6] Ngomsik, A.-F., Bee, A., Draye, M., Cote, G., Cabuil, V., 2005. Magnetic nano- and microparticles for metal removal and environmental applications: a review. Comptes Rendus Chimie 8, 963–970. doi:10.1016/j.crci.2005.01.001

[7] McClements, D.J., 2018. Encapsulation, protection, and delivery of bioactive proteins and peptides using nanoparticle and microparticle systems: A review. Advances in Colloid and Interface Science 253, 1–22. doi:10.1016/j.cis.2018.02.002

[8] Gao, Y., Wu, M., Lin, Y., Xu, J., 2020. Acoustic Microfluidic Separation Techniques and Bioapplications: A Review. Micromachines 11, 921. doi:10.3390/mi11100921

[9] Bowen, W.R., Jenner, F., 1995. Theoretical descriptions of membrane filtration of colloids and fine particles: An assessment and review. Advances in Colloid and Interface Science 56, 141–200. doi:10.1016/0001-8686(94)00232-2

[10] Dizge, N., Soydemir, G., Karagündüz, A., Keskinler, B., 2011. Influence of type and pore size of membranes on cross flow microfiltration of biological suspension. Journal of Membrane Science 366, 278–285. doi:10.1016/j.memsci.2010.10.010

[11] Narong, P., James, A.E., 2008. Efficiency of ultrafiltration in the separation of whey suspensions using a tubular zirconia membrane. Desalination 219, 348–357. doi:10.1016/j.desal.2007.04.057

[12] Al-Faqheri, W., Thio, T.H.G., Qasaimeh, M.A., Dietzel, A., Madou, M., Al-Halhouli, A., 2017. Particle/cell separation on microfluidic platforms based on centrifugation effect: a review. Microfluidics and Nanofluidics 21, 102. doi:10.1007/s10404-017-1933-4

[13] Bloesch, J., Burns, N.M., 1980. A critical review of sedimentation trap technique. Schweizerische Zeitschrift für Hydrologie 42, 15–55. doi:10.1007/BF02502505

[14] Sajeesh, P., Sen, A.K., 2014. Particle separation and sorting in microfluidic devices: a review. Microfluidics and Nanofluidics 17, 1–52. doi:10.1007/s10404-013-1291-9

[15] McGrath, J., Jimenez, M., Bridle, H., 2014. Deterministic lateral displacement for particle separation: a review. Lab on a Chip 14, 4139–4158. doi:10.1039/C4LC00939H

[16] Dijkshoorn, J.P., Schutyser, M.A.I., Wagterveld, R.M., Schroën, C.G.P.H., Boom, R.M., 2017. A comparison of microfiltration and inertia-based microfluidics for large scale suspension separation. Separation and Purification Technology 173, 86–92. doi:10.1016/j.seppur.2016.09.018

[17] Trujillo, F.J., Juliano, P., Barbosa-Cánovas, G., Knoerzer, K., 2014. Separation of suspensions and emulsions via ultrasonic standing waves – A review. Ultrasonics Sonochemistry, AOSS 2013 21, 2151–2164. doi:10.1016/j.ultsonch.2014.02.016

[18] Leong, T., Johansson, L., Juliano, P., McArthur, S.L., Manasseh, R., 2013. Ultrasonic Separation of Particulate Fluids in Small and Large Scale Systems: A Review. Industrial & Engineering Chemistry Research 52, 16555–16576. doi:10.1021/ie402295r

[19] Oberteuffer, J., 1974. Magnetic separation: A review of principles, devices, and applications. IEEE Transactions on Magnetics 10, 223–238. doi:10.1109/TMAG.1974.1058315

[20] Martel, J.M., Toner, M., 2014. Inertial Focusing in Microfluidics. Annual Review of Biomedical Engineering 16, 371–396. doi:10.1146/annurev-bioeng-121813-120704

[21] Einstein, A., 2019. The meaning of relativity. San Bernardino, CA.

[22] Prest, J.E., Treves Brown, B.J., Fielden, P.R., Wilkinson, S.J., Hawkes, J.J., 2015. Scaling-up ultrasound standing wave enhanced sedimentation filters. Ultrasonics 56, 260–270. doi:10.1016/j.ultras.2014.08.003

[23] Hawkes, J.J., Limaye, M.S., Coakley, W.T., 1997. Filtration of bacteria and yeast by ultrasound-enhanced sedimentation. Journal of Applied Microbiology 82, 39–47. doi:10.1111/j.1365-2672.1997.tb03295.x

[24] Hawkes, J.J., Limaye, M.S., Coakley, W.T., 1995. An ultrasonic method for filtering and separating cell suspensions, in: 1995 IEEE Ultrasonics Symposium. Proceedings. An International Symposium. Presented at the 1995 IEEE Ultrasonics Symposium. Proceedings. An International Symposium, pp. 1069–1072 vol.2. doi:10.1109/ULTSYM.1995.495746

[25] Bosma, R., van Spronsen, W.A., Tramper, J., Wijffels, R.H., 2003. Ultrasound, a new separation technique to harvest microalgae. Journal of Applied Phycology 15, 143–153. doi:10.1023/A:1023807011027

[26] Feng, X., Deng, J., Lei, H., Bai, T., Fan, Q., Li, Z., 2009. Dewaterability of waste activated sludge with ultrasound conditioning. Bioresource Technology 100, 1074–1081. doi:10.1016/j.biortech.2008.07.055

[27] Silva, G.T., 2014. Acoustic radiation force and torque on an absorbing compressible particle in an inviscid fluid. The Journal of the Acoustical Society of America 136, 2405–2413. doi:10.1121/1.4895691

[28] Bruus, H., 2012. Acoustofluidics 7: The acoustic radiation force on small particles. Lab on a Chip 12, 1014–1021. doi:10.1039/C2LC21068A

[29] Gor'kov, L.P., 1962. On the Forces Acting on a Small Particle in an Acoustical Field in an Ideal Fluid. Soviet Physics Doklady 6, 773.

[30] Doinikov, A.A., 1997. Acoustic radiation force on a spherical particle in a viscous heat-conducting fluid. I. General formula. The Journal of the Acoustical Society of America 101, 713–721. doi:10.1121/1.418035

[31] Gröschl, M., 1998. Ultrasonic Separation of Suspended Particles - Part I: Fundamentals. Acta Acustica united with Acustica 84, 432–447.

[32] King, L.V., 1934. On the acoustic radiation pressure on spheres. Proceedings of the Royal Society of London. Series A - Mathematical and Physical Sciences 147, 212–240. doi:10.1098/rspa.1934.0215

[33] Yosioka, K., Kawasima, Y., 1955. Acoustic radiation pressure on a compressible sphere. Acta Acustica united with Acustica 5, 167–173.

[34] Lenshof, A., Laurell, T., 2010. Continuous separation of cells and particles in microfluidic systems. Chemical Society Reviews 39, 1203–1217. doi:10.1039/B915999C

[35] Iv, C.W.S., Reyes, C.D., López, G.P., 2015. Microfluidic cell sorting: a review of the advances in the separation of cells from debulking to rare cell isolation. Lab on a Chip 15, 1230–1249. doi:10.1039/C4LC01246A

[36] Yeo, L.Y., Friend, J.R., 2009. Ultrafast microfluidics using surface acoustic waves. Biomicrofluidics 3. doi:10.1063/1.3056040

[37] Franke, T., Braunmüller, S., Schmid, L., Wixforth, A., Weitz, D.A., 2010. Surface acoustic wave actuated cell sorting (SAWACS). Lab on a Chip 10, 789–794. doi:10.1039/B915522H

[38] Nam, J., Lim, H., Kim, C., Yoon Kang, J., Shin, S., 2012. Density-dependent separation of encapsulated cells in a microfluidic channel by using a standing surface acoustic wave. Biomicrofluidics 6, 024120. doi:10.1063/1.4718719

[39] Shi, J., Huang, H., Stratton, Z., Huang, Y., Huang, T.J., 2009. Continuous particle separation in a microfluidic channel via standing surface acoustic waves (SSAW). Lab on a Chip 9, 3354–3359. doi:10.1039/B915113C

[40] Ding, X., Lin, S.-C.S., Kiraly, B., Yue, H., Li, S., Chiang, I.-K., Shi, J., Benkovic, S.J., Huang, T.J., 2012. On-chip manipulation of single microparticles, cells, and organisms using surface acoustic waves. Proceedings of the National Academy of Sciences of the United States of America 109, 11105–11109. doi:10.1073/pnas.1209288109

[41] Li, P., Mao, Z., Peng, Z., Zhou, L., Chen, Y., Huang, P.-H., Truica, C.I., Drabick, J.J., El-Deiry, W.S., Dao, M., Suresh, S., Huang, T.J., 2015. Acoustic separation of circulating tumor cells. Proceedings of the National Academy of Sciences of the United States of America 112, 4970–4975. doi:10.1073/pnas.1504484112

[42] Nam, J., Lee, Y., Shin, S., 2011. Size-dependent microparticles separation through standing surface acoustic waves. Microfluidics and Nanofluidics 11, 317–326. doi:10.1007/s10404-011-0798-1

[43] Laurell, T., Petersson, F., Nilsson, A., 2007. Chip integrated strategies for acoustic separation and manipulation of cells and particles. Chemical Society Reviews 36, 492–506. doi:10.1039/B601326K

[44] Destgeer, G., Lee, K.H., Jung, J.H., Alazzam, A., Sung, H.J., 2013. Continuous separation of particles in a PDMS microfluidic channel via travelling surface acoustic waves (TSAW). Lab on a Chip 13, 4210–4216. doi:10.1039/C3LC50451D

[45] Lenshof, A., Evander, M., Laurell, T., Nilsson, J., 2012. Acoustofluidics 5: Building microfluidic acoustic resonators. Lab on a Chip 12, 684–695. doi:10.1039/C1LC20996E

[46] Schmid, L., Weitz, D.A., Franke, T., 2014. Sorting drops and cells with acoustics: acoustic microfluidic fluorescence-activated cell sorter. Lab on a Chip 14, 3710–3718. doi:10.1039/C4LC00588K

[47] Wang, K., Zhou, W., Lin, Z., Cai, F., Li, F., Wu, J., Meng, L., Niu, L., Zheng, H., 2018. Sorting of tumour cells in a microfluidic device by multi-stage surface acoustic waves. Sensors and Actuators B: Chemical 258, 1174–1183. doi:10.1016/j.snb.2017.12.013

[48] Vakarelski, I.U., Li, E.Q., Abdel-Fattah, A.I., Thoroddsen, S.T., 2016. Acoustic separation of oil droplets, colloidal particles and their mixtures in a microfluidic cell. Colloids and Surfaces A: Physicochemical and Engineering Aspects 506, 138–147. doi:10.1016/j.colsurfa.2016.06.013

[49] Shen, Y., Yalikun, Y., Tanaka, Y., 2019. Recent advances in microfluidic cell sorting systems. Sensors and Actuators B: Chemical 282, 268–281. doi:10.1016/j.snb.2018.11.025

[50] Ma, Z., Collins, D.J., Guo, J., Ai, Y., 2016. Mechanical Properties Based Particle Separation via Traveling Surface Acoustic Wave. Analytical Chemistry 88, 11844–11851. doi:10.1021/acs.analchem.6b03580

[51] Huang, T.J., 2019. Acoustofluidics: Merging acoustics and microfluidics for biomedical applications. The Journal of the Acoustical Society of America 145, 1786–1786. doi:10.1121/1.5101531

[52] Xie, Y., Mao, Z., Bachman, H., Li, P., Zhang, P., Ren, L., Wu, M., Huang, T.J., 2020. Acoustic Cell Separation Based on Density and Mechanical Properties. Journal of Biomechanical Engineering 142. doi:10.1115/1.4046180

[53] Clark, C.P., Xu, K., Scott, O., Hickey, J., Tsuei, A.-C., Jackson, K., Landers, J.P., 2019. Acoustic trapping of sperm cells from mock sexual assault samples. Forensic Science International: Genetics 41, 42–49. doi:10.1016/j.fsigen.2019.03.012

[54] Benes, E., Groschl, M., Nowotny, H., Trampler, F., Keijzer, T., Bohm, H., Radel, S., Gherardini, L., Hawkes, J.J., Konig, R., Delouvroy, C., 2001. Ultrasonic separation of suspended particles, in: 2001 IEEE Ultrasonics Symposium. Proceedings. An International Symposium (Cat. No.01CH37263). Presented at the 2001 IEEE Ultrasonics Symposium. Proceedings. An International Symposium (Cat. No.01CH37263), pp. 649–659 vol.1. doi:10.1109/ULTSYM.2001.991812

[55] Brodeur, P.H., 1994. Acoustic separation in a laminar flow, in: 1994 Proceedings of IEEE Ultrasonics Symposium. Presented at the 1994 Proceedings of IEEE Ultrasonics Symposium, pp. 1359–1362 vol.3. doi:10.1109/ULTSYM.1994.401842

[56] Jönsson, H., Holm, C., Nilsson, A., Petersson, F., Johnsson, P., Laurell, T., 2004. Particle Separation Using Ultrasound Can Radically Reduce Embolic Load to Brain After Cardiac Surgery. The Annals of Thoracic Surgery 78, 1572–1577. doi:10.1016/j.athoracsur.2004.04.071

[57] Hawkes, J.J., Radel, S., 2013. Acoustofluidics 22: Multi-wavelength resonators, applications and considerations. Lab on a Chip 13, 610–627. doi:10.1039/C2LC41206C

[58] Gómez, E.H., Marchese, A.J., 2015. An ultrasonically enhanced inclined settler for microalgae harvesting. Biotechnology Progress 31, 414–423. doi:10.1002/btpr.2031

[59] Setayeshgar, A., Lipsett, M.G., Koch, C.R., Nobes, D.S., 2015. Particle Motion in a Macroscale, Multiwavelength Acoustic Field. Journal of Fluids Engineering 137. doi:10.1115/1.4027777

[60] Riera, E., Gallego-Juárez, J.A., Mason, T.J., 2006. Airborne ultrasound for the precipitation of smokes and powders and the destruction of foams. Ultrasonics Sonochemistry 13, 107–116. doi:10.1016/j.ultsonch.2005.04.001

[61] Benes, E., Groschl, M., Nowotny, H., Bohm, H., Radel, S., Hauser, C., Power, J., Lowe, K., Briarty, G., Davey, M., 2003. The Ultrasonic h-shape Separator: Harvesting of the Alga Spirulina Platensis under Zero-Gravity Conditions. Presented at the World Congress on Ultrasonics, pp. 1631–1638.

[62] Böhm, H., Briarty, L.G., Lowe, K.C., Power, J.B., Benes, E., Davey, M.R., 2003. Quantification of a novel h-shaped ultrasonic resonator for separation of biomaterials under terrestrial gravity and microgravity conditions. Biotechnology and Bioengineering 82, 74–85. doi:10.1002/bit.10546

[63] Hill, M., Wood, R.J.K., 2000. Modelling in the design of a flow-through ultrasonic separator. Ultrasonics 38, 662–665. doi:10.1016/S0041-624X(99)00134-1

[64] Hawkes, J.J., Barrow, D., Cefai, J., Coakley, W.T., 1998. A laminar flow expansion chamber facilitating downstream manipulation of particles concentrated using an ultrasonic standing wave. Ultrasonics 36, 901–903. doi:10.1016/S0041-624X(98)00018-3

[65] Liu, Y., Lim, K.-M., 2011. Particle separation in microfluidics using a switching ultrasonic field. Lab on a Chip 11, 3167–3173. doi:10.1039/C1LC20481E

[66] Drinkwater, B.W., 2016. Dynamic-field devices for the ultrasonic manipulation of microparticles. Lab on a Chip 16, 2360–2375. doi:10.1039/C6LC00502K

[67] Glynne-Jones, P., Boltryk, R.J., Harris, N.R., Cranny, A.W.J., Hill, M., 2010. Mode-switching: A new technique for electronically varying the agglomeration position in an acoustic particle manipulator. Ultrasonics 50, 68–75. doi:10.1016/j.ultras.2009.07.010

[68] Manneberg, O., Vanherberghen, B., Önfelt, B., Wiklund, M., 2009. Flow-free transport of cells in microchannels by frequency-modulated ultrasound. Lab on a Chip 9, 833–837. doi:10.1039/B816675G

[69] Trujillo, F.J., Eberhardt, S., Möller, D., Dual, J., Knoerzer, K., 2013. Multiphysics modelling of the separation of suspended particles via frequency ramping of ultrasonic standing waves. Ultrasonics Sonochemistry 20, 655–666. doi:10.1016/j.ultsonch.2012.08.014

[70] Lipkens, B., Costolo, M., Rietman, E., 2008. The Effect of Frequency Sweeping and Fluid Flow on Particle Trajectories in Ultrasonic Standing Waves. IEEE Sensors Journal 6, 667–677. doi:10.1109/JSEN.2008.922675

[71] Grinenko, A., Ong, C.K., Courtney, C.R.P., Wilcox, P.D., Drinkwater, B.W., 2012. Efficient counter-propagating wave acoustic micro-particle manipulation. Applied Physics Letters 101, 233501. doi:10.1063/1.4769092

[72] Courtney, C.R.P., Ong, C.-K., Drinkwater, B.W., Bernassau, A.L., Wilcox, P.D., Cumming, D.R.S., 2012. Manipulation of particles in two dimensions using phase controllable ultrasonic standing waves. Proceedings of the Royal Society A: Mathematical, Physical and Engineering Sciences 468, 337–360. doi:10.1098/rspa.2011.0269

[73] Meng, L., Cai, F., Zhang, Z., Niu, L., Jin, Q., Yan, F., Wu, J., Wang, Z., Zheng, H., 2011. Transportation of single cell and microbubbles by phase-shift introduced to standing leaky surface acoustic waves. Biomicrofluidics 5, 44104–4410410. doi:10.1063/1.3652872

[74] Orloff, N.D., Dennis, J.R., Cecchini, M., Schonbrun, E., Rocas, E., Wang, Y., Novotny, D., Simmonds, R.W., Moreland, J., Takeuchi, I., Booth, J.C., 2011. Manipulating particle trajectories with phase-control in surface acoustic wave microfluidics. Biomicrofluidics 5, 44107–441079. doi:10.1063/1.3661129

[75] Skotis, G.D., Cumming, D.R.S., Roberts, J.N., Riehle, M.O., Bernassau, A.L., 2015. Dynamic acoustic field activated cell separation (DAFACS). Lab on a Chip 15, 802–810. doi:10.1039/C4LC01153H

[76] Andrade, M.A.B., Skotis, G.D., Ritchie, S., Cumming, D.R.S., Riehle, M.O., Bernassau, A.L., 2016. Contactless Acoustic Manipulation and Sorting of Particles by Dynamic Acoustic Fields. IEEE Transactions on Ultrasonics, Ferroelectrics, and Frequency Control 63, 1593–1600. doi:10.1109/TUFFC.2016.2608759

[77] Rhyou, C., Park, S., Lee, H., 2019. Optimal rate for continuous phase modulation in standing surface acoustic waves. Journal of Mechanical Science and Technology 33, 3819–3829. doi:10.1007/s12206-019-0725-z

[78] Simon, G., Andrade, M.A.B., Riehle, M.O., Desmulliez, M.P.Y., Bernassau, A.L., 2018. Numerical simulation of particle motion in a phase modulated surface acoustic wave microfluidic device. 2018 IEEE International Ultrasonics Symposium (IUS) 8579942. doi:10.1109/ULTSYM.2018.8579942

[79] Andrade, M.A.B., Pérez, N., Adamowski, J.C., 2018. Review of Progress in Acoustic Levitation. Brazilian Journal of Physics 48, 190–213. doi:10.1007/s13538-017-0552-6

[80] Townsend, R.J., Hill, M., Harris, N.R., McDonnell, M.B., 2008. Performance of a quarter-wavelength particle concentrator. Ultrasonics, Selected Papers from ICU 2007 48, 515–520. doi:10.1016/j.ultras.2008.06.005

[81] Leo, D.J., 2007. Engineering analysis of smart material systems. Wiley, Hoboken, N.J.

2 CONSIDERATIONS ABOUT A LINEARIZED SINGLE DEGREE-OF-FREEDOM MODEL TO PREDICT PARTICLE BEHAVIOR IN MICROSCALE ACOUSTOPHORESIS

A version of this chapter has been submitted to Acta Acoustica as:

Kandemir, M. H., Wagterveld, R. M., Yntema, D. R., & Keesman, K. J. (2020). Considerations about a linearized single degree-of-freedom model to predict particle behavior in microscale acoustophoresis.

Abstract

Acoustophoresis is a method employed in particle separation and fractionation. Behavior of particles in an acoustic standing wave field is modeled by a non-linear second-order differential equation, which has no analytical solution. An approximate analytical solution, where the inertia of the particle is ignored and the order of the equation is reduced to one, is widely used in half-wavelength separators with only one pressure node. This solution predicts that a particle will asymptotically converge to the pressure node, usually in the middle of the channel. Alternatively, this article aims at presenting and investigating a linear single degree-of-freedom (SDOF) model that predicts the non-specific particle behavior in an acoustic standing wave field. The region of interest (ROI) is defined by the starting position of a particle and the desired target position of a particle in a half-wavelength separator. The non-linear acoustic radiation force term is stepwise linearized within the ROI, leading to a linear second-order differential equation. Consequently, the particle behavior is modelled in terms of a linear SDOF vibrating system, which allows for analytical solutions, and thus well suited to support the design of particle separators. The stepwise linearization allows a user-defined accuracy of the particle trajectory and transition time, while being computationally efficient compared to numerical solutions. The SDOF model also allows the prediction of oscillation and overshoot under known excitation conditions. Consequently, this new model brings a methodology to directly predict the effect of particle and excitation parameters on particle behavior in half-wavelength separators.

.

2.1 Motivation

Acoustophoresis is a widely studied phenomenon in particle separation and fractionation. It employs the fact that a particle in a sound field is affected by the acoustic radiation force. This effect on particles is exploited in applications such as particle manipulation [1, 2], particle separation [3, 4] and acoustic levitation [5, 6]. To use these processes more efficiently, it is important to predict how particles behave under known conditions. Forces on the particle govern the motion of the particle, which can be represented by a second-order ordinary differential equation of motion (EOM). The primary forces on a particle moving in an acoustic standing-wave field are the acoustic radiation force, drag and inertial forces.

Acoustic radiation forces on spherical particles in traveling and standing wave fields were presented by King (1938) [7]. In addition to primary radiation forces, secondary interparticle forces are also present. The interparticle forces result in particles to form clusters, but they are much smaller than primary forces [8, 9]. A generic expression for compressible particles was later developed in 1962 [10]. The moving particles also experience drag forces by the surrounding fluid, and energy is dissipated due to fluid viscosity. In laminar flow, the drag force is often modeled as Stokes drag [11].

A homogenous ordinary differential EOM is obtained by combining the inertial, acoustic radiation and drag forces [11-15]. The acoustic radiation force, however, leads to a non-linear term in the equation. The resulting non-linear differential equation can only be solved by numerical methods. However, a change in operational conditions or model parameters requires new numerical solutions which, e.g. in design and optimization studies, can be time-consuming [11, 15].

As an alternative to numerical solutions, ignoring the inertial effects leads to approximate analytical solutions [13-14, 16-20]. The inertia-neglecting model, which in what follows is referred to as the non-linear model, has been solved analytically in combination with different flow profiles [16]. Particle behavior predicted by the numerical solution and inertia-neglecting approximations have been verified experimentally [12, 15]. A review of the experimental studies can be found in [21]. It is also possible to combine the experimental data and the mathematical models to estimate the parameters of the sound field [17, 18]. The non-linear first-order model was also utilized to simulate some previous experiments [19]. Dependence of particle behavior on particle size has been exploited by Peterson et al. [20]. With the non-linear first-order model the motion

is described by a first-order ordinary differential equation. Its solution predicts that the particle asymptotically converges to the equilibrium position or the pressure node/antinode, by implicitly assuming that the system is overdamped.

The objective of this article is to present and investigate a linearized single degree-of-freedom (SDOF) model (in what follows referred to as linear model), represented by a second-order linear differential equation, for the prediction of non-specific particle behavior in an acoustic standing wave field. Thus, in this study, the particle inertia is not ignored, but the non-linear acoustic radiation force term is linearized, leading to new approximate analytical solutions for further understanding of the particle behavior and for design of a particle separator.

The chapter is structured as follows. First, the equivalent SDOF system and calculation of the SDOF parameters, using a one-step linearization approach, are introduced. By using the SDOF parameters, the damping condition of the particle in a standing wave field is checked. Subsequently, the linear model is used to predict the particle trajectory and the time required (the transition time) to reach a target position from an initial position. After this, a sequential application of the linear model, based on a multi-step linearization approach, is introduced. The effect of initial particle velocity is also investigated. The performance of the linear model, in terms of particle trajectory and transition time, is evaluated against the numerical solution of the EOM and the non-linear model.

2.2 Materials and Methods

2.2.1 Equation of Motion of a Particle in an Acoustic Standing Wave Field

The pressure distribution in a one dimensional plane standing wave field can be expressed by the following equation [10],

$$P(x,t) = P_0 \cos(kx) \sin(\omega t) \tag{2.1}$$

Where $P(x,t)$ (Pa) represents the acoustic pressure as a function of the coordinate x (m) and time (s). P_0 is the amplitude of the sound pressure, $k = \frac{\omega}{2\pi c_0}$ (m^{-1}) is the

wavenumber, ω (rad s^{-1}) is the angular frequency and c_0 (m s^{-1}) is the speed of sound in the medium. The EOM for a particle in such an acoustic field is given by

$$\left(\frac{4}{3}\pi r^3\rho\right)\ddot{x} + (6\pi\mu r)\dot{x} + 4\pi k r^3 E_{ac}\Phi(\rho, c)\sin(2kx) = 0 \tag{2.2}$$

The first term in Equation (2.2) is the inertial force, as a function of the mass of the spherical particle, where r (m) is the particle radius and ρ (kg m^{-3}) is the density of the particle. The second term is the Stokes drag force, where μ (Pa s) is the viscosity of the host medium. The third term is the acoustic radiation force. The variable $E_{ac} = \frac{P_0^2}{4\rho_0 c_0^2}$ (J m^{-3}) denotes the acoustic energy density, where ρ_0 is the density of the host medium. $\Phi(\rho, c) = \frac{\rho + \frac{2}{3}(\rho - \rho_0)}{2\rho + \rho_0} - \frac{1}{3}\frac{\rho_0 c_0^2}{\rho c^2}$ (-) is the acoustic contrast factor (ACF), where c is the speed of sound in the particle material. A particle with a positive ACF is pushed towards the pressure node whereas a particle with a negative ACF is pushed towards the pressure antinode. Equation (2.2) is a second-order ordinary differential equation (ODE), and can only be solved numerically. Assuming the particle mass is negligible and the particle is initially at rest, however, an analytical solution is possible. Such an assumption makes Equation (2.2) a first-order ODE, and intuitively assumes no oscillatory behavior of the particle and where the particle reaches its terminal velocity instantly [13, 16]. Under these conditions, the particle path can be expressed as [14]

$$x(t) = \frac{1}{k}\operatorname{acot}(\cot(kx(0))\, e^{\frac{4}{3}k^2 r^2 \Phi(\rho,c)\frac{E_{ac}}{\mu}t} \tag{2.3}$$

Due to the $acot$ function in Equation (2.3), the particle does not cross the equilibrium position (i.e. the pressure node for a particle with positive ACF) but asymptotically converges to the equilibrium position. In addition to the particle path, the transition time between two positions x_0 and x_f can be estimated as [14]

$$t_{t1} = \frac{3\mu}{4\Phi(\rho, c)k^2 r^2 E_{ac}} \ln\left(\frac{cot(kx_f)}{cot(kx_0)}\right) \tag{2.4}$$

An alternative approach to approximately solve Equation (2.2) is to preserve the order of the ODE by linearizing the acoustic radiation force term. After such

linearization, the particle can be considered a linear SDOF mass-spring-damper system. Analytical solutions are possible after the linearization.

2.2.2 Equivalent Single Degree-of-Freedom System

The linearization of the acoustic radiation force enables the particle to be treated as an SDOF vibrating system. Such a system consists of a mass connected to a fixed reference with a spring and a damper. The EOM for a linear SDOF system is given by

$$m\ddot{x} + b\dot{x} + \mathrm{K}x = F_{ext} \tag{2.5}$$

Equation (2.5) and Equation (2.2) are analogous, with the mass (of the particle) $m = \frac{4}{3}\rho\pi r^3$, the viscous damping coefficient $b = 6\pi\mu r$, the (location-dependent) spring coefficient $\mathrm{K} = \frac{1}{x}(4\pi k r^3 E_{ac}\, \Phi(\rho, c)\, \sin(2kx))$. The effect of the acoustic radiation force is here expressed as a spring, the Stokes drag force can be represented as a linear viscous damper. Assuming there is no external force acting on the system, thus $F_{ext} = 0$, the right hand side of the equation is zero and the differential equation becomes homogenous as in Equation (2.2).

For linear SDOF systems, the type of response depends on the dissipation in the system. The damping ratio of the system is defined as $\zeta = b/(2\sqrt{\mathrm{K}m})$. Depending on the value of the damping ratio, the system may be underdamped ($\zeta < 1$), critically damped ($\zeta = 1$) or overdamped ($\zeta > 1$). In each case, the response has a specific shape. Derivation of the solutions are available in the literature and will not be repeated here [22].

Another critical parameter for a SDOF system is the natural frequency of the system. The undamped natural frequency of the linear SDOF system is $\omega_n = \sqrt{\mathrm{K}/m}$ and the damped natural frequency is defined as $\omega_d = \omega_n\sqrt{\zeta^2 - 1}$.

In the absence of external forces, when a SDOF system is perturbed, it returns to the equilibrium position. If the system is underdamped, before returning to equilibrium the mass oscillates around the equilibrium, while the oscillation amplitude exponentially decays. The critically damped system goes to the equilibrium fastest among all three cases, without making any oscillations. An

overdamped system goes to the equilibrium state without making any oscillations. For a particle (with positive acoustic contrast factor) in a standing wave field, the equilibrium position is the pressure node. Hence, in order to be comparable to the non-linear first-order model, a representative linear SDOF system must be overdamped. Response of an overdamped system is given in Equation (2.6).

$$x_{od}(t) = C_1 e^{s_1 t} + C_2 e^{s_2 t} \tag{2.6}$$

The constants $s_1 = \left(-\zeta + \sqrt{\zeta^2 - 1}\right)\omega_n$ and $s_2 = \left(-\zeta - \sqrt{\zeta^2 - 1}\right)\omega_n$ depend solely on the mass, spring and damper parameters, while $C_1 = (\dot{x}(0) - x(0)s_2)/(s_1 - s_2)$ and $C_2 = (-\dot{x}(0) + x(0)s_1)/(s_1 - s_2)$ are also affected by the initial conditions.

Similarly, the response of an underdamped system is $x_{ud}(t) = X_0 e^{-\zeta\omega_n t}\cos(\omega_d t - \phi)$ where $X_0 = \sqrt{x(0)^2 + \dot{x}(0)^2/\omega_n^2}$ and $\phi = \mathrm{atan}(\dot{x}(0)/x(0)\omega_n)$ are the constants determined by the initial conditions and the undamped natural frequency. For a critically damped system, the response is $x_{cd}(t) = \left(x(0) + \left(\dot{x}(0) + \omega_n x(0)\right)t\right)e^{-\omega_n t}$.

For the equivalent SDOF system, if m, b and K are constant, it is possible to solve the particle motion analytically. The mass (m) and damper (b) parameters are already constant. The spring force $\mathrm{K}x$, however, is non-linear as the acoustic radiation force contains a sine function. Consequently, the spring force can be expressed as a multiplication of two factors $\mathrm{K}x = \mathrm{K}_l \cdot \mathrm{K}_n x$. The linear part is given by $\mathrm{K}_l = 4\pi k r^3 E_{ac}\Phi(\rho, c)$ and the non-linear part is given by $\mathrm{K}_n x = \sin(2kx)$. Since the spring coefficient also depends on the position, the linearization is affected by the initial position of the particle. If a region of interest (ROI) is defined such that there is a starting position of the particle and a target position, the linearization can be carried out to correspond to the response between these positions [23-28]. Here, the linearization is performed by taking the average of the term $\sin(2kx)\ /x$ within the ROI. Different methods for linearization are presented elsewhere [29].

If the ROI is selected as $[x_0, x_f]$, the response, i.e. the trajectory of the particle is calculated in one step. The interval can alternatively be divided into several sub-intervals, resulting in a stepwise solution. In such a case, the total response will be the concatenation of the responses on each sequential sub-interval.

Unless otherwise specified, the numerical calculations were made using a set of parameters adopted from [14, 18]. Particle radius was taken as $r = 5$ μm, the particle density and speed of sound in the particle were $\rho = 1050$ kg m^{-3} and $c = 1700$ m s^{-1}, respectively. The density and speed of sound for water were $\rho_0 = 999.62$ kg m^{-3} and $c_0 = 1520$ m s^{-1}. The amplitude of the standing wave was $P = 1$ MPa, and the excitation frequency was $f = 2$ MHz. Total height of the channel was $\frac{\lambda}{2} = 380\mu m$, where the pressure node lies in the middle of the channel. The starting position of the particle was $x_0 = 0.9\frac{\lambda}{4} = 171$ μm and the target position of the particle was $x_f = 0.1\frac{\lambda}{4} = 19$ μm, all measured from the equilibrium position, which is the pressure node in the middle of the channel. The initial velocity of the particle was taken as zero and the ROI was determined by the starting position and the final position. Numerical solutions were carried out by using Matlab r2018b and Mathcad 14.

2.3 Results and Discussion

2.3.1 Damping Ratio

The non-linear solution (Equation (2.3)) corresponds to the solution of an overdamped SDOF system, where both assume no oscillatory behavior and the particle (mass) converges to the equilibrium position asymptotically. To verify this assumption, the damping ratio of a particle in an acoustic standing wave field is calculated by

$$\zeta = \frac{b}{2\sqrt{\mathrm{K}m}} = \frac{6\pi\mu r}{2\sqrt{4\pi k^2 r^3 E_{ac}\Phi(\rho, c)\mathrm{K}_n\left(\frac{4}{3}\pi r^3\rho\right)}} \tag{2.7}$$

The variation of the damping ratio ζ as a function of the acoustic pressure, excitation frequency (through the wave number) and particle parameters is illustrated in Figure 2.1.

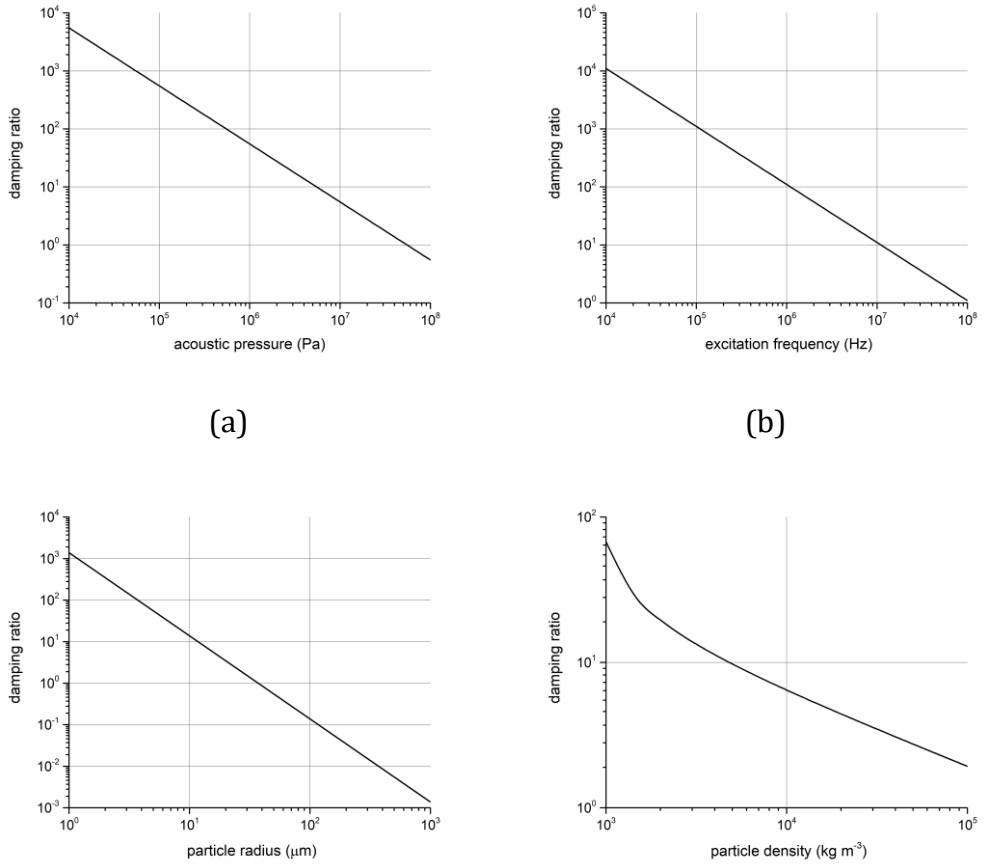

Figure 2.1- Damping ratio as a function of (a) acoustic pressure, (b) excitation frequency, (c) particle radius, and (d) particle density

Equation (2.7) and Figure 2.1 indicate that the damping ratio is inversely proportional to the square of the particle radius, the acoustic pressure amplitude and the excitation frequency. There is a possibility of having an underdamped system. For example, Figure 2.1c suggests the trajectory of a particle with $r = 40\ \mu\text{m}$ would be underdamped under this excitation conditions. The damping ratio is also a function of ROI. The damping ratios calculated for different ROI are illustrated in Figure 2.2.

Figure 2.2 indicates that the choice of ROI can affect the damping ratio significantly. When $r = 5\ \mu\text{m}$, the system is overdamped for all possible choices of ROI, whereas

for a particle with $r = 15$ μm the SDOF system can be underdamped for some cases. The choice of ROI is naturally depending on the initial and target positions of the particle. In order to check the overdamped criterion, a wider range of ROI yields safer estimates.

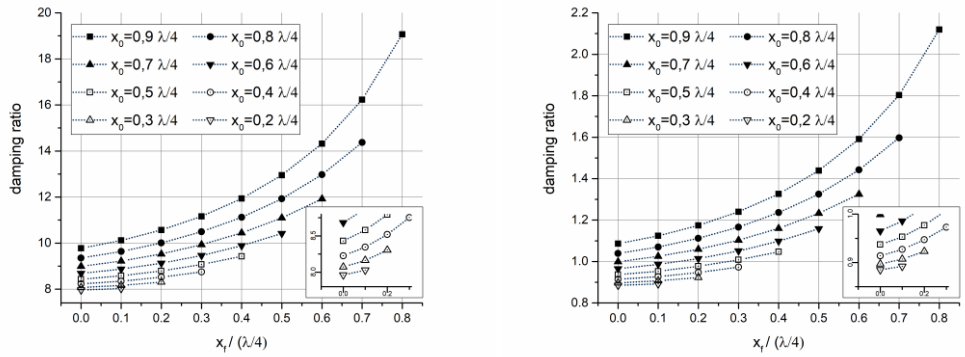

(a) (b)

Figure 2.2 - Damping ratio as a function of ROI, for a particle with (a) r = 5 μm and (b) r = 15 μm. Starting position of the ROIs are given in the legends of each panel and end position is given on the x axes. Markers represent the damping ratios for each ROI and lines are added to guide the eye.

2.3.2 Particle Response

Equation (2.7) and Figure 2.1 can thus be used to verify whether a system is overdamped for a given set of parameters. Provided the system is overdamped, the transition time can also be calculated for a linear SDOF system from Equation (2.6). For an overdamped system, with $\zeta \gg 1$, it turns out that $|s_i| \gg |s_j|$ with $i, j = 1, 2$ and the first or second term in Equation (2.6) goes to zero much quicker than the other term. Time required to reach to a final position from an initial position is therefore approximated as

$$t_{t2} = \frac{1}{s_1} \ln\left(\frac{x_f}{C_1}\right) \tag{2.8}$$

Particle trajectories using a numerical solution, or analytical solutions of the non-linear and linear model are illustrated in Figure 2.3

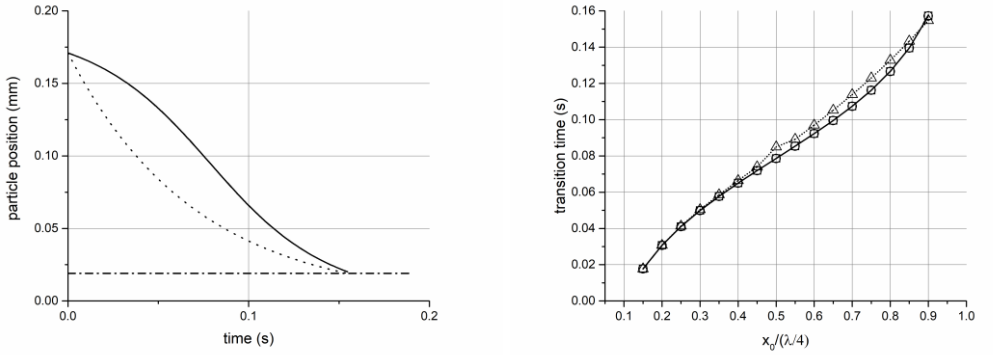

(a) (b)

Figure 2.3 - (a) Particle trajectories calculated by numerical solution (solid line), non-linear model (dashed line, overlaps with solid line) and one-step linear model (dotted line). The target location is indicated by dash-dot line. (b) Transition times calculated by numerical solution (squares), non-linear model (circles) and linear model (triangles) for different starting positions, whereas the target position was kept the same.

Figure 2.3 indicates that the linear model deviates from the numerical solution for path calculations and transition time calculations. The damping ratio calculated for the particle was $\zeta = 55.18$ and confirms that the system is indeed heavily overdamped. Taking the numerical solution as a benchmark, the root mean square error for the particle trajectory from the linear model was $31.35\ \mu m$, whereas the error in the transit time was $1.6\ \%$. For the non-linear model the errors were $0.012\ \mu m$ and $0.004\ \%$, respectively. Even though Fig. 3b suggests that the transition times get closer as the starting position gets closer to the equilibrium position, the linear model cannot cover the whole range, mainly because it fails to catch the changes in the sinusoidal force profile as it assumes a constant spring coefficient on the whole ROI. Better approximate solutions from the linear model can be found when the ROI, i.e., the interval $[x_0, x_f]$, is divided into sub-intervals. The total particle trajectory and transition time is then the concatenation or sum, respectively, of solutions on sequential sub-intervals. This stepwise approach is introduced in the next section.

2.3.3 Stepwise Application of the Linear Model

The stepwise application of the linear model requires the interval $[x_0, x_f]$ to be divided into sub-intervals. If the interval is divided into N sub-intervals the total particle trajectory can be calculated by Equation (2.9).

$$x(t) = \bar{x}_1(t) \cup \ldots \cup \bar{x}_N(t) \tag{2.9}$$

where $\bar{x}_i(t)$ for $i = 1, \ldots, N$ is the solution on the i^{th} sub-interval, given by Equation (2.6). Equation (2.8) is applicable for each interval and also enables the transition time to be calculated. The total transition time hence is the sum of the individual transition times.

$$t_{t2} = \sum_{i=1}^{N} t_{t2i} \tag{2.10}$$

where t_{t2i} follows from Equation (2.8). In Equation (2.9) and (2.10) each x_f, s_1, s_2, C_1 and C_2 is defined on the i^{th} interval, as follows. First, the linearization was carried out for the specific sub-intervals, leading to the calculation of ζ on that interval. Subsequently, the coefficients s_1 and s_2 were updated for each interval. Similarly, C_1 and C_2 were updated by using the updated initial conditions. Using s_1, C_1 and the endpoint x_f of each sub-interval, the transition time was calculated. The transition time was subsequently used to estimate the particle velocity at the end of each interval, which was then used as initial condition for the next interval.

Figure 2.4 demonstrates the case with stepwise solutions. As suggested by Figure 2.4, the multi-step linearization significantly improved the application of the linear model. The errors in transit time (with respect to the numerical solution) for 5-step linear, 25-step linear and first-order non-linear solutions were 1.8%, 0.1% and 0.004%, respectively. The RMS errors in trajectories were $4.4\ \mu\text{m}$, $0.23\ \mu\text{m}$ and $0.013\ \mu\text{m}$. Using Matlab r2018b, the numerical solution took on average 2.4 s to calculate, whereas the 5-step solution took 46 ms and the 25-step solution took 65 ms. Even though the stepwise linear model incorporates a for-loop, it is still computationally more efficient than the numerical solution.

In the example given in Figure 2.4, the damping ratio of the particle was always larger than 40. Another example of an overdamped case, but with much smaller damping ratios, is given in Figure 2.5. Here, $x_0 = 0.152\ \mu\text{m}$, $r = 20\ \mu\text{m}$ and $P_0 = 0.8\ \text{MPa}$ while every other parameter was kept unchanged.

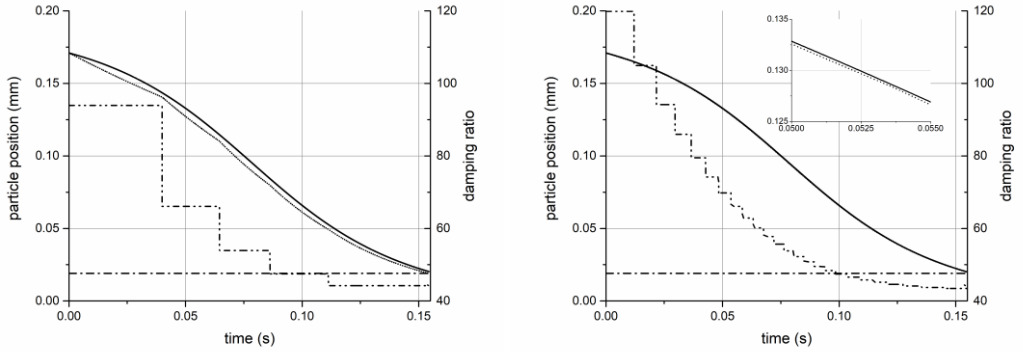

(a) (b)

Figure 2.4 - Particle trajectories calculated stepwise by linear model in (a) 5 steps (b) 25 steps. Solid line represents the numerical solution where dotted line represents the linear model. Dash-dot line indicates the target position. Dash-dot-dot line represents the damping ratio of the particle in each step with values presented on the secondary y axis. A zoomed in view is given in (b) to demonstrate the accuracy of the linear model.

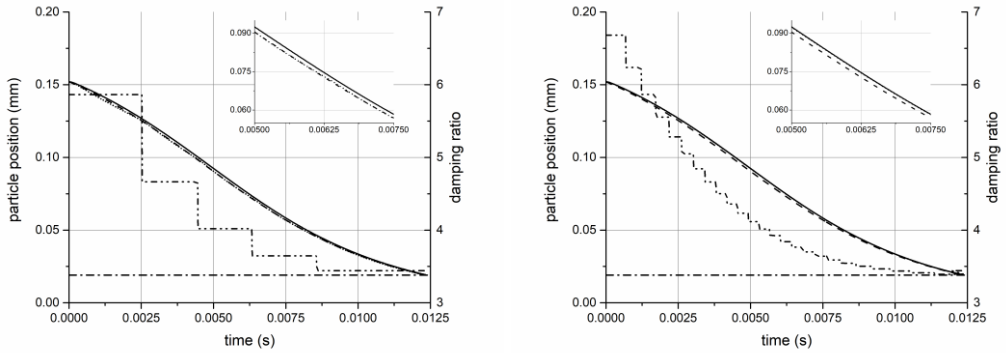

(a) (b)

Figure 2.5 - Particle trajectories calculated stepwise by linear model for x_0 = 152 μm, r = 20 μm and P_0 = 0.8 MPa, in (a) 5 steps (b) 25 steps. Solid line represents the numerical solution, dashed line represents the non-linear model and dotted line represents the linear model. Dash-dot line indicates the target position. Dash-dot-dot line represents the damping ratio of the particle in each step with values presented on the secondary y axis. Zoomed in views are provided in both panels to demonstrate the accuracy.

In Figure 2.5 the 5-step linear model had a 0.57% error in transit time and a RMS error $1.7\ \mu m$ in the trajectory. The 25-step solution had those errors as 0.07% and $0.13\ \mu m$, respectively. The errors for the first-order non-linear solution were 0.26% and $1.5\ \mu m$.

Those examples confirm that as the damping ratio of the particle gets lower, the commonly used approximate non-linear model deviates from the numerical solution. This deviation is due to the implicit assumption that the system is overdamped. For overdamped systems with lower damping ratio, however, stepwise solutions using the linear model yields closer results to the numerical solution, while being computationally more efficient than the numerical solution. Clearly, the more linearization steps the better the approximation. So far, numerical calculations suggest that a 25-step linearization is enough to have an accurate estimate of both transit time and particle trajectory.

2.3.4 Effect of Initial Velocity

In the examples given so far, the particle was assumed to be a rest at the beginning, hence with zero initial velocity. Whereas in the microscale applications this is a valid assumption, more complicated geometries and flow patterns can result in a particle with an initial velocity at the entrance of the acoustic field [30,31]. Due to its second-order nature, the linear model is able to include the effect of initial velocity. Stepwise application of the linear model was used for the following examples.

For the case in Figure 2.6a, the errors in transition time for the non-linear model and the 25-step linear model were 0.09% and 0.1%, respectively. The RMS error in trajectories were $0.16\ \mu m$ and $0.25\ \mu m$. For the case in Figure 2.6b, the transition time errors were $1.13\ \%$ and $0.15\ \%$, whereas the RMS error in trajectories were $2.8\ \mu m$ and $0.25\ \mu m$. The solutions and error calculations confirmed that in a heavy-damped case (Fig. 6a) the initial kinetic energy of the particle affects the trajectory less than the case given in Figure 2.6b. Similar to the zero initial velocity case, the non-linear model performs accurately for a nonzero initial velocity case, provided that the damping his high enough. Since the linear model can incorporate the initial velocity, the accuracy of the solution in both cases were similar to each other. However, in underdamped cases the linear model is the only alternative to the numerical solution.

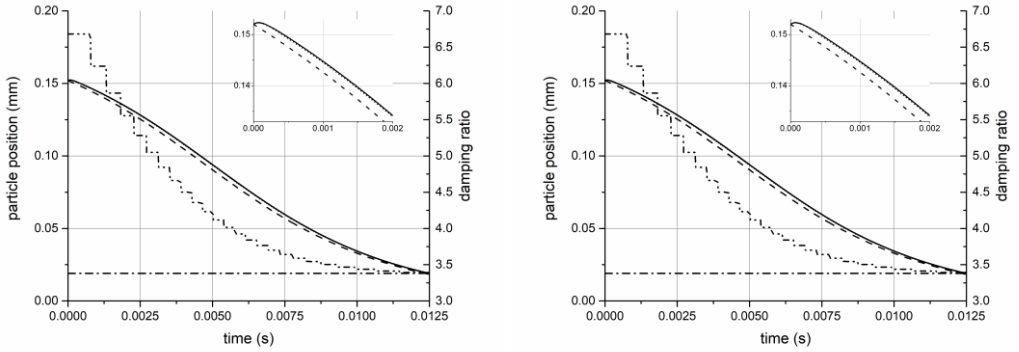

(a) (b)

Figure 2.6 - Particle trajectories calculated for a case with initial velocity v_0 = 10 mm s^{-1} and (a) x_0 = 171 μm, r = 5 μm and P_0 = 1 MPa, (b) x_0 = 152 μm, r = 20 μm and P_0 = 0.8 MPa. Solid line represents the numerical solution, dashed line represents the non-linear model and dotted line represents the linear model. Dash-dot line indicates the target position. Dash-dot-dot line represents the damping ratio of the particle in each step with values presented on the secondary y axis. Zoomed in views are provided in both panels to demonstrate the accuracy.

2.4 Conclusions

This study investigated a linearized single degree-of-freedom (SDOF) model of a non-linear mass-spring-damper system to approximately predict particle behavior in microscale acoustophoresis. The performance of the linear model was evaluated, based on numerical simulations, against both the frequently used approximate non-linear model and the numerical solution to the equation of motion (EOM), a second-order ODE. The damping ratio of the system was evaluated as a function of the particle and excitation parameters, predicting when the system will show overdamped, critically damped or underdamped behavior.

The performance of the linear model was evaluated on two criteria, the transit time from initial and final positions and the particle trajectory. The one-step linearization of the model resulted in inaccurate transit time and trajectory projections. Multi-step linearization of the EOM allows accurate analytical predictions of the particle trajectories and transition time compared to the numerical solution of the EOM. When the system is not heavily overdamped, the linear model resulted in more accurate predictions than the first-order non-linear model. In the examples, the

multi-step linearization procedure, with errors in particle trajectory and transit time smaller than $0.25\ \mu m$ and 0.15%, respectively, showed promising results and is computationally (by a factor of approximately 50) more efficient than the numerical solution of the ODE.

References

[1] Laurell, T., Petersson, F., Nilsson, A., 2007. Chip integrated strategies for acoustic separation and manipulation of cells and particles. Chemical Society Reviews 36, 492–506. doi:10.1039/B601326K

[2] Hertz, H.M., 1995. Standing-wave acoustic trap for nonintrusive positioning of microparticles. Journal of Applied Physics 78, 4845–4849. doi:10.1063/1.359770

[3] Adams, J.D., Ebbesen, C.L., Barnkob, R., Yang, A.H.J., Soh, H.T., Bruus, H., 2012. High-throughput, temperature-controlled microchannel acoustophoresis device made with rapid prototyping. Journal of Micromechanics and Microengineering 22, 075017. doi:10.1088/0960-1317/22/7/075017

[4] Lipkens, B., Dionne, J., Trask, A., Szczur, B., Stevens, A., Rietman, E., 2010. Separation of micron-sized particles in macro-scale cavities by ultrasonic standing waves. Physics Procedia 3, 263–268. doi:10.1016/j.phpro.2010.01.035

[5] Kandemir, M.H., Çalışkan, M., 2016. Standing wave acoustic levitation on an annular plate. Journal of Sound and Vibration 382, 227–237. doi:10.1016/j.jsv.2016.06.043

[6] Andrade, M.A.B., Pérez, N., Adamowski, J.C., 2018. Review of Progress in Acoustic Levitation. Brazilian Journal of Physics 48, 190–213. doi:10.1007/s13538-017-0552-6

[7] King, L.V., 1934. On the acoustic radiation pressure on spheres. Proceedings of the Royal Society of London. Series A - Mathematical and Physical Sciences 147, 212–240. doi:10.1098/rspa.1934.0215

[8] Doinikov, A.A., 2001. Acoustic radiation interparticle forces in a compressible fluid. Journal of Fluid Mechanics 444, 1–21. doi:10.1017/S0022112001005055

[9] Gröschl, M., 1998. Ultrasonic Separation of Suspended Particles - Part I: Fundamentals. Acta Acustica united with Acustica 84, 432–447.

[10] Gor'kov, L.P., 1962. On the Forces Acting on a Small Particle in an Acoustical Field in an Ideal Fluid. Soviet Physics Doklady 6, 773.

[11] Townsend, R.J., Hill, M., Harris, N.R., White, N.M., 2004. Modelling of particle paths passing through an ultrasonic standing wave. Ultrasonics, Proceedings

of Ultrasonics International 2003 42, 319–324. doi:10.1016/j.ultras.2004.01.025

[12] Kapishnikov, S., Kantsler, V., Steinberg, V., 2006. Continuous particle size separation and size sorting using ultrasound in a microchannel. Journal of Statistical Mechanics: Theory and Experiment 2006, P01012–P01012. doi:10.1088/1742-5468/2006/01/P01012

[13] Bruus, H., 2011. Theoretical microfluidics. Oxford University Press, Oxford.

[14] Bruus, H., 2012. Acoustofluidics 7: The acoustic radiation force on small particles. Lab on a Chip 12, 1014–1021. doi:10.1039/C2LC21068A

[15] Zhou, D., Luo, Z., Fang, M., Lu, M., Jiang, J., Chen, H., He, M., 2017. Numerical calculation of particle movement in sound wave fields and experimental verification through high-speed photography. Applied Energy, Clean, Efficient and Affordable Energy for a Sustainable Future 185, 2245–2250. doi:10.1016/j.apenergy.2016.02.006

[16] Garofalo, F., 2015. Analytical characterization of particle kinematics and transverse dispersion in free-flow acoustophoretic devices. Microfluidics and Nanofluidics 3, 367–382. doi:10.1007/s10404-014-1452-5.

[17] Barnkob, R., Augustsson, P., Laurell, T., Bruus, H., 2010. Measuring the local pressure amplitude in microchannel acoustophoresis. Lab on a Chip 10, 563–570. doi:10.1039/B920376A

[18] Barnkob, R., Iranmanesh, I., Wiklund, M., Bruus, H., 2012. Measuring acoustic energy density in microchannel acoustophoresis using a simple and rapid light-intensity method. Lab on a Chip 12, 2337–2344. doi:10.1039/C2LC40120G

[19] Büyükkoçak, S., Özer, M.B., Çetin, B., 2014. Numerical modeling of ultrasonic particle manipulation for microfluidic applications. Microfluidics and Nanofluidics 17, 1025–1037. doi:10.1007/s10404-014-1398-7.

[20] Petersson, F., Åberg, L., Swärd-Nilsson, A.-M., Laurell, T., 2007. Free Flow Acoustophoresis: Microfluidic-Based Mode of Particle and Cell Separation. Analytical Chemistry 79, 5117–5123. doi:10.1021/ac070444e

[21] Lenshof, A., Laurell, T., 2010. Continuous separation of cells and particles in microfluidic systems. Chemical Society Reviews 39, 1203–1217. doi:10.1039/B915999C.

[22] Çalışkan, M., Özgüven, H.N., Platin, B., 1988 Dynamics of engineering systems. Middle East Technical University Press, Ankara.

[23] Cadwell, L.H., Boyko, E.R., 1991. Linearization of the simple pendulum. American Journal of Physics 59, 979–981. doi:10.1119/1.16655

[24] Chung, C.C., Hauser, J., 1995. Nonlinear control of a swinging pendulum. Automatica 31, 851–862. doi:10.1016/0005-1098(94)00148-C

[25] Molina, M.I., 1997. Simple linearizations of the simple pendulum for any amplitude. The Physics Teacher 35, 489–490. doi:10.1119/1.2344777

[26] Parwani, R.R., 2004. An approximate expression for the large angle period of a simple pendulum. European Journal of Physics 25, 37–39. doi:10.1088/0143-0807/25/1/006

[27] Lima, F.M.S., Arun, P., 2006. An accurate formula for the period of a simple pendulum oscillating beyond the small angle regime. American Journal of Physics 74, 892–895. doi:10.1119/1.2215616

[28] Beléndez, A., Hernández, A., Márquez, A., Beléndez, T., Neipp, C., 2006. Analytical approximations for the period of a nonlinear pendulum. European Journal of Physics 27, 539. doi:10.1088/0143-0807/27/3/008

[29] Kandemir, M.H., Wagterveld, R.M., Yntema, D., Keesman, K.J., 2017. Methods to linearize acoustic radiation force for acoustophoresis applications. Acoustofluidics, 28-29 August, 2017, San Diego, CA.

[30] Cappon, H.J., 2014. Numerical and experimental design of ultrasonic particle filters for water treatment (PhD). Wageningen University, Wageningen.

[31] Kandemir, M.H., Wagterveld, R.M., Yntema, D.R., Keesman, K.J., 2019. Selective Particle Filtering in a Large Acoustophoretic Serpentine Channel. Scientific Reports 9, 7156. doi:10.1038/s41598-019-43711-8

3 SELECTIVE PARTICLE FILTERING IN A LARGE ACOUSTOPHORETIC SERPENTINE CHANNEL

A version of this chapter has been published as:

Kandemir, M. H., Wagterveld, R. M., Yntema, D. R., & Keesman, K. J. (2019). Selective particle filtering in a large acoustophoretic serpentine channel. *Scientific Reports*, *9*(1), 1-10.

Abstract

The objective of this study is to investigate the performance of a serpentine channel for acoustic driven selective particle filtering. The channel consists of sharp corners and straight sections, and the acoustic field is affecting the particles throughout the channel. A prototype of the separator channel is manufactured using 3D printing. Acoustic waves are generated by a piezoelectric transducer operating near 2 MHz. Computer simulations are carried out to explore and visualize the flow field and sound field in the separator. Selective particle trapping is aimed to be achieved in the hairpin sections, which is confirmed by experiments. Spherical polyethylene particles of 34 µm, 70 µm and 100 µm diameter are used to demonstrate selective trapping by adjusting the flow rate in the channel or voltage input to the transducer. In addition, wheat beer containing yeast up to 20 µm size is selectively filtered by adjusting the flow rate to the channel. Experiments demonstrate that selective particle filtering is possible in the serpentine channel as both methods yield clear separation thresholds.

3.1 Introduction

Manipulation of particles by acoustics is known as “acoustophoresis”. Applications of acoustophoresis cover a wide range of applications, from centimeter-scale [1] to micrometer-scale sized particles. In the micrometer-scale, acoustophoresis is one of the methods for particle filtering in solid-liquid mixtures among inertial, gravitational, magnetic and optical methods [2-6].

Enhanced sedimentation is one of the common applications of acoustophoresis in particle-liquid separation [7-9]. Particles are aggregated by virtue of the acoustic radiation force and sedimentation is thus enhanced. This method can be combined with flow fields to selectively retain viable cells [10-13]. Apart from enhanced sedimentation, most applications in acoustophoresis utilize a single acoustic node in the separator channel. Since the frequency is often high and wavelength is therefore low, dimensions of such channels are in micrometer range. Hence, these are referred to as microchannels. Selective separation for model particles and bioparticles using microchannels are demonstrated in a number of studies [14-18]. Selective particle retention and fractionation can also be achieved with methods other than enhanced sedimentation and acoustophoresis. Examples are inclined sedimentation [19], dielectrophoresis [20-22], and flow manipulation [23-25]. Acoustic filtering can be an alternative for existing applications in food processing [6]. For example, in rough beer filtration processes, membranes recently offer a competitive alternative to traditional kieselguhr method [26-28]. The potential of acoustic filtration is yet to be explored for this application. Possible benefits include the absence of fouling, no addition of chemicals, not having internals and less cleaning.

A disadvantage of a single node channel is the relatively low throughput. The throughput can be increased by operating multiple set-ups in parallel [29], but also by employing multiple nodes. To have multiple nodes in the resonator, the resonator dimensions must be around multiple wavelengths at the excitation frequency. In such systems, it is also possible to employ relative motion between the fluid flow and the acoustic field, by either pushing the flow against the acoustic field or creating a dynamic acoustic field [30]. Recently, multi-wavelength setups utilizing surface acoustic waves have been proposed [31]. A review on multiple wavelength resonators was done by Hawkes et al. [32].

To understand acoustic particle filtering, it is crucial to know how the acoustic field affects particles. A body in an acoustic field experiences a force called acoustic

radiation force. Expressions for the acoustic radiation forces on spherical particles were presented by King, for traveling and standing wave fields [33]. Later, an expression for compressible particles in a generic sound field was developed by Gor'kov [34]. As compared to travelling wave fields standing wave sound fields have higher energy density, thus leading to higher time-averaged forces [33]. In acoustic standing wave separators particles are trapped in specific grid points (the acoustic nodes, or antinodes), thus making it possible to separate particles from the suspension [6].

Depending on the particle properties, acoustically different particles can be forced to different locations in the same acoustic field. When a particle moves relative to the liquid, the particle will also experience a so-called drag force. If the liquid flow is characterized by a low Reynolds number, the drag force is typically modeled as Stokes drag force [35]. Interestingly, some particles are trapped with relatively lower effort compared to others as acoustic radiation force scales with particle properties like volume, density and compressibility while drag force scales with particle size. Such diverse behavior can be used in selective filtering using acoustic fields.

Combining those external forces on particles, the equation of motion for a particle can be constructed, which is a second-order nonlinear ordinary differential equation. In general, particle trajectories can be calculated numerically, but under some assumptions analytical solutions are also possible. The solution of the equation of motion can be combined with the flow profile in the separator, leading to more complex modeling [36-40]. Thus, the dominant external forces on a particle in an acoustic field are drag force and acoustic radiation force. Being able to adjust those external forces enables the particles to be selectively trapped. If the particles are pushed relative to the acoustic field by the fluid flow, the drag force can be controlled by the fluid velocity whereas the acoustic force can be controlled by the voltage input to the system. A serpentine channel consisting of hairpins and linear sections can be used to control the fluid flow and acoustic input.

The aim of this study is to investigate the possibility for selective filtering in an acoustophoretic serpentine channel and to demonstrate it on solid polyethylene particles and on wheat beer flocs. The width of the channel is such that multiple wavelengths at operating frequencies fit in the channel. Furthermore, the channel dimensions and shape are chosen such that particles are trapped in multiple nodal locations, while keeping the liquid flow inside the channel close to laminar. The serpentine structure has low velocity hairpin turns connected by straight sections.

Drag force on the particles becomes weaker in the hairpins and the straight sections ensure that the flow becomes fully developed before entering the hairpins. This selective filtering ability is shown in simulation and in experiments on a 3D printed prototype, by adjusting the flow rate in the channel or voltage input to the system. Model polyethylene particles of 34 μm, 70 μm and 100 μm diameter are used to demonstrate the ability of selective particle separation in the prototype by either changing the input flow rate or voltage input to the transducer. The other test mixture, wheat beer, contains yeast up to 20 μm in size and has a more or less continuous size distribution of yeast particles. Wheat beer is used to demonstrate the ability to selectively separate compressible flocs by changing the input flow rate.

3.2 Materials and Methods

The experimental set-up consists of a signal generator (Keysight Trueform 33512B), a custom made amplifier, an oscilloscope (Tektronix TDS2024C), a syringe pump (Aitecs PRO SP-12S) and the separator prototype, Figure 3.1. The amplifier drives the piezoelectric transducer (Noliac NCE41), the oscilloscope monitors the voltage across the transducer. While acting as a sound source, the piezoelectric transducer is immersed in water and in order to prevent electrical leakage it was covered with polyurethane paint. The particle-water mixture is fed by the syringe pump. Base and inner wall parts of the separator prototype are 3D printed using Polylactic acid (PLA) by Ultimaker 2+. Base part contains the inlet and outlet sections, connection holes for the top PMMA cover and beds for rubber rings. Inner part creates the serpentine structure inside, having straight sections and $180\,^{\circ}$ turns, i.e. hairpins. During the experiments the separator was always laid on the horizontal plane.

Two particle mixtures were used in the experiments. Mixture (1) contains model spherical polyethylene particles with known dimensions and density. Mixture (2) is a commercially available wheat beer.

The properties of particles of mixture (1) are listed in Table 3.1. A bottle of mixture consists of $500\ \mathrm{mL}$ MilliQ water , $0.84\ \mathrm{g\,L^{-1}}$ of the surfactant CTAB (Hexadecyltrimethylammonium bromide), $0.99\ \mathrm{mM}$ HCl and $0.02\ \mathrm{g\,L^{-1}}$ of each particle type, while multiple bottles of mixtures are consumed during the experiments. CTAB prevents the particles from sticking to each other and the PMMA cover whereas HCl prevents the particles from sticking to the PLA parts.

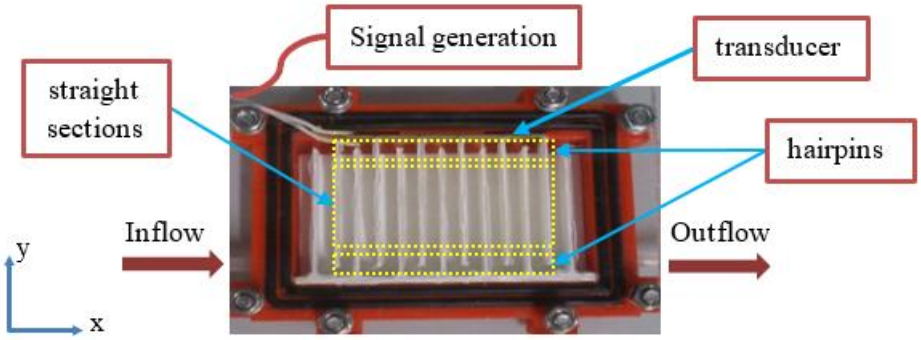

Figure 3.1 - Schematic top view representation of the system. Red part in the separator is the base, white parts are inner walls. Black parts are rubber rings. Yellow rectangles highlight the hairpins and the straight sections among the inner walls. To ensure the flow is following the serpentine path, 1 mm thick silicone sealant layer is also applied between the inner walls and the PMMA cover.

Table 3.1 – Properties of the polyethylene particles in the mixture

Color	Blue	Orange	Red
Size (µm)	$90-106$	$63-75$	$32-36$
Density (kg m^{-3})	1002	1006	980
Speed of Sound (m s^{-1})	1720	1717	1739

Mixture (2), Hoegaarden wheat beer, contains dissolved carbon dioxide in very small bubbles and it produces foam when moved or shaken. To be able to remove all carbon dioxide the beer mixture was acidified. The acidification shifts the carbonate equilibrium towards carbonic acid and dissolved carbon dioxide. The gas was removed by keeping the solution under vacuum for 2.5 hours.

During the treatment of mixture (1), the selective separation thresholds were determined visually using a microscope with camera and ImageJ [41]. Whether particles got trapped or not was first checked by observing the experiments live and later verified by analyzing the particle trajectories using ImageJ. Separation

thresholds were adjusted by changing the voltage input or flow rate for mixture (1). Prior to operation, the admittance of the system, filled with degassed MilliQ water and particle mixtures, was measured with an impedance analyzer (HP 4194A) between $1800 - 2000\ \mathrm{kHz}$. Computer simulations were carried out to compute the acoustic field, where a frequency of $1979\ \mathrm{kHz}$ was selected as excitation frequency, since at $1979\ \mathrm{kHz}$ the sound field appeared to be most favorable for trapping in the hairpins. Admittance calculations by computer simulation, with an isotropic structural loss factor of 0.1 included in the PLA material, suggested that there is more than one resonance in the frequency range of $1800 - 2000\ \mathrm{kHz}$. The selected frequency of $1979\ \mathrm{kHz}$ coincided with the frequency of minimum imaginary admittance in the simulations. In the measurements the phase is closest to zero at $1924\ \mathrm{kHz}$ in mixture (1) and $1972\ \mathrm{kHz}$ in mixture (2) indicating the minimum imaginary admittance occurs there. Thus, excitation frequencies for both mixtures are chosen accordingly. For mixture (2), separation threshold was adjusted only by changing the flow rate. After separation, the particle size distribution was analyzed with a DIPA 2000 particle size analyzer.

The dimensions of the acoustic separator allow for multiple wavelengths in the operating frequency range. Ideally, in this type of resonator the sound field is a one-dimensional standing acoustic plane wave field. The equation of motion for a spherical particle in such a field is given by

$$\left(\frac{4}{3}\pi r^3\rho\right)\ddot{y} + (6\pi\mu r)(\dot{y} - u) + 4\pi k r^3\left(\frac{P_0^2}{4\rho_0 c_0^2}\right)\Phi(\rho, c)\sin(2ky) = 0 \tag{3.1}$$

Here r is the particle radius (m), y is the distance of particle from the source (m), ρ_0 is the density of the medium $(\mathrm{kg\ m^{-3}})$, c_0 is the speed of sound $(\mathrm{m\ s^{-1}})$ in the medium, P_0 is the amplitude of the sound pressure, ω is the angular frequency $(\mathrm{rad\ s^{-1}})$, k is the wavenumber (m^{-1}) and $\Phi(\rho, c)$ is the acoustic contrast factor. The acoustic contrast factor is a measure on how much the particle differs from the surrounding media in terms of acoustics [36]. Particle density is denoted by ρ whereas c represents the speed of sound in the particle, μ is the dynamic viscosity $(\mathrm{Pa\ s})$ of the medium, u is the velocity $(\mathrm{m\ s^{-1}})$ of the flow in the direction of acoustic radiation force. With a known sound field and particle properties, Equation (3.1) can be solved numerically in order to predict particle trajectories. Application of the acoustic radiation force on a particle is readily available in COMSOL Multiphysics.

The flow field and acoustic field inside the separator were computed using COMSOL Multiphysics, version 5.3a. The 2D computer representation of the separator is given in Figure 3.2.

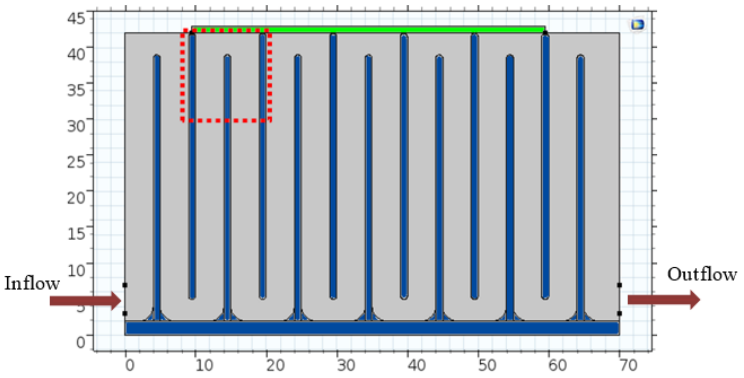

Figure 3.2 - 2D representation of the separator for computer modeling. Size of the transducer (green) on top of flow cell with depth of 9.5 mm, thickness of the inner walls (blue) 1 mm, and length of the walls 37 mm. Channel width is 5 mm before outlet and 4 mm elsewhere. Bottom corners are rounded with 1 mm radius. The area monitored during experiments is indicated by the red dotted rectangle.

The flow field is computed by a stationary solver in COMSOL Multiphysics, obtaining the steady state fluid velocity distribution in the separator. The mesh size is selected such that the maximum elements size is $3.71\ \mathrm{mm}$, with an average element quality of 0.834 given by the software.

Acoustic field simulations of the separator were also carried out in COMSOL Multiphysics, using acoustic-solid interaction physics. Electrostatics, solid mechanics and pressure acoustics are used to calculate the acoustic field by frequency domain solver. Laminar flow is used to calculate the flow field by stationary solver. Particle paths are calculated using particle tracing for fluid flow physics by time dependent solvers. Multiphysics interactions and boundary/compatibility conditions are automatically generated by the software.

The transducer material is Noliac NCE41 and the dimensions are 1 mm×10 mm×50 mm. Piezoelectric properties of the transducer are adopted from previous work of Cappon [6]. Water properties are taken as built-in values in COMSOL Multiphysics. Properties of PLA are set as $\rho_{PLA} = 1300\ \mathrm{kg\ m^{-3}}$, $E_{PLA} = 1.28\ \mathrm{GPa}$, $\nu = 0.36$ (Poisson's ratio) and the isotropic structural loss factor of 0.1. Outer walls are represented as impedance boundary condition while inner walls are included in the

simulations by including the PLA material. Simulations are carried out for frequencies between $1.8\ \mathrm{MHz}$ and $2.2\ \mathrm{MHz}$ with $500\ \mathrm{Hz}$ steps. Voltage input to transducers was set to $2\ \mathrm{V_{pp}}$. The mesh is adjusted so that maximum element size is smaller than $\lambda/8$ for every simulated frequency in the corresponding material. There are 1458967 elements in total, where the average element quality is given as 0.9 by COMSOL Multiphysics. Boundary and compatibility conditions at material interfaces and multiphysics couplings are also generated by COMSOL Multiphysics. In addition to the acoustic field, the impedance and admittance of the transducer were also calculated. The resonant frequency of the system can also be found by the admittance plot due to the coupling between the system and piezoelectric material [42]. Based on the computed flow and sound field, particle trajectories were simulated.

3.3 Results and Discussion

In order to gain insight of the properties in the system, first computer simulations were carried out to calculate the resonance frequencies, the acoustic field and the flow field. Excitation frequency of the system was selected based on admittance measurements and simulations. A simulation plot of the sound field corresponding to $1979\ \mathrm{kHz}$ is given in Figure 3.3. Voltage across the transducers is set to $2\ \mathrm{V_{pp}}$ during the simulations. The acoustic field, more or less perpendicular to the flow direction, is strongest with the highest absolute sound pressure in the most colored (red and blue) area in Figure 3.3.

The flow field was computed in COMSOL Multiphysics and given in Figure 3.4. The flow field solutions suggest that the flow is close to laminar even for the highest possible flow rate for this experiment. Figure 3.4a represents the flow inside the channel for an input flow rate of $100\ \mathrm{mL\ h^{-1}}$ and (b) represents the flow for an input flow rate of $500\ \mathrm{mL\ h^{-1}}$. For a flow rate of $100\ \mathrm{mL\ h^{-1}}$ Reynolds number is around 5. The channel provides a fully developed flow in the middle sections and for a flow rate of $500\ \mathrm{mL\ h^{-1}}$ the Reynolds number is around 25, indicating that the flow inside the channels is indeed close to laminar. Higher Reynolds numbers affect the flow especially around the corners, resulting in leaning as can be seen in Figure 3.4b. Figure 3.4c and 3.4d shows the vertical velocity amplitudes.

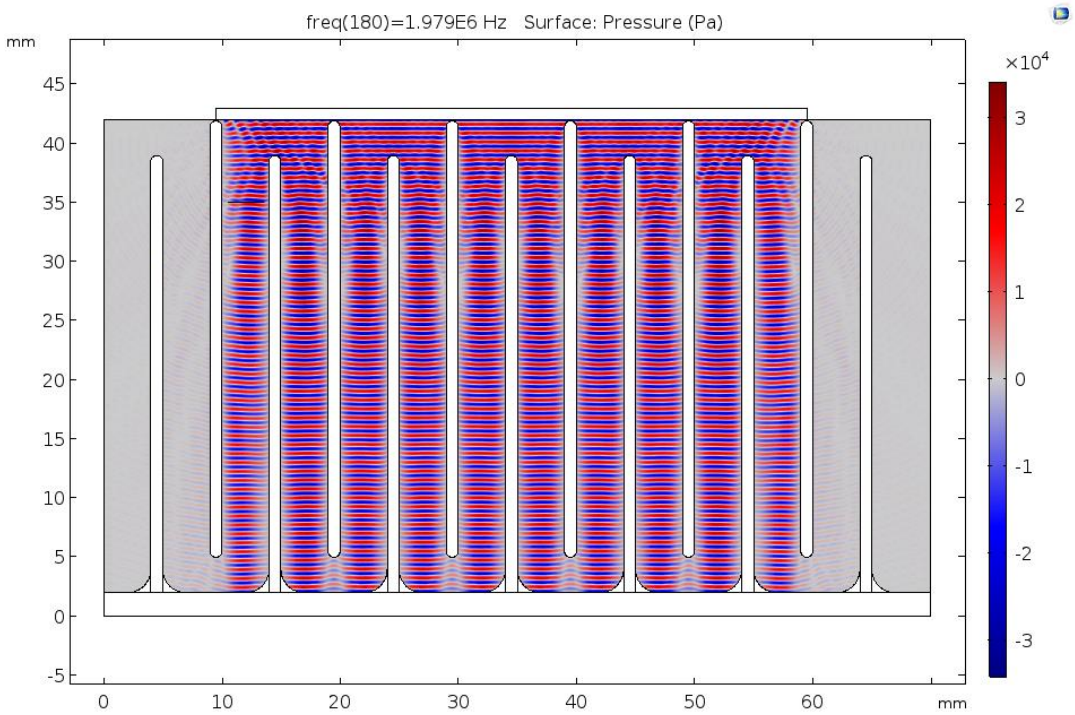

Figure 3.3 - Acoustic pressure field (Pa) computation in COMSOL Multiphysics at 1979 kHz with 2 V_{pp} across the transducers. Red areas represent positive acoustic pressure where blue areas represent negative acoustic pressure. Grey lines between the blue and red areas corresponding to pressure nodes.

Particle paths have also been simulated in COMSOL Multiphysics for the sound field (Figure 3.3) assuming $100\ \mathrm{mL\ h^{-1}}$ flow rate (Figure 3.4). Only the blue and orange particles were included in this simulation. Of the 15 particles released of each type to the system all of blue particles and $2/15$ of orange particles are trapped in the first hairpin. The remaining orange particles continued unobstructed. The 2D simulations in Figure 3.5 do not take into account the variation of the sound field along the depth of the prototype, which differs from the real experimental case as shown in what follows. Figure 3.5 also confirms that small particles are trapped, as well, by the field if they are located in the outermost streamline, where the drag force in vertical direction is the weakest.

The dominant external forces on a particle are drag force and acoustic force according to Equation (3.1). Hence, by changing the voltage input, the amplitude of the sound pressure, and thus acoustic force, can be adjusted whereas it is possible to adjust the drag force by changing the input flow rate to the system.

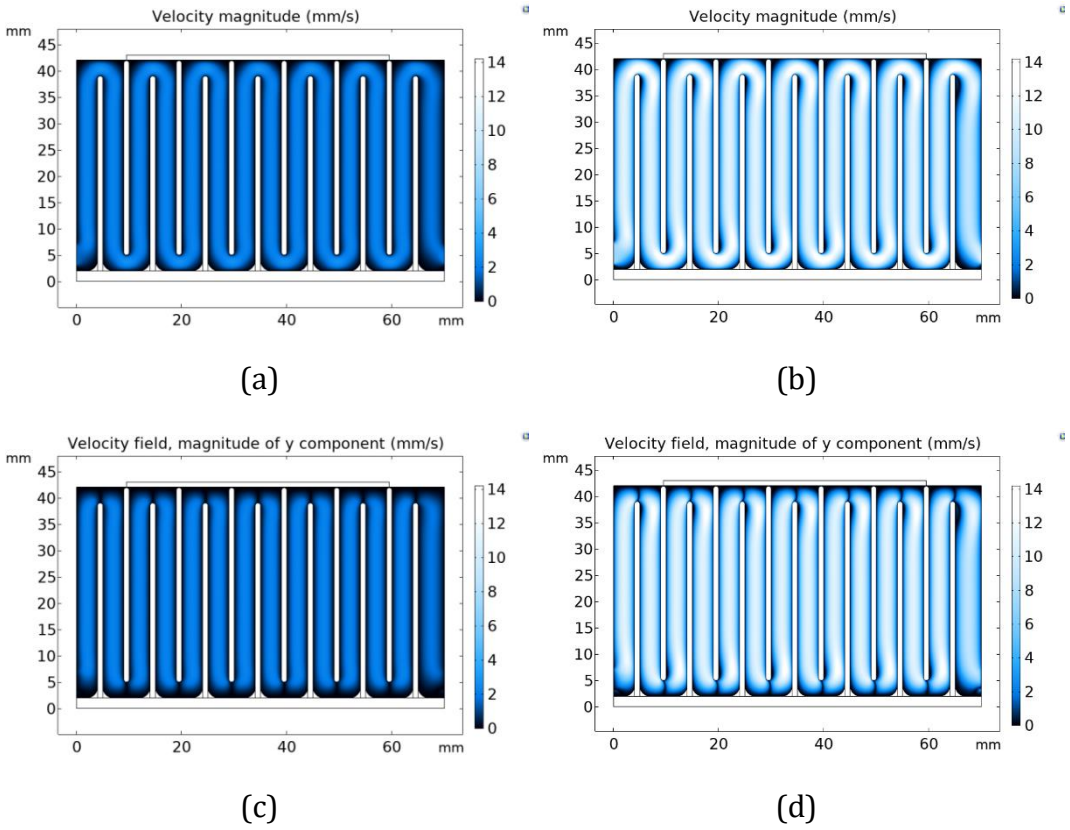

Figure 3.4 - Flow solutions in COMSOL Multiphysics. (a) velocity magnitude (mm s^{-1}) plot for 100 mL h^{-1} flow rate. (b) velocity magnitude plot for 500 mL h^{-1} flow rate. (c) magnitude plot of vertical velocity for 100 mL h^{-1} flow rate. (d) magnitude plot of vertical velocity for 500 mL h^{-1} flow rate.

Mixture (1) is selectively separated by changing the acoustic force or drag force; and mixture (2) is selectively separated by changing the drag force only. Mixture (2) contained smaller particles with unknown properties. In this case, the maximum voltage input was used to ensure the particles are trapped and the flow rate was controlled to achieve selectivity.

To investigate the selective retention capability by adjusting the voltage input, mixture (1) is pumped through the experimental flow cell with a constant flow rate of $100\ \mathrm{mL\ h^{-1}}$. For this flow rate it is possible to trap all particles by applying the maximum available voltage. When the acoustic field is off, no particle trapping is observed and the particle size distributions before and after passing through the cell were similar.

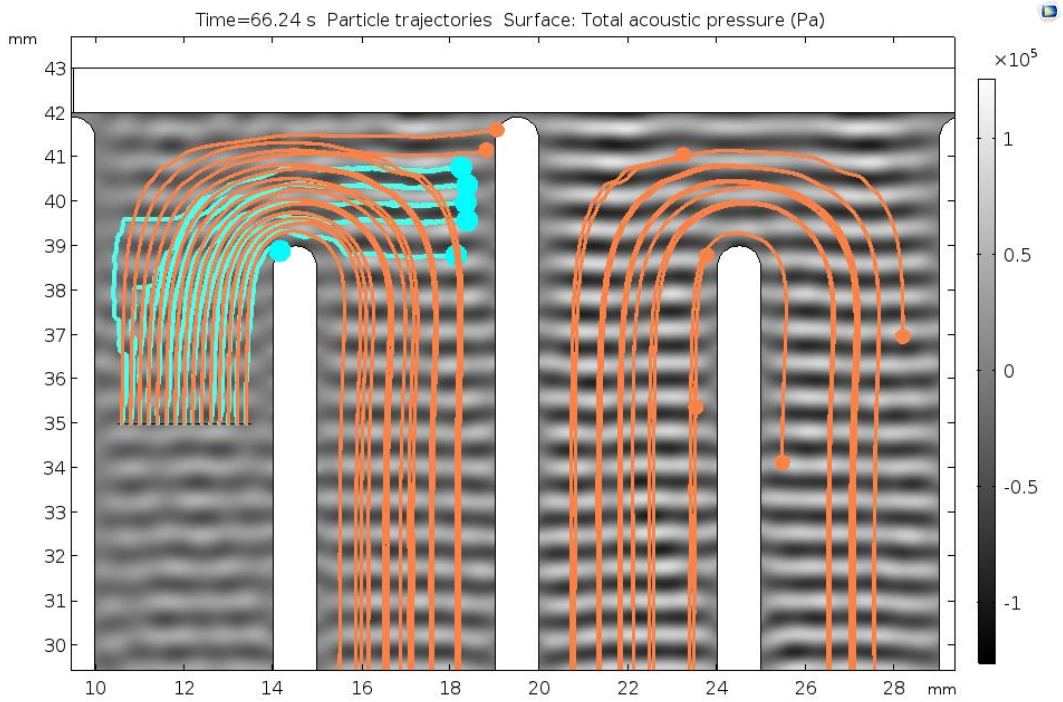

Figure 3.5 - 2D simulation of particle paths in COMSOL Multiphysics for 100 μm (blue) and 75 μm (orange) particles. The input flow rate is 100 mL h^{-1} . Standing wave pattern is presented in grayscale.

Selective separation thresholds were determined visually while adjusting the voltage input to the transducers, and subsequently verified by analyzing the particle trajectories using ImageJ. Particles are trapped in the hairpins of the separator rather than in the straight sections. This behavior is due to the lower vertical flow velocities in the hairpin corners where the drag force is small enough to be overruled by the acoustic force. Figure 3.6 presents the particle path lines in the monitored area of the separator.

Blue and orange particles are affected by the sound field and red particles are continuously unaffected. The path lines of the red particles follow the streamlines of the laminar flow field, as can be seen in Figure 3.6. The corresponding path lines of the blue, orange and red particles are indicated in the left panel of Figure 3.6. There are also some stationary blue and orange particles in the pictures. Those are trapped by the sound field before recording and settled in the small surface grooves of the 3D printed base.

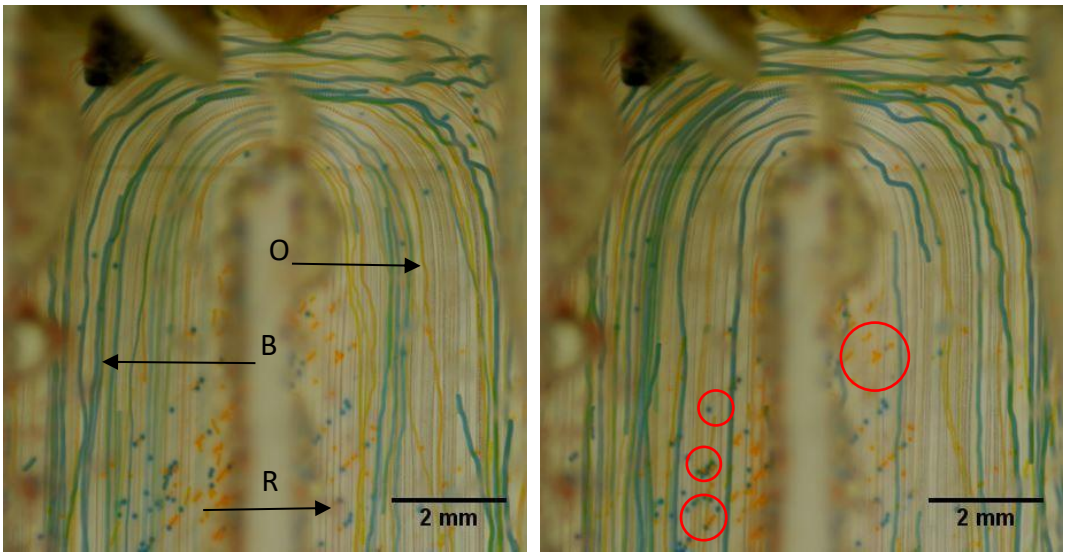

(a) (b)

Figure 3.6 - Particle path lines at the monitoring area of the prototype, recorded by stacking two sets of images over 30 s in 60fps. Blue (B), orange (O) and red (R) lines represent the path lines of the corresponding particles while the system is operated at 26% of maximum voltage available and 100 mL h^{-1}. The path lines are indicated by arrows in (a). Some particles that are stuck in the grooves of the 3D printed base are indicated by circles in (b).

As a result of imperfections in the sound field as well as variations in the third dimension, some particles escaped the trapping positions and continued with the flow. Even though some blue and orange particles initially continued with the flow, they were eventually trapped in one of the following hairpins. Selective retention of particles is achieved by changing the voltage input. When increasing the voltage first the largest particles (blue) retained in the system with 26% of maximum voltage, followed by the largest and medium (orange and blue) particles with 48% of maximum voltage. Lastly, all particles including the smallest (red) particles are retained with 96% of maximum available voltage (Figure 3.7a). Another experiment with only blue and orange particles was also carried out. The blue particles got stuck in the corner while orange particles continued with the flow (Figure 3.7b).

After some time, multiple particles trapped in a single node will form particle aggregates. As the aggregate gets bigger its size gets comparable to the wavelength. The particles on the edge of the aggregate are no longer experiencing sufficient acoustic radiation force to counter the drag. Therefore, these particles got detached from the aggregate and got trapped by a nearby node.

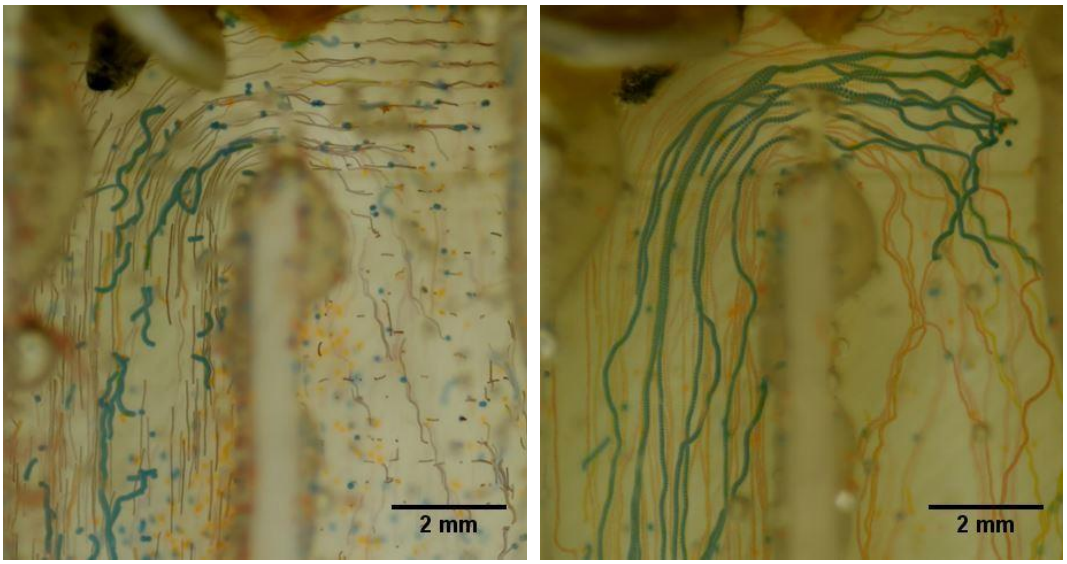

(a) (b)

Figure 3.7 - All blue, orange and red particles are trapped at 96% of the available voltage input (a) and selective retention of blue particles with 26% of available voltage input (b). In case (b), there are no red particles in the mixture. In both cases, flow rate is set to 100 mL h^{-1}

Although the experiments were not continued long enough to explore the limits, eventually the nodes will be saturated and the set-up will require a washout. The prototype was kept in a horizontal position during the experiments and the aggregates did settle down as they grew bigger. Also, some particles got stuck in the grooves of the 3D printed part. The stuck particles can be removed by a washout. Figure 3.8 illustrates the volume histogram of the original mixture, treatment with 26% of maximum available voltage and treatment with 48% of maximum available voltage. After the treatment with 96% of the maximum available voltage, particle size analyzer was unable to detect particles in the given range.

Assuming the resistance of the system is independent of the applied voltage, the power consumption scales with voltage squared. Thus, 96% of the maximum voltage input approximately corresponds to 92% of the maximum power input. Other power input ratios can be calculated similarly.

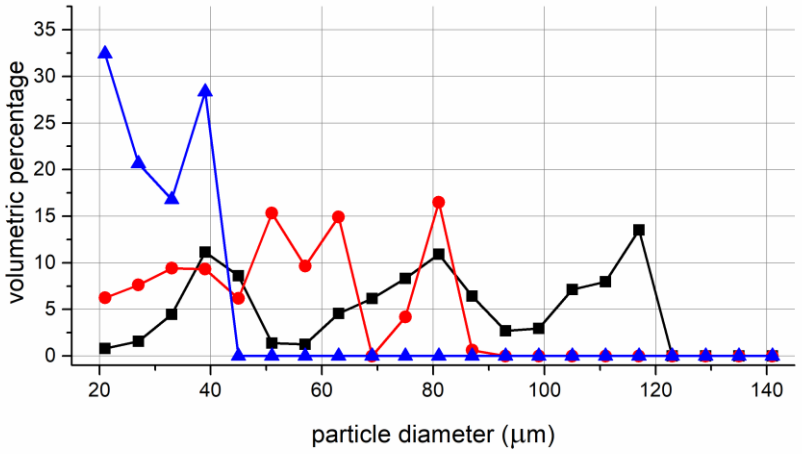

Figure 3.8 - Particle size distribution before and after treatment. Measurement data of the original mixture (black squares), treatment with 26% of maximum available voltage (red circles) and treatment with 48% of maximum available voltage (blue triangles) is shown. Lines are used to guide the eye. Flow rate of the system is set to 100 mL h^{-1} while the excitation frequency is 1924 kHz.

The selectivity can also be achieved by altering the flow rate while keeping the voltage input constant for mixture (1). Voltage input was set to 50% of the maximum available voltage and the flow rate is changed step-wise. Figure 3.9 illustrates the volume particle size distribution histogram of the original mixture, treatment with $400\ \mathrm{mL\,h^{-1}}$, $200\ \mathrm{mL\,h^{-1}}$, $100\ \mathrm{mL\,h^{-1}}$ and $80\ \mathrm{mL\,h^{-1}}$ of input flow rate. Thus, the separation threshold can be shifted to smaller sizes by either increasing the voltage input or decreasing the input flow rate. It can be shifted to larger size by doing the opposite.

While processing mixture (2), the wheat beer, the acoustic separator was operated at $1972\ \mathrm{kHz}$ and at maximum voltage as the size of the particles are small and acoustic contrast factor is unknown. Flow rate in the syringe pump was adjusted to $100\ \mathrm{mL\,h^{-1}}$, $80\ \mathrm{mL\,h^{-1}}$, $50\ \mathrm{mL\,h^{-1}}$ and $20\ \mathrm{mL\,h^{-1}}$, respectively. Figure 3.10 presents the volume histogram of samples taken before and after treatment with different flow rates. The untreated sample contained yeast up to $19\ \mu\mathrm{m}$ diameter. Treatment with $100\ \mathrm{mL\,h^{-1}}$ filtered the particles larger than $17\ \mu\mathrm{m}$ and with $20\ \mathrm{mL\,h^{-1}}$, flow rate particles larger than $9\ \mu\mathrm{m}$ were filtered.

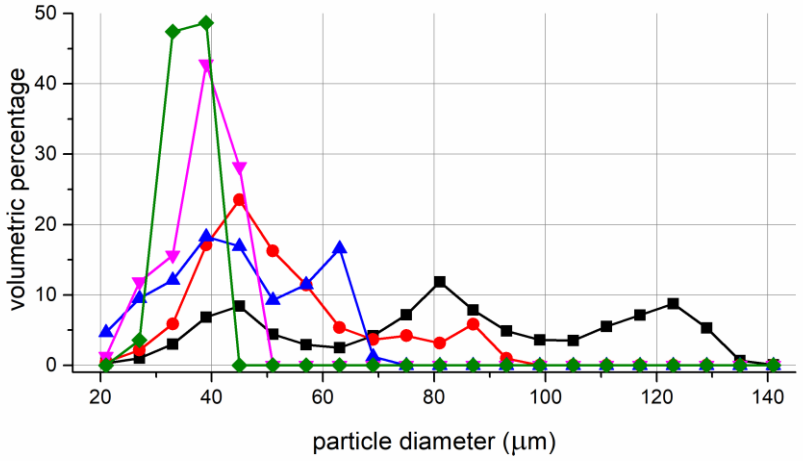

Figure 3.9 - Particle size distribution before and after treatment. Measurement data of the original mixture (black squares), treatment with 400 mL h^{-1} (red circles), treatment with flowrate of 200 mL h^{-1} (blue triangles), treatment with 100 mL h^{-1} (pink inverted triangles) and treatment with 80 mL h^{-1} (green diamonds) is shown. Lines are used to guide the eye. Voltage input to the system is set to 50% while the excitation frequency is 1924 kHz.

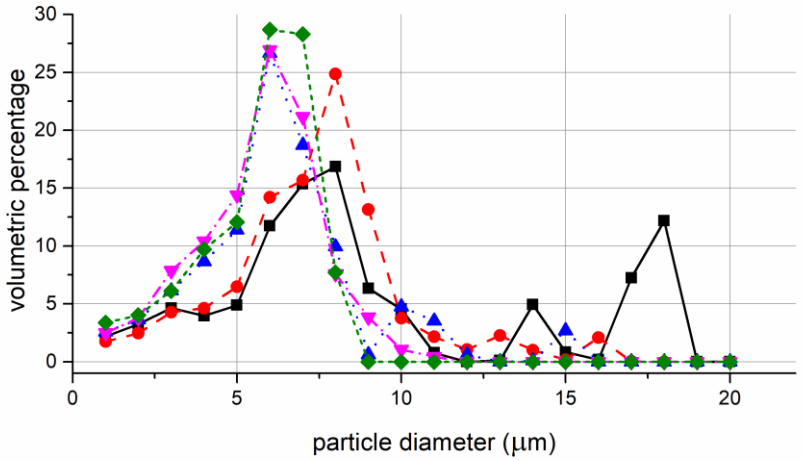

Figure 3.10 - Particle size distributions for the untreated beer samples and after treatment with different flow rates while operating at 1972 kHz and maximum available voltage. Measurement data of the original mixture (black squares), treatment with 100 mL h^{-1} (red circles), treatment with flowrate of 80 mL h^{-1} (blue triangles), treatment with 50 mL h^{-1} (pink inverted triangles) and treatment with 20 mL h^{-1} (green diamonds) is shown. Lines are used to guide the eye.

Experiments and simulations confirm that the particles are trapped at the hairpin sections. Acoustic forces are acting in the vertical direction and the flow speed in vertical direction is lower in the hairpin sections. The acoustic force experienced by particles is large enough to counter the drag force around the hairpins. Ideally the sound field is a plane acoustic wave field and therefore the peak acoustic pressure is similar throughout the field. If the acoustic force is large enough to trap a particle in the middle of the channel, it can also trap the particle at the hairpins due to a locally lower velocity in vertical direction (Figure 3.10). The aim of trapping larger particles selectively in the middle section may result in trapping smaller particles around the hairpins and in turn no selective separation or less efficient separation takes place. Thus, selective separation is achieved around the hairpins while the straight middle sections will carry remaining particles to the next hairpin.

This study demonstrated the possibility for selective filtering in an acoustophoretic serpentine channel. Interplay of acoustic and drag forces results in particle trapping in hairpin sections, and multiple hairpin sections provide multiple areas for particles to be retained. The acoustic field inside the prototype may be improved by changing the inside wall material with a material that provides stronger reflections than PLA. Ensuring that the flow will be laminar and fully developed before entering the hairpins, shortening the linear sections and therefore the distance between the source and reflector would also provide stronger acoustic field. With a stronger acoustic field, the separator can be operated more efficiently and with higher flow rates.

3.4 Conclusions

A standing wave acoustic field is generated by a piezoelectric transducer and the resulting acoustic radiation force is able to selectively trap particles in the hairpin sections of the serpentine separator. Simulations confirm that particles are captured in the hairpins of the separator. A single hairpin does not capture all targeted particles, but as the system contains multiple hairpins, effective particle trapping is ensured. Selective separation is achieved by changing the voltage input or flow rate in case of model polyethylene particles. For wheat beer, the separation threshold is tuned by changing the input flow rate only. Both types of experiments demonstrated clear separation thresholds. Decreasing the flow rate or increasing the power input moves the threshold towards smaller particle sizes while increasing the flow rate or decreasing the power input creates the opposite effect. The

efficiency of the system can be improved by adjusting the channel dimensions and reducing the losses in the system; stronger acoustic field will result with higher throughput possibility.

References

[1] Andrade, M.A.B., Pérez, N., Adamowski, J.C., 2018. Review of Progress in Acoustic Levitation. Brazilian Journal of Physics 48, 190–213. doi:10.1007/s13538-017-0552-6

[2] Castilho, L.R., Medronho, R.A., 2002. Cell Retention Devices for Suspended-Cell Perfusion Cultures, in: Schügerl, K., Zeng, A.-P., Aunins, J.G., Bader, A., Bell, W., Biebl, H., Biselli, M., Carrondo, M.J.T., Castilho, L. R., Chang, H.N., Cruz, P.E., Fuchs, C., Han, S.J., Han, M.-R., Heinzle, E., Hitzmann, B., Köster, D., Jasmund, I., Jelinek, N., Lang, S., Laatsch, H., Lee, J., Miirkl, H., Maranga, L., Medronho, R. A., Meiners, M., Nath, S., Noll, T., Scheper, T., Schmidt, S., Schüigerl, K., Stäirk, E., Tholey, A., Wagner-Döbler, I., Wandrey, C., Wittmann, C., Yim, S.-C., Zeng, A.-P. (Eds.), Tools and Applications of Biochemical Engineering Science, Advances in Biochemical Engineering/Biotechnology. Springer, Berlin, Heidelberg, pp. 129–169. doi:10.1007/3-540-45736-4_7

[3] Lenshof, A., Laurell, T., 2010. Continuous separation of cells and particles in microfluidic systems. Chemical Society Reviews 39, 1203–1217. doi:10.1039/B915999C

[4] Leong, T., Johansson, L., Juliano, P., McArthur, S.L., Manasseh, R., 2013. Ultrasonic Separation of Particulate Fluids in Small and Large Scale Systems: A Review. Industrial & Engineering Chemistry Research 52, 16555–16576. doi:10.1021/ie402295r

[5] Sajeesh, P., Sen, A.K., 2014. Particle separation and sorting in microfluidic devices: a review. Microfluidics and Nanofluidics 17, 1–52. doi:10.1007/s10404-013-1291-9

[6] Cappon, H.J., 2014. Numerical and experimental design of ultrasonic particle filters for water treatment (PhD). Wageningen University, Wageningen.

[7] Kilburn, D.G., Clarke, D.J., Coakley, W.T., Bardsley, D.W., 1989. Enhanced sedimentation of mammalian cells following acoustic aggregation. Biotechnology and Bioengineering 34, 559–562. doi:10.1002/bit.260340415

[8] Pui, P.W.S., Trampler, F., Sonderhoff, S.A., Groeschl, M., Kilburn, D.G., Piret, J.M., 1995. Batch and Semicontinuous Aggregation and Sedimentation of Hybridoma Cells by Acoustic Resonance Fields. Biotechnology Progress 11, 146–152. doi:10.1021/bp00032a005

[9] Trampler, F., Sonderhoff, S.A., Pui, P.W.S., Kilburn, D.G., Piret, J.M., 1994. Acoustic Cell Filter for High Density Perfusion Culture of Hybridoma Cells. Bio/Technology 12, 281–284. doi:10.1038/nbt0394-281

[10] Hawkes, J.J., Coakley, W.T., 1996. A continuous flow ultrasonic cell-filtering method. Enzyme and Microbial Technology 19, 57–62. doi:10.1016/0141-0229(95)00172-7

[11] Gaida, T., Doblhoff-Dier, O., Strutzenberger, K., Katinger, H., Burger, W., Gröschl, M., Handl, B., Benes, E., 1996. Selective retention of viable cells in ultrasonic resonance field devices. Biotechnology Progress 12, 73–76. doi:10.1021/bp950040k

[12] Hawkes, J.J., Limaye, M.S., Coakley, W.T., 1997. Filtration of bacteria and yeast by ultrasound-enhanced sedimentation. Journal of Applied Microbiology 82, 39–47. doi:10.1111/j.1365-2672.1997.tb03295.x

[13] Gorenflo, V.M., Smith, L., Dedinsky, B., Persson, B., Piret, J.M., 2002. Scale-up and optimization of an acoustic filter for 200 L/day perfusion of a CHO cell culture. Biotechnology and Bioengineering 80, 438–444. doi:10.1002/bit.10386

[14] Kapishnikov, S., Kantsler, V., Steinberg, V., 2006. Continuous particle size separation and size sorting using ultrasound in a microchannel. Journal of Statistical Mechanics: Theory and Experiment 01, 01012. doi:10.1088/1742-5468/2006/01/P01012

[15] Petersson, F., Åberg, L., Swärd-Nilsson, A.-M., Laurell, T., 2007. Free Flow Acoustophoresis: Microfluidic-Based Mode of Particle and Cell Separation. Analytical Chemistry 79, 5117–5123. doi:10.1021/ac070444e

[16] Svennebring, J., Manneberg, O., Skafte-Pedersen, P., Bruus, H., Wiklund, M., 2009. Selective bioparticle retention and characterization in a chip-integrated confocal ultrasonic cavity. Biotechnology and Bioengineering 103, 323–328. doi:10.1002/bit.22255

[17] Adams, J.D., Soh, H.T., 2010. Tunable acoustophoretic band-pass particle sorter. Applied Physics Letters 97. doi:10.1063/1.3467259

[18] Evander, M., Nilsson, J., 2012. Acoustofluidics 20: Applications in acoustic trapping. Lab on a Chip 12, 4667–4676. doi:10.1039/C2LC40999B

[19] Batt, B.C., Davis, R.H., Kompala, D.S., 1990. Inclined Sedimentation for Selective Retention of Viable Hybridomas in a Continuous Suspension Bioreactor. Biotechnology Progress 6, 458–464. doi:10.1021/bp00006a600

[20] Docoslis, A., Kalogerakis, N., Behie, L.A., Kaler, K.V.I.S., 1997. A novel dielectrophoresis-based device for the selective retention of viable cells in cell culture media. Biotechnology and Bioengineering 54, 239–250. doi:10.1002/(SICI)1097-0290(19970505)54:3<239::AID-BIT5>3.0.CO;2-G

[21] Suehiro, J., Zhou, G., Imamura, M., Hara, M., 2003. Dielectrophoretic filter for separation and recovery of biological cells in water. IEEE Transactions on Industry Applications 39, 1514–1521. doi:10.1109/TIA.2003.816535

[22] Shafiee, H., Sano, M.B., Henslee, E.A., Caldwell, J.L., Davalos, R.V., 2010. Selective isolation of live/dead cells using contactless dielectrophoresis (cDEP). Lab on a Chip 10, 438–445. doi:10.1039/B920590J

[23] Wang, C., Jalikop, S.V., Hilgenfeldt, S., 2011. Size-sensitive sorting of microparticles through control of flow geometry. Applied Physics Letters 99, 034101. doi:10.1063/1.3610940

[24] Collins, D.J., Alan, T., Neild, A., 2014. Particle separation using virtual deterministic lateral displacement (vDLD). Lab on a Chip 14, 1595–1603. doi:10.1039/C3LC51367J

[25] Dijkshoorn, J.P., Wagterveld, R.M., Boom, R.M., Schutyser, M.A.I., 2017. Sieve-based lateral displacement technology for suspension separation. Separation and Purification Technology 175, 384–390. doi:10.1016/j.seppur.2016.11.057

[26] Fillaudeau, L., Boissier, B., Moreau, A., Blanpain-avet, P., Ermolaev, S., Jitariouk, N., Gourdon, A., 2007. Investigation of rotating and vibrating filtration for clarification of rough beer. Journal of Food Engineering 80, 206–217. doi:10.1016/j.jfoodeng.2006.05.022

[27] Ambrosi, A., Cardozo, N.S.M., Tessaro, I.C., 2014. Membrane Separation Processes for the Beer Industry: a Review and State of the Art. Food and Bioprocess Technology 7, 921–936. doi:10.1007/s11947-014-1275-0

[28] Lemma, S.M., Esposito, A., Mason, M., Brusetti, L., Cesco, S., Scampicchio, M., 2015. Removal of bacteria and yeast in water and beer by nylon nanofibrous membranes. Journal of Food Engineering 157, 1–6. doi:10.1016/j.jfoodeng.2015.02.005

[29] Laurell, T., Petersson, F., Nilsson, A., 2007. Chip integrated strategies for acoustic separation and manipulation of cells and particles. Chemical Society Reviews 36, 492–506. doi:10.1039/B601326K

[30] Kambayashi, T., Nakamura, K. 2016. U.S. Patent No. 9,375,662. Washington, DC: U.S. Patent and Trademark Office.

[31] Sehgal, P., Kirby, B.J., 2017. Separation of 300 and 100 nm Particles in Fabry–Perot Acoustofluidic Resonators. Analytical Chemistry 89, 12192–12200. doi:10.1021/acs.analchem.7b02858

[32] Hawkes, J.J., Radel, S., 2013. Acoustofluidics 22: Multi-wavelength resonators, applications and considerations. Lab on a Chip 13, 610–627. doi:10.1039/C2LC41206C

[33] King, L.V., 1934. On the acoustic radiation pressure on spheres. Proceedings of the Royal Society of London. Series A - Mathematical and Physical Sciences 147, 212–240. doi:10.1098/rspa.1934.0215

[34] Gor'kov, L.P., 1962. On the Forces Acting on a Small Particle in an Acoustical Field in an Ideal Fluid. Soviet Physics Doklady 6, 773.

[35] Bruus, H. (2011). Acoustofluidics 1: Governing equations in microfluidics. Lab on a Chip, *11*(22), 3742-3751.

[36] Townsend, R.J., Hill, M., Harris, N.R., White, N.M., 2004. Modelling of particle paths passing through an ultrasonic standing wave. Ultrasonics, Proceedings of Ultrasonics International 2003 42, 319–324. doi:10.1016/j.ultras.2004.01.025

[37] Bruus, H., 2012. Acoustofluidics 7: The acoustic radiation force on small particles. Lab on a Chip 12, 1014–1021. doi:10.1039/C2LC21068A

[38] Zhou, D., Luo, Z., Fang, M., Lu, M., Jiang, J., Chen, H., He, M., 2017. Numerical calculation of particle movement in sound wave fields and experimental verification through high-speed photography. Applied Energy, Clean, Efficient and Affordable Energy for a Sustainable Future 185, 2245–2250. doi:10.1016/j.apenergy.2016.02.006

[39] Garofalo, F., 2015. Analytical characterization of particle kinematics and transverse dispersion in free-flow acoustophoretic devices. Microfluidics and Nanofluidics 18, 367–382. doi:10.1007/s10404-014-1452-5

[40] Büyükkoçak, S., Özer, M.B., Çetin, B., 2014. Numerical modeling of ultrasonic particle manipulation for microfluidic applications. Microfluidics and Nanofluidics 17, 1025–1037. doi:10.1007/s10404-014-1398-7

[41] Schindelin, J., Arganda-Carreras, I., Frise, E., Kaynig, V., Longair, M., Pietzsch, T., Preibisch, S., Rueden, C., Saalfeld, S., Schmid, B., Tinevez, J.-Y., White, D.J., Hartenstein, V., Eliceiri, K., Tomancak, P., Cardona, A., 2012. Fiji: an open-source platform for biological-image analysis. Nature Methods 9, 676–682. doi:10.1038/nmeth.2019

[42] Gröschl, M., 1998. Ultrasonic Separation of Suspended Particles - Part I: Fundamentals. Acta Acustica united with Acustica 84, 432–447.

4 DYNAMIC ACOUSTIC FIELDS FOR SIZE SELECTIVE PARTICLE SEPARATION ON CENTIMETER SCALE

A version of this chapter has been published as:

Kandemir, M. H., Beelen, M., Wagterveld, R. M., Yntema, D. R., & Keesman, K. J. (2021). Dynamic acoustic fields for size selective particle separation on centimeter scale. *Journal of Sound and Vibration, 490*, 115723

Abstract

Dynamic acoustic fields offer an interesting alternative for acoustic standing-wave fields in acoustic separation applications. This paper reports on an investigation of two methods for generating dynamic acoustic fields and their applicability for selective particle separation. The first method applies a dual-frequency excitation to generate a standing-wave field that in which the pressure nodes travel at constant velocity. The second method uses frequency-ramping, where the velocity of the nodes in the resulting standing-wave field depends on both time and position. Both methods were investigated with analytical and computer models, yielding a dimensionless number that predicts particle behavior without having to solve the differential equations of motion. This dimensionless number can also be used to estimate the acoustic pressure in practical applications. Experiments carried out with polyethylene particles and the two prototypes confirmed the theoretical and numerical predictions. Both methods are suitable for selective particle separation applications.

4.1 Introduction

Acoustophoresis employs an acoustic radiation force (or sometimes called acoustophoretic radiation force) mostly in a standing-wave field and is one of the methods that can be used to separate particles from suspensions. It is potentially of use for applications in water treatment [1, 2]. However, acoustophoresis also offers possibilities for selective separation of particles, as the acoustic radiation force pushes a particle towards either pressure nodes or antinodes, depending on the particle's properties and the drag force it experiences. When a particle has a relative motion with respect to the surrounding liquid, it experiences a drag force. Such relative motion can be in any direction, for example towards a node in an acoustic field [3, 4] resulting from an acoustic force, or perpendicular to the acoustic field as a result of flow [5]. The acoustic radiation force scales with the volume of a particle, while the drag force scales with the diameter of the (spherical) particle. Selective particle separation is thus possible based on the size of particles. However, from the theory of acoustic radiation force, it follows that separation can also take place on the basis of differences in density and compressibility, as acoustic radiation force on a particle depends on these specific particle parameters [2].

Current research on selective particle separation by acoustics mostly focuses on applications in microchannels. The width of such a channel is typically a half-wavelength at the excitation frequency, which means that there is a standing-wave with one pressure node in the middle of the channel. Since the operating frequency is typically in the MHz range, the size of such a channel is in the micrometer range [6-9]. In a dynamic acoustic field, the acoustic force profile is time dependent, in contrast to a stationary standing-wave field [4]. Surface acoustic wave (SAW) applications are examples in which dynamic acoustic fields are used to transport particles [10-21]. Bulk acoustic waves (BAW) also offer possibilities for particle manipulation with dynamic acoustic fields [22]. Whitworth *et al.* [23], for instance, demonstrated a method for transporting particles with two different signals and the use of frequency sweeps. In addition to frequency-ramping, particle manipulation in one or two dimensions is also possible by employing phase differences [24, 25]. However, in BAW applications, reflections may significantly disturb the dynamic acoustic field, as addressed by Grinenko *et al.* [26]. Two groups of researchers have numerically investigated particle filtering with frequency-ramped BAW excitation [27, 28], and Lipkens *et al.* [29] provided the experimental confirmation. Frequency-ramping is employed in several particle transport applications utilizing BAW [30-32]. Although dynamic BAW fields, in principle, offer

the possibility of selective separation on the centimeter scale with multiple nodes, such possibilities have not yet been investigated in detail, to our knowledge.

The objective of the study was therefore to investigate the ability of dynamic BAW fields for selective particle separation on the centimeter scale, and to assess two different methods through numerical simulations and lab experiments. The first method is to excite the field with two different sources operating at slightly different frequencies, effectively resulting in a phase difference that varies linearly with time. The second method is to excite the field with a single source while ramping the excitation frequency, effectively generating a frequency sweep. Theoretical acoustic radiation force expressions were used to estimate particle behavior, a numerical investigation of both methods was carried out using COMSOL Multiphysics. Laboratory experiments with prototypes were conducted to validate the numerical models, and evaluate the performance of these two methods for selective particle separation.

4.2 Materials and methods

4.2.1 Dynamic acoustic fields

A standing-wave field results when two counter-propagating waves with the same amplitude and frequency interact with each other. This interaction can be created by either using two sound sources or using a source and a reflector. With both configurations, it is also possible to generate dynamic BAW fields. In the case of two sound sources with the same amplitude and slightly different frequencies, a pseudo standing-wave field pattern is generated where the nodes move at a constant speed. A dynamic BAW field can also be accomplished by a single sound source operating at a varying frequency, i.e. a frequency sweep. This frequency sweep also leads to a pseudo standing-wave field, but in this case the nodal speed depends on both position and time (see Figure. 4.1).

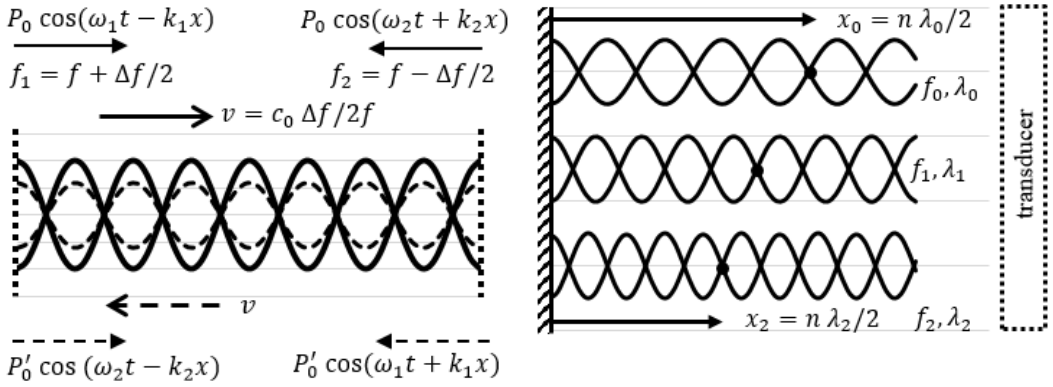

(a) (b)

Figure 4.1 - Two methods for obtaining a pseudo standing-wave field, illustrating the pressure amplitude. (a) Dual-transducer setup, in which two counter-propagating waves create a standing-wave field, which moves at a constant velocity (v, in m s^{-1}) as a result of a small frequency difference (Δf, in s^{-1}) between the two transducers. (b) Transducer-reflector setup, in which the reflector surface is a pressure antinode and use of a frequency sweep (starting at wavelength λ_0) causes the nodes to move.

4.2.1.1 Dual frequency type dynamic fields

Figure 4.1a illustrates how two sound sources create a moving standing-wave field. When two acoustic waves with the same amplitude but different frequencies propagate in opposite directions, the total pressure field becomes as follows[1]:

$$P(x,t) = P_0 \cos\left(\omega_2 t + \frac{\omega_2}{c_0} x\right) + P_0 \cos\left(\omega_1 t - \frac{\omega_1}{c_0} x\right) \tag{4.1}$$

Here, P_0 (Pa) is the common amplitude of the waves, $\omega_1 = 2\pi f_1$ and $\omega_2 = 2\pi f_2$ (rad s^{-1}) are the excitation frequencies, t (s) is time, x (m) is distance from the high frequency source and c_0 (m s^{-1}) is the speed of sound in the host medium. If $\omega_1 = \omega_2$, the sum will be a stationary standing-wave field. When $\omega_1 = \omega_2 + \epsilon$ and $\omega = (\omega_1 + \omega_2)/2$, the field can be written as given by Equation (4.2).

[1] For the sake of simplicity in demonstration, only the cosine parts of the waves are considered here.

$$P(x,t) = 2P_0 \cos\left(\frac{\omega}{c_0}x - \frac{\epsilon}{2}t\right)\cos\left(\frac{\epsilon}{2\,c_0}x - \omega t\right) \tag{4.2}$$

In such an acoustic field, where $P_D = 2P_0$, the force on a spherical particle is given by

$$F_x(x,t) = 4\pi k r^3 \left(\frac{P_D^2}{4\rho_0 c_0^2}\right)\Phi(\rho,c)\sin(2kx - \epsilon t) \tag{4.3}$$

Here, r (m) is the particle radius, ρ_0 (kg m^{-3}) is the density of the medium, ρ is the density of the particle, c is the speed of sound in the particle, $\Phi(\rho,c)$ (-) is the acoustic contrast factor, $k = \omega/c_0$ (m^{-1}) is the wave number and the force field will travel from the higher-frequency source to the lower-frequency source at a constant velocity of $v = \epsilon/2k$ (m s^{-1}). If the frequencies of excitation are given by: $f_1 = f_2 + \Delta f$ and $f = (f_1 + f_2)/2$ (Hz), the velocity of the wave pattern is $v = \frac{\Delta f}{2f}c_0$. A similar field can be created by introducing a phase difference between two sound sources with equal frequencies. Thus, a frequency difference between the sources corresponds to a case in which the phase is shifted linearly and continuously.

In Figure 4.1a, the reflected waves (depicted by the dashed line) from the transducer surfaces create a similar but weaker field, which moves in the opposite direction with the same velocity as the applied field. In such a case, with reflections from each transducer surface with a reflection coefficient $R \leq 1$, and neglecting secondary reflections [26], the equation of motion (EOM) of a particle in such a moving field reads as follows:

$$\begin{aligned}\left(\frac{4}{3}\pi r^3\rho\right)\ddot{x} + (6\pi\mu r)(\dot{x} + u) \\ + 4\pi k r^3\left(\frac{P_D^2}{4\rho_0 c_0^2}\right)\Phi(\rho,c)\sin(2kx - \epsilon t) \\ + 4\pi k r^3\left(\frac{(RP_D)^2}{4\rho_0 c_0^2}\right)\Phi(\rho,c)\sin(2kx + \epsilon t) = 0\end{aligned} \tag{4.4}$$

Here, u (m s^{-1}) is the constant flow velocity of the liquid from the high-frequency source to the low-frequency source and μ (Pa s) is the viscosity of host medium.

4.2.1.2 Frequency-sweep type dynamic fields

Figure 4.1b illustrates the frequency-ramping method, which employs a sound source and a reflector to obtain the standing-wave field. In this case, the velocity of the nodes depends on position and time and the number of nodes depends on the excitation frequency. A higher frequency wave has more wavelengths per distance, and therefore creates more pressure nodes. When using this method, the modulation type of interest is the frequency sweep. A frequency sweep can be expressed as $f(t) = f_0 + S\,t$ where f_0 is the starting frequency, S is the sweep rate and t is time. The sweep rate S is defined as $S = \Delta f/\Delta t$, where Δf is the sweep frequency and Δt is the sweep period. For practical reasons, the sweep cannot continue infinitely, thus the expression is only valid for a given sweep time and is periodic with sweep period Δt . With the changing frequency, the wavelength also changes, as $\lambda(t) = c/f(t)$. The velocity of any point in the wave pattern is then expressed as (see Appendix 4A):

$$v(x,t) = -f_0\,/(f_0 + S\,t)^2\,S\,x \tag{4.5}$$

The distance x is measured from the reflector side. The negative sign of the velocity is due to fact that the reflector is taken as the reference point. Since the frequency changes in time, the wave number $k(t) = \omega(t)/c_0$ also becomes a function of time. Assuming that the maximum pressure amplitude does not vary significantly during the sweep period, the EOM of a particle in such a field therefore becomes

$$\left(\frac{4}{3}\pi r^3\rho\right)\ddot{x} + (6\pi\mu r)(\dot{x} + u) + 4\pi k(t) r^3 \left(\frac{P_0^2}{4\rho_0 c_0^2}\right)\Phi(\rho, c)\sin(2k(t)x) = 0 \tag{4.6}$$

Equations (4.4) and (4.6) are non-linear, second-order differential equations of motion and have no analytical solution.

4.2.2 Experimental setup

The particles used in the experiments were polyethylene particles with a diameter of $70\ \mu\text{m}$ (orange) and $100\ \mu\text{m}$ (blue). The particles had a density of $\rho =$

$1050\ \mathrm{kg\,m^{-3}}$ and the speed of sound in the particles was $c = 1720\ \mathrm{m\,s^{-1}}$. The used particle mixture contained $1000\ \mathrm{cm^3}$ MilliQ water, with $0.23\ \mathrm{g}$ CTAB (hexadecyltrimethylammonium bromide) as surfactant, $0.35\ \mathrm{g}$ orange particles and $0.35\ \mathrm{g}$ blue particles. Each experimental set-up consisted of a dual-channel signal generator (Keysight Trueform 33512B), a custom-made amplifier, an oscilloscope (Tektronix TDS2024C), two syringe pumps (Aitecs PRO SP-12S) and a separator prototype with piezoelectric transducers. The dual-frequency prototype (Figure 4.2a) contained two piezoelectric transducers (Noliac NCE41, dimensions 50 mm × 10 mm × 1 mm), two acoustically transparent polyurethane sheets as inner walls and two absorbing blocks (Ecolab kitchen sponge 5 cm × 1 cm × 1 cm). The frequency-sweep prototype (Figure 4.2b) contained one piezoelectric transducer and a stainless steel reflector plate. Both prototypes, illustrated in Figure 4.2, included 3D-printed polylactic acid (PLA) walls and poly(methyl 2-methylpropenoate) (PMMA) covers. The transducers were coated with a thin layer of polyurethane paint to provide electrical insulation. Polyurethane paint is used because it has a similar acoustic impedance as water. In order to verify the effect of the absorbing blocks, admittance measurements are carried out in the prototype. First, the admittance of the transducer placed underwater and away from reflective surfaces is recorded as a function of frequency between $1.8\ \mathrm{MHz}$ and $2.5\ \mathrm{MHz}$. When the transducer is placed in the prototype, the admittance was affected due to the natural modes of the water mass between the transducer and the reflective surface, the graph included peaks and valleys related to the natural frequencies of the water mass. When the reflective surfaces are covered with the absorbing block, the peaks and valleys vanished and the admittance graph became similar to that of the transducer alone. Thus, it was concluded that by not reflecting the sound generated by the transducer, the absorbing blocks were preventing the transducer to detect the vibrational modes of the water mass. Admittance measurements for both prototypes are given in Appendix 4B.

For the dual-frequency experiments, the average frequency was $2.4\ \mathrm{MHz}$ and Δf was chosen between $0\ \mathrm{Hz}$ and $5\ \mathrm{Hz}$. For the frequency-sweep experiments, the starting frequency f_0 was $2\ \mathrm{MHz}$. The frequency sweep rate, $(f(\Delta t) - f_0\ )/\Delta t$, is defined by the end frequency ($f(\Delta t)$ and the sweep period (Δt). To enable bubbles (entering from the inlets) to escape the system quickly, the prototypes were on an inclined surface at an angle of $5°$ with respect to the horizontal plane. Particle motion was recorded by a microscope camera and the particle velocities were calculated by analyzing the movies with ImageJ software [33].

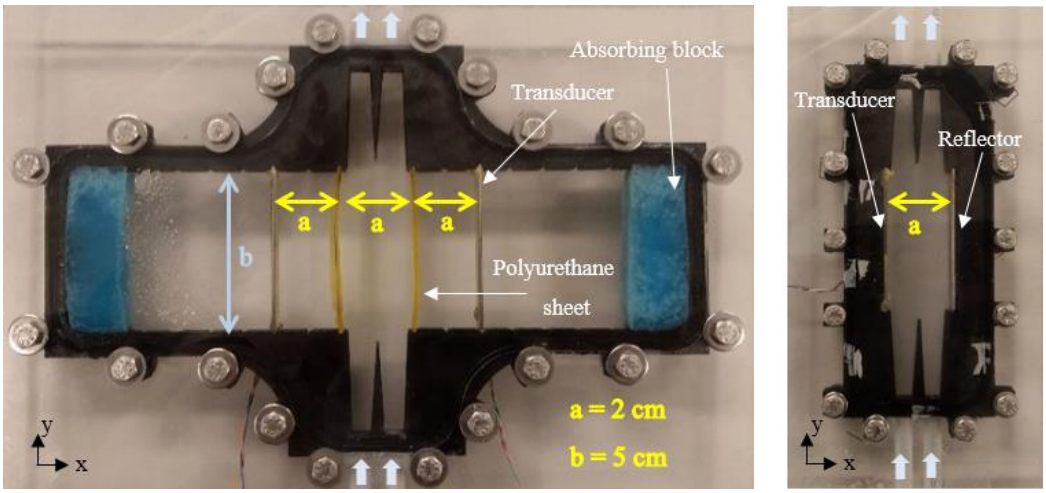

(a) (b)

Figure 4.2 - Prototypes used in the experiments. Black parts are 3D-printed base structures, with rubber rings used as sealing between base and cover. Each prototype had two inlets and two outlets divided by triangular dividers in the middle of the channel. The width of each separation channel was 20 mm and the depth 10 mm. In prototype (a), used in the dual frequency experiments, the separation channel was bordered by polyurethane sheets with a thickness of 1 mm and the distance between two transducers was 60 mm. The blue parts in (a) are sound-absorbing materials to eliminate back reflections, placed in contact with the end walls and at a distance of 50 mm from each transducer. Prototype (b) was used in the frequency sweep experiments.

4.3 Results and discussion

4.3.1 Computer simulations

Equations (4.4) and (4.6) are ordinary differential equations (ODEs) of motion for a particle in a dual-frequency type dynamic field with reflection and frequency-sweep type dynamic field, respectively. In these dynamic fields the nodal pattern is not stationary. Therefore, depending on the particle and excitation properties, a particle may or may not follow the nodal movement. Having the nodal movement in such a way that only the targeted particles are captured is the key for selectivity. For further understanding of the dynamic behavior of the acoustic field and particles within the field numerical simulations were performed.

Figure 4.3 illustrates some typical trajectories of captured and non-captured particles in both type of dynamic fields.

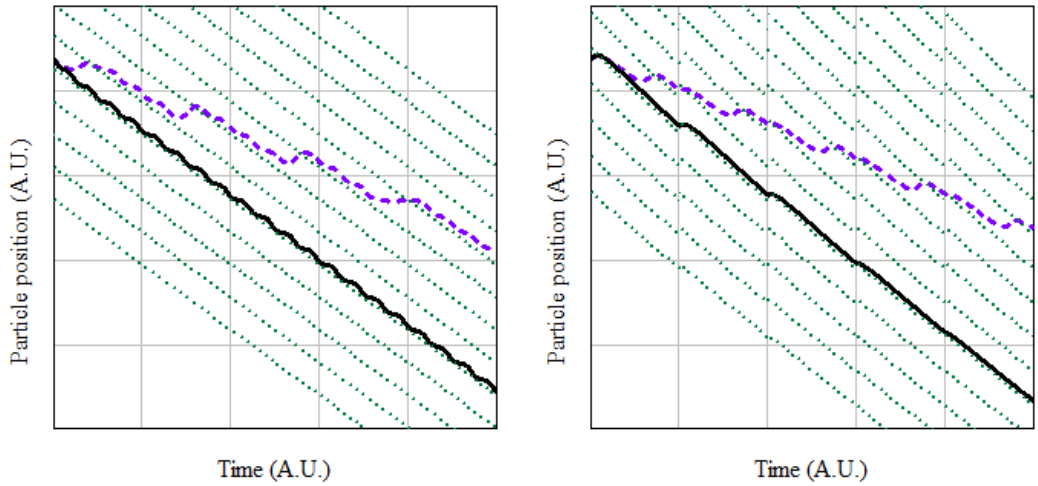

(a) (b)

Figure 4.3 - Typical particle trajectories for particles in dynamic acoustic fields, plotted in arbitrary units for illustration purposes. The captured particle (black solid line) is able to follow the nodal pattern movement (green dotted line) while another particle (purple dashed line) is unable to follow the nodal movement but is still moving downwards. Left panel illustrates a case with a dual-frequency type field and right panel illustrates a frequency-sweep type field. In both cases, the standing wave field is moving downwards. In the dual-frequency case, the reflected field is moving upwards. In the absence of the reflected field a captured particle follows a straight line as the nodal pattern movement.

Equations (4.4) and (4.6) can be solved by any software that is capable to solve ODEs. Those equations include the analytical acoustic radiation force expressions on the particle obtained from Gor'kov's method. To check the validity of the analytical force expressions and the equations of motion, the particle trajectories are compared with the trajectories obtained in COMSOL Multiphysics. The comparison is made by including the acoustic radiation force through the use of two different methods in COMSOL. The first method defines the external acoustic radiation force on particles, as given in Equations (4.4) and (4.6), while the second method numerically calculates the acoustic radiation force on a particle given an acoustic field by using the acoustic field input to the software.

To calculate the acoustic radiation force COMSOL Multiphysics requires the input of the acoustic pressure field and the velocity field. Given that the sound source is much larger than the wavelength, the sound field in our acoustophoresis device is a plane wave field. For small acoustofluidic devices, operating in MHz range and

with transducer surface dimensions larger than a millimeter, this is also the case. Hence, the acoustic velocity field can directly be calculated from the pressure field by using the specific acoustic impedance, that is $u(x,t) = \frac{1}{c_0\rho_0}p(x,t)$, where $c_0\rho_0$ is the specific acoustic impedance in the host medium and $u(x,t)$ is the acoustic particle velocity.

Figure 4.4 illustrates the case with dual frequency excitation (Figure 4.3a) and the resulting particle trajectories calculated in COMSOL by using both methods.

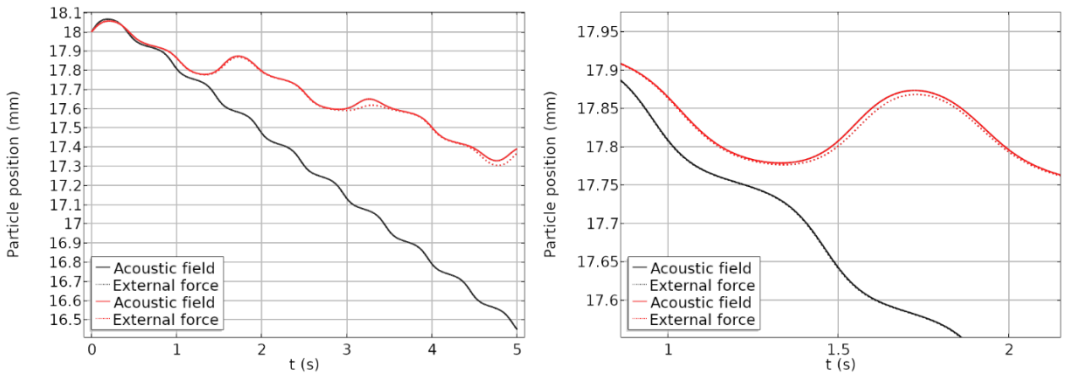

Figure 4.4 - Particle trajectories calculated by COMSOL. Black lines correspond to the captured particle's (d = 70 μm) trajectories and red lines correspond to that of non-captured (d = 60 μm) particle. Solid lines are calculated by applying the acoustic radiation force as an external force as in Equation (4.4). Dotted lines are calculated by giving the dynamic acoustic fields to COMSOL and the software calculates the acoustic force. (b) Zoomed in view of particle trajectories.

The diameter of the large (captured) particle is 70 μm and that of the small (non-captured) particle 60 μm. For both particles, $\rho = 1050\ \mathrm{kg\,m^{-3}}$, $c = 1720\ \mathrm{m\,s^{-1}}$ and $\nu = 0.47125$ (Poisson's ratio). The host medium is water with $\mu = 0.0010093\ \mathrm{Pa\,s}$, $\rho_0 = 999.62\ \mathrm{kg\,m^{-3}}$ and $c_0 = 1481.4\ \mathrm{m\,s^{-1}}$. For the dual-frequency type of field excitation parameters are $f = 2.4$ MHz, $\Delta f = 1$ Hz, $u = 0$, $R = 0.8$ and $P_D = 65$ kPa. The two calculated trajectories of the captured particle, which is thus able to follow the nodal pattern, are (almost) matching and hard to distinguish. Both represent the typical staircase-like movement depicted in Figure 4.3a. Trajectories of the small, non-captured particle follow a similar trend, however, they differ especially when the particle is affected more by the next node catching up with the particle.

Figure 4.5 illustrates the case with frequency-sweep excitation and the resulting particle trajectories calculated by COMSOL.

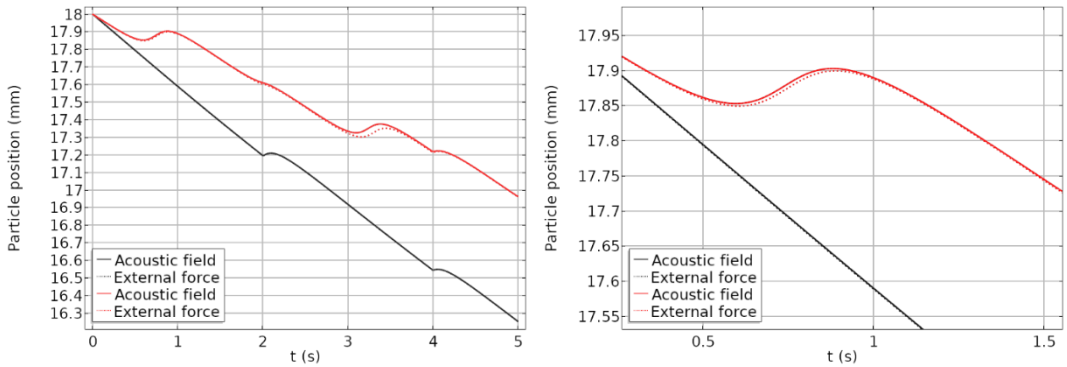

(a) (b)

Figure 4.5 - Particle trajectories calculated by COMSOL. Black lines correspond to the captured particle's (d = 70 μm) trajectories and red lines correspond to that of non-captured (d = 60 μm) particle. Solid lines are calculated by applying the acoustic radiation force as an external force as in Equation (4.6). Dotted lines are calculated by giving the dynamic acoustic fields to COMSOL and the software calculates the acoustic force. (b) Zoomed in view of particle trajectories.

In Figure 4.5, particle properties are the same as the case in Figure 4.4. The excitation parameters are $P_0 = 65$ kPa, $f_0 = 2.19$ MHz, $\Delta f = 100$ kHz and $\Delta t = 2$ s. Similar to the dual-frequency case, trajectories of the large, nodal pattern following, particles are matching well. For the small particles, the trajectories follow the same trend while having a deviation especially when the particle is moving upwards as the next node is catching up with the particle.

It should be noted that in both methods, the acoustic field was not calculated by COMSOL. When the force is given as an external force, a generic force node is added to the particle tracing physics tree with the acoustic force expressions in Equations (4.4) and (4.6) as input. When the acoustic field is input to the "acoustophoretic radiation force" node, the pressure and velocity fields, as shown in Figure 4.1, are input for the calculation. Hence, the assumption was that the software does not require a mesh fine enough to resolve the harmonic wave pattern, as the forces acting on the particle were already calculated from functions of time and position. To check this assumption, the same simulations are carried out with the default 'coarse' mesh size in COMSOL and with custom-input mesh size that has maximum element size of $\lambda/12$ at $f = 2.4$ MHz. The acoustic force amplitudes calculated by

each method differs less than 0.1%. However, it still makes a difference, especially at moments when the particle is affected by the reflected wave field, as illustrated in Figure 4.4.

4.3.2 Experiments

To compare the particle behavior in simulations with those in experiments, a mixture of particles with $70\ \mu\mathrm{m}$ diameter was pumped through the dual-frequency prototype. In one inlet the water-particle mixture was fed and the other inlet was fed with water only, each at a flow rate of $100\ \mathrm{cm^3\ h^{-1}}$. Fig. 6 compares the particle trajectories calculated in simulations and the particle trajectories recorded in the experiments, created by overlaying 300 consecutive pictures taken in a span of $10\ \mathrm{s}$.

Figure 4.6 confirms the staircase-like particle trajectories, as in Figures 4.3 and 4.4, in case of dual-frequency type excitation and reflection. Figure 4.6c includes some particles that do not follow the staircase-like trajectory, which was concluded to be due to the non-uniform size of the particles in the mixture and non-uniformity of the standing wave field. The non-uniformity of the standing wave field is also resulting in some deviations from expected trajectories of particles, without affecting the general trend. The experiments indeed show that if a particle follows the nodal movement, average speed of the particle can be estimated from $v = \frac{\Delta f}{2f} c_0$.

In the dual-frequency type field the nodal pattern and the captured particle velocity is constant and can be estimated by the average frequency and the frequency difference. In the frequency-sweep type field, however, the velocity of the nodal movement is not constant. Taking the origin ($x = 0$) at the reflector surface, Equation (4.5) gives the velocity as a function of time and space, which can be used to approximate the average velocity within a sweep period. The average velocity of a captured particle starting from an initial position x_0, within one sweep period, can be calculated by using Equation (4.7).

$$v_{av} = -\frac{x_0}{\Delta t}\left(1 - \frac{f_0}{f_0 + S\,\Delta t}\right) \tag{4.7}$$

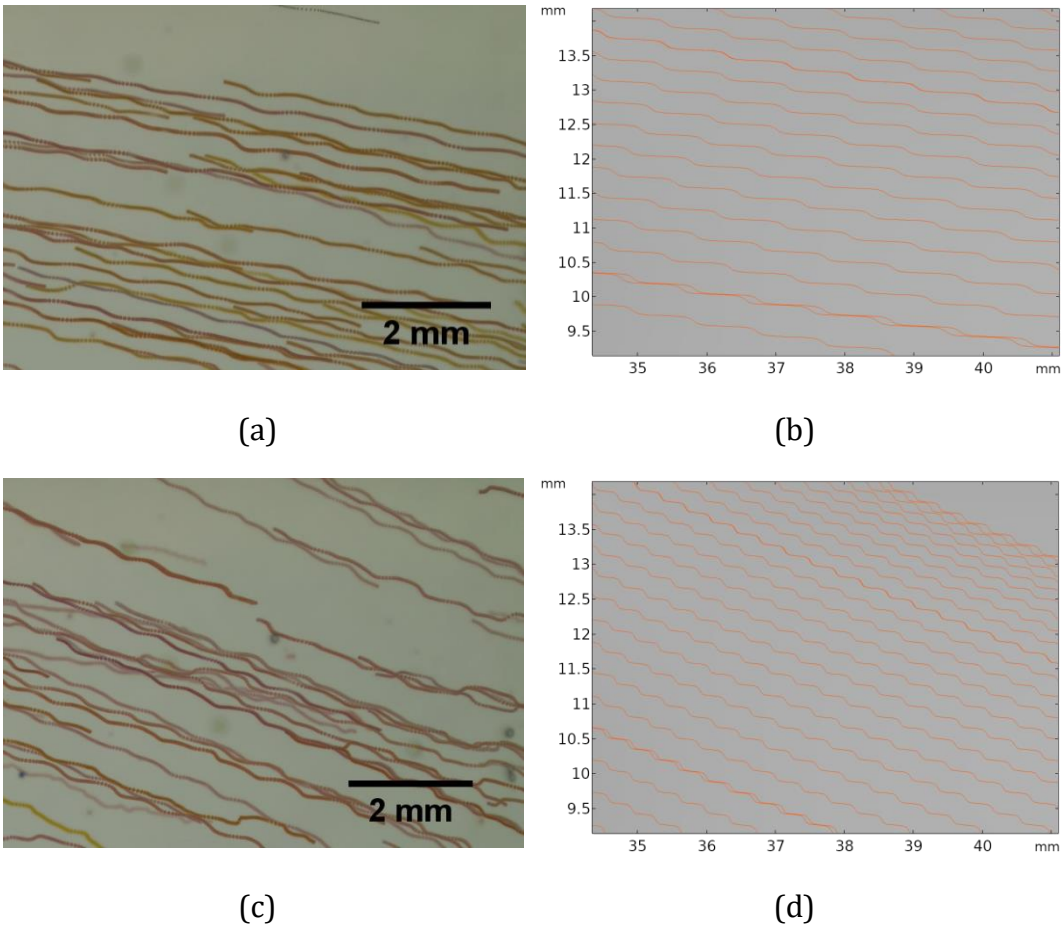

Figure 4.6 - Experimental and simulated trajectories of the particles in dual-frequency type dynamic field.[2] Flow direction is from left to right and the acoustic field movement is downward. (a) experimental particle trajectories when $\Delta f = 0.4$ Hz. (b) particle trajectories calculated by COMSOL when $\Delta f = 0.4$ Hz. (c) experimental particle trajectories when $\Delta f = 1$ Hz. (d) particle trajectories calculated by COMSOL when $\Delta f = 1$ Hz. In simulations and experiments, $f = 2.4$ MHz. In the experiments, the transducers were excited with 20 V_{pp} while in the simulations $P_D = 70$ kPa. In simulations all particles start outside the frame whereas in the experimental recordings particles do not have a common starting position

[2] Movies showing the typical particle behavior can be found in the supplementary material S1 in the published version of the chapter.

Figure 4.7 compares the particle trajectories resulting from a frequency sweep, calculated in simulations and recorded in experiments. The experimental image is created by overlaying 300 consecutive pictures taken in a span of 10 s.

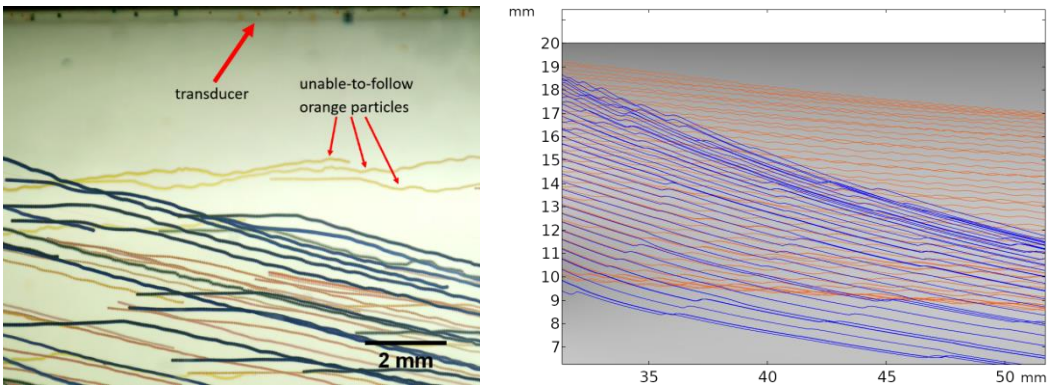

(a) (b)

Figure 4.7 - (a) Experimentally recorded trajectories of two sizes of particles in a frequency-sweep-type dynamic field, obtained by stacking multiple images over time of 10 s, including multiple sweep periods ($\Delta t = 3$ s).[3] Starting frequency was $f_0 = 2.19$ MHz and $f(\Delta t) - f_0 = 300$ kHz. (b) Trajectories of particles from computer simulations with $P_0 = 55$ kPa.

Figure 4.7a displays the experimentally obtained trajectories of particles in a mixture where blue particles having a diameter of 100 µm and orange particles having a diameter of 70 µm. Figure 4.7b illustrates trajectories of particles in the same mixture, with $P_0 = 55$ kPa, simulated with COMSOL. The simulation results suggest that even though a particle cannot follow the nodal pattern it will still have a downward motion, as seen in the dual-frequency method. The experimental trajectories do not display a clear separation between the two groups of particles. Besides, the unable-to-follow orange particles are moving in the opposite direction of the nodal pattern.

This last observation can be attributed to a possible aliasing effect that pushes the particles to the closest node, but the closest node is always in the upwards direction. A basic assumption in the simulations is that the pressure amplitude in the standing wave field during the frequency sweep is constant. Depending on the

[3] Movies showing the typical particle behaviour can be found in the supplementary material S2 (varying sweep frequency, $S\,\Delta t$) and S3 (varying sweep period, Δt) in the published version of the chapter.

dynamic properties of the transducer, the electromechanical response may differ and result in different peak acoustic pressure. Hence, especially for the non-captured particles the experimental trajectories indicate that there is a force gradient pushing the particles in the opposite direction of the nodal movement.

The velocity expression in Equations (4.5) and (4.7) suggests that the nodal movement will slow down with increasing time and frequency (Figure 4.1b). The nodes further from the reflector ($x = 0$) move faster than the nodes closer to the reflector. For a captured particle, the numerical model and Equation (4.7) always yielded lower velocities than those measured in the experiments: This underestimation appears because Equation (4.7) predicts the average velocity of a point in the nodal pattern, whereas an actual particle following the nodal pattern has a relative motion with respect to nodal pattern because of the fact that the acoustic force experienced by the particle also changes. Such behavior is explained in detail in Appendix 4C.

4.3.3 Conditions for particle capturing

In both types of dynamic fields a captured particle will travel along with the nodal pattern. For the dual-frequency type fields, the nodal pattern has a constant velocity, whereas for the frequency-sweep type fields the nodal velocity can be calculated by Equations (4.5) and (4.7). Hence, the acoustic radiation force experienced by a particle is proportional to the velocity of the particle in the direction of the nodal movement, therefore balancing the drag force. Figure 4.8 illustrates the force experienced by a particle and the corresponding particle velocity in Figures 4.4 and 4.5.

The top panels of Figure 4.8 correspond to the dual-frequency type dynamic field and the bottom panels correspond to the frequency-sweep type dynamic field. In both cases the force and velocity graphs overlap, indicating that the acoustic force is in balance with the drag force proportional to the velocity, except for Figure 4.8c.

Figure 4.8c confirms, however, by comparing the rate of change of the force (solid line) and velocity (dashed line) for example between $t = 2.5 - 4$ s, that if a particle is following the nodal pattern, it must be moving as fast as or faster than the nodal pattern.

Force distribution on a particle in dual-frequency type of field

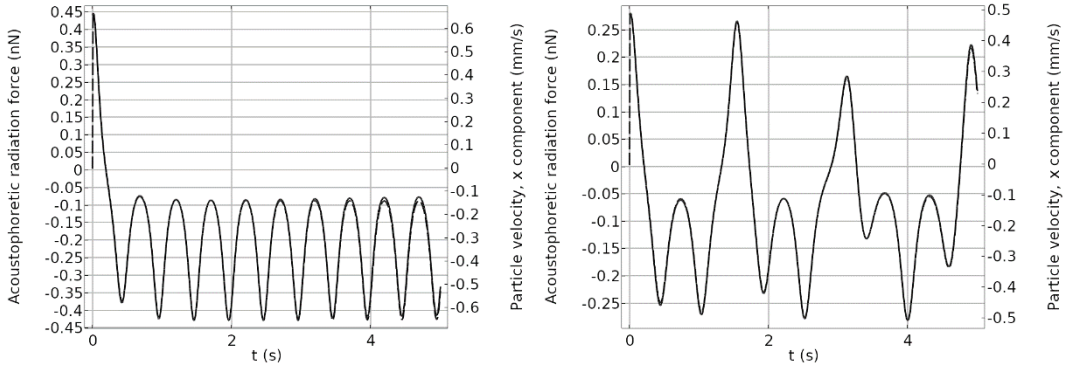

(a) (b)

Force distribution on a particle in frequency-sweep type of field

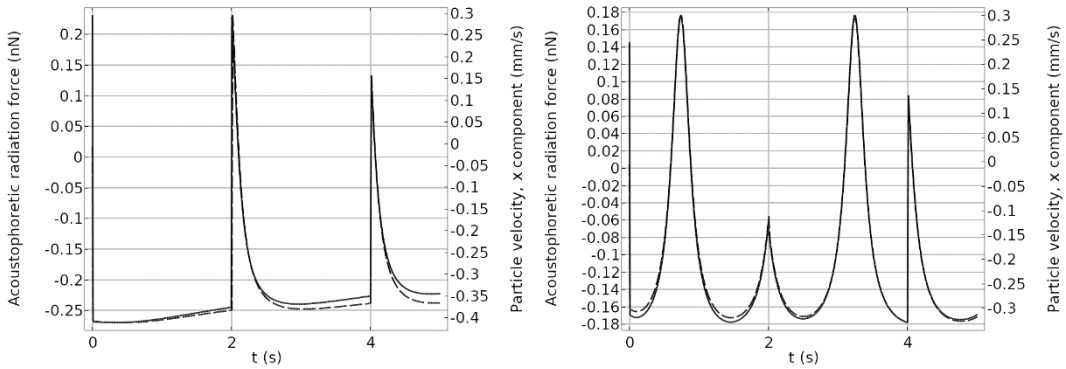

(c) (d)

Figure 4.8 - Time-varying forces (solid lines) and velocities (dashed lines): (a) force and velocity of a captured particle in Figure 4.4. (b) force and velocity of a non-captured particle in Figure 4.4. (c) force and velocity of a captured particle in Figure 4.5. (d) force and velocity of a non-captured particle in Figure 4.5.

Under the condition that the particle is following the nodal pattern, the acoustic force must be large enough to overcome the drag force experienced by the particle. Under dual-frequency excitation with $\Delta f \neq 0$, and $u = 0$ and $R = 0$, the following dimensionless number can therefore be defined as in Equation (4.8).

$$K_0 = \frac{F_{acoustic}^{max}}{F_{drag}^{max}} = \frac{4\pi k r^3 \left(\frac{P_D^2}{4\rho_0 c_0^2}\right) \Phi(\rho, c)}{6\pi\mu r \left(\frac{\Delta f}{2f} c_0\right)} \tag{4.8}$$

This dimensionless number K_0 describes whether the particle is experiencing a large enough acoustic force to follow the nodal pattern. If $K_0 < 1$, the acoustic force on the particle is not large enough to enable it to keep up with the nodal movement $\left(\frac{\Delta f}{2f} c_0\right)$. $K_0 = 1$ means that the maximum acoustic force equals the drag force on the particle, while $K_0 > 1$ indicates that the particle is able to follow the nodal movement. Figure 4.4 showed that, when reflections are present, particles that are able to follow the nodal pattern, thus with $K_0 > 1$, do not move at a constant speed. The counter-propagating dynamic fields interact with each other, and the particles oscillate around the straight-line pattern, forming a staircase-like trajectory. Similar oscillations are present in the paths of the non-captured particles.

In the case of Figure 4.4, $K_0 = 1.467$ for the captured particle and $K_0 = 1.078$ for the non-captured particle. Given these K_0 values, both particles should have been able to follow the nodal movement. The presence of reflections, however, disturbs the maximum acoustic force experienced by the particle, although the average force experienced by the particle remains the same, owing to the periodic nature of the two dynamically changing fields. The effect of reflections was explored in numerical simulations with different excitation parameters (see Appendix 4D), yielding the following expression for the K number corrected for reflections:

$$K = \frac{K_0}{1 - 3.696 \times 10^{-4}(1 - e^{7.582R})} \tag{4.9}$$

Equation (4.9) gives an empirical estimate of K to check whether a particle can follow the nodal movement or not, regardless of whether reflections are present in the system. For the case of Figure 4.4, this results in $K = 1.266$ for the captured particle while $K = 0.93$ for the non-captured particle.

For the frequency-sweep type field, Equation (4.5) gives the velocity as a function of time and space, which can be used to approximate the average velocity within a sweep period, given in Equation (4.7). Hence, Equation (4.7) can be inserted into the expression for the K number to estimate if the particle is able to follow the

nodal movement. Since the acoustic radiation force also scales with the time-varying wave number, the midpoint at $\frac{1}{2}\Delta t$, should be taken into account. For frequency-sweep type dynamic fields, the dimensionless K number is therefore defined as follows:

$$K = \frac{4\pi k \left(\frac{1}{2}\Delta t\right) r^3 \left(\frac{P_0^2}{4\rho_0 c_0^2}\right) \Phi(\rho, c)}{6\pi\mu r \, \frac{x_0}{\Delta t}\left(1 - \frac{f_0}{f(\Delta t)}\right)} \tag{4.10}$$

Equation (4.10) estimates whether the particle is able to follow the nodal pattern or not, under frequency-sweep conditions. In Figure 4.5, $K = 1.07$ for the captured particle and $K = 0.786$ for the non-captured particle. Although the K number estimates the behavior for the first sweep period only (in this case, from 0 to 2 s), it successfully predicts whether the particle is able to follow the field or not.

Numerical simulations suggest that the particle may still be able to move in the direction of the nodal movement and stay between two adjacent nodes if K is larger than 0.9. However, $K \geq 1$ ensures that the particle moves parallel to the nodal movement. If the properties of the particle and of the excitation are known, the K number can also be used to estimate the acoustic pressure in the system. Since $K \geq 1$ implies that the particle is able to follow the nodal movement, it will give a lower bound for the pressure estimate.

Theoretically, the dual-frequency method requires, from Equations (4.1) and (4.2), that the pressure amplitudes from each source to be equal. The experimental results showed that the captured particles move with average velocity $v = \frac{\Delta f}{2f} c_0$ as predicted by the theory, indicating that the equal pressure amplitude condition is satisfied. If the transducers are identical, equal pressure amplitudes can be assumed and this can be indirectly verified by experiments. Otherwise, the pressure amplitudes need to be calibrated. A common amplitude can be found with the help of, for instance, laser vibrometers. The frequency-sweep method, on the other hand, requires only one source and one reflector, thus a simpler set-up to operate. This simpler set-up creates a nodal movement whose velocity is a function of time and position in the field. Hence, there is no constant nodal velocity among the field. As only one transducer is needed in the system, frequency-sweep methods are expected to consume less energy.

In both cases, the numerical solution of the EOM provides information about the particle path. The analytical force expressions on a spherical particle in a dynamic acoustic field are verified by comparison with the numerical solutions. Expressing the acoustic force as an external force circumvents the necessity of calculating the pressure gradient in COMSOL in order to calculate the acoustic force on a particle. Thus, for simulations where the number of particles are large, the analytical force expressions offer more efficient computation. Whether a particle can follow the nodal movement or not, however, can be estimated without solving the corresponding differential equation (Equation (4.4) or (4.6)). The K number predicts whether the particle can follow the nodal movement.

In summary, computer simulations in COMSOL confirmed the theoretical acoustic radiation force models for both types of dynamic acoustic field. Also, experimental measurements, for both types of dynamic acoustic field, are in line with the particle velocity and trajectory estimates. The dual-frequency type dynamic field creates a constant velocity among the field. The presence of reflections prevents the captured particles to follow a straight line. However, numerical simulations suggest that it is still possible to trap and move particles selectively. This is shown in Figures 4.3 and 4.4, which indicate that it is possible to put a significant distance (in the order of millimeters while particles are in the order of micrometers) between different particles that started at the same location, even when reflections are present in the system. Since reflections disturb the average acoustic force experienced by the particle, it requires a larger pressure for particles to be able to follow the nodal movement when reflections are present. Nevertheless, both methods are suitable for selective particle separation at centimeter scale, the choice of method depends on the expected complexity of the physical system and the predictability of particle behavior.

4.4 Conclusions

Since dynamic acoustic fields can force different particles into different channels, such fields are particularly useful for selective particle separation as an alternative to stationary standing-wave field applications at centimeter scale. Whether a particle is able to follow the nodal movement in a dynamic acoustic field depends on the properties of the particle and the medium and of the type of excitation, and can thus be predicted beforehand. This study explored two types of dynamic

acoustic fields with regard to their applicability toward selective particle separation at centimeter scale.

One type explores dual-frequency dynamic fields, which are generated by two transducers operating at slightly different frequencies, offering constant nodal movement velocities in the separation channel. Although the presence of reflections disturbs the field, these perturbations appear to have little effect on the effectiveness of selective particle separation. Dual-frequency type fields theoretically require equal amplitudes of pressure from both sources.

The other type of investigated dynamic acoustic field is based on frequency-sweep excitation. Such a field is generated with a transducer and a reflector and by ramping the excitation frequency periodically. This is a simpler system with only one transducer and a reflector, but frequency-sweep type dynamic fields do not have a constant nodal velocity in the field. Instead, the nodal velocity depends on position and time. Locations closer to the transducer are more selective with respect to particle separation, as the velocity of the nodal pattern is higher there.

Using the theoretical acoustic radiation force expressions, the dimensionless K number is defined as the ratio between maximum acoustic force and drag force on a particle. The K number, defined for each specific type of dynamic acoustic field, is able to predict whether the particle can follow the nodal movement or not without solving the equations. If $K < 1$ the particle is unable to follow the nodal pattern. The K number can also be used to estimate a lower bound on the acoustic pressure in the system.

Our numerical experiments confirmed the theoretical acoustic radiation force on a spherical particle in a dynamic acoustic field, and lab experiments confirmed the paths and nodal velocities obtained from the numerical models. Both methods for the generation of dynamic acoustic fields, i.e. dual frequency excitation and frequency ramping, are suitable for selective particle separation.

(4.A) Theory for frequency sweep excitation

If two linear acoustic waves with the same amplitude are traveling in opposite directions, a standing wave pattern is obtained. The simplest way to obtain such a field is by using a transducer as a sound source and a reflector. If the reflector has much higher specific acoustic impedance than the excited medium, the reflector will always be a pressure antinode. Hence, if the frequency of excitation is not constant but changing as a function of time, as in case of frequency sweep excitation while allowing a standing wave to form between the source and the reflector, the standing wave field becomes

$$P(x,t) = P_0 \cos(k(t)x) \cos(\omega(t)t) \tag{4.A1}$$

Here, $\omega(t)$ and $k(t)$ are both function of time as the frequency is changed with time. According to Gor'kov[1], the force acting on a spherical particle in x direction can be expressed as

$$F_x = VA_1 \frac{\partial}{\partial x} \langle \mathrm{KE} \rangle - VA_2 \frac{\partial}{\partial x} \langle \mathrm{PE} \rangle \tag{4.A2}$$

Here, $V = \frac{4}{3}\pi r^3$ is the particle volume, $A_1 = \frac{3(\rho - \rho_0)}{2\rho + \rho_0}$ and $A_2 = 1 - \frac{\rho_0 c_0^2}{\rho c^2}$ are constants determined by the particle and host medium densities and compressibilities, KE and PE are the temporal averages of the kinetic and potential energy densities of the acoustic field, respectively. Assuming that standing wave field responds fast enough to the change in the excitation frequency, in a plane wave field, the time-averaged potential and kinetic energy densities can be expressed as

$$\langle \mathrm{PE} \rangle = E_{ac} \cos^2\left(\frac{\omega}{c_0} x\right) \tag{4.A3}$$

And

$$\langle \mathrm{KE} \rangle = E_{ac}\left(1 - \cos^2\left(\frac{\omega}{c_0}x\right)\right) \tag{4.A4}$$

Here, $E_{ac} = \frac{P_0^2}{4\rho_0 c_0^2}$ is the acoustic energy density in the host medium. The acoustic radiation force acting on a spherical particle in x direction is subsequently expressed as

$$F_x(x,t) = V(A_1 + A_2)E_{ac}\frac{\omega(t)}{c_0}\sin\left(\frac{2\omega(t)}{c_0}x\right) \tag{4.A5}$$

Considering that $k(t) = \omega(t)/c_0$ and replacing the terms for V, A_1 and A_2, the following expression can then be obtained:

$$F_x(x,t) = 4\pi k(t) r^3 \left(\frac{P_D^2}{4\rho_0 c_0^2}\right)\Phi(\rho, c)\sin(2k(t)x) \tag{4.A6}$$

In this equation, $\Phi(\rho, c) = \frac{\rho + \frac{2}{3}(\rho - \rho_0)}{2\rho + \rho_0} - \frac{1}{3}\frac{\rho_0 c_0^2}{\rho c^2}$ which is the acoustic contrast factor. In the acoustic contrast factor expression, ρ and ρ_0 denote the particle and host medium densities, respectively. Similarly, c and c_0 denote the speed of sound in the particle and in the host medium, respectively.

In such a standing wave field, velocity of the nodal pattern, and therefore the force pattern is calculated. Taking the reflector as the reference, at the beginning of the sweep period and neglecting the time needed to move from an original position to the closest (anti)nodal line, the distance of a point to the reflector can be expressed as $x(0) = n\,\lambda(0)$. Here, $\lambda(0)$ is the acoustic wavelength in the host medium for $f_0 = f(0)$ and n is a positive number representing the ratio between the wavelength and the initial position. When n is an integer, such positions correspond to the antinodes in the wave field as in Fig. 1b. As time changes, assuming there is a significant acoustic impedance difference between the reflector and the host medium, the reflector will always remain a pressure antinode or a pressure node (Fig. 1b). Therefore, the wave pattern will compress toward the reflector if the frequency is increased. At any time within the sweep period, the

distance of the same point in the wave pattern to the reflector is $x(t) = n\,\lambda(t)$ with $\lambda(t) = \frac{c_0}{f(t)}$. Taking $n = x(0)/\lambda(0)$ with $x_0 = x(0)$ and evaluating the time derivative, the velocity of a point in the wave pattern within the sweep period can be expressed as follows:

$$x(t) = \frac{x_0 f_0}{(f_0 + S\,t)} \tag{4.A7}$$

$$v(x_0, t) = -\frac{f_0}{(f_0 + S\,t)^2}\,S\,x_0 \tag{4.A8}$$

Here f_0 is the starting frequency, S is the sweep rate and t is time. $S := \Delta f/\Delta t$, where Δf is the change of frequency within sweep period Δt. The velocity expression is valid only for the duration of a sweep period and the distance x_0 is measured from the reflector. The velocity expression, Equation (4.A8), can be used for any point in the acoustic field at any time within the sweep period. The negative sign is due to the nodes getting closer to the reflector, which is taken as the reference point.

The velocity expression is a function of time and position and makes it possible to calculate the average velocity expressions for different cases. The average velocity for a fixed location x between t_0 and t_1 is calculated as

$$v_{\mathrm{av}}(x, t_0, t_1) = \frac{1}{t_1 - t_0}\int_{t_0}^{t_1} v(x, t)\,dt = -\frac{f_0\,S\,x}{(f_0 + S\,t_0)(f_0 + S\,t_1)} \tag{4.A9}$$

Similarly, the average velocity in a region between x_0 and x_1 at a given time t is calculated as

$$v_{\mathrm{av}}(t, x_0, x_1) = \frac{1}{x_1 - x_0}\int_{x_0}^{x_1} v(x, t)\,dx = -\frac{1}{2}\frac{f_0\,S\,(x_0 + x_1)}{(f_0 + S\,t)^2} \tag{4.A10}$$

Finally, the average velocity in a region x_0 and x_1 and in a time interval between t_0 and t_1 is calculated as

$$v_{\mathrm{av}}(x_0, x_1, t_0, t_1) = \frac{1}{x_1 - x_0}\int_{x_0}^{x_1} v_{av}(x, t_0, t_1)\, dx = -\frac{1}{2}\frac{f_0\, S\, (x_0 + x_1)}{(f_0 + S\, t_0)(f_0 + S\, t_1)} \tag{4.A11}$$

Equations (4.A9 – 4.A11) can be particularly useful to estimate the average velocity of a group of particles in a region.

For single particles, however, these equations may not be accurate. Assuming that a single particle is able to follow the nodal movement, the velocity of the particle, given Equation (4.A10) and $x_1 = x_0 v_{\mathrm{av}}(t_1 - t_0)$, can be expressed as

$$v_{\mathrm{av}}(x_0, t_0. t_1) = \frac{f_0^2\, x_0}{2(t_1 - t_0)}\left(\frac{1}{(f_0 + S\, t_1)^2} - \frac{1}{(f_0 + S\, t_0)^2}\right) \tag{4.A12}$$

Equation (4.A12) requires the knowledge of the initial position and the time. To estimate the average velocity of a particle within one sweep period, since the location of the node will also depend on the time, and using Equation (4.A7), the following expression can be used:

$$v_{\mathrm{av}} = \frac{x - x_0}{\Delta t} = -x_0 \frac{S}{f_0 + S\, \Delta t} \tag{4.A13}$$

Provided that t_0 and t_1 are within the sweep period and $t_1 > t_0$, the average velocity for a point x between t_0 and t_1 is given by Equation (4.A9). The average velocity in a region between x_1 and x_0 at a given time t is given by Equation (4.A10). The average velocity in a region $x_0 - x_1$ in a given time interval $t_0 - t_1$ is given by Equation (4.A11) but requires the start and end positions as input. Another estimate of the average particle velocity that only requires its initial position to be known is also possible and given by Equation (4.A12).

Assuming that the particle is able to follow the nodal movement, all of the four expressions given by Equations (4.A9 - 4.A12) can be used to approximate the velocity. Such expressions are particularly useful to estimate the average speed of a group of particles in a given time interval and spatial region. The exact average

speed of a particle in the first sweep period is given by Equation (4.A13). Equation (4.A13) was used to estimate the particle velocity and compare it with experimentally derived estimates.

(4.B) Admittance measurements of the prototypes

In order to check the absorbing blocks are minimizing the reflections, admittance measurements of the prototype were evaluated. Figure 4.B1 illustrates the admittance measurements for the dual-frequency prototype.

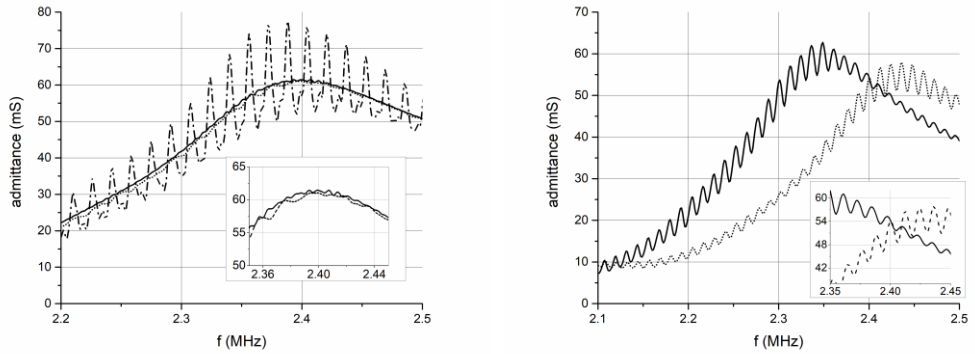

(a) (b)

Figure 4.B1 - (a) Admittance of a single transducer. Dash-dot line represents the admittance of the transducer placed in the prototype, solid line represents the admittance of the transducer under water and outside the prototype, dotted line represents the admittance of the transducer when the transducer, absorbing blocks and polyurethane sheets are placed in the prototype. Zoomed window illustrates the latter two cases only. (b) Admittance measurement for two transducers in the prototype including particle solution, absorbing blocks and polyurethane sheets (Figure 4.2a). In order to illustrate the effects better zoomed windows were added.

When the absorbing blocks are placed in the prototype, the effect of reflections vanishes as shown in Figure 4.B1a. In the actual configuration the presence of both transducers causes inevitable reflections, as seen in Figure 4.B1b. In the operating frequency, both of the transducers have similar admittance.

Figure 4.B2 illustrates the admittance measurements for the frequency-sweep prototype on the range $1.8 - 2.6\ \mathrm{MHz}$. Sharp peaks indicate high Q factor resonances. The operating range is $2.19 - 2.49\ \mathrm{MHz}$.

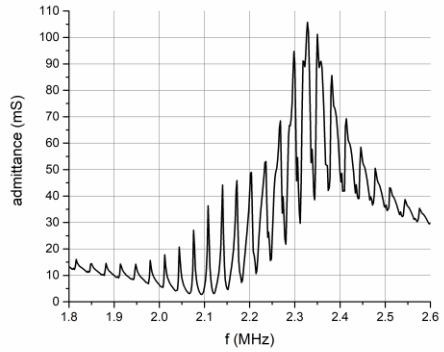

Figure 4.B2 - Admittance of the transducer in the frequency-sweep prototype including particle mixture and reflector (Figure 4.2b).

(4.C) Relative motion of a particle in a frequency sweep type field

If a particle is captured with a frequency-sweep type field, it is expected to follow the nodal pattern. The nodal pattern, however, does not have a constant velocity as indicated in Equation (4.5). The velocity of the nodal pattern changes with time and position. Moreover, since the excitation frequency changes, the acoustic energy density in the field also changes. This phenomenon results in a relative motion between a captured particle and the nodal pattern, illustrated in Figure 4.C1.

In Figure 4.C1 the nodal pattern is moving in the positive direction. Black line indicates the force field when $f = f_1$ and red line indicates the force field when $f = f_2$, where $f_2 > f_1$. The horizontal axis gives the distance relative to the wavelength, where $\bar{x} = x/(\lambda/2)$.

Consider a particle, initially trapped by the force field given by the black solid line, at $\bar{x}_1$ with force $F = F_1$ in the $\bar{x}$ direction and at time instant $t = t_1$. Assuming the inertial forces are negligible [2], the forces acting on the particle are the drag force and the acoustic radiation force. Given the speed of the nodal pattern, the particle experiences a drag force F_D. In order the particle to be trapped, there must be an acoustic force F_{AC} balancing the drag force, thus $F_{AC} = -F_D$ with magnitude F_1. The line $F = F_1$ intersects the black line in two locations, that is one around $\bar{x} = 0.12$ and another around $\bar{x} = 0.35$. In the absence of an external flow or nodal movement, the acoustic force pattern acts as a restoring force around $\bar{x} = 0.5$, which is the stable trapping location. When a drag force is present, however, the

stable trapping location shifts to the intersection at $\bar{x} \approx 0.35$, where $|F_{AC}| = |F_D| = F_1$. Hence, the particle indicated by the circle is initially trapped at location x_1 indicated in Figure 4.C1. A force equilibrium is also possible around $\bar{x} \approx 0.15$. In this case, however, disturbances at this position result in the particle being trapped away from that location. The latter case is analogous to a particle with positive acoustic contrast factor trapped in the pressure antinode of a stationary standing wave field.

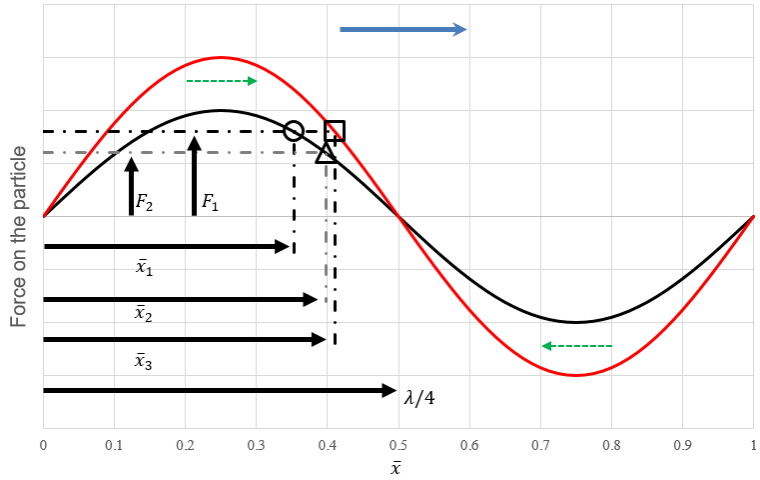

Figure 4.C1 - Equilibrium position of a trapped particle with respect to the moving nodal pattern. Black and red solid lines indicate, in a frequency-sweep-type dynamic field the acoustic radiation force profile acting on a particle as a function of position. Blue arrow indicates the direction of movement of the nodal pattern. Green dashed arrows indicate the direction of acoustic force acting on the particles. The x axis is scaled such that $\bar{x} = x/(\lambda/2)$

According to Equation (4.5), within one sweep period the speed of the nodal pattern slows down with time. Hence, the particle experiences a weaker drag force $|F_D| = F_2$ for $t_2 > t_1$. In the same nodal pattern the particle at t_2, and indicated by the triangle in Figure 4.C1, has an equilibrium position at x_2, due to similar reasoning with the previous case. The new position x_2 is closer to the pressure node at $\bar{x} = 0.5$ than x_1, therefore the particle goes faster than the nodal pattern while staying in force equilibrium with $|F_{AC}| = |F_D| = F_2$.

In frequency-sweep type fields also the frequency of excitation increases. Equation (4.6) suggests that the force amplitude increases with increased frequency. When the frequency is increased from f_1 to f_2, the acoustic radiation force pattern becomes the red solid line in Figure 4.C1. Keeping the speed of the nodal pattern the same, the particle indicated by the circle has a new equilibrium position,

indicated by the square, at x_3 in order to have $|F_{AC}| = |F_D| = F_1$. The new position x_3 is closer to the pressure node at $\bar{x} = 0.5$ than x_1, therefore, again, the particle goes faster than the nodal pattern in order to stay in equilibrium.

The effects mentioned above individually induce a relative motion between the particle and the nodal pattern. In reality, the effects occur simultaneously, hence they together result in a relative motion between the captured particle and the nodal pattern, making the captured particle travel faster than the nodal pattern.

(4.D) Empirical estimation of the K number in the presence of reflections

In the following, the K_0 number is calculated from the ratio of the maximum acoustic force and the maximum drag force on a spherical particle without reflection. The particle will experience the maximum drag force only if it follows the nodal movement. This derivation assumes that there are no reflections in the system, thus there is only the primary dynamic field acting on the particles. When reflections are present, however, a weaker field, due to reflections, still acts on the particles. Numerical simulations were carried out to understand the effect of the reflections on the system.

In the numerical simulations, different random combinations of particle (ρ, c, r) and excitation $(\Delta f, f, P_0)$ parameters were evaluated in order to check whether the particle is able to follow the nodal movement or not. The random values are taken from the intervals $500 < \rho < 2000$, $800 < c < 5000$, $2 \times 10^{-6} < r < 100 \times 10^{-6}$ for particle parameters in appropriate SI units, and $0.5 < \Delta f < 10$, $1.5 \times 10^6 < f < 3 \times 10^6$ and $10 \times 10^3 < P_0 < 2 \times 10^6$ for excitation parameters in appropriate SI units. Due to the undiscounted reflections, the condition $K_0 \geq 1$ no longer ensures that the particle is able to follow the nodal movement. The threshold values of K_0, thus under conditions with reflection, for which the particle is able to follow the nodal movement, were recorded from simulations for many combinations of parameters. The threshold K_0 value is a function of reflection coefficient only. Table 4.D1 summarizes the threshold K_0 values for different values of the reflection coefficient.

Table 4.D1 - The threshold K_0 values for different reflection coefficients

R	0	0.1	0.2	0.3	0.4	0.5	0.6	0.7	0.8	0.9
K_0	1	1	1	1.001	1.006	1.02	1.037	1.073	1.157	1.34

When the reflection coefficient is larger than 0.9, the threshold values for K_0 become inconsistent, therefore they are excluded from the results. Based on the data obtained in the numerical simulations, the threshold K_0 values can be expressed as a function of the reflection coefficient, that is

$$f(R) = 1 - 3.696 \times 10^{-4}(1 - e^{7.582R}) \tag{4.D1}$$

With a correlation coefficient of 0.999 for the non-smoothed simulation data. Figure 4.D1 presents the simulated data points and the fitted function.

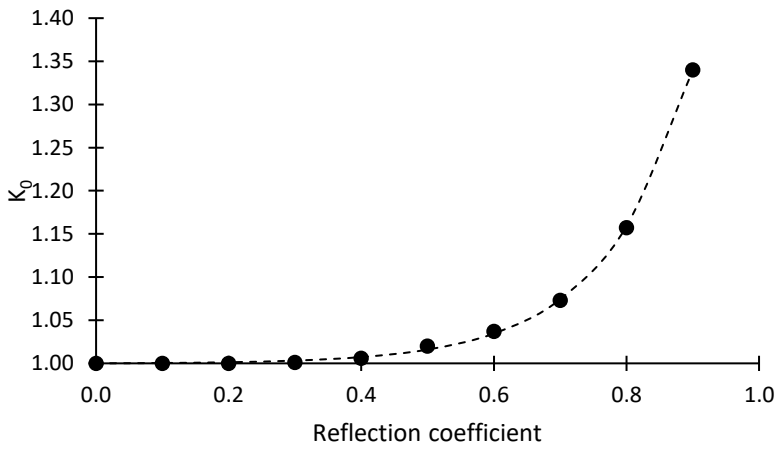

Figure 4.D1 - The threshold K_0 values and the fitted function, *f(R)*. Dots represent the threshold K_0 values for a particle to follow the nodal pattern when reflections are present with given coefficient. The dashed line represents the empirical estimations given by Equation (4.D1).

Based on the fitted function using the data from the numerical experiment, the K number as a function of reflection coefficient can be expressed as

$$K = \frac{K_0}{1 - 3.696 \times 10^{-4}(1 - e^{7.582R})} \tag{4.D2}$$

with K_0 given by Equation (4.8). Numerical simulations confirm that for $R \leq 0.9$, the K number successfully predicts whether the particle is able to follow the nodal movement or not. When $R = 1$, the system shows full reflection, and in such a case a particle simply oscillates around its initial location without following the nodal pattern.

References

[1] Gor'kov, L.P., 1962. On the Forces Acting on a Small Particle in an Acoustical Field in an Ideal Fluid. Soviet Physics Doklady 6, 773.

[2] Bruus, H., 2012. Acoustofluidics 7: The acoustic radiation force on small particles. Lab on a Chip 12, 1014–1021. doi:10.1039/C2LC21068A

[3] Bruus, H., 2011. Acoustofluidics 1: Governing equations in microfluidics. Lab on a Chip 11, 3742–3751. doi:10.1039/C1LC20658C

[4] Cappon, H.J., 2014. Numerical and experimental design of ultrasonic particle filters for water treatment (PhD). Wageningen University, Wageningen.

[5] Drinkwater, B.W., 2016. Dynamic-field devices for the ultrasonic manipulation of microparticles. Lab on a Chip 16, 2360–2375. doi:10.1039/C6LC00502K

[6] Ding, X., Lin, S.-C.S., Lapsley, M.I., Li, S., Guo, X., Chan, C.Y., Chiang, I.-K., Wang, L., McCoy, J.P., Huang, T.J., 2012. Standing surface acoustic wave (SSAW) based multichannel cell sorting. Lab on a Chip 12, 4228–4231. doi:10.1039/C2LC40751E

[7] Kapishnikov, S., Kantsler, V., Steinberg, V., 2006. Continuous particle size separation and size sorting using ultrasound in a microchannel. Journal of Statistical Mechanics: Theory and Experiment 01, 01012. doi:10.1088/1742-5468/2006/01/P01012

[8] Petersson, F., Åberg, L., Swärd-Nilsson, A.-M., Laurell, T., 2007. Free Flow Acoustophoresis: Microfluidic-Based Mode of Particle and Cell Separation. Analytical Chemistry 79, 5117–5123. doi:10.1021/ac070444e

[9] Laurell, T., Petersson, F., Nilsson, A., 2007. Chip integrated strategies for acoustic separation and manipulation of cells and particles. Chemical Society Reviews 36, 492–506. doi:10.1039/B601326K

[10] Simon, G., Marques-Hueso, J., Desmulliez, M.P.Y., Bernassau, A.L., Roolvink, D., Burns, G., Cormack, P. a. G., Andrade, M.A.B., Reboud, J., Cooper, J.M., Riehle, M.O., 2017. Reconfigurable particle separation by dynamic acoustic fields in microfluidic devices, in: Proceedings of the 24th International Congress on Sound and Vibration. Presented at the 24th International Congress on Sound and Vibration: London Calling, International Institute of Acoustics and Vibrations, pp. 1–7.

[11] Guo, F., Mao, Z., Chen, Y., Xie, Z., Lata, J.P., Li, P., Ren, L., Liu, J., Yang, J., Dao, M., Suresh, S., Huang, T.J., 2016. Three-dimensional manipulation of single cells using surface acoustic waves. Proceedings of the National Academy of Sciences of the United States of America 113, 1522–1527. doi:10.1073/pnas.1524813113

[12] Tran, S.B.Q., Marmottant, P., Thibault, P., 2012. Fast acoustic tweezers for the two-dimensional manipulation of individual particles in microfluidic channels. Applied Physics Letters 101, 114103. doi:10.1063/1.4751348

[13] Orloff, N.D., Dennis, J.R., Cecchini, M., Schonbrun, E., Rocas, E., Wang, Y., Novotny, D., Simmonds, R.W., Moreland, J., Takeuchi, I., Booth, J.C., 2011. Manipulating particle trajectories with phase-control in surface acoustic wave microfluidics. Biomicrofluidics 5, 044107. doi:10.1063/1.3661129

[14] Meng, L., Cai, F., Zhang, Z., Niu, L., Jin, Q., Yan, F., Wu, J., Wang, Z., Zheng, H., 2011. Transportation of single cell and microbubbles by phase-shift introduced to standing leaky surface acoustic waves. Biomicrofluidics 5, 044104-044104–10. doi:10.1063/1.3652872

[15] Wood, C.D., Cunningham, J.E., O'Rorke, R., Wälti, C., Linfield, E.H., Davies, A.G., Evans, S.D., 2009. Formation and manipulation of two-dimensional arrays of micron-scale particles in microfluidic systems by surface acoustic waves. Applied Physics Letters 94, 054101. doi:10.1063/1.3076127

[16] Simon, G., Andrade, M.A.B., Reboud, J., Marques-Hueso, J., Desmulliez, M.P.Y., Cooper, J.M., Riehle, M.O., Bernassau, A.L., 2017. Particle separation by phase modulated surface acoustic waves. Biomicrofluidics 11, 054115. doi:10.1063/1.5001998

[17] Simon, G., Pailhas, Y., Andrade, M.A.B., Reboud, J., Marques-Hueso, J., Desmulliez, M.P.Y., Cooper, J.M., Riehle, M.O., Bernassau, A.L., 2018. Particle separation in surface acoustic wave microfluidic devices using reprogrammable, pseudo-standing waves. Applied Physics Letters 113, 044101. doi:10.1063/1.5035261

[18] Ding, X., Lin, S.-C.S., Kiraly, B., Yue, H., Li, S., Chiang, I.-K., Shi, J., Benkovic, S.J., Huang, T.J., 2012. On-chip manipulation of single microparticles, cells, and organisms using surface acoustic waves. Proceedings of the National Academy of Sciences of the United States of America 109, 11105–11109. doi:10.1073/pnas.1209288109

[19] Collins, D.J., O'Rorke, R., Devendran, C., Ma, Z., Han, J., Neild, A., Ai, Y., 2018. Self-Aligned Acoustofluidic Particle Focusing and Patterning in Microfluidic

Channels from Channel-Based Acoustic Waveguides. Physical Review Letters 120, 074502. doi:10.1103/PhysRevLett.120.074502

[20] Lee, J., Rhyou, C., Kang, B., Lee, H., 2017. Continuously phase-modulated standing surface acoustic waves for separation of particles and cells in microfluidic channels containing multiple pressure nodes. Journal of Physics D: Applied Physics 50, 165401. doi:10.1088/1361-6463/aa62d5

[21] Rhyou, C., Park, S., Lee, H., 2019. Optimal rate for continuous phase modulation in standing surface acoustic waves. Journal of Mechanical Science and Technology 33, 3819–3829. doi:10.1007/s12206-019-0725-z

[22] Skotis, G.D., Cumming, D.R.S., Roberts, J.N., Riehle, M.O., Bernassau, A.L., 2015. Dynamic acoustic field activated cell separation (DAFACS). Lab on a Chip 15, 802–810. doi:10.1039/C4LC01153H

[23] Whitworth, G., Grundy, M.A., Coakley, W.T., 1991. Transport and harvesting of suspended particles using modulated ultrasound. Ultrasonics 29, 439–444. doi:10.1016/0041-624X(91)90073-H

[24] Courtney, C.R.P., Ong, C.-K., Drinkwater, B.W., Wilcox, P.D., Demore, C., Cochran, S., Glynne-Jones, P., Hill, M., 2010. Manipulation of microparticles using phase-controllable ultrasonic standing waves. The Journal of the Acoustical Society of America 128, EL195–EL199. doi:10.1121/1.3479976

[25] Courtney, C.R.P., Ong, C.-K., Drinkwater, B.W., Bernassau, A.L., Wilcox, P.D., Cumming, D.R.S., 2012. Manipulation of particles in two dimensions using phase controllable ultrasonic standing waves. Proceedings of the Royal Society A: Mathematical, Physical and Engineering Sciences 468, 337–360. doi:10.1098/rspa.2011.0269

[26] Grinenko, A., Ong, C.K., Courtney, C.R.P., Wilcox, P.D., Drinkwater, B.W., 2012. Efficient counter-propagating wave acoustic micro-particle manipulation. Applied Physics Letters 101, 233501. doi:10.1063/1.4769092

[27] Lipkens, B., Costolo, M., Rietman, E., 2008. The Effect of Frequency Sweeping and Fluid Flow on Particle Trajectories in Ultrasonic Standing Waves. IEEE Sensors Journal 8, 667–677. doi:10.1109/JSEN.2008.922675

[28] Trujillo, F.J., Eberhardt, S., Möller, D., Dual, J., Knoerzer, K., 2013. Multiphysics modelling of the separation of suspended particles via frequency ramping of ultrasonic standing waves. Ultrasonics Sonochemistry 20, 655–666. doi:10.1016/j.ultsonch.2012.08.014

[29] Lipkens, B., Dionne, J., Trask, A., Szczur, B., Stevens, A., Rietman, E., 2010. Separation of micron-sized particles in macro-scale cavities by ultrasonic standing waves. Physics Procedia, International Congress on Ultrasonics, Santiago de Chile, January 2009 3, 263–268. doi:10.1016/j.phpro.2010.01.035

[30] Manneberg, O., Vanherberghen, B., Önfelt, B., Wiklund, M., 2009. Flow-free transport of cells in microchannels by frequency-modulated ultrasound. Lab on a Chip 9, 833–837. doi:10.1039/B816675G

[31] Haake, A., Neild, A., Radziwill, G., Dual, J., 2005. Positioning, displacement, and localization of cells using ultrasonic forces. Biotechnology and Bioengineering 92, 8–14. doi:10.1002/bit.20540

[32] Haake, A., Dual, J., 2005. Contactless micromanipulation of small particles by an ultrasound field excited by a vibrating body. The Journal of the Acoustical Society of America 117, 2752–2760. doi:10.1121/1.1874592

[33] Schindelin, J., Arganda-Carreras, I., Frise, E., Kaynig, V., Longair, M., Pietzsch, T., Preibisch, S., Rueden, C., Saalfeld, S., Schmid, B., Tinevez, J.-Y., White, D.J., Hartenstein, V., Eliceiri, K., Tomancak, P., Cardona, A., 2012. Fiji: an open-source platform for biological-image analysis. Nature Methods 9, 676–682. doi:10.1038/nmeth.2019

5 SIZE SELECTIVE PARTICLE FILTERING ON CENTIMETER SCALE BY FREQUENCY SWEEP TYPE DYNAMIC ACOUSTIC FIELD

A version of this chapter has been published as:

Kandemir, M. H., Mohan, K., Wagterveld, R. M., Yntema, D. R., & Keesman, K. J. (2021) Size selective particle separation on centimeter scale by frequency sweep type dynamic acoustic field. *Separation and Purification Technology*, *259*, 118188

Abstract

The objective of the study was to investigate and demonstrate the application of frequency-sweep dynamic acoustic fields for size-selective particle filtration on centimeter scale in a regulated continuous flow. The 3D-printed prototype of the acoustic separator has two inlets and two outlets, whereas the dynamic acoustic field is generated between a transducer and a reflector. The measured frequency response of the prototype was input to computer models, and simulations were carried out to explore the effects of the sweep period and the flow parameters on the filtration performance. A design-of-experiments study showed that the filtration performance is largely affected by the sweep period and the outlet flow rate. Lab experiments with model particle mixtures demonstrated the size selective filtration performance of the prototype with a total flow rate of $1\ \mathrm{L\ h^{-1}}$. A mixture with unknown properties was also used to demonstrate the selective filtration performance of the prototype.

5.1 Introduction

Filtration of mixtures is an important step in industrial processes. Such mixtures can be in the form of emulsions or suspensions. For example, pharmaceutical, food, biomedical and water industries commonly incorporate filtration processes of suspensions. Utilizing filtration in a selective manner can improve the quality of the product and process. With the ability to perform filtration in continuous flow without blocking or affecting the flow, acoustophoresis is one of the methods to achieve selective particle filtering in suspensions [1-5].

A particle in an acoustic field experiences an acoustic radiation force. In an acoustic standing wave field this force pushes the particle towards either a pressure node or antinode, depending on the acoustic properties of the particle and the surrounding medium [6, 7]. While moving in a fluid due to the combined effect of an acoustic field and flow field, the particle also experiences drag force [7, 8]. Consequently, selective particle filtering can be achieved based on the interplay between the acoustic radiation force and the drag force on a particle.

With given surrounding medium and excitation parameters the acoustic radiation force scales with particle volume, density and compressibility whereas the drag force scales with particle size [6-8]. On microscale, this interplay is used to separate particles based on their size [9-13] or acoustic contrast factor, which is a combination of density and compressibility [14-16]. Cells can also be selectively separated using acoustic radiation force only [17-23]. Typically, in microscale acoustophoresis devices an acoustic standing wave field is utilized in a chamber with a width equal to the half-wavelength at the excitation frequency in the medium, referred to as half-wavelength separators. In such devices, the particles are forced towards a single pressure node in the middle of the channel. The amplitude of the acoustic radiation force increases with frequency and pressure amplitude. If the particle size is comparable to or larger than the wavelength of excitation, it cannot be manipulated by the acoustic radiation force. Hence, for micrometer-sized particles the excitation is typically in the MHz range and the channel width of such devices are in the order of hundreds of micrometers [24].

On centimeter scale, acoustophoretic devices become multi-wavelength resonators [25-29]. Instead of one pressure node in the middle of the channel, multiple pressure nodes and antinodes exist in such devices. While the acoustic radiation force is typically due to an acoustic standing wave field, clever arrangement of flow patterns open up possibilities for selective particle filtration in

a continuous flow on microscale [30] as well as on centimeter scale [2, 31, 32]. Alternatively, application of dynamic acoustic fields on centimeter scale offers more possibilities for selective filtration [33-38]. In dynamic acoustic fields, the pressure nodes are not fixed and their motion can be controlled. One possible way of obtaining a dynamic acoustic field is using frequency-sweep excitation, in which the applied frequency is periodically ramped and the pressure nodes move away from the sound source. Particle separation and concentration using frequency-sweep excitation on centimeter scale and microscale is demonstrated in multiple studies [39-42]. These studies made use of the nodes moving away from the sound source and concentrate the particles in one end.

The controllability of the nodal motion greatly enhances the capabilities of the separator. The acoustic force pattern in the separator and the speed of the nodal movement, hence captured particles, as well as the flow profile in the separator can be adjusted to possibly create a size selective filtration mechanism. This adjustability makes a frequency sweep-based system a good candidate to scale-up selective filtration applications from microscale to centimeter scale. However, such possibilities offered by this type of excitation are not explored yet.

This study aimed to explore and demonstrate the selective particle filtration capability of frequency sweep type dynamic acoustic fields on centimeter scale in a continuous flow separator, by adjusting the excitation and flow parameters. First, the frequency response of the transducer was obtained in the excitation range. Computer simulations were carried out in order to examine the effects of the excitation and flow parameters on the particle size distribution of model polyethylene particles. Subsequently, lab experiments were performed to demonstrate the selective filtering capability of the combination of frequency sweep type field and flow pattern on model polyethylene particles in water and on wheat beer.

5.2 Materials and methods

5.2.1 Frequency sweep excitation

In the frequency-sweep method, the excitation frequency is ramped periodically from a starting frequency to a higher frequency within a given period. Excitation by a single sound source, with a reflector placed parallel to that source, generates at

each frequency a standing wave field in between. During a frequency sweep, the resulting acoustic wave field can be considered a dynamic acoustic field in which the quasi-standing wave field is contracted by introducing new nodes from the source side. The distance between the source and reflector is kept constant while with increasing frequency the wave includes more wavelengths over that distance. Figure 5.1 illustrates the change in frequency and the corresponding change in the standing wave pattern

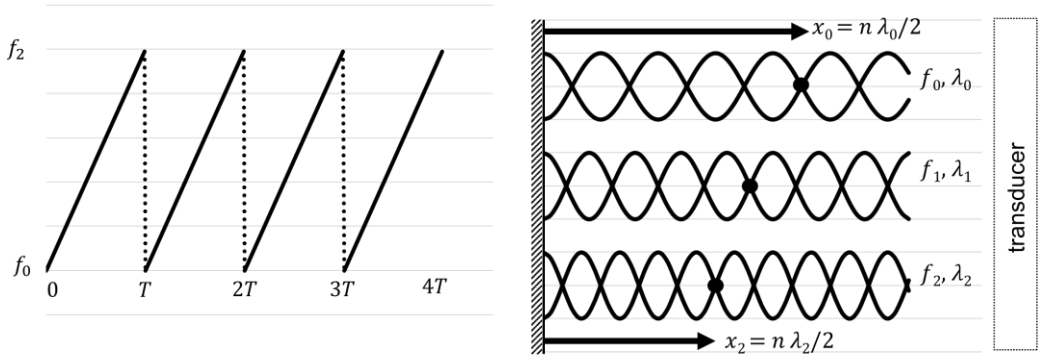

(a) (b)

Figure 5.1 - Change in the excitation frequency (a) and the corresponding standing wave pattern in the dynamic acoustic field at specific time instances (b). The frequency is ramped from f_0 to $f_2 = f_0+ST$ within the sweep period T and with S the sweep rate, leading to waves with wavelengths $\lambda_I = c_0/f_i$ with c_0 the speed of sound. As the excitation frequency increases, new nodes are introduced from the source (transducer) side, in turn contracting the standing wave pattern.

If the acoustic impedance of the reflector is much higher than the medium it reflects the incoming wave with the same amplitude and phase. Hence, ignoring the attenuation in the medium, the resulting standing wave, as a function of the time-varying frequency $f(t)$, can be expressed as

$$P(x,t) = 2P_s(t)\cos(k(t)x)\cos(\omega(t)t) \tag{5.1}$$

In Equation (5.1), x (m) is the distance of the particle from the reflector (Figure 5.1b) and t (s) is time. $P_s(t)$ (Pa) is the pressure amplitude of the incoming wave from the source and it is a constant for the case the transducer vibrates equally at every frequency during the sweep period. The function $\omega(t) = 2\pi f(t)$ (rad s^{-1}) is

the angular frequency of excitation whereas $k(t) = \omega(t)/c_0$ (m^{-1}) is the wavenumber and c_0 (m s^{-1}) is the speed of sound in the medium. Defining the total pressure $P_t(t) := 2P_s(t)$, the equation of motion for a particle in a frequency sweep type dynamic acoustic field is given by

$$\left(\frac{4}{3}\pi r^3\rho\right)\ddot{x} + (6\pi\mu r)(\dot{x} + u) + 4\pi k(t) r^3 \left(\frac{P_t^2(t)}{4\rho_0 c_0^2}\right)\phi(\rho, c)\sin(2k(t)x) = 0 \tag{5.2}$$

In Equation (5.2), r (m) is the particle radius, ρ_0 (kg m^{-3}) is the density of the medium, ρ is the density of the particle, c_0 is the speed of sound in the medium, c is the speed of sound in the particle material, $P_t(t)$ is the amplitude of the sound pressure, $\omega(t)$ is the angular frequency, $k(t)$ is the wave number, $\phi(\rho, c)$ (-) is the acoustic contrast factor and u (m s^{-1}) is the constant flow velocity of the liquid from the reflector to the source. The first term in Equation (5.2) is the inertial force on the particle whereas the second term is the drag force acting on the particle. The last term, $4\pi k(t) r^3 \left(\frac{P_t^2(t)}{4\rho_0 c_0^2}\right)\phi(\rho, c)\sin(2k(t)x)$, is the acoustic radiation force acting on a spherical particle in a frequency-sweep type dynamic acoustic field [38].

As new nodes are introduced in the quasi-standing wave pattern with linearly increasing frequency (Figure 5.1a), the contraction rate of the pattern is not constant. The velocity of any point in the dynamic acoustic field towards the reflector, hence the negative sign, is a function of time and position and is given, within one sweep period, by:

$$v(x, t) = -\frac{f_0}{(f_0 + S\,t)^2}\,S\,x \tag{5.3}$$

In Equation (5.3), $S = \Delta f / T$ is the sweep rate. As a particle trapped in the pressure nodes will follow the movement of the nodes, the velocity of a trapped particle can be estimated from Equation (5.3) [38].

5.2.2 Experimental setup

The experimental set-up consists of a dual-channel signal generator (Keysight Trueform 33512B), a custom-made amplifier, an oscilloscope (Tektronix TDS2024C), two syringe pumps for inlets (Aitecs PRO SP-12S), two syringe pumps for outlet (HARVARD Apparatus Pump 33) and a separator prototype with piezoelectric transducer (Noliac NCE41, dimensions 50 mm × 10 mm × 1 mm) and a reflector (stainless steel). The prototype (Figure 5.2) includes 3D-printed polylactic acid base and walls and a PMMA cover. The X-shaped prototype consists of two inlets and two outlets that can be separately regulated. This ability allows the manipulation of the streamlines, hence the drag force experienced by the particles. Furthermore, the geometry of the prototype was designed such that the pipe entrance is expanding smoothly to the main resonator channel, avoiding turbulence due to sudden expansion. The transducer was coated with a thin layer of polyurethane paint to provide electrical insulation, as polyurethane has a similar acoustic impedance as water.

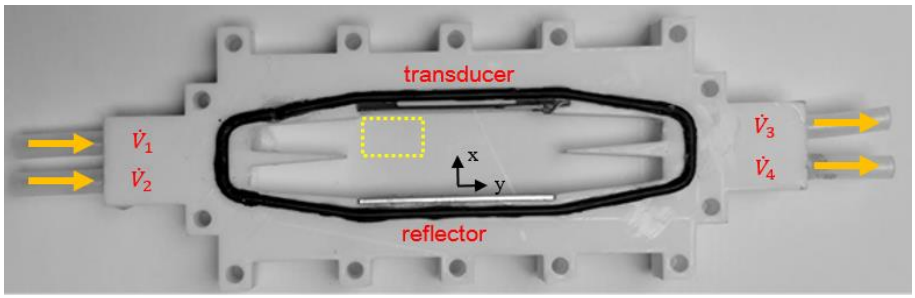

Figure 5.2 - X-shaped prototype used in the experiment. The transducer is connected to the amplifier. The reflector is a stainless steel plate with the same dimensions as the transducer. Particle mixture is fed from the transducer-side inlet, with flow rate $\dot{V}_1$ whereas samples are taken from the transducer-side outlet, with flow rate $\dot{V}_3$. Yellow rectangle indicates the area in which the particle trajectories are presented in Figure 5.7.

The transducer was excited by a sweeping frequency signal. The electrical admittance of the prototype was measured by using an HP 4194A impedance analyzer, to check for resonant frequencies in the prototype and the amount of nodes introduced during the sweep period. Each peak and valley introduced in the admittance spectrum corresponds to a resonance in the system, while sharper peaks indicate higher Q factor for those resonances. The generated pressure was derived by measuring the surface velocity of the immersed transducer with a Laser Doppler Vibrometer (LDV: Polytec OFV-5000 single-point vibrometer) during the

frequency sweep. During the measurement the transducer was placed on a special stand imitating the fixture in the prototype, immersed in water, outside the prototype to ensure sufficient signal quality. The pressure was calculated by using the specific acoustic impedance of the host medium. Pressure values were calculated by taking the average of 10 recordings for each sweep period and multiplying the velocity with the specific acoustic impedance. This pressure information was used as input for the computer simulations.

For the simulations and experiments polyethylene particles were used ($c = 1700\ \mathrm{m\ s^{-1}}$) of sizes: 36 (red), 56 (cyan), 70 (orange) and $100\ \mu\mathrm{m}$ (blue). Densities of the different set of particles are $\rho_{red} = 998\ \mathrm{kg\ m^{-3}}$, $\rho_{cyan} = 1000\ \mathrm{kg\ m^{-3}}$, $\rho_{orange} = 1006\ \mathrm{kg\ m^{-3}}$ and $\rho_{blue} = 1002\ \mathrm{kg\ m^{-3}}$. The particle mixture contained $1\ L$ MilliQ water, $0.075\ \mathrm{g}$ CTAB (hexadecyltrimethylammonium bromide) as surfactant, $0.03\ \mathrm{g}$ red, $0.08\ \mathrm{g}$ cyan, $0.2\ \mathrm{g}$ orange and $0.5\ \mathrm{g}$ blue particles.

Particle motion was recorded by a microscope with camera and particle trajectories were visualized with ImageJ software [43] and particle size distributions were analyzed using a DIPA2000 particle analyzer. DIPA 2000 uses laser obscuration time to measure the diameter of particles; a rotating laser beam scans the mixture and by the obscuration time the diameter of individual particles are calculated.

5.2.3 Computer simulations

Computer simulations were done to calculate particle trajectories (COMSOL Multiphysics 5.5) and particle size distributions (MATLAB r2018b). Each set of excitation parameters was an arbitrary combination of a sweep period and input and output flow rates. The sweep range, Δf , was set to $500\ \mathrm{kHz}$ where $f_0 = 1.9\ \mathrm{MHz}$. Total flow rate was set to $1\ \mathrm{L\ h^{-1}}$ and the transducer was excited at $20\ \mathrm{V_{pp}}$. A design of experiments (DOE) study was carried out in order to explore the effect of the variable excitation and flow conditions. As in the lab experiments, the particle mixture was fed from the transducer-side inlet, with flow rate $\dot{V}_1$. In the plots presented throughout the article, volumetric percentage refers to the ratio of the volume of particles within a given range to the total particle volume in the mixture. Table 1 presents the range of the variable parameters used in the DOE.

Table 5.1 - Range of variables for the DOE study

T (s)	$\dot{V}_1$ (mL h^{-1})	$\dot{V}_4$ (mL h^{-1})
3	300	300
5	400	400
7	500	500

DOE study and analysis were done by using Minitab 14. The study consisted of in total 27 simulations, which are all possible combinations of parameters given in Table 5.1. The flow rates were selected such that when the flow rates are unequal at both outlets and inlets, with a preference to have larger flow rates at the transducer-side outlet, the streamlines are bent towards the transducer-side outlet. Hence the drag force resulting from this bending effect in the vertical direction acts against the acoustic radiation force. As the acoustic radiation force carries the particles towards the reflector, the drag force carries the particles mostly towards the transducer-side outlet, in turn enhancing the interplay between those two forces.

For the computer model, particle sizes were randomized in order to represent a continuous particle size distribution. Number of particles used for each simulation is given in Table 5.2. Same set of the particles were used for each simulation. Size and initial position data of the particles can be found in the supplementary material[4].

The simulations were done in 2D by taking into account of the depth of the prototype for flow rate inputs. Particle-particle interactions, secondary acoustic radiation force effects, gravity and lift force were ignored. Under this assumptions, all particles were independent of each other, leading to the possibility to release them to the system at the same time. Consequently, the computational load was reduced and the simulation times were shortened.

Assuming only the acoustic radiation force and drag forces are significant on the particle, COMSOL Multiphysics was used to solve Equation (5.2) in combination

[4] The supplementary material can be found in the published version of the chapter

with the drag force resulting due to flow in x and y directions. The solutions were carried out for each particle, eventually solving for particle trajectories.

Table 5.2 - Parameters of particles used in the simulations

Particle color	Diameter (μm)	STD of Diameter (μm)	Number of particles	Density ($\mathrm{kg\,m^{-3}}$)
Red	35	6.36	1756	998
Cyan	50	6.34	602	1000
Orange	71	13.11	220	1006
Blue	99	13.11	200	1002

5.3 Results and discussion

5.3.1 Frequency response of the prototype

First, the electrical admittance was measured in the range that covers the range of operation, that is $f_0 = 1.9\,\mathrm{MHz}$ and $\Delta f = 500\,\mathrm{kHz}$, in order to verify the calculations prior to the lab experiments. The electrical admittance of the prototype is given in Figure 5.3a. In the electrical admittance plot, every peak corresponds to a resonance frequency of the system. Notice that the resonances in the sweep period have sharp peaks indicating high Q factors. At higher frequencies more pressure nodes in the system are generated, as the number of nodes is given by $N_{node} = 2\,\frac{h\,f_r}{c_0}$, where h is the distance between the transducer and the reflector, f_r is the corresponding resonant frequency and the right-hand side of the equation is rounded down to the closest integer. A small frequency range and low number of nodes may generate a nodal pattern that cannot be contracted fast enough to carry a captured particle to the desired outlet. Based on the ratio of the given start and end frequency, every point in the nodal pattern is approximately 20% closer to the reflector at the end of the sweep period, due to the contraction illustrated in Figure 5.1b.

In addition to the admittance measurement, the pressure induced by the transducer was also calculated by measuring the vibrations on the transducer surface (Figure 5.3b). Assuming the transducer is only vibrating longitudinally in the

thickness direction, the surface velocity of the transducer was measured by a Polytec OFV-5000 single-point laser vibrometer. For this measurement it is implicitly assumed that at the water-transducer interface the water and transducer have the same velocity. Hence, by multiplying the measured velocity with the specific acoustic impedance of water the pressure was calculated. The velocity measurements were carried out for different sweep periods. The corresponding pressure amplitudes for $T = 5s$ are illustrated in Figure 5.3b.

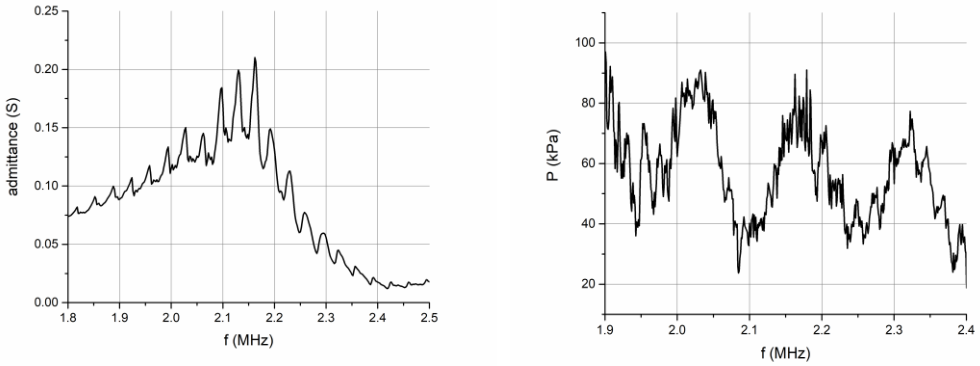

(a) (b)

Figure 5.3 - (a) Electrical admittance of the transducer in the prototype when the prototype is filled with the mixture. (b) Acoustic pressure induced to the medium by the transducer when excited with 20 V_{pp}, for T = 5 s.

Figure 5.3a indicates that during the sweep period there were at least 15 new nodes introduced to the standing wave pattern. Pressure values were calculated by taking the average of 10 recordings for each sweep period and multiplying the velocity with the specific acoustic impedance. Calculated pressure values were used in simulations with different sweep periods. The average pressures are $58\ \mathrm{kPa}$, $57\ \mathrm{kPa}$ and $49\ \mathrm{kPa}$ for 3 s, 5 s and 7 s of sweep periods, respectively.

5.3.2 Computer simulations

Equation (5.2) is a second-order non-linear differential equation that describes the particle motion in a frequency-sweep type dynamic acoustic field. COMSOL Multiphysics was used to calculate the particle trajectories in the prototype. First, the steady state flow field was computed using laminar flow physics. Subsequently, a non-stationary simulation study was carried out in order to calculate particle

trajectories for the given laminar flow pattern. For this simulation study, the ideal acoustic pressure field given by Equation (5.1), using the average pressure amplitude $55\ \mathrm{kPa}$ for all sweep periods, was input as a plane wave field and the corresponding acoustic radiation force was calculated by COMSOL.

Figure 5.4 illustrates the simulation results for $\dot{V}_1 = 300\ \mathrm{mL\ h^{-1}}$, $\dot{V}_4 = 400\ \mathrm{mL\ h^{-1}}$ and $T = 5\ \mathrm{s}$. In order to improve visibility, the number of particles were reduced to 10% of values given in Table 5.2.

Figure 5.4 indicates that since the flow rate is higher in the reflector-side (bottom) inlet and the transducer-side (top) outlet the streamlines are carrying the particles towards the transducer-side outlet. If the flow rates are all equal at each inlet and outlet, the streamlines in the region of the acoustic field will be horizontal in Figure 5.4 and parallel to the pressure nodes, thus the flow does not result in a drag force against the acoustic field. When the flow rates are unequal, with $\dot{V}_3 > \dot{V}_4$, the streamlines are always bent towards the transducer-side outlet. The acoustic field, however, pushes particles towards the reflector-side. Hence, in contrast to the case with parallel streamlines where the drag force from the fluid is perpendicular to the acoustic force, the drag force from the fluid flow has a component opposite to the acoustic force. Depending on the position where the particle enters the acoustic field, a small particle in the middle of the channel may not be captured by the nodal pattern but still be affected enough to exit from the reflector-side outlet. Consequently, such a particle potentially exiting from the reflector-side outlet may be pushed to the transducer-side outlet with the help of the additional drag force from the streamlines.

In the example given in Figure 5.4, all of the blue (largest) particles (see Table 5.2) are pushed to the reflector-side outlet. Most of the orange particles and few cyan particles are pushed toward the reflector-side outlet. Red (smallest) particles, on the other hand, all exit from the transducer side outlet. Particle position data from the simulations in COMSOL was extracted in order to analyze the particle size distribution in the transducer-side outlet and the reflector-side outlet. Particle size distributions in terms of total particle volume were calculated with MATLAB and illustrated in Figure 5.5. Results presented in Figure 5.5 are based on the full number of particles given in Table 5.2.

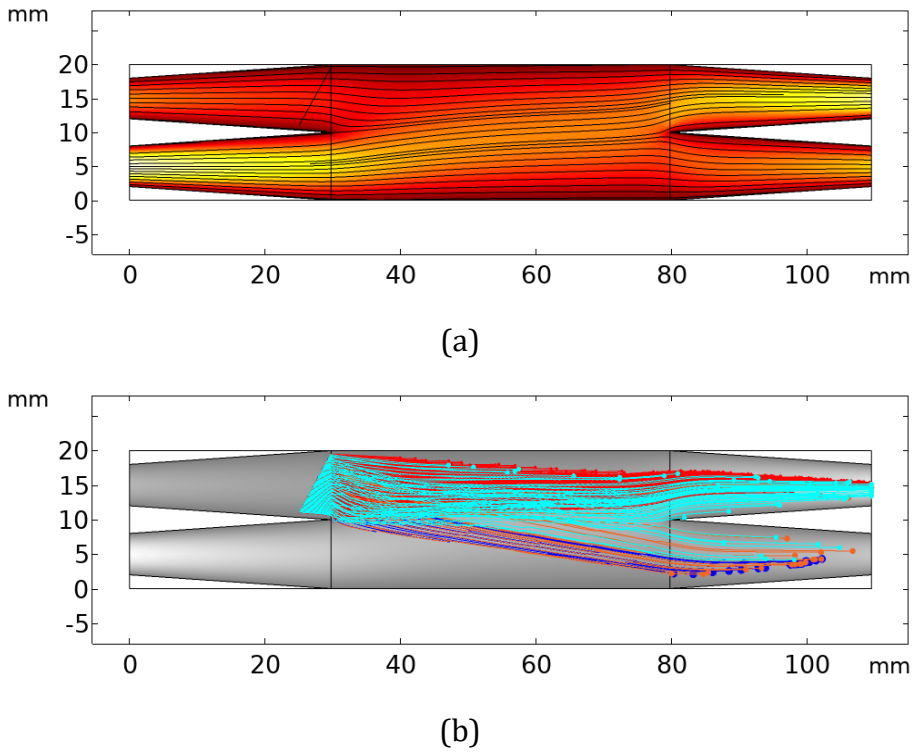

Figure 5.4 - Steady state flow velocity (a) and particle paths (b) calculated by COMSOL Multiphysics with $\dot{V}_1 = 300$ mL h^{-1}, $\dot{V}_4 = 400$ mL h^{-1} and $T = 5$ s. Flow direction is from left to right. Transducer is placed on the top and reflector is at the bottom. The particles are released from the line on the top left inlet.

In Figure 5.5, there is an overlap between the particle size distributions from the transducer-side and reflector-side outlets, indicating that there is not a single cut-off diameter for a clear separation between the two outlets. The interplay between the drag force from the fluid flow and the acoustic forces pushed larger particles towards the reflector-side outlet. In the transducer-side outlet (Figure 5.5b) 90 % of the particles were smaller than 87 µm whereas the largest particle exited from that outlet was 98 µm in diameter. For the reflector-side outlet 90% of the particles were larger than 88 µm and the smallest particle pushed to that outlet was 83 µm in diameter.

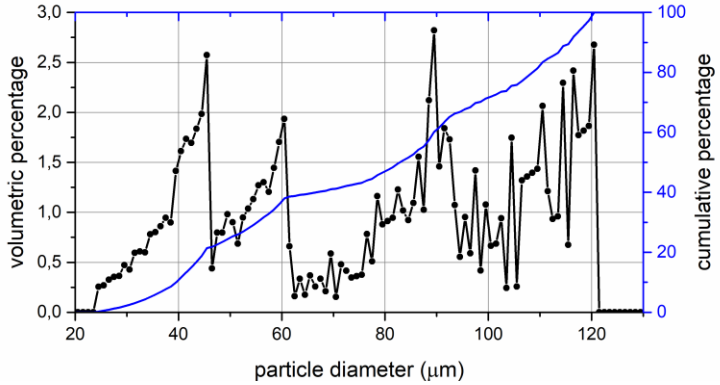
volumetric percentage
cumulative percentage
particle diameter (μm)
3,0
2,5
2,0
1,5
1,0
0,5
0,0
100
80
60
40
20
0
20
40
60
80
100
120

(a)

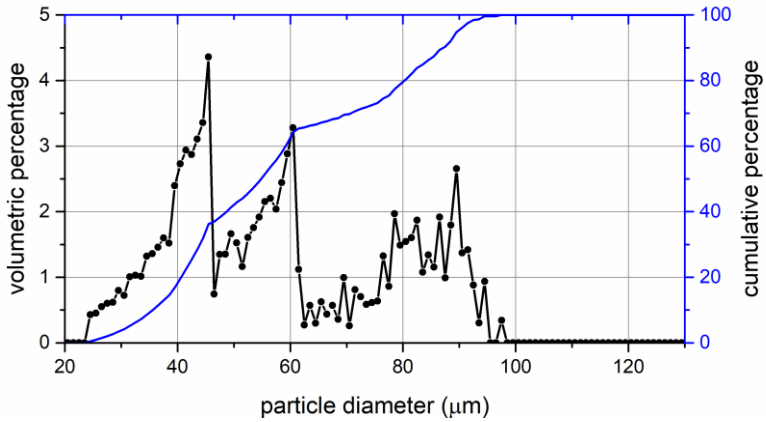
volumetric percentage
cumulative percentage
particle diameter (μm)
5
4
3
2
1
0
100
80
60
40
20
0
20
40
60
80
100
120

(b)

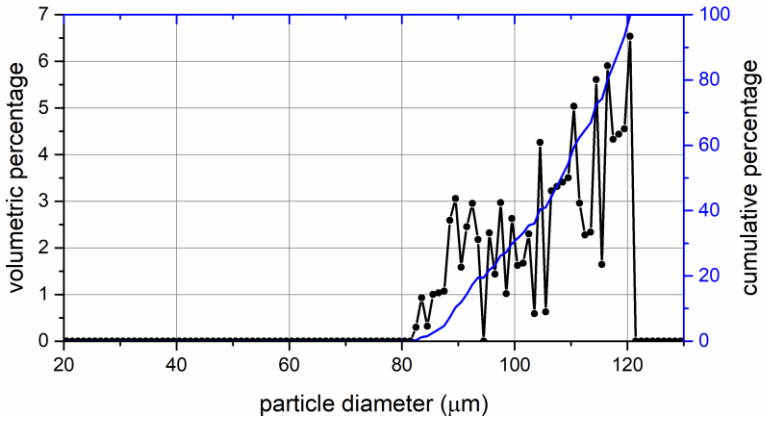

(c)

Figure 5.5 - Particle size distribution in terms of total particle volume (black dots) and the cumulative totals (blue line) for the input mixture (a), mixture from transducer-side outlet (b) and mixture from reflector-side outlet (c). These simulation results correspond to a case with $\dot{V}_1 = 300\ \mathrm{mL\,h^{-1}}$, $\dot{V}_4 = 400\ \mathrm{mL\,h^{-1}}$ and $T = 5$ s. Dots represent the percentage of the particles with diameter between neighboring integers. Lines connect the dots to guide the eye. Notice the different ranges of the y-axis. For the acoustic pressure, pressure data from Figure 5.3b is used.

5.3.3 Effects of flow and sweep period on filtration

In order to explore the effect of the combinations of flow rates and sweep period, a DOE study was carried out using Minitab 14. Simulations without acoustic field were done to check the effect of the flow field only. These simulations did not show any separation, i.e. all particles exited from the transducer-side outlet. The effect of combinations of flow rates and sweep period on the selective separation performance were evaluated based on three metrics, which are (i) the diameter of the largest particle from the transducer-side outlet, indicated as threshold; (ii) $\mathrm{d90_T}$, the diameter at which $90\ \%$ of the particles ends up in the transducer-side outlet; (iii) $\mathrm{d10_R}$, the diameter at which $10\ \%$ of the particles ends up in the reflector-side outlet. Figure 5.6 presents the effects of the flow and sweep period on the three metrics, using the average pressure amplitude of $55\ \mathrm{kPa}$ for all sweep periods.

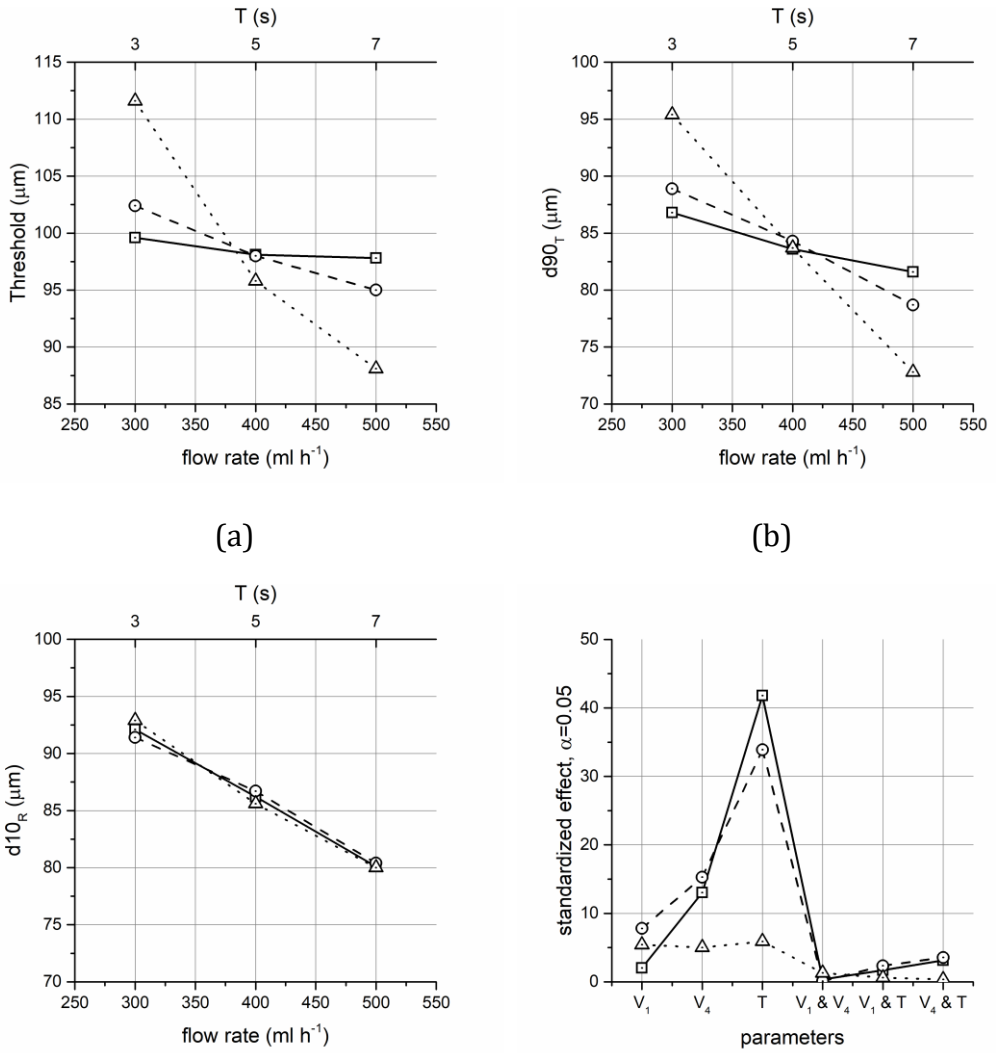

Figure 5.6 - Effects of the flow parameters $\dot{V}_1$ (squares, black line), $\dot{V}_4$ (circles, dashed line), T (triangles, dotted line), after averaging the effect of the other factors, on the threshold (a), $d90_T$ (b) and $d10_R$ (c) based on computer simulations. Bottom-right panel (d) shows the standardized effects chart based on all 27 simulations, for confidence level of 95% for threshold (squares, black line), $d90_T$ (circles, dashed line), and $d10_R$ (triangles, dotted line).

Figures 5.6a-c show more or less linear relationships between the three metrics and the three factors, $\dot{V}_1$, $\dot{V}_4$ and T. Figure 5.6d shows that the flow threshold and $d90_T$ are affected most by T and to a lesser extent by $\dot{V}_4$, whereas $d10_R$ is more or less equally affected by the flow rates and sweep period. The combined effects, based

on the coefficients in the regression equation which multiplies the product of factors, are all relatively small.

Unequal outlet flows affect particles close to the outlets as indicated in Figure 5.4b, thereby, and forced by the streamlines, giving the acoustic radiation force less time to counteract and carry particles in the opposite direction. On the other hand, in the beginning of the acoustic field the effect of unequal inlet flows is more easily countered by the acoustic field, because the acoustic field has more time to affect the particles.

Equation (5.3) suggests that for longer sweep periods with the same start and end frequency, the sweep rate S gets smaller, therefore the nodal pattern moves slower on average [38]. If a particle is moving with a nodal pattern that moves slower, it is experiencing less drag force. Hence, an excitation with longer sweep period is able to capture and carry smaller particles. It is also theoretically expected that with a constant acoustic pressure equal for all sweep periods the threshold, $\mathrm{d90_T}$ and $\mathrm{d10_R}$ values are getting smaller with a larger sweep period [38].

5.3.4 Laboratory experiments

According to the computer simulations it is possible to manipulate the particle size distribution from the transducer outlet by a combination of sweep rate and flow parameters. In order to determine and confirm such possibilities, lab experiments with polyethylene particles were carried out using the prototype given in Figure 5.2. As in the numerical experiments, the particle mixture was fed from the transducer-side inlet and samples were taken from the transducer-side outlet. As in the computer simulations, experiments with only flow manipulation did not result in any separation. Figure 5.7 displays the experimentally obtained trajectories of particles, as a result of both acoustic and flow fields.

Figure 5.7 confirms that the particles are size-selectively following the nodal movement. Trajectories of the particles clearly display the slope difference. Smaller particles, with red and cyan color, are mostly following the streamlines of the flow. The nodal velocity is depending on time and position (Equation (5.3)), where for positions further away from the transducer the velocity is lower, as *x* becomes smaller.

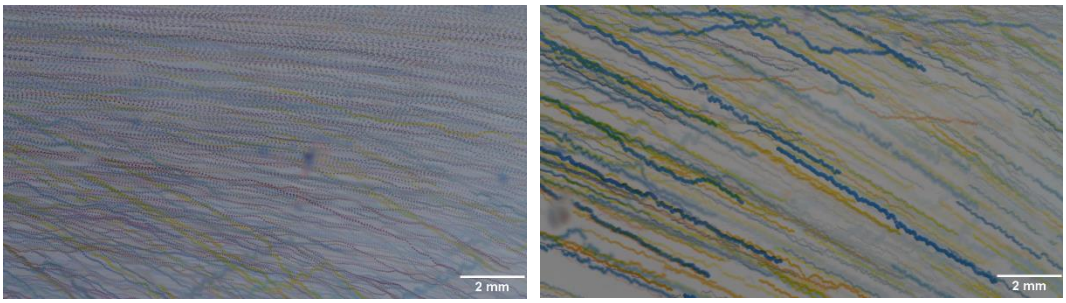

(a) (b)

Figure 5.7 - Particle trajectories recorded in the experiments. The transducer is on the top side of the image. The flow is from left to right whereas the acoustic field pushes the particles downwards. $\dot{V}_1 = 300$ mL h^{-1}, $\dot{V}_4 = 400$ mL h^{-1} and $T = 5$ s. Smaller (red, cyan) particles are in general unable to follow the nodal pattern (a), whereas larger (orange, blue) particles are moving downwards with the nodal pattern (b). The images were created by overlaying 300 consecutive pictures taken in a span of 10 s.

As seen in the left bottom corner of Figure 5.7a, small (red and cyan) particles, which escaped from the dominant flow towards the transducer-side outlet, have a steeper downward slope of their trajectory than the small particles close to the transducer. As the nodal velocity is higher in the regions close to the transducer, although affected by the acoustic field, small particles were not captured and carried by the nodes. In the regions further away from the transducer, however, the nodal speed becomes lower and the acoustic field moves slow enough to carry these small particles. Consequently, near the transducer the small particles experience the effect of the acoustic field, leading to an increasing downward slope of their trajectories as they get further away from the transducer. Furthermore, in Figure 5.7b, large blue particles captured by the field have steeper slope in the regions close to the transducer, as the velocity of the nodal pattern with the trapped (large) particles is highest here. In the regions close to the transducer, however, there are still some large particles unable to follow the nodal pattern. Hence, whether a particle is trapped or not is not only determined by the flow, excitation and size parameters. The location of the particle when entering the acoustic field also affects the particle movement. For example, a large particle close to the transducer and not captured by the nodal movement, as a result of irregularities in the acoustic field, can still follow the streamlines and exit from the transducer-side outlet, whereas a small particle away from the transducer can follow the nodal pattern and exit from the reflector-side outlet. This results in an overlap between the particle size distributions from both outlets, as indicated in

Figure 5.8. Figure 5.8 displays the particle size distributions from the transducer-side outlet for different combinations of flow and sweep periods.

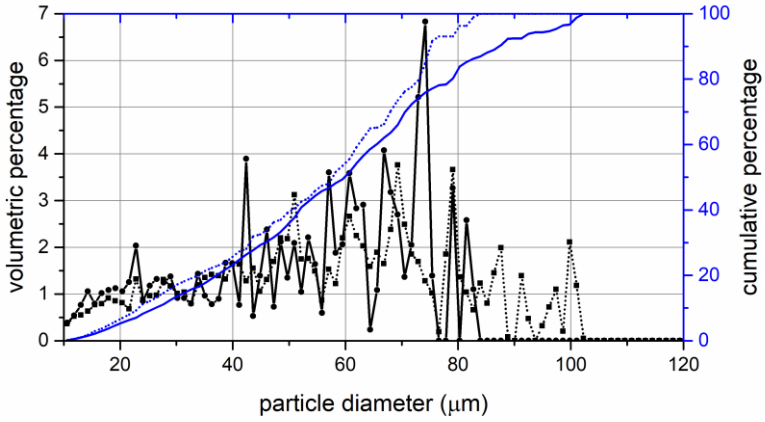

(a)

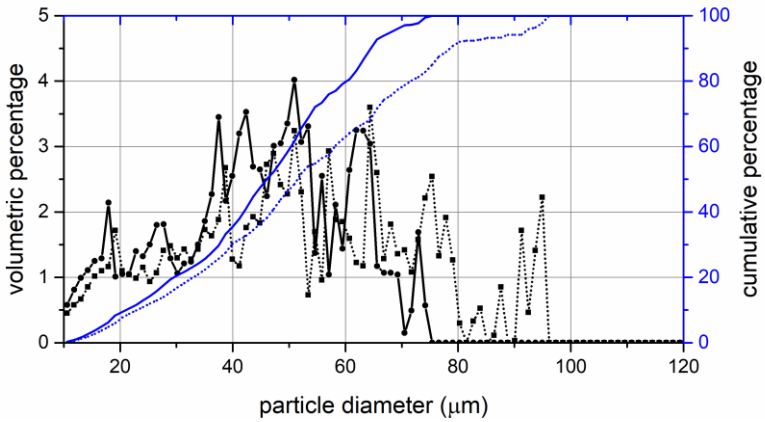

(b)

Figure 5.8 - Experimentally obtained particle size distributions of samples from transducer-side outlet with $T = 3$ s (a) and $T = 5$ s (b). Black squares connected by black dotted lines and black circles connected by black lines indicate the volumetric percentage of particle sizes for equal and unequal flow rates, respectively. Blue dotted and solid lines give the cumulative percentage of particle sizes for equal and unequal flow rates cases, respectively. Equal flow rates correspond to $\dot{V}_1 = \dot{V}_4 = 500$ mL h^{-1} whereas unequal flow rates correspond to $\dot{V}_1 = 300$ mL h^{-1} and $\dot{V}_4 = 400$ mL h^{-1}.

The particle mixture used in the experiment was contained in multiple bottles. Even though for each input the particle size distribution is not exactly the same, all input mixtures contained particles sizes in the full range of $10\text{-}120\ \mu\text{m}$. Figure 5.8 confirms the trends indicated by Figure 5.6a-c, where for unequal flow rates the threshold decreases from $T = 3$ s to $T = 5$ s. For the case with equal flow rates, the thresholds were $103\ \mu\text{m}$ and 94 μm for $T = 3$ s and $T = 5$ s, respectively. For the case with unequal flow rate, the thresholds were $82\ \mu\text{m}$ and $74\ \mu\text{m}$. The thresholds obtained in the experiments were lower than the thresholds estimated by the simulations. In the simulations, the pressure field was assumed to be a perfect plane wave in the vertical direction, as indicated by Equation (5.1). The pressure amplitude in the simulations was $55\ \text{kPa}$ for all simulations, whereas in the experiments the pressure generated by the transducer is a function of frequency (Figure 5.3b) and therefore not constant. The experiments suggest that the actual pressure field generated by the transducer has a stronger effect on particles than the constant peak amplitude field used in the simulations. Nevertheless, experiments confirm that the threshold values can be tuned by the flow and sweep time parameters, enabling selective filtration from the transducer outlet.

5.3.4.1 Wheat beer experiment

Another experiment, that aimed to further investigate the previous findings using hard model particles, was carried out with wheat beer, containing yeast particles (soft matter) with unknown properties. The prototype has shorter entrance length due to the lower flow rate used. Normally the beer contains bubbles and the bubbles disrupt the acoustic field by creating discontinuities in the medium as well as improving the likelihood of cavitation. Hence, before the start of the experiment the beer was degassed using a vacuum pump. In this experiment, the excitation frequency was swept from $1.9\ \text{MHz}$ to $2.3\ \text{MHz}$. Voltage applied to the transducer was $20\ \text{V}_{\text{pp}}$ while the flow rate was set to $100\ \text{mL h}^{-1}$ in total, equal at both inlets and outlets. Sweep periods were set to $T = 8$ s and $\text{T} = 10$ s. Samples were taken from the transducer side outlet. Particle size distributions for each case is given in Figure 5.9.

As the properties of the yeast cells are unknown, we chose a lower flow rate with higher residence time in the separator than in the previous experiments. Together with longer sweep periods the nodes move slower, according to Equation (5.3). Such adjustments to the flow and excitation ensured that the yeast cells were trapped. The beer initially contained yeast cells up to $21\ \mu\text{m}$ in diameter. After

passing through the separator while $T = 8$ s, the sample from the transducer outlet contained yeast cells up to 14 μm in diameter. Similarly, for $T = 10$ s maximum particle size in the transducer outlet was 11 μm.

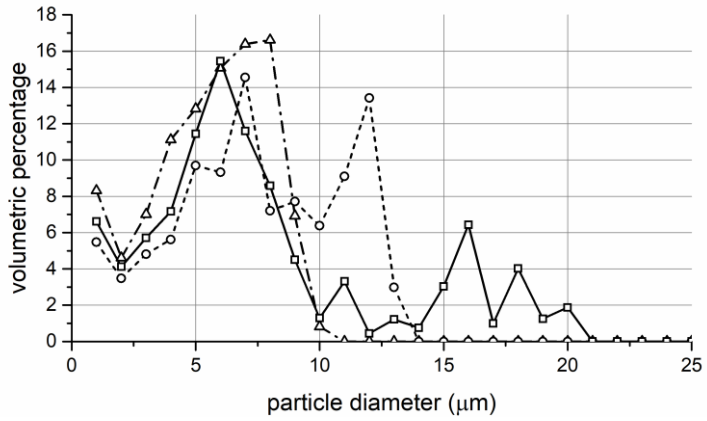

Figure 5.9 - Particle size distribution of wheat beer before and after the application. Squares connected by the solid line represents the particle size distribution of the input mixture. Circles connected by the dashed line and triangles connected by the dash-dot line represent the particle size distribution for $T = 8$ s and $T = 10$ s, respectively.

5.4 Conclusions

This study explored selective filtering on centimeter scale by frequency sweep excitation and regulation of flow rates. The interplay of the forces on a particle, that is acoustic force and drag force, creates possibilities for selective filtering. A DOE study of computer simulations demonstrated that the filtration threshold can be manipulated by adjusting the inlet and outlet flow rates and the sweep period. The filtration threshold is mainly affected by the outlet flow conditions and the sweep period, as the effects of inlet flow conditions can be countered by the acoustic force. Experiments with a mixture of model polyethylene particles confirmed the tunability of the filtering threshold with a total flow rate of 1 L h^{-1}.

A lab experiment with wheat beer confirmed the applicability of the method on soft matter with smaller particle sizes and using a lower flow rate.

The numerical and lab experiments in this explorative study confirmed the selective filtration capability of dynamic acoustic fields with regulated flows on centimeter

scale, and open up possibilities for future optimization studies of the X-shaped separator.

References

[1] Leong, T., Johansson, L., Juliano, P., McArthur, S.L., Manasseh, R., 2013. Ultrasonic Separation of Particulate Fluids in Small and Large Scale Systems: A Review. Industrial & Engineering Chemistry Research 52, 16555–16576. doi:10.1021/ie402295r

[2] Cappon, H.J., Stefanova, L.A., Keesman, K.J., 2013. Concentration based flow control in acoustic separation of suspensions. Separation and Purification Technology 103, 321–327. doi:10.1016/j.seppur.2012.10.033

[3] Sajeesh, P., Sen, A.K., 2014. Particle separation and sorting in microfluidic devices: a review. Microfluidics and Nanofluidics 17, 1–52. doi:10.1007/s10404-013-1291-9

[4] Dijkshoorn, J.P., Schutyser, M.A.I., Wagterveld, R.M., Schroën, C.G.P.H., Boom, R.M., 2017. A comparison of microfiltration and inertia-based microfluidics for large scale suspension separation. Separation and Purification Technology 173, 86–92. doi:10.1016/j.seppur.2016.09.018

[5] Dizge, N., Soydemir, G., Karagunduz, A., Keskinler, B., 2011. Influence of type and pore size of membranes on cross flow microfiltration of biological suspension. Journal of Membrane Science 366, 278–285. doi:10.1016/j.memsci.2010.10.010

[6] Gor'kov, L.P., 1962. On the Forces Acting on a Small Particle in an Acoustical Field in an Ideal Fluid. Soviet Physics Doklady 6, 773.

[7] Bruus, H., 2012. Acoustofluidics 7: The acoustic radiation force on small particles. Lab on a Chip 12, 1014–1021. doi:10.1039/C2LC21068A

[8] Gröschl, M., 1998. Ultrasonic Separation of Suspended Particles - Part I: Fundamentals. Acta Acustica united with Acustica 84, 432–447.

[9] Lenshof, A., Laurell, T., 2010. Continuous separation of cells and particles in microfluidic systems. Chemical Society Reviews 39, 1203–1217. doi:10.1039/B915999C

[10] Nam, J., Lee, Y., Shin, S., 2011. Size-dependent microparticles separation through standing surface acoustic waves. Microfluidics and Nanofluidics 11, 317–326. doi:10.1007/s10404-011-0798-1

[11] Laurell, T., Petersson, F., Nilsson, A., 2007. Chip integrated strategies for acoustic separation and manipulation of cells and particles. Chemical Society Reviews 36, 492–506. doi:10.1039/B601326K

[12] Kapishnikov, S., Kantsler, V., Steinberg, V., 2006. Continuous particle size separation and size sorting using ultrasound in a microchannel. Journal of Statistical Mechanics: Theory and Experiment 2006, P01012–P01012. doi:10.1088/1742-5468/2006/01/P01012

[13] Büyükkoçak, S., Özer, M.B., Çetin, B., 2014. Numerical modeling of ultrasonic particle manipulation for microfluidic applications. Microfluidics and Nanofluidics 17, 1025–1037. doi:10.1007/s10404-014-1398-7

[14] Nam, J., Lim, H., Kim, C., Yoon Kang, J., Shin, S., 2012. Density-dependent separation of encapsulated cells in a microfluidic channel by using a standing surface acoustic wave. Biomicrofluidics 6, 024120. doi:10.1063/1.4718719

[15] Vakarelski, I.U., Li, E.Q., Abdel-Fattah, A.I., Thoroddsen, S.T., 2016. Acoustic separation of oil droplets, colloidal particles and their mixtures in a microfluidic cell. Colloids and Surfaces A: Physicochemical and Engineering Aspects 506, 138–147. doi:10.1016/j.colsurfa.2016.06.013

[16] Townsend, R.J., Hill, M., Harris, N.R., McDonnell, M.B., 2008. Performance of a quarter-wavelength particle concentrator. Ultrasonics, Selected Papers from ICU 2007 48, 515–520. doi:10.1016/j.ultras.2008.06.005

[17] Iv, C.W.S., Reyes, C.D., López, G.P., 2015. Microfluidic cell sorting: a review of the advances in the separation of cells from debulking to rare cell isolation. Lab on a Chip 15, 1230–1249. doi:10.1039/C4LC01246A

[18] Franke, T., Braunmüller, S., Schmid, L., Wixforth, A., Weitz, D.A., 2010. Surface acoustic wave actuated cell sorting (SAWACS). Lab on a Chip 10, 789–794. doi:10.1039/B915522H

[19] Ding, X., Lin, S.-C.S., Kiraly, B., Yue, H., Li, S., Chiang, I.-K., Shi, J., Benkovic, S.J., Huang, T.J., 2012. On-chip manipulation of single microparticles, cells, and organisms using surface acoustic waves. Proceedings of the National Academy of Sciences of the United States of America 109, 11105–11109. doi:10.1073/pnas.1209288109.

[20] Li, P., Mao, Z., Peng, Z., Zhou, L., Chen, Y., Huang, P.-H., Truica, C.I., Drabick, J.J., El-Deiry, W.S., Dao, M., Suresh, S., Huang, T.J., 2015. Acoustic separation of circulating tumor cells. Proceedings of the National Academy of Sciences of

the United States of America 112, 4970–4975. doi:10.1073/pnas.1504484112

[21] Wang, K., Zhou, W., Lin, Z., Cai, F., Li, F., Wu, J., Meng, L., Niu, L., Zheng, H., 2018. Sorting of tumour cells in a microfluidic device by multi-stage surface acoustic waves. Sensors and Actuators B: Chemical 258, 1174–1183. doi:10.1016/j.snb.2017.12.013

[22] Shen, Y., Yalikun, Y., Tanaka, Y., 2019. Recent advances in microfluidic cell sorting systems. Sensors and Actuators B: Chemical 282, 268–281. doi:10.1016/j.snb.2018.11.025

[23] Xie, Y., Mao, Z., Bachman, H., Li, P., Zhang, P., Ren, L., Wu, M., Huang, T.J., 2020. Acoustic Cell Separation Based on Density and Mechanical Properties. Journal of Biomechanical Engineering 142. doi:10.1115/1.4046180

[24] Lenshof, A., Evander, M., Laurell, T., Nilsson, J., 2012. Acoustofluidics 5: Building microfluidic acoustic resonators. Lab on a Chip 12, 684–695. doi:10.1039/C1LC20996E

[25] Hawkes, J.J., Radel, S., 2013. Acoustofluidics 22: Multi-wavelength resonators, applications and considerations. Lab on a Chip 13, 610–627. doi:10.1039/C2LC41206C.

[26] Gómez, E.H., Marchese, A.J., 2015. An ultrasonically enhanced inclined settler for microalgae harvesting. Biotechnology Progress 31, 414–423. doi:10.1002/btpr.2031

[27] Setayeshgar, A., Lipsett, M.G., Koch, C.R., Nobes, D.S., 2015. Particle Motion in a Macroscale, Multiwavelength Acoustic Field. Journal of Fluids Engineering 137. doi:10.1115/1.4027777

[28] Benes, E., Groschl, M., Nowotny, H., Bohm, H., Radel, S., Hauser, C., Power, J., Lowe, K., Briarty, G., Davey, M., 2003. The Ultrasonic h-shape Separator: Harvesting of the Alga Spirulina Platensis under Zero-Gravity Conditions. Presented at the World Congress on Ultrasonics, pp. 1631–1638.

[29] Böhm, H., Briarty, L.G., Lowe, K.C., Power, J.B., Benes, E., Davey, M.R., 2003. Quantification of a noveL h-shaped ultrasonic resonator for separation of biomaterials under terrestrial gravity and microgravity conditions. Biotechnology and Bioengineering 82, 74–85. doi:10.1002/bit.10546

[30] Manneberg, O., Melker Hagsäter, S., Svennebring, J., Hertz, H.M., Kutter, J.P., Bruus, H., Wiklund, M., 2009. Spatial confinement of ultrasonic force fields in

microfluidic channels. Ultrasonics 49, 112–119. doi:10.1016/j.ultras.2008.06.012

[31] Cappon, H., Keesman, K.J., 2013. Numerical modeling, calibration, and validation of an ultrasonic separator. IEEE Transactions on Ultrasonics, Ferroelectrics, and Frequency Control 60, 614–621. doi:10.1109/TUFFC.2013.2603

[32] Kandemir, M.H., Wagterveld, R.M., Yntema, D.R., Keesman, K.J., 2019. Selective Particle Filtering in a Large Acoustophoretic Serpentine Channel. Scientific Reports 9, 7156. doi:10.1038/s41598-019-43711-8

[33] Drinkwater, B.W., 2016. Dynamic-field devices for the ultrasonic manipulation of microparticles. Lab on a Chip 16, 2360–2375. doi:10.1039/C6LC00502K

[34] Grinenko, A., Ong, C.K., Courtney, C.R.P., Wilcox, P.D., Drinkwater, B.W., 2012. Efficient counter-propagating wave acoustic micro-particle manipulation. Applied Physics Letters 101, 233501. doi:10.1063/1.4769092

[35] Glynne-Jones, P., Boltryk, R.J., Harris, N.R., Cranny, A.W.J., Hill, M., 2010. Mode-switching: A new technique for electronically varying the agglomeration position in an acoustic particle manipulator. Ultrasonics 50, 68–75. doi:10.1016/j.ultras.2009.07.010

[36] Courtney, C.R.P., Ong, C.-K., Drinkwater, B.W., Bernassau, A.L., Wilcox, P.D., Cumming, D.R.S., 2012. Manipulation of particles in two dimensions using phase controllable ultrasonic standing waves. Proceedings of the Royal Society A: Mathematical, Physical and Engineering Sciences 468, 337–360. doi:10.1098/rspa.2011.0269

[37] Skotis, G.D., Cumming, D.R.S., Roberts, J.N., Riehle, M.O., Bernassau, A.L., 2015. Dynamic acoustic field activated cell separation (DAFACS). Lab on a Chip 15, 802–810. doi:10.1039/C4LC01153H

[38] Kandemir, M.H., Beelen, M., Wagterveld, R.M., Yntema, D.R., Keesman, K.J., 2021. Dynamic acoustic fields for size selective particle separation on centimeter scale. Journal of Sound and Vibration 490, 115723. doi:10.1016/j.jsv.2020.115723

[39] Lipkens, B., Costolo, M., Rietman, E., 2008. The Effect of Frequency Sweeping and Fluid Flow on Particle Trajectories in Ultrasonic Standing Waves. IEEE Sensors Journal 8, 667–677. doi:10.1109/JSEN.2008.922675

[40] Trujillo, F.J., Eberhardt, S., Möller, D., Dual, J., Knoerzer, K., 2013. Multiphysics modelling of the separation of suspended particles via frequency ramping of ultrasonic standing waves. Ultrasonics Sonochemistry 20, 655–666. doi:10.1016/j.ultsonch.2012.08.014

[41] Lipkens, B., Dionne, J., Trask, A., Szczur, B., Stevens, A., Rietman, E., 2010. Separation of micron-sized particles in macro-scale cavities by ultrasonic standing waves. Physics Procedia 3, 263–268. doi:10.1016/j.phpro.2010.01.035.

[42] Kozuka, T., Yasui, K., Hatanaka, S., Tuziuti, T., Suzuki, K., Towata, A., 2011. Manipulation of Particles in a Microchannel with Various Geometric Spaces Using Ultrasound. Japanese Journal of Applied Physics 50, 07HE27. doi:10.1143/JJAP.50.07HE27

[43] Schindelin, J., Arganda-Carreras, I., Frise, E., Kaynig, V., Longair, M., Pietzsch, T., Preibisch, S., Rueden, C., Saalfeld, S., Schmid, B., Tinevez, J.-Y., White, D.J., Hartenstein, V., Eliceiri, K., Tomancak, P., Cardona, A., 2012. Fiji: an open-source platform for biological-image analysis. Nature Methods 9, 676–682. doi:10.1038/nmeth.2019

6 SELECTIVE PARTICLE SEPARATION ON CENTIMETER SCALE USING DUAL FREQUENCY TYPE DYNAMIC ACOUSTIC FIELD

A version of this chapter has been published as

Kandemir, M. H., Wagterveld, R. M., Yntema, D. R., & Keesman, K. J. (2021) Selective particle separation on centimeter scale using a dual frequency dynamic acoustic field. *Ultrasonics*, 114, 106411

Abstract

This study investigated the application of dual-frequency type dynamic acoustic fields for size-selective particle separation on centimeter scale in a continuous flow. The 3D-printed X-shaped prototype has two inlets and two outlets. The dynamic acoustic field is generated by two transducers positioned under an angle of $60°$ and operating at slightly different frequencies. The acoustic reflections are eliminated by placing sound-absorbing material inside the prototype and the non-resonant operation is confirmed by the electrical admittance measurements. Numerical calculations suggested that pressure generated by each transducer need not to have an equal amplitude. Computer simulations and lab experiments were carried out for different frequency differences and flow rates. The results demonstrated the ability of dual-frequency type dynamic acoustic fields for size-selective particle filtration on centimeter scale, with a total flow rate up to $1\ \mathrm{L\ h^{-1}}$.

.

6.1 Introduction

Many industries, such as food, biomedical, pharmaceutical and water industries, utilize particle filtration processes. Filtration is often performed on suspensions in order to improve the quality of the product and the process. Several methods exist to perform filtration on several types of mixtures. Acoustophoresis is one of such methods and can perform filtration in continuous flows without blocking and affecting the flow [1-5]

Selective particle separation using acoustophoresis is achieved through the interplay between forces acting on particles, namely the acoustic radiation force and the drag force [6]. Acoustic radiation force acts on a particle in an acoustic field and scales with particle volume, density and compressibility. In an acoustic standing wave field, depending on the acoustic properties of the particle and the surrounding medium, the particle is pushed either towards a pressure node or antinode [7, 8]. A drag force acts on particles as a result of the motion of the particle due to the combined effect of an acoustic field and flow field, and scales with particle size [8, 9].

Microscale acoustophoretic separation exploits this interplay to selectively separate cells and particles based on their size, density and compressibility [10-16]. In a half-wavelength separator particles are pushed towards a single pressure node in the middle of the chamber at appropriate excitation frequencies. Acoustic radiation force also scales with frequency and the manipulated particle should not be larger than the wavelength of excitation. Due to this limitations, the excitation frequency is typically in the MHz range for micrometer-sized particles. Consequently, the width of half-wavelength microfluidic devices are in the order of hundreds of micrometers. Scaling up half-wavelength devices to centimeter scale implies the frequency to be in the range of a few kHz to match physically, but therefore reducing the force enormously. As a result, centimeter scale acoustophoretic devices were designed as multi-wavelength resonators with multiple pressure nodes and antinodes in the system [17-21]. As in microscale applications, the interplay between acoustic radiation force and drag force can still be exploited for selectivity by clever arrangement of the flow [21, 22].

On centimeter scale, as an alternative to acoustic standing wave fields, dynamic acoustic fields offer more possibilities and allow a higher degree of configurability [6, 23]. One way of obtaining a dynamic acoustic field is exciting the medium by two transducers. Counter-propagating waves from each transducer subsequently

generate a standing wave pattern in between. If both of the transducers are operated at the same frequency and amplitude, an acoustic standing wave field results. Moreover, when a phase difference between the waves is introduced, it becomes possible to regulate the position of the nodes in the acoustic standing wave pattern. A less frequently used alternative is the dual frequency method, where one of the transducers is operated at a slightly different frequency, corresponding to a linear continuous phase shift. The phase shift results in a quasi-standing wave field moving with constant velocity. In both bulk and surface acoustic wave applications, such manipulations enable particle transport in single and multi-wavelength systems [6, 23-34], but may also enhance sedimentation processes. Especially in bulk acoustic wave applications, however, the transducers also act as reflectors. By adjusting the dimensions of the matching layers in the system or operating the system at the resonant frequencies of the transducers, it is still possible to manipulate the wave pattern when reflections are present [6, 24, 30, 31].

Instead of including or eliminating reflections, it is also possible to generate a quasi-standing wave field by orienting the transducers to generate sound in an angle to each other. Using such a method, pressure nodes are generated parallel to the plane of symmetry between two transducers [35, 36]. These crossing sound beams can eliminate the reflections completely, while keeping the acoustic wave field suitable for particle manipulation. By manipulating the excitation, a quasi-standing wave field can be obtained and controlled in the desired area. Controlling the acoustic wave field allows the control of the acoustic radiation force and thus enhances the interplay between the acoustic radiation force and the drag force. Such possibilities make this method a good candidate for applications of selective particle separation on centimeter scale in continuous flows. However, this method, combining acoustic radiation and drag forces and using dual transducers with slightly different frequencies, has not been explored for selective particle separation on centimeter scale, yet.

The aim of this study was to explore and demonstrate the selective particle separation capability of dual frequency type dynamic acoustic fields on centimeter scale in a continuous flow separator. The dynamic acoustic field is obtained by crossing the fields from two transducers with an angle of $60°$ in between. The frequency responses of the transducers were examined in order to determine the optimal excitation frequency. Computer simulations were carried out to discover the effects of the excitation parameters on the filtration performance. Lab

experiments confirm the size selective separation capability of the X-shaped prototype.

6.2 Materials and methods

6.2.1 Dual frequency excitation

In order to obtain an acoustic standing wave, two identical counter-propagating waves are needed. When the waves are not identical but are with similar frequency and amplitude, the resulting pressure field, at position x and time t, is expressed as

$$P(x,t) = \delta_{P1} P_0 \cos\left(\omega_1 t - \frac{\omega_1}{c_0} x\right) + \delta_{P2} P_0 \cos\left(\omega_2 t + \frac{\omega_2}{c_0} x\right) \tag{6.1}$$

Here, P_0 (Pa) is the average peak amplitude of the two waves, δ_{P1} and δ_{P2}, with $\delta_{P1} + \delta_{P2} = 2$ and $\delta_{P1}, \delta_{P2} \geq 0$, are the multipliers of the pressure from each transducer, $\omega_1 = 2\pi f_1$ and $\omega_2 = 2\pi f_2$ (rad s^{-1}) are the excitation frequencies, t (s) is time, x (m) is distance from the high frequency source and c_0 (m s^{-1}) is the speed of sound in the host medium. If $\omega_1 = \omega_2$ and $\delta_{P1} = \delta_{P2} = 1$, the result will be a stationary standing-wave field. When $\delta_{P1} = \delta_{P2} = 1$, $\omega_1 = \omega_2 + \epsilon$, $\omega = (\omega_1 + \omega_2)/2$ and $\epsilon \ll \omega$, the pressure field can be written as follows [6]:

$$P(x,t) = 2P_0 \cos\left(\frac{\omega}{c_0} x - \frac{\epsilon}{2} t\right) \cos\left(\frac{\epsilon}{2\, c_0} x - \omega t\right) \tag{6.2}$$

The acoustic radiation force on a spherical particle in such a field, with $P_D = 2P_0$, is given by [6]

$$F_{ac}(x,t) = 4\pi k r^3 \left(\frac{P_D^2}{4\rho_0 c_0^2}\right) \Phi(\rho, c) \sin(2kx - \epsilon t) \tag{6.3}$$

Here, r (m) is the particle radius, ρ_0 (kg m^{-3}) is the density of the medium, ρ is the density of the particle, c is the speed of sound in the particle, $\Phi(\rho, c) = \frac{\rho + \frac{2}{3}(\rho - \rho_0)}{2\rho + \rho_0} - \frac{1}{3}\frac{\rho_0 c_0^2}{\rho c^2}$ (-) is the acoustic contrast factor, $k = \omega/c_0$ (m^{-1}) is the wave number. The resulting sinusoidal-shaped force field will travel from the higher-frequency source

to the lower-frequency source at a constant velocity of $v = \epsilon/2k$ (m s^{-1}). If the frequencies of excitation are given by: $f_1 = f_2 + \Delta f$ and $f = (f_1 + f_2)/2$ (Hz), the velocity of the wave pattern is $v = \frac{\Delta f}{2f} c_0$ [6, 34]. This type of a field is analogous to a field created by introducing a linear continuous phase shift between two transducers.

Theoretically [6], it is required that the amplitudes of two waves are equal. In practical applications, however, this may not always be the case. When $\delta_{P1} \neq \delta_{P2}$ and still $\delta_{P1} + \delta_{p2} = 2$, the force on a particle scales as (see Appendix 6A for numerical validation)

$$F'_{ac}(x,t) = \frac{2\delta_{P1}\delta_{P2}}{\delta_{\mathrm{P1}} + \delta_{P2}} F_{ac}(x,t) \tag{6.4}$$

In Equation (6.4), the term multiplying the acoustic radiation force, for the case $\delta_{P1} \neq \delta_{P2}$, is the harmonic average of δ_{P1} and δ_{P2}. The force on a particle is thus maximized when $\delta_{P1} = \delta_{P2} = 1$. The case $\delta_{P1} = 0$ and $\delta_{P1} = 2$, for instance, gives $F'_{ac}(x,t) = 0$, which corresponds to a travelling wave and zero acoustic radiation force on a particle. Assuming there are no reflections and denoting the harmonic average as H, with $0 \leq H \leq 1$, the equation of motion (EOM) of a particle in a dual frequency type dynamic acoustic field reads as follows:

$$\left(\frac{4}{3}\pi r^3 \rho\right)\ddot{x} + (6\pi\mu r)(\dot{x} + u) + 4\pi k r^3 H\left(\frac{P_D^2}{4\rho_0 c_0^2}\right)\Phi(\rho, c)\sin(2kx - \epsilon t) = 0 \tag{6.5}$$

In Equation (6.5), u (m s^{-1}) is the constant flow velocity of the liquid from the high-frequency source to the low-frequency source and μ (Pa s) is the viscosity of host medium.

6.2.2 Experimental setup

The experimental set-up consists of a 3D-printed polylactic acid (PLA) prototype of a separator with piezoelectric transducer (Noliac NCE41, dimensions 50 mm × 10 mm × 1 mm) , a dual-channel signal generator (Keysight Trueform 33512B), a custom-made amplifier, an oscilloscope (Tektronix TDS2024C), two syringe pumps

for inlets (Aitecs PRO SP-12S) and two syringe pumps for outlet (HARVARD Apparatus Pump 33).

The geometry of the prototype is designed such that the angle between the transducers is $60°$ and each transducer therefore makes an angle $30°$ with the horizontal plane. Figure 6.1 illustrates the prototype.

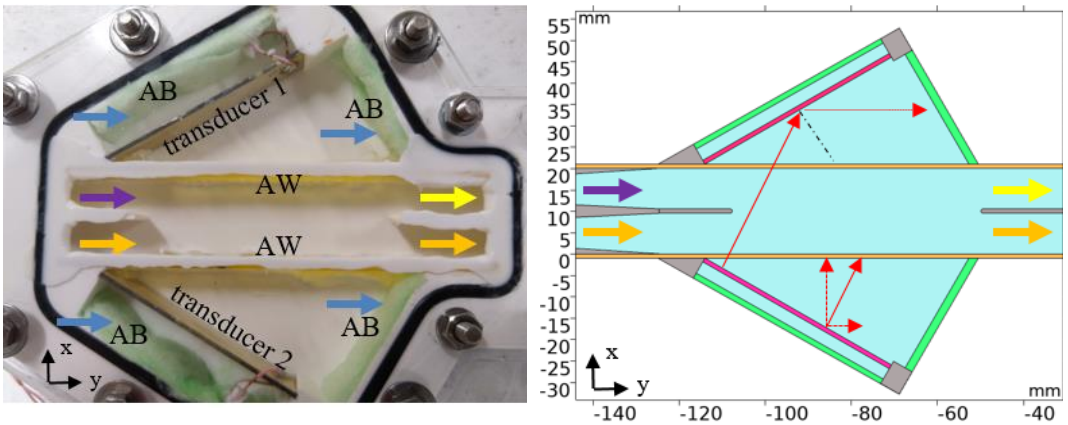

(a) (b)

Figure 6.1 - (a) The 3D printed prototype and (b) the schematic representation. The transducers are electrically connected to the two channels of the amplifier. The inlets and outlets have equal flow rates. Particle mixture is fed from the inlet indicated by the purple (darkest) arrow. Samples are taken from the outlet indicated by the yellow (lightest) arrow. Acoustic windows (AW) are displayed in orange, transducers are displayed in pink and absorbing blocks (AB) are displayed in green in (b). Due to the geometry, the reflected waves are directed towards the absorbing blocks (b). Consequently, a standing wave is generated as if there were no reflections. Blue arrows in (a) indicate the location of cooling water inlets and outlets.

The transducers were excited by signals generated in the separate but synchronized channels of the signal generator. When the angle between the transducers is larger than $60°$, the reflected waves are directed away from the flow channel. Hence, the angle of $60°$ ensures that the reflections do not disturb the acoustic field while keeping the x-component as large as possible. The flow entrances were designed to be smooth, so that in the main resonator channel turbulence is avoided. The resonator channel was created by placing inner walls, $2\,\mathrm{cm}$ apart from polyurethane sheets as polyurethane is acoustically transparent. The prototype is closed by a PMMA cover on top. Between the transducers and the inner wall, cooling water was circulated between experiments to cool the transducers. In order to isolate the resonator channel from the cooling liquids, silicone lines were applied

between the cover and the inner wall, closing any remaining gaps. The absorbing blocks were cut from polystyrene blocks and glued to the transducer wall. Small holes on the absorbing blocks were pinched to ensure that the cooling liquid can be pumped to the chambers.

In order to check whether the reflections were absorbed by the absorbing blocks and no resonances are present in the system, the electrical admittance of the prototype was measured by using an HP4194A impedance analyzer. The excitation frequency of the transducers was determined based on the frequency response of the transducers measured by the impedance analyzer.

A Polytec OFV-5000 single-point vibrometer was used to measure the vibrations and calculate the pressure generated by each transducer. For the laser vibrometer measurements, the transducers were placed on a special stand imitating the fixture in the prototype, immersed in water to ensure sufficient signal quality. The pressure was later calculated by using the specific acoustic impedance of the host medium.

Polyethylene particles ($c = 1700\ \mathrm{m\ s^{-1}}$) of sizes: 36 (red), 56 (cyan), 70 (orange) and $100\ \mu\mathrm{m}$ (blue) were used for both the simulations and experiments. Densities of the different set of particles are $\rho_{red} = 998\ \mathrm{kg\ m^{-3}}$, $\rho_{cyan} = 1000\ \mathrm{kg\ m^{-3}}$, $\rho_{orange} = 1006\ \mathrm{kg\ m^{-3}}$ and $\rho_{blue} = 1002\ \mathrm{kg\ m^{-3}}$. The particle mixture contained $1\ L$ MilliQ water, 0.075 g CTAB (hexadecyltrimethylammonium bromide) as surfactant, 0.03 g red, 0.08 g cyan, 0.2 g orange and 0.5 g blue particles.

Particle motion was recorded by a microscope with camera and particle trajectories were visualized with ImageJ software [37]. Particle size distributions were analyzed using a Mastersizer 3000 particle size analyzer.

6.2.3 Computer simulations

For the computer simulations, COMSOL Multiphysics (5.5) was used to calculate the particle trajectories and MATLAB (r2018b) was used to generate particle size distributions. Due to the angled orientation of the transducers the dynamic acoustic field is generated in a limited area in the prototype, as illustrated in Figure 6.2.

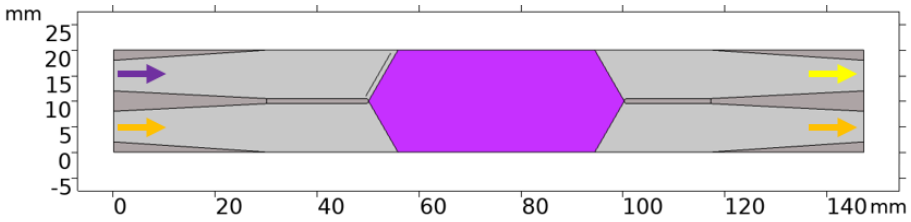

Figure 6.2 - Geometry of the prototype used in the computer simulations. The inlets and outlets have equal flow rates. Particle mixture was fed from the inlet indicated by the purple (darkest) arrow. Particle size analysis were done for the outlet indicated by the yellow (lightest) arrow. Purple area highlights the region of the acoustic field.

In the simulations the total flow rate was set to $600\ \mathrm{mL\ h^{-1}}$, $800\ \mathrm{mL\ h^{-1}}$ and $1000\ \mathrm{mL\ h^{-1}}$. The average frequency of excitation was $2.19\ \mathrm{MHz}$ while the top transducer was excited at a higher frequency. The frequency difference between the transducers was set $1\ \mathrm{Hz}$, $2\ \mathrm{Hz}$ and $3\ \mathrm{Hz}$. Simulations were carried out for all combinations of flow rates and frequency differences. Particles were released from the tilted line at the left-hand side of the acoustic field region (Figure 6.2) in order to limit simulation time. Particle sizes were randomized around the average sizes for each group and particles started at a random location along the starting line. For each simulation, the same particle set was used with the same particle starting location. Table 6.1 summarizes the particle properties used in the simulations.

Table 6.1 – Parameters of particles used in the simulations

Particle color	Diameter (µm)	STD of Diameter (µm)	Number of particles	Density ($\mathrm{kg\ m^{-3}}$)
Red	35	6.36	1756	998
Cyan	50	6.34	602	1000
Orange	71	13.11	220	1006
Blue	99	13.11	200	1002

For the simulations and experiments, the filtration performance was evaluated based on the commonly used $d90$ value of the particle size distribution at the top outlet.

6.3 Results and discussion

6.3.1 Frequency response of the prototype

The electrical admittance of both transducers was measured while they were placed in the prototype filled with water. Figure 6.3 displays the electrical admittance of the transducers between 2 MHz and 2.5 MHz.

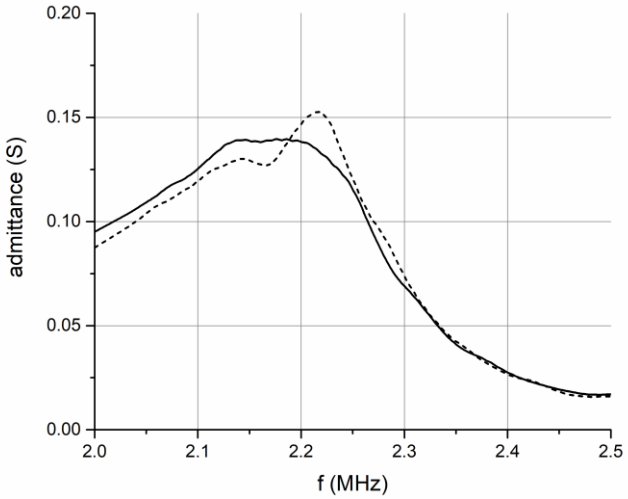

Figure 6.3 - Admittance of the transducers placed in the prototype. Solid black line represents the admittance of transducer 1 and dashed black line represents the admittance of transducer 2. The two lines intersect near 2.19 MHz.

The absence of sharp peaks and valleys in the admittance graphs confirms that the reflections are absorbed by the absorbing blocks, and the device is not operated at a resonance. Measurements without the absorbing blocks contained many sharp peaks resulting from resonances [6]. The admittance curves of the transducers intersect at $f = 2.19$ MHz, and this intersection frequency was chosen as the average excitation frequency. Each transducer was separately excited at 2.19 MHz and with $20\ \mathrm{V_{pp}}$. The calculations on the basis of the vibrometer measurements suggest that each transducer produces 35 ± 2 kPa. According to Figure 6.1, the x-components of each wave creates the dynamic acoustic field in the highlighted area in Figure 6.2.

6.3.2 Computer simulations

For the computer simulations, it was assumed that the transducers are generating equal pressure and the x-component of pressure from each transducer is taken as 30 kPa. First, the steady state flow field was computed assuming laminar flow in the prototype. Subsequently, given the stationary flow field, particle trajectories were calculated. The acoustic field from the transducers was assumed to be an ideal plane wave field. Therefore, the highlighted area contains an acoustic quasi-standing wave field with pressure nodes parallel to the y-axis. Figure 6.4 illustrates the simulation results for $\dot{V} = 1000\ \mathrm{mL\ h^{-1}}$, thus through each channel 500 mL h^{-1}, and $\Delta f = 1$ Hz. In order to improve the visibility, the number of particles were reduced to 10% of values given in Table 6.1.

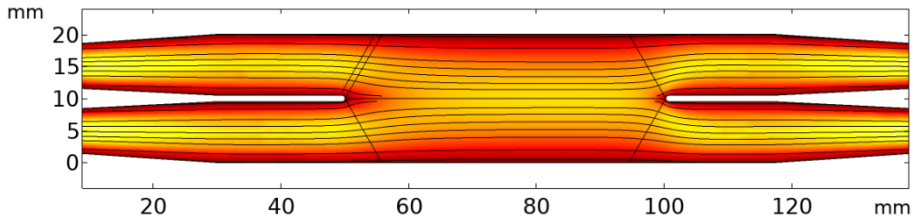

(a)

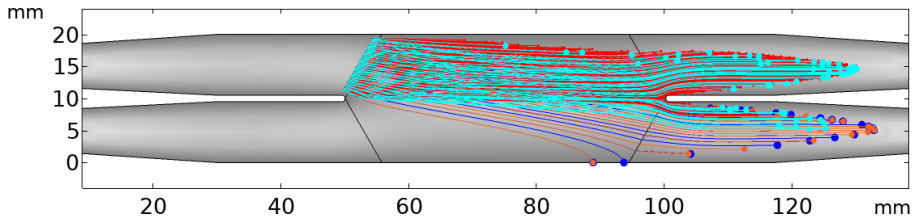

(b)

Figure 6.4 - (a) Steady state flow pattern for $\dot{V} = 1000\ \mathrm{mL\ h^{-1}}$. Flow direction is from left to right. (b) Particle trajectories for $\Delta f = 1$ Hz. Top transducer has a higher frequency than the bottom one.

Figure 6.4 indicates that the particles following the nodal movement have a downwards slope and are pushed towards the bottom outlet. All blue (largest) particles were able to follow the nodal pattern. Some orange particles (71 µm) were able to follow the movement whereas none of the small, cyan and red, particles could follow. Even though a particle cannot follow the nodal movement, it may still have a downwards motion, as a result of the flow and the acoustic radiation force.

Nevertheless, these particle trajectories have a smaller slope than the trajectories of particles that can follow the nodal movement. As a result, a small particle entering the acoustic field near the center of the prototype can still be pushed towards the bottom outlet. Thus, some cyan and red particles end up in the bottom outlet. Particle size distributions in terms of total particle volume were calculated and analyzed with MATLAB to calculate the $d90$ value. The analyses were based on the simulations using on the full number of particles given in Table 6.1.To evaluate the effect of flow rates (600, 800, 1000 mL h^{-1}) and frequency difference (1, 2, 3 Hz) on the $d90$ value, computer simulations were carried out for all combinations of flow rates and frequency differences. Figure 6.5 displays the $d90$ values for the top outlet for each combination.

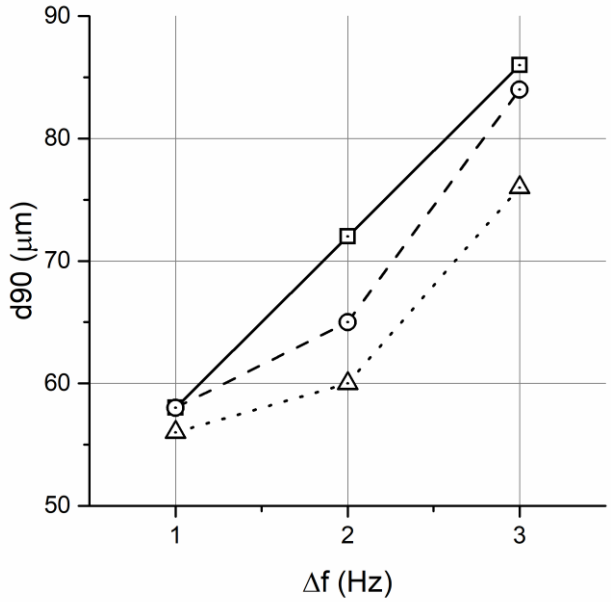

Figure 6.5 - The $d90$ values from computer simulations for the top outlet for the different combinations of flow rates and frequency differences. Squares connected by solid line correspond to $\dot{V} = 1000$ mL h^{-1}, circles connected by the dashed line correspond to $\dot{V} = 800$ mL h^{-1} and triangles connected by dotted line correspond to $\dot{V} = 600$ mL h^{-1}.

Figure 6.5 suggests that the higher the frequency difference, the higher the $d90$ values for each flow rate. The speed of the nodal movement increases linearly with the frequency difference. As a result, the drag force on a node-following particle increases with frequency difference, while the acoustic radiation force on the

particle is limited [6]. This effect increases the $d90$ value of the top outlet, as larger particles cannot follow the nodal movement and end up in the top outlet. In addition to this, simulations were carried out without an acoustic field and such simulations did not result in any separation, as all the particles exited from the top outlet.

In order to explore the possibility of density selective separation, a separate set of simulations was carried out with the same combination of flow rates and frequency differences. A total of 1000 particles with $d = 70\ \mu\mathrm{m}$ were released from the release location and each particle has a random density value in the range $1000 \pm 100\ \mathrm{kg\,m^{-3}}$. Of all the simulations, only the case with $\Delta f = 1\ \mathrm{Hz}$ and $\dot{V} = 1000\ \mathrm{mL\,h^{-1}}$ resulted in differences in density spectrums from the two outlets. All particles exited from the top outlet were heavier than $1031\ \mathrm{kg\,m^{-3}}$. In all other simulations, there was not a distinct cut-off density in both outlets.

6.3.3 Lab experiments

The simulations suggest that the particles can be size and/or density selectively separated by adjusting the frequency difference between the transducers. The geometrical arrangement of the transducers allows the generation of acoustic (quasi-)standing waves in the flow channel, with pressure nodes parallel to the flow direction. Figure 6.6 displays the particle trajectories during the experiments.

The pictures were taken immediately after the entrance, near the top inner wall, see also Figure 6.1. In the first 30 frames of Figure 6.6b, particles can still be seen following the nodal pattern, whereas the nodal lines lie parallel to the plane of symmetry of transducers. Larger particles in Figure 6.6b were captured by the dynamic acoustic field and were following the nodal movement. The non-captured particles still have a downward motion due to acoustic radiation forces, but with a less steep slope, as shown in Figure 6.6b. Therefore, smaller particles can possibly exit from the bottom side outlet.

Figure 6.7 illustrates the $d90$ values of the samples from the top side outlet.

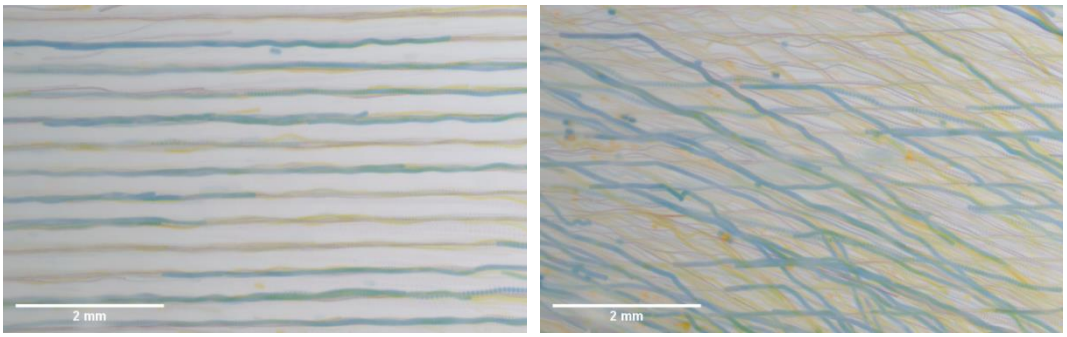

(a) (b)

Figure 6.6 - Particle trajectories recorded in the experiments. The flow is from left to right whereas the acoustic field is moving downwards. (a) when $\Delta f = 0$ Hz the particles are concentrated in the nodes of the standing wave. (b) when $\Delta f = 1$ Hz, the particles captured by the nodal movement go downwards on a straight line, whereas the non-captured particles still have vertical motion due to the acoustic radiation force. The frequency difference was introduced after 1 seconds, thus initially the particles were trapped in the stationary nodes, shown in Figure 6.6a. The images were created by overlaying 300 consecutive pictures taken in a span of 10 s.

Figure 6.7 confirms the dependency of the $d90$ values on the flow and excitation parameters, as suggested by the computer simulations. Similar to the computer simulations, the higher frequency difference or higher flow rate resulted in a higher $d90$ value. The effect of the frequency difference on the $d90$ value seems weaker in the experiments than in the simulations.

Also, the $d90$ values measured in the experiments are in general lower than those calculated in the simulations. This observation indicates that in the experiments the acoustic field was stronger than in the simulations. In the simulations, acoustic pressure from each transducer in the x-direction was set at 30 kPa. Particle motion in Figure 6.6b shows that the blue particles ($\mathrm{d} \cong 100$ µm) are captured by the nodal movement. Using the K number presented in [6], it can be estimated that the acoustic pressure in the system was locally greater than 39 kPa.

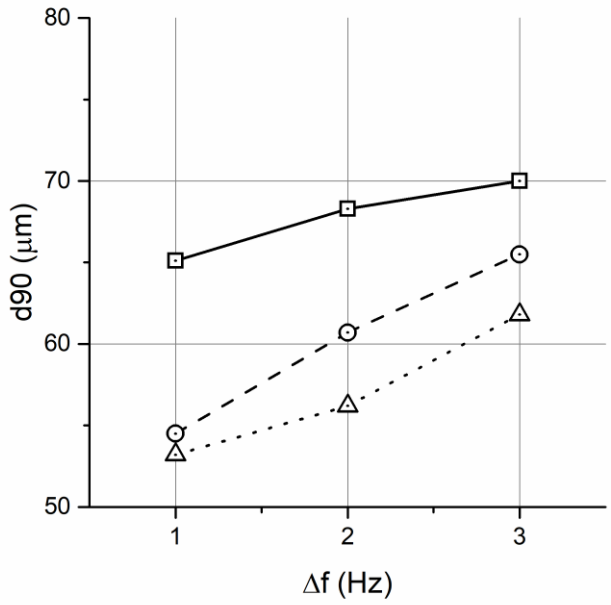

Figure 6.7 - The $d90$ values from lab experiments for the top outlet for the different combinations of flow rates and frequency differences. Squares connected by solid line correspond to $\dot{V} = 1000$ mL h^{-1}, circles connected by the dashed line correspond to $\dot{V} = 800$ mL h^{-1} and triangles connected by dotted line correspond to $\dot{V} = 600$ mL h^{-1}. Data points are averages of multiple measurements, with standard deviation less than 5%.

6.4 Conclusions

This study explored the selective particle separation on centimeter scale by dual frequency type dynamic field. Admittance measurements confirmed the non-resonant operation of the 3D-printed prototype. The selectivity was made possible by adjusting the frequency difference between two signals and the total flow rate in the separator. Lower frequency differences or lower flow rates resulted in lower $d90$ values from the top outlet of the separator. Computer simulations and lab experiments confirmed that the selectivity can be adjusted by the frequency difference and/or the total flow rate.

The 3D-printed prototype confirmed the ability of dual frequency type dynamic field for selective particle separation on centimeter scale in a continuous flow. The successful application opens up possibilities for future optimization studies of the separator.

(6.A) Acoustic radiation force in case of unequal amplitudes from each source

For a spherical particle with diameter much smaller than the wavelength of the acoustic wave field in the medium, the acoustic radiation force is given by [7, 8]

$$F_{ac} = -\frac{4}{3}\pi r^3 \nabla \left(\frac{1}{2}\chi_1 \frac{1}{\rho_0 c_0^2} \langle p_{in}^2 \rangle - \frac{3}{4}\chi_2 \rho_0 \langle v_{in}^2 \rangle \right) \tag{6.A1}$$

In Equation (6.A1) the terms $\chi_1 = \mathrm{Re}\left(1 - \frac{\rho_0 c_0^2}{\rho c^2}\right)$ and $\chi_2 = \mathrm{Re}\left(\frac{2\left(\frac{\rho}{\rho_0} - 1\right)}{2\frac{\rho}{\rho_0} + 1}\right)$ are the monopole and dipole scattering coefficients, respectively. The combination of these coefficients results in the so-called acoustic contrast factor. The terms p_{in} and v_{in} are the incident pressure and velocity fields at the location of particle. In order to use Equation (6.A1), the incident pressure need not to follow from a standing wave field. The expression is applicable to any plane wave field. For a traveling wave field the average force over one period will be zero. When two waves with different pressure amplitude and different frequency propagate against each other, the resulting wave field is expressed as

$$\begin{aligned} p(x, t, \delta_{P1}, \delta_{P2}) = {} & \delta_{P1} P_0 \cos\left(\omega_1 t - \frac{\omega_1}{c_0} x\right) \\ & + \delta_{P2} P_0 \cos\left(\omega_2 t + \frac{\omega_2}{c_0} x\right) \end{aligned} \tag{6.A2}$$

For a spherical particle in a plane wave field, the force becomes

$$\begin{aligned} & F_{ac}(x, t, \delta_{P1}, \delta_{P2}) \\ & = 2\pi r^3 \left(\frac{1}{3} \frac{1}{\rho_0 c_0^2} \chi_1 \, p(x, t, \delta_{P1}, \delta_{P2}) \frac{\partial}{\partial x} p(x, t, \delta_{P1}, \delta_{P2}) \right. \\ & \left. - \frac{1}{2} \rho_0 \chi_2 v(x, t, \delta_{P1}, \delta_{P2}) \frac{\partial}{\partial x} v(x, t, \delta_{P1}, \delta_{P2}) \right) \end{aligned} \tag{6.A3}$$

For a plane wave field, $p(x, t, \delta_{P1}, \delta_{P2}) = \rho_0 c_0 \, v(x, t, \delta_{P1}, \delta_{P2})$. Hence Eq. (A3) can be used to calculate the acoustic radiation force on a particle with the given pressure field. Numerical calculations suggest that, when $\delta_{P1}, \delta_{P2} \geq 0$ and $\delta_{P1} + \delta_{P2} = 2$, the acoustic force scales with the harmonic mean of δ_{P1} and δ_{P2}. The average acoustic radiation force acting on the particle over one period (T) can be defined by Equation (6.A4). Figure 6.A1 displays examples of a force distribution when the pressures from each source are unequal.

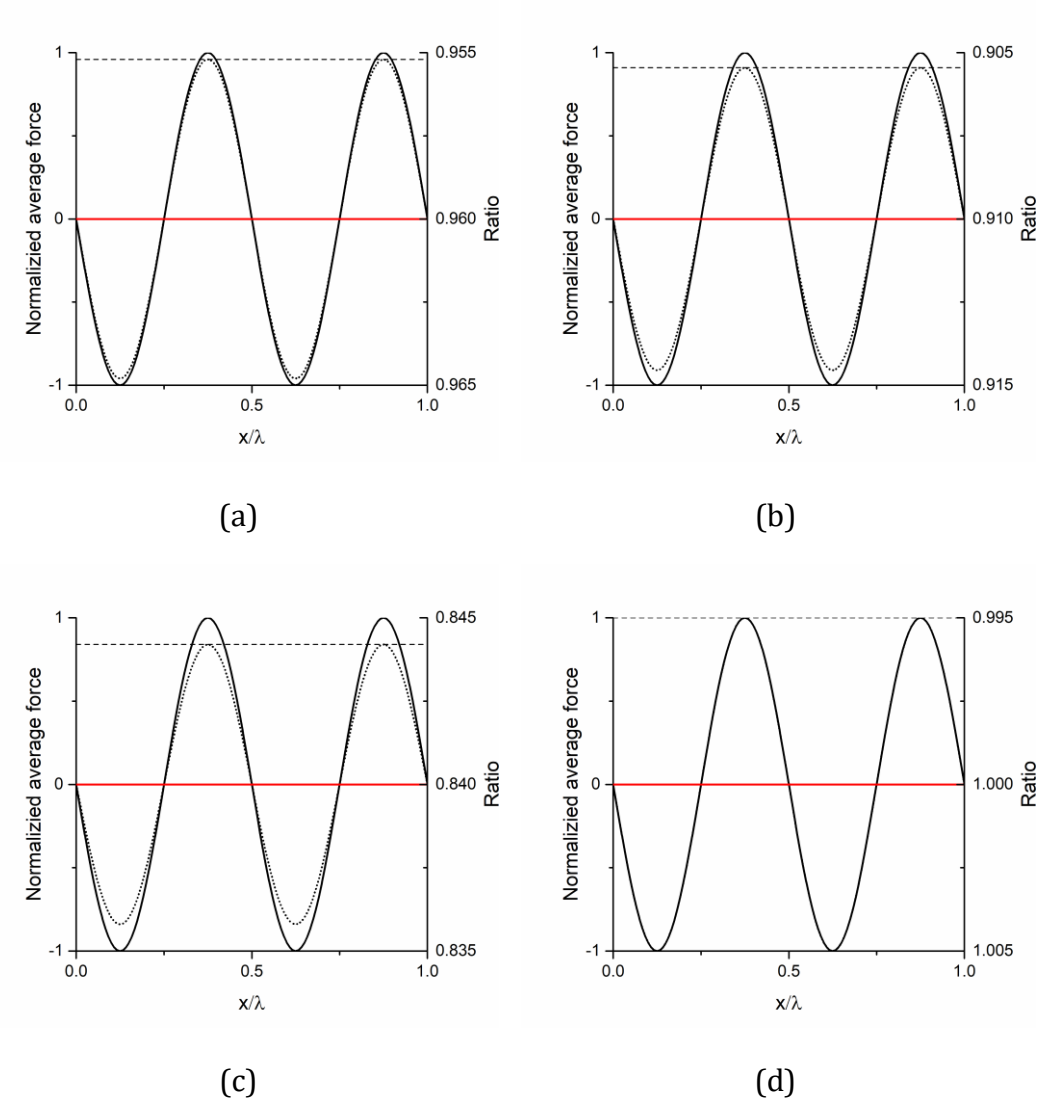

Figure 6.A1 - Two numerical examples when the pressure amplitudes are unequal. Black solid line represents the acoustic radiation force when the pressures are equal, and black dashed line represents the acoustic radiation force when the pressures are unequal. Force distributions are normalized by the maximum force given by the solid line. Red line represents the ratio of force of unequal pressures case to the force of equal pressures case. (a-c) solid line represents $\delta_{P1} = \delta_{P2} = 1$ and dotted line, maximum amplitude is represented by the dashed line, represents the case with (a) $\delta_{P1} = 0.8$ and $\delta_{P2} = 1.2$, thus $H = 0.96$, (b) $\delta_{P1} = 0.7$ and $\delta_{P2} = 1.3$, $H = 0.91$ (c) $\delta_{P1} = 0.6$ and $\delta_{P2} = 1.4$, $H = 0.84$ (d) solid line represents case when $P_D = 2\sqrt{H}\,P_0$ and dotted line (not visible due to overlap) represents the case with $\delta_{P1} = 1$ and $\delta_{P2} = 1$.

$$F_{av}(x, \delta_{P1}, \delta_{P2}) = \frac{1}{T} \int_0^T F_{ac}(x, t, \delta_{P1}, \delta_{P2}) dt \tag{6.A4}$$

Where $T = 1/f$ is the period of excitation.

Figure 6.A1 displays force distributions for several cases of unequal pressures. Numerical calculations suggested that the acoustic radiation force scales with the harmonic mean of the pressure multipliers δ_{P1} and δ_{P2}. A special case is also displayed in Figure 6.A1d. Solid line represents the force distribution when $p(x,t) = 2\sqrt{H}P_0 \cos\left(\frac{\omega}{c_0}x - \frac{\epsilon}{2}t\right)\cos\left(\frac{\epsilon}{2\,c_0}x - \omega t\right)$. Dashed line represents the force distribution when $\delta_{P1} \neq \delta_{P2} \neq 1$. The overlap of the two distributions and the ratio confirms that the acoustic radiation force on a particle scales with the harmonic mean of the individual pressure multipliers.

When the counter-propagating waves have different frequencies but equal amplitudes, the pressure distribution given in Equation (6.2) is an approximation which is only applicable when $\epsilon \ll \omega$. When the amplitudes are unequal the resulting pressure field cannot be simplified to such an expression. As a result, an analytical proof for the relation between the ratio of forces and the harmonic mean of the pressures is to the best of our knowledge not possible. The numerical calculations, however, confirm that when the two frequencies and amplitudes are not equal but similar enough, the resulting acoustic wave field acts as a quasi-standing wave field and able to manipulate the particles.

References

[1] Leong, T., Johansson, L., Juliano, P., McArthur, S.L., Manasseh, R., 2013. Ultrasonic Separation of Particulate Fluids in Small and Large Scale Systems: A Review. Industrial & Engineering Chemistry Research 52, 16555–16576. doi:10.1021/ie402295r

[2] Cappon, H.J., Stefanova, L.A., Keesman, K.J., 2013. Concentration based flow control in acoustic separation of suspensions. Separation and Purification Technology 103, 321–327. doi:10.1016/j.seppur.2012.10.033

[3] Sajeesh, P., Sen, A.K., 2014. Particle separation and sorting in microfluidic devices: a review. Microfluidics and Nanofluidics 17, 1–52. doi:10.1007/s10404-013-1291-9

[4] Dijkshoorn, J.P., Schutyser, M.A.I., Wagterveld, R.M., Schroën, C.G.P.H., Boom, R.M., 2017. A comparison of microfiltration and inertia-based microfluidics for large scale suspension separation. Separation and Purification Technology 173, 86–92. doi:10.1016/j.seppur.2016.09.018

[5] Dizge, N., Soydemir, G., Karagunduz, A., Keskinler, B., 2011. Influence of type and pore size of membranes on cross flow microfiltration of biological suspension. Journal of Membrane Science 366, 278–285. doi:10.1016/j.memsci.2010.10.010

[6] Kandemir, M.H., Beelen, M., Wagterveld, R.M., Yntema, D.R., Keesman, K.J., 2021. Dynamic acoustic fields for size selective particle separation on centimeter scale. Journal of Sound and Vibration 490, 115723. doi:10.1016/j.jsv.2020.115723.

[7] Gor'kov, L.P., 1962. On the Forces Acting on a Small Particle in an Acoustical Field in an Ideal Fluid. Soviet Physics Doklady 6, 773.

[8] Bruus, H., 2012. Acoustofluidics 7: The acoustic radiation force on small particles. Lab on a Chip 12, 1014–1021. doi:10.1039/C2LC21068A

[9] Gröschl, M., 1998. Ultrasonic Separation of Suspended Particles - Part I: Fundamentals. Acta Acustica united with Acustica 84, 432–447.

[10] Lenshof, A., Laurell, T., 2010. Continuous separation of cells and particles in microfluidic systems. Chemical Society Reviews 39, 1203–1217. doi:10.1039/B915999C.

[11] Kapishnikov, S., Kantsler, V., Steinberg, V., 2006. Continuous particle size separation and size sorting using ultrasound in a microchannel. Journal of Statistical Mechanics: Theory and Experiment 2006, P01012–P01012. doi:10.1088/1742-5468/2006/01/P01012

[12] Nam, J., Lim, H., Kim, C., Yoon Kang, J., Shin, S., 2012. Density-dependent separation of encapsulated cells in a microfluidic channel by using a standing surface acoustic wave. Biomicrofluidics 6, 024120. doi:10.1063/1.4718719

[13] Iv, C.W.S., Reyes, C.D., López, G.P., 2015. Microfluidic cell sorting: a review of the advances in the separation of cells from debulking to rare cell isolation. Lab on a Chip 15, 1230–1249. doi:10.1039/C4LC01246A

[14] Ding, X., Lin, S.-C.S., Kiraly, B., Yue, H., Li, S., Chiang, I.-K., Shi, J., Benkovic, S.J., Huang, T.J., 2012. On-chip manipulation of single microparticles, cells, and organisms using surface acoustic waves. Proceedings of the National Academy of Sciences of the United States of America 109, 11105–11109. doi:10.1073/pnas.1209288109.

[15] Shen, Y., Yalikun, Y., Tanaka, Y., 2019. Recent advances in microfluidic cell sorting systems. Sensors and Actuators B: Chemical 282, 268–281. doi:10.1016/j.snb.2018.11.025

[16] Xie, Y., Mao, Z., Bachman, H., Li, P., Zhang, P., Ren, L., Wu, M., Huang, T.J., 2020. Acoustic Cell Separation Based on Density and Mechanical Properties. Journal of Biomechanical Engineering 142. doi:10.1115/1.4046180.

[17] Lenshof, A., Evander, M., Laurell, T., Nilsson, J., 2012. Acoustofluidics 5: Building microfluidic acoustic resonators. Lab on a Chip 12, 684–695. doi:10.1039/C1LC20996E

[18] Hawkes, J.J., Radel, S., 2013. Acoustofluidics 22: Multi-wavelength resonators, applications and considerations. Lab on a Chip 13, 610–627. doi:10.1039/C2LC41206C.

[19] Setayeshgar, A., Lipsett, M.G., Koch, C.R., Nobes, D.S., 2015. Particle Motion in a Macroscale, Multiwavelength Acoustic Field. Journal of Fluids Engineering 137. doi:10.1115/1.4027777

[20] Benes, E., Groschl, M., Nowotny, H., Bohm, H., Radel, S., Hauser, C., Power, J., Lowe, K., Briarty, G., Davey, M., 2003. The Ultrasonic h-shape Separator: Harvesting of the Alga Spirulina Platensis under Zero-Gravity Conditions. Presented at the World Congress on Ultrasonics, pp. 1631–1638.

[21] Cappon, H., Keesman, K.J., 2013. Numerical modeling, calibration, and validation of an ultrasonic separator. IEEE Transactions on Ultrasonics, Ferroelectrics, and Frequency Control 60, 614–621. doi:10.1109/TUFFC.2013.2603.

[22] Kandemir, M.H., Wagterveld, R.M., Yntema, D.R., Keesman, K.J., 2019. Selective Particle Filtering in a Large Acoustophoretic Serpentine Channel. Scientific Reports 9, 7156. doi:10.1038/s41598-019-43711-8

[23] Drinkwater, B.W., 2016. Dynamic-field devices for the ultrasonic manipulation of microparticles. Lab on a Chip 16, 2360–2375. doi:10.1039/C6LC00502K

[24] Grinenko, A., Ong, C.K., Courtney, C.R.P., Wilcox, P.D., Drinkwater, B.W., 2012. Efficient counter-propagating wave acoustic micro-particle manipulation. Applied Physics Letters 101, 233501. doi:10.1063/1.4769092

[25] Skotis, G.D., Cumming, D.R.S., Roberts, J.N., Riehle, M.O., Bernassau, A.L., 2015. Dynamic acoustic field activated cell separation (DAFACS). Lab on a Chip 15, 802–810. doi:10.1039/C4LC01153H

[26] Simon, G., Andrade, M.A.B., Reboud, J., Marques-Hueso, J., Desmulliez, M.P.Y., Cooper, J.M., Riehle, M.O., Bernassau, A.L., 2017. Particle separation by phase modulated surface acoustic waves. Biomicrofluidics 11, 054115. doi:10.1063/1.5001998

[27] Simon, G., Pailhas, Y., Andrade, M.A.B., Reboud, J., Marques-Hueso, J., Desmulliez, M.P.Y., Cooper, J.M., Riehle, M.O., Bernassau, A.L., 2018. Particle separation in surface acoustic wave microfluidic devices using reprogrammable, pseudo-standing waves. Applied Physics Letters 113, 044101. doi:10.1063/1.5035261

[28] Meng, L., Cai, F., Zhang, Z., Niu, L., Jin, Q., Yan, F., Wu, J., Wang, Z., Zheng, H., 2011. Transportation of single cell and microbubbles by phase-shift introduced to standing leaky surface acoustic waves. Biomicrofluidics 5, 44104–4410410. doi:10.1063/1.3652872.

[29] Orloff, N.D., Dennis, J.R., Cecchini, M., Schonbrun, E., Rocas, E., Wang, Y., Novotny, D., Simmonds, R.W., Moreland, J., Takeuchi, I., Booth, J.C., 2011. Manipulating particle trajectories with phase-control in surface acoustic wave microfluidics. Biomicrofluidics 5, 44107–441079. doi:10.1063/1.3661129

[30] Courtney, C.R.P., Ong, C.-K., Drinkwater, B.W., Bernassau, A.L., Wilcox, P.D., Cumming, D.R.S., 2012. Manipulation of particles in two dimensions using phase controllable ultrasonic standing waves. Proceedings of the Royal Society A: Mathematical, Physical and Engineering Sciences 468, 337–360. doi:10.1098/rspa.2011.0269.

[31] Courtney, C.R.P., Ong, C.-K., Drinkwater, B.W., Wilcox, P.D., Demore, C., Cochran, S., Glynne-Jones, P., Hill, M., 2010. Manipulation of microparticles using phase-controllable ultrasonic standing waves. The Journal of the Acoustical Society of America 128, EL195–EL199. doi:10.1121/1.3479976

[32] Lee, J., Rhyou, C., Kang, B., Lee, H., 2017. Continuously phase-modulated standing surface acoustic waves for separation of particles and cells in microfluidic channels containing multiple pressure nodes. Journal of Physics D: Applied Physics 50, 165401. doi:10.1088/1361-6463/aa62d5

[33] Rhyou, C., Park, S., Lee, H., 2019. Optimal rate for continuous phase modulation in standing surface acoustic waves. Journal of Mechanical Science and Technology 33, 3819–3829. doi:10.1007/s12206-019-0725-z

[34] Whitworth, G., Grundy, M.A., Coakley, W.T., 1991. Transport and harvesting of suspended particles using modulated ultrasound. Ultrasonics 29, 439–444. doi:10.1016/0041-624X(91)90073-H

[35] Kozuka, T., 2003. Non-Contact Acoustic Manipulation using Crossing Ultrasound. Presented at the World Congress on Ultrasonics, pp. 483–486.

[36] Kozuka, T., Tuziuti, T., Mitome, H., Fukuda, T., Arai, F., 1998. Control of position of a particle using a standing wave field generated by crossing sound beams, in: 1998 IEEE Ultrasonics Symposium. Proceedings (Cat. No. 98CH36102). Presented at the 1998 IEEE Ultrasonics Symposium. Proceedings (Cat. No. 98CH36102), pp. 657–660 vol.1. doi:10.1109/ULTSYM.1998.762234

[37] Schindelin, J., Arganda-Carreras, I., Frise, E., Kaynig, V., Longair, M., Pietzsch, T., Preibisch, S., Rueden, C., Saalfeld, S., Schmid, B., Tinevez, J.-Y., White, D.J., Hartenstein, V., Eliceiri, K., Tomancak, P., Cardona, A., 2012. Fiji: an open-source platform for biological-image analysis. Nature Methods 9, 676–682. doi:10.1038/nmeth.2019

7 GENERAL DISCUSSION AND OUTLOOK

In terms of particle selectivity, acoustophoresis is a successful and versatile separation technique at microscale. The literature contains several examples of selective separation based on particle size and other properties [1-9]. The devices are often complex and expensive. Due to their size the flow rate is in the range of several hundreds of $\mu L\ h^{-1}$. Under such conditions, the application of microscale acoustophoresis is limited to very specific cases. For instance, in cases where the separation needs to be very precise and/or the separated material is very valuable [7-9]. In order to be applicable in industry, this technique needs to be able to treat larger volumes while keeping the ability to be selective and to be as precise as possible. This thesis follows a (chrono)logical path towards acoustophoresis on centimeter scale.

7.1 From microscale to centimeter scale: a review

Before any scale up attempt, the first research question addressed the need to understand the particle behavior under the effect of an acoustic field. The particle behavior in an acoustic field is numerously studied in the literature [10-12]. In Chapter 2, however, the physical model of the motion of a particle in a half-wavelength resonator is revisited and a linear equation of motion (EOM) was introduced. The linear model, represented by a linear, second-order differential equation, describes the particle behavior from the point of view of a linear single degree-of-freedom (SDOF) vibrating particle. This new analogy pointed out that the existing non-linear first-order differential equation model, in which the inertial term of the physical model was neglected, assumes the particle in a liquid to be an overdamped system. This assumption implies that the particle asymptotically converges to the pressure node (or antinode). The overdamped assumption can be confirmed by the linear model beforehand. Moreover, the linear model provides more insight about how the damping ratio relates to the excitation and particle parameters. Subsequently, the linear model was used to evaluate the possible consequences of scaling up microscale acoustophoresis.

The size of the microscale devices is determined by the excitation frequency. For a half-wavelength device operating with water, and a frequency of excitation (f) of $2\ MHz$, the channel width is approximately $375\ \mu m$. A typical application is given in Figure 7.1, where particles enter from a pre-defined position. The interplay between the acoustic force and drag force results in a distance between particles, and each size of particle is forced to pre-defined outlets [13]. In order to scale up

this concept to a channel width of $1\ \mathrm{cm}$, the excitation frequency must be lowered to approximately $75\ \mathrm{kHz}$. The results given in Chapter 2 suggest that lowering the frequency results in a higher damping ratio. A higher damping ratio means slower particle motion towards the pressure node. In order to lower the damping ratio, the pressure (P_0) can be increased. However, this brings the risk of acoustic cavitation. For example, assuming the excitation parameters as $f = 75\ \mathrm{kHz}$ and $P_0 = 100\ \mathrm{kPa}$ and the particle and medium parameters as given in Chapter 2, a particle with $r = 50\ \mu\mathrm{m}$ can be pushed from $x_0 = 4.56\ \mathrm{mm}$ to $x_f = 0.5\ \mathrm{mm}$ in $112\ \mathrm{s}$, whereas a particle with $r = 45\ \mu\mathrm{m}$ requires $138\ \mathrm{s}$. In both cases, the particles have damping ratios higher than 100. The difference in the transit times implies that with these parameters selective separation in a continuous flow might be possible. However, considering the channel width will be limited by the half-wavelength and assuming the same dimensions of the transducer ($50\ \mathrm{mm} \times 10\ \mathrm{mm} \times 1\ \mathrm{mm}$), it can be roughly estimated that the flow rate must be around $160\ \mathrm{mL\ h^{-1}}$. Furthermore, the smaller the particle size, the longer the transit time between the two positions; resulting in lower flow rates. Even though the channel dimensions are significantly increased, the increase failed to enable higher flow rates, and increased the likelihood of acoustic cavitation. Thus, it is concluded that a half wavelength separator is not a suitable option for acoustophoresis on centimeter scale.

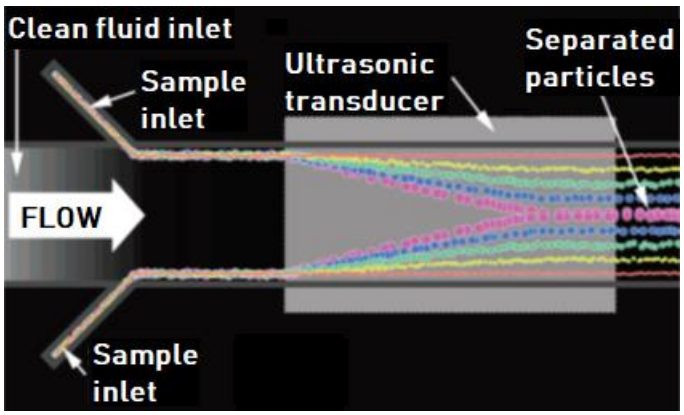

Figure 7.1 - Typical application of acoustophoresis on microscale in continuous flow. The excitation frequency is 2 MHz and the distance between the transducer and the reflector is 375 μm [13].

Another possibility for scaling up was to keep the excitation frequency at $2\ \mathrm{MHz}$ and obtain a multi-wavelength resonator. In water, a $1\ \mathrm{cm}$ wide resonator includes

more than 25 pressure nodes at 2 MHz . Figure 7.2 illustrates a case when the width of the resonator is 2 cm.

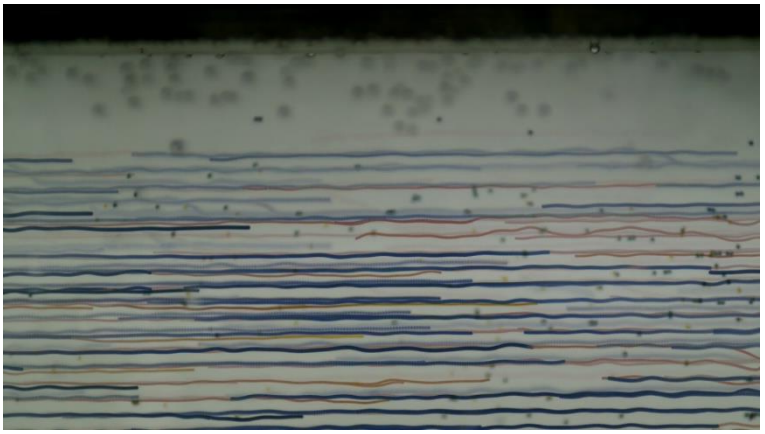

Figure 7.2 - Particle trajectories under an excitation frequency of 2 MHz and channel width of 2 cm. The particles were trapped in the pressure nodes and pushed with the flow. The horizontal lines correspond to the pressure nodes in the system. Distance between adjacent horizontal lines is 375 μm.

Figure 7.2 indicates that even though it may be possible to obtain a significant distance between the particles, removing them separately from the resonator part would be practically impossible. Microscale (also referred to as microfluidic) devices require precise manufacturing processes, where the pre-determined inlet for mixtures and outlets for different particles are precisely positioned. A 2 cm wide channel contains more than 50 pressure nodes, and building inlets and outlets for each pressure node would be extremely expensive for any application, even though it is theoretically possible. Furthermore, as the dimensions increase, imperfections in the standing waves arise, as seen in Figure 7.2. In an ideal acoustic field, the particle trajectories would be straight horizontal lines, whereas in this case imperfections in the field result in wavelets in particle trajectories. Considering the issues in manufacturing and precision, a multi-wavelength resonator is thus not directly applicable in continuous flow on centimeter scale. Even though it cannot be used as a straightforward scale-up idea for selective separation, multi-wavelength resonators are very useful for particle separation in large scale applications [14].

Large scale separators operate either in batch, perfusion or continuous mode [15]. Batch systems treat larger volumes at once, while significant amounts of time may be required for sample collection [16, 17]. Parallel operation of multiple batches,

however, may compensate for the downtime. A common use is, for instance, ultrasonically enhanced sedimentation devices [18] Alternatively, such systems can be operated in semi-continuous mode [19, 20]. In continuous flow, clever arrangement of the flow pattern enhances the interplay between the drag force and acoustic radiation force on the particle [14, 21, 22]. However, such devices have not explored the selectivity potential, their common aim was to separate and/or concentrate all the particles as good as possible. Table 7.1 summarizes these different methods.

Table 7.1 – Summary of notable large scale applications

Mode	Throughput	Range of particle size
Batch [16, 17]	Several L Batch	< 40 μm fat droplets
Perfusion [19, 20]	Several L day^{-1}	< 35 μm cells
Continuous [22]	58 L day^{-1}	< 500 μm straight cells
Continuous [21]	3.6 L h^{-1}	< 300 μm starch

In microscale, selective separation happens mostly by fractionation of the particles into two groups [5]. Such applications mainly take place in the application of cell separation from blood and due to the low amount of required sample volume, the size becomes an advantage rather than a drawback [5]. There are, however, few studies dealt with continuous particle size distributions and achieved selective separation [23-25]. Table 7.2 summarizes these studies.

Table 7.2 – Summary of notable size-selective applications

Mode	Throughput	Range of particle sizes
Continuous flow half λ [23]	2 mL h^{-1}	$2 - 60$ μm polystyrene spheres
Multi λ surface acoustic wave [24]	0.06 mL h^{-1}	$200 - 1000$ nmpolystyrene spheres
Continuous flow half λ (in air) [25]	70 L h^{-1}	$2 - 22$ μm glass spheres

The studies given in Table 7.2 all resulted in different particle size distributions as a result of different excitation combinations. However, except for reference [25], they are all in micrometer size range and show low throughput.

In all cases, selectivity of acoustophoresis arises due to the interplay between the drag force and acoustic radiation force. Instead of standing acoustic wave fields dynamic acoustic fields can be used, as well [26]. Main advantages of dynamic acoustic fields are deemed to be the configurability and non-resonant operation [27]. Chapter 3 demonstrates size selective separation by using a multi-wavelength acoustic standing wave field in combination with a defined flow profile. Chapters 4-6 evaluate and demonstrate dynamic acoustic fields for selective particle separation in centimeter scale. Prototypes demonstrated in the corresponding Chapters can selectively separate polyethylene particles between $20 - 120\ \mu\mathrm{m}$ with flow rates up to $1\ \mathrm{L\ h^{-1}}$. In addition, in Chapters 3 and 5, wheat beer with yeast particles up to $20\ \mu\mathrm{m}$ was filtered with flow rates up to $100\ \mathrm{mL\ h^{-1}}$.

Main challenges faced among the path towards selective separation on centimeter scale are listed below, and are addressed in the following section:

- Challenges in representing the particle behavior with a linear model
- Validity of the assumption of ideal 1D plane wave field
- Presence and significance of reflections, and their effects on the selective particle capturing
- Validity of modelling the prototypes in 2D during simulations and completeness of the models
- Challenges in representation of the particle mixture in the computer models and comparison between simulations and experiments in terms of separation performance
- Minimizing the deviations during manufacturing of prototypes and eliminating the disturbances in the system during the experiments such as leakage, pulsation and overheating

7.2 From microscale to centimeter scale: challenges

7.2.1 Theoretical issues

Theoretical predictions and computer simulations were crucial to provide fundamental understanding of the concepts and experiments. The linear SDOF model introduced in Chapter 2 resulted in valuable insights, especially with respect to the damping ratio. However, it was initially unable to correctly predict the particle trajectory and transition time. The damping ratio, as a function of, for instance, pressure and frequency, predicts whether a particle shows oscillatory behavior. Some cases resulting in oscillatory behavior, such as at high pressure and high frequency, were impractical. The particle trajectory predicted by the linear model did not match the numerical solution of the EOM and the transition time was within $\pm 6\%$ of those predicted by the numerical solution and the non-linear first-order model. The nonlinearity of the equation of motion was due to the sinusoidal force profile. Hence, a linear approximation of the profile between two points is, in general, inappropriate. Consequently, the difference in force profiles resulted in very different particle trajectories, especially at the beginning of the motion. As a solution to this a stepwise application of the linear model was introduced. Solving the particle trajectory in 25 linearization steps was enough to properly approximate the sinusoidal force profile and, compared to the non-linear first-order model, the results were closer to the numerical solution. Even though the stepwise application yielded better results, it also leads to higher computational load. Depending on the aim of the users, the extra efforts may not be worthwhile. However, the SDOF model can still be used for predicting oscillatory behavior without conducting any simulation and for double-check purposes.

Computer simulations were a fundamental part of this research in all steps. Mathcad 14 was used especially in Chapter 2 to do symbolic calculations and relatively fast solutions of ODEs. MATLAB r2018b was used to numerically solve more complicated cases. To simulate the prototypes in 2D, COMSOL Multiphysics (versions 5.4 and 5.5) were used. The computer simulations utilized an idealized representation of the prototypes. The pressure field in the prototype of Chapter 3 was calculated by including the piezoelectric transducer in the computer model. The mechanical response of the transducer was generating the pressure field in the prototype, and all solutions were carried out in frequency domain. For this purpose, material properties of the piezoelectric transducer were taken from the manufacturer's website and from [16]. The resulting pressure field was depending on the frequency of excitation, due to dynamics of both the transducer and the

inside material. However, due to reflections in the prototype the pressure field was not a perfect plane wave field. These reflections resulted in wavy particle trajectories in both simulations and experiments.

Nevertheless, in the theoretical analyses, the pressure field was always assumed to be an ideal 1-D plane wave field. For the analysis of dynamic acoustic fields such an assumption was necessary to derive the pressure field as a function of time and position. Thus, in order to get full information a time-dependent study was the only option. However, even when using the most simplified models such solutions were extremely cumbersome and time consuming, hence practically impossible. As a result, the pressure fields in these prototypes were not calculated, they were assumed as given *a priori*. Such assumptions ignored any imperfections in the acoustic field. The assumed ideal acoustic fields were only valid in certain regions of the prototype, but in reality due to dispersion and reflections the particles must be experiencing acoustic forces outside the immediate area between the sources (or the source and the transducer), albeit weaker.

The results in Chapter 4 show that even though there are reflections from each transducer, selective particle capturing is possible. At $2\ \mathrm{MHz}$ and underwater, it is practically impossible to measure the reflection coefficient of a material reliably. Thus, a reflection coefficient had to be assumed. A deeper investigation of particle behavior in such fields, however, may lead to reliable estimations of the pressure field.

Throughout the research all the simulations were done in 2D. For the flow solutions the depth of the prototype was taken into account in order to calculate the average flow velocities. The acoustic fields were assumed not to change in the depth direction. For the simulations done in COMSOL Multiphysics, the mesh size for every simulation and material was chosen such that at the frequency of interest, there are at least 12 elements per wavelength in the corresponding material. Considering the size and multi-wavelength nature of the prototypes, the computational load was already high for 2D simulations. Introducing the third dimension, even with applying all possible symmetries to reduce the model, made finding approximate solutions practically impossible. For the flow, however, some 3D simulations were carried out to verify the reliability of 2D simulations. As a result, it was concluded that 2D simulations were providing a good enough representation of the system.

In the simulations of Chapters 5 and 6, the particle sizes were randomized. This provided a continuous size distribution in the range of $20 - 120\ \mu\mathrm{m}$. The particle size distribution was generated in COMSOL Multiphysics, and in each simulation was exactly the same. In order to compare the effects of different parameters, like flow rate, such similarity was very useful and enabled an objective evaluation of parameters. In the lab experiments, however, different particle size distributions were found, as every sample had a slightly different distribution. Nevertheless, the particle sizes in the simulations were considered representative enough of the experimental mixtures.

In the simulations other forces than the acoustic radiation force, such as gravity and lift force, were also introduced to examine their effects. The simulation results were compared based on the threshold and $d90$ metrics. For these metrics the additional forces did not result in any difference. As a result, those forces were subsequently neglected in order to reduce computational load. Also, particle-particle interactions and secondary acoustic radiation force effects were ignored in the simulations. Under this assumption, all particles were independent of each other. Consequently, it was possible to release them to the system at the same time and thus shortening the simulation times.

7.2.2 Practical issues

The prototypes used throughout this research were 3D printed from polylactic acid (PLA). This technology enabled relatively fast implementations of new ideas. All prototypes were printed using a nozzle diameter of $0.4\ \mathrm{mm}$. The printer specifications resulted in some limitations in design. For example, a wall in the prototype had to be thicker than the nozzle diameter.

In order to obtain a steady and continuous flow, syringe pumps were used. In the experiments of Chapter 3, only one syringe was pumping the mixture from the inlet. In the experiments of Chapter 4, two syringe pumps were used. However, it was found that, unless the exit flow rates were also regulated, the flow rates were mostly pulsating and not equal. The aim of Chapter 4 was to investigate the particle behavior and determine when it can and cannot follow the dynamic acoustic field. Particle velocity measurements indicated that the pulsating flows were not detrimental. For more advanced separator prototypes as used in Chapter 5 and 6, however, two more syringe pumps were used at the exits, in order to make sure that the flow is steady and constant all the time. In the prototypes, the entrances were made smooth so that the flow did not result in any turbulence. As the size

increases, avoiding turbulence and unsteady effects is crucial in multi wavelength resonators [14]. Turbulence and unsteady effects may arise due to irregularities in flow, bubbles in the system, leakage or dead volumes in the system. During the experiments, the condition of the flow was carefully assessed by injecting dyes to the flow. Separation experiments were carried out after the flow was steady and laminar. Even though it was carefully controlled, there may be still some unseen issues regarding the flow. The serpentine prototype of Chapter 3 was simple in terms of flow, with only one inlet and one outlet, and showed the least problems. The X-shaped separator for frequency sweep, introduced in Chapters 4 and 5 required careful installation of the connections to the syringes, so that bubbles were avoided. The prototype of Chapter 6 is the most complicated one, as it also includes a cooling liquid volume. Isolation of the main separator compartment and cooling liquid compartments is a necessity in order to have a steady flow, possibly due to convection effects.

The 3D printed prototypes had some inherent problems due to the nature of the manufacturing. In order to have holes in the system, for connections of cables and pipes, support material had to be used. The layer-by-layer construction sometimes caused leakages. Water was sometimes able to pass through the layers. This problem was minimized when the prototype was printed with $100\ \%$ infill. Pipes were attached to the prototype with superglue, and the remaining gaps were filled with silicone after the cables were installed. The prototypes were closed with PMMA covers, with rubber rings filling the gap between the PLA blocks and the covers. In some prototypes, there was still some dead volume between the cover and the main block. In prototype of Chapter 6, for instance, silicone layers were applied between the polyurethane sheets and the PMMA cover in order to separate the cooling liquid volumes. In all the prototypes, leakage was a recurrent problem, but after careful installation of all the parts it was possible to avoid leakage. After initializing the flow without leakage, bubbles and pulsation, the flow was steady for long enough time to take samples from the prototypes. The prototypes were initially filled with demineralized water and samples were taken from the syringes in the corresponding exits.

Before starting the separation experiments, the frequency response of the transducers were checked using an HP 4194 A impedance analyzer. Any reflections from the PLA walls and PMMA covers were ignored, as the effect of reflections was found to only slightly disturb the acoustic standing wave fields. In Chapter 4 it was concluded that even though reflections are present, selective particle trapping is

still possible. The results of the lab experiments confirmed that the reflections disturb the acoustic field, but without much affecting the selectivity.

While the transducers pump acoustic energy into the system, overheating issues were observed during the experiments. When the flow rate is high enough and there were no dead volumes in the prototype, the heat generated by the transducers was being dissipated by the flow. At the end of the wheat beer experiment in Chapter 3 for the lowest flow rate the inner walls of the prototype started to melt. Until that point, no overheating issue was observed. In the lab experiments of Chapter 6, cooling liquid was circulated between each experiment in order to avoid overheating. In addition, observations with a thermal camera on the prototype presented in Chapter 5 yielded no overheating issues.

In Chapters 5 and 6, the mechanical response of the transducer was measured using a Polytec OFV 5000 Laser Doppler vibrometer. The measurements were taken from a special stand outside the prototype, where the laser beam could hit the transducer surface perpendicularly. This configuration ensured that the signal quality was as good as possible. Measurements without normal incidence, with any angle of inclination, did not yield reliable results. Consequently, it was not possible to measure the mechanical response of the transducer inside the prototype.

During the work of Chapters 3 and 5, the particle size analyzer at Wetsus was DIPA 2000. In August 2020, the machine was replaced by Mastersizer 3000. It was not possible to compare the results between these two machines, though with calibration mixtures both machines provided reliable and repeatable results. Mastersizer 3000, however, provides the $d90$ value of the mixture as an output. Hence, an appropriate comparison between the prototypes should utilize $d90$ values. However, unlike the threshold, $d90$ is a relative metric, and depends on the distribution in the sample. The selectivity of the methods was demonstrated for size selective separation, as it is a relatively straightforward measurement supported by the current equipment. Nevertheless, the methods are in theory equally applicable to other means of selectivity, such as density.

In order to avoid particle agglomeration, surfactants were used in each mixture. Too much surfactant causes the mixture to foam and may change the viscosity. The concentrations in the mixtures did not reveal any issue of foaming or viscosity change. Rarely, particle agglomerates were observed and sometimes particles were sticking to the PLA walls. Before each experiment, the prototype was rinsed

thoroughly so that the agglomerates from the previous experiment did not affect the next experiment.

7.2.2.1 Energy consumption

Throughout this research the focus was on finding and exploring the selective separation possibilities of the resonator rather than reducing the energy consumption. The transducers were driven by a custom-made amplifier and a DC power supply unit was providing energy to the amplifier. Based on the readings on the DC power supply unit, the energy consumption by the amplifier was $10\ \mathrm{W}$ throughout all experiments. However, due to losses in the amplifier, this is not the power supplied to the transducers. Based on the admittance measurements of the transducers, the energy supplied to one transducer can be estimated. In the prototypes, the average admittance of the transducers in the excitation ranges was roughly $60\ \mathrm{mS}$. When the transducer was driven with $20\ \mathrm{V_{PP}}$, the energy consumed by one transducer was roughly estimated as $3\ \mathrm{W_{RMS}}$. Considering the 3D printed prototypes, the custom made amplifier and no optimization study was carried out, it is well possible that similar selective separation performance can be reached with less power input.

Furthermore, in addition to the prototype, amplifier and DC power supply unit, the set-up also consisted of a signal generator, an oscilloscope and four syringe pumps. A simpler set-up, optimized towards a specific application, can be designed such that less energy is consumed.

7.3 Areas of application

This research focused on developing selective separation methods rather than targeting one particular application. The prototypes introduced in this research were able to separate particles from approximately $50 - 80\ \mu\mathrm{m}$ with a total throughput up to $1\ \mathrm{L\ h^{-1}}$. Furthermore, in order to verify the methods, model polyethylene particles with well-known properties were used in experiments. The possibility of treating biological material was also demonstrated. Theoretically, as long as particles are in suspension or emulsion, the proposed designs and way of operation are applicable to other cases.

Especially on microscale, acoustophoresis is utilized as a method for cell separation in mostly lab-on-a-chip applications [1]. Multi-wavelength resonators are mostly used as enhanced sedimentation devices [14]. In each case, there are very few ultrasonic resonators that can be compared to the prototypes introduced in this research [14, 21-27].

As long as a particle is acoustically different from the surrounding medium, meaning that it has a non-zero acoustic contrast factor, it experiences an acoustic radiation force. This property indicates that the methods can be used in combination with other methods. One example is a combination with centrifuging. In that case, naturally buoyant particles can be removed from suspensions before or after the centrifuge. Another possibility is pre-treatment of process streams using physical filters, such as membranes. Pre-filtering of large particles would help tackling the fouling problem in membrane applications.

In Section 7.4.5 some calculations on fibers in an acoustic field are presented. Starting from such simulations and preliminary experiments, applications towards microfiber removal and recovery can be developed [28].

Finally, the methods presented in this study can also be applied to enhance crystallization and control the size of the agglomerates. The concept of size selective particle removal can be applied to size selective crystal harvesting. In this type of application, the particles are concentrated at pressure nodes (or antinodes) and thus, agglomerates are formed faster. Under continuous flow and inside the serpentine separator, when the agglomerate gets large enough, they are captured by the acoustic field. If the agglomerate grows to a size comparable to the wavelength, it cannot be trapped by the acoustic field anymore and may start to settle and may even be reduced in size due to the acoustic field. Hence, the serpentine prototype of Chapter 3 can be used to accelerate a crystallization process and control the crystal size through acoustic radiation and drag forces. Similarly, under a dynamic field, if the agglomerate gets big enough (which would be the threshold size), it starts to follow the acoustic field movement and can be removed from the reactor. For such a purpose, the dual-frequency method would be more useful than the frequency sweep method, as the acoustic field movement is more uniform and due to the non-resonant nature of the dynamic field, the field is less affected by temperature changes [27].

7.4 Explorative studies

This section contains supplementary material related the methods proposed and tested in this thesis, but not well-developed enough to be put in the corresponding chapters. This material can, still, provide a basis for future studies on this topic.

7.4.1 Linear model with oscillatory behavior

In Chapter 2, the linearized or simply linear model was used to model the particle behavior when the corresponding SDOF system was overdamped. In the one- and multi-step approach, the acoustic radiation force was linearized in a region of interest (ROI), defined by the starting position of the particle and target position of the particle. The equilibrium position, $x = 0$, was taken at the pressure node, and the boundaries of the ROI had positive values. When the corresponding system is underdamped, however, the particle will oscillate around the pressure node before coming to equilibrium. Therefore, defining the ROI by using the initial and target positions does not work in this case. Furthermore, at each spatial step a transition time was calculated and used to estimate the particle velocity for the next step. For an underdamped system, however, the transition time cannot be calculated analytically. As a result, the solution methodology in Chapter 2 was not applicable to an underdamped system using the spatial multi-step approach.

A different approach, however, is still possible by modeling the particle as a linear time invariant (LTI) system [28] and linearizing the acoustic radiation force at each time step instead of each spatial step. Using the parameters as given in Chapter 2, and for a particle radius of $r = 50\ \mu\mathrm{m}$, Figure 7.3 illustrates sample solutions using this approach. The particle path is solved between $t = 0$ and $\mathrm{t} = 0.01\ \mathrm{s}$.

Figure 7.3 indicates that such an approach becomes close to the numerical solution as the time steps get smaller. Whilst the numerical solution solves the full EOM at each time step, the LTI approach solution solves the linearized EOM at each time step, making the methodology very similar to the numerical solution. In addition, the corresponding SDOF system parameters, such as natural frequency and damping ratio, can be calculated at each time step.

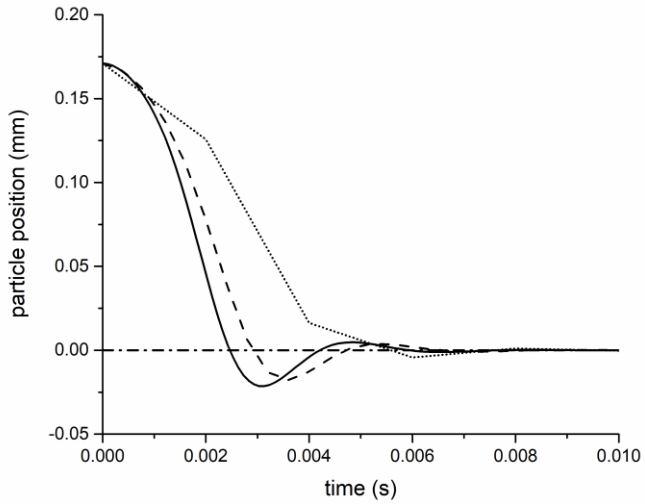

Figure 7.3 - Particle trajectories calculated by numerical solution (solid line), 5-step solution (dotted line) and 25-step solution (dashed line). The equilibrium position is indicated by the dash-dot line.

7.4.2 Backwards frequency sweep

The frequency sweep type dynamic acoustic field was introduced in Chapter 3 and demonstrated in Chapter 4. In these chapters, the frequency was periodically ramped from a starting frequency, f_0, until an end frequency, f_2, where $f_2 > f_0$. As a result, the number of nodes were increasing as the frequency of excitation increases. The nodal movement was from transducer side towards reflector side, and it was slowing down in time, as the frequency increases, and in space, as the nodes get closer to the transducer. An alternative application would be sweeping the frequency in the opposite direction, meaning $f_0 > f_2$. An example solution is illustrated in Figure 7.4. The total flow rate is $1\ \mathrm{L\ h^{-1}}$ with equal flow rates from each inlet and outlet, so that the particle motion is affected only by the acoustic field. The particle properties are the same as in Chapter 4.

In the example, shown in Figure 7.4, almost all particles have an upwards motion at the beginning of the channel. Even though all particles move towards the transducer, only the largest particles are able to follow the nodal movement. The increase in the nodal speed can be observed from the trajectories of four blue particles, whose trajectories ended in the transducer surface at $20\ \mathrm{mm}$. Still, some

small (cyan) particles exit through the top channel. Another interesting particle behavior occurs at the very bottom. A cyan (56 μm) and a red (36 μm) particle starts very close to the reflector, where the nodal movement is very slow. After one sweep period, they are not displaced enough to move to the next node. As a result, they end up oscillating around the same position near the reflector.

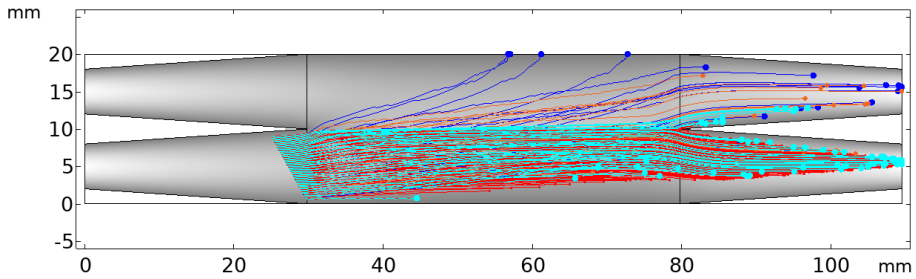

Figure 7.4 - Particle trajectories (36 (red), 56 (cyan), 70 (orange) and 100 (blue) μm) in backwards frequency sweep with $f_0 = 2.4$ MHz, $f_2 = 1.9$ MHz, $P_0 = 55$ kPa and $T = 5$ s. Flow direction is from left to right. Transducer is placed on the top and the reflector is at the bottom.

An interesting application of this method can be as follows: if all particles with different sizes start at the same location next to the reflector, they can be ordered based on their size. As the nodal velocity gets faster, smaller particles cannot follow the anymore. Eventually, largest particle will be displaced farthest.

7.4.3 Acoustic pressure as a function of frequency in frequency sweep

In Chapter 4, Laser Doppler vibrometer (LDV) measurements for the transducer were shown. The measurements indicated that the surface velocity of the transducer is not constant within the sweep period, it is rather a function of frequency. Considering the transducer has its own dynamics, this is a very reasonable result. During the design of experiments study, however, a common constant pressure for every sweep period was assumed. This value was the average of the pressures in 3 s, 5 s and 7 s sweep periods. The average pressures are 58 kPa, 57 kPa and 49 kPa for 3 s, 5 s and 7 s of sweep periods, respectively. Consequently, in all sweep periods an average pressure amplitude of 55 kPa was assumed. Without such an assumption, the effects of sweep period and acoustic pressure would be intertwined in the simulations. Figure 7.5 illustrates the pressure calculations based on the LDV measurements as a function of frequency, for each sweep period.

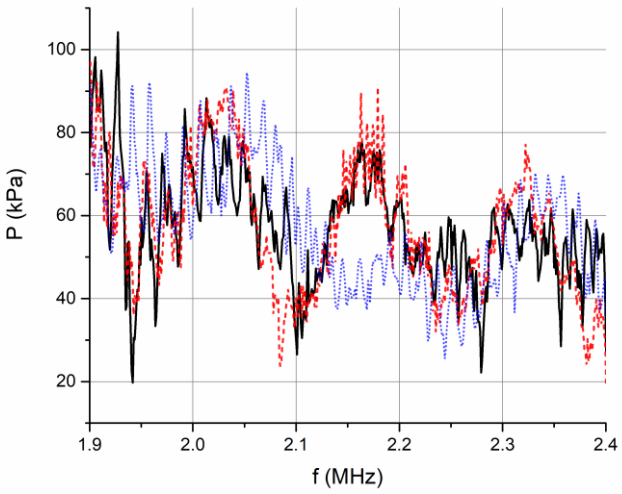

Figure 7.5 - Pressure calculations as a function of frequency. Black solid line, red dashed line and blue dotted line represent the calculations for 3 s, 5 s and 7 s sweep periods, respectively.

A design of experiments (DOE) study was carried out by using the pressure values calculated and the results are presented in Figure 7.6. All other parameters were kept the same.

Figure 7.6 indicates that, the lower pressure in 7 s sweep period possibly affects the results, by yielding higher metrics in all cases contrary to the linear downwards trends shown in Chapter 4. Nevertheless, the main conclusion of the DOE study remains the same.

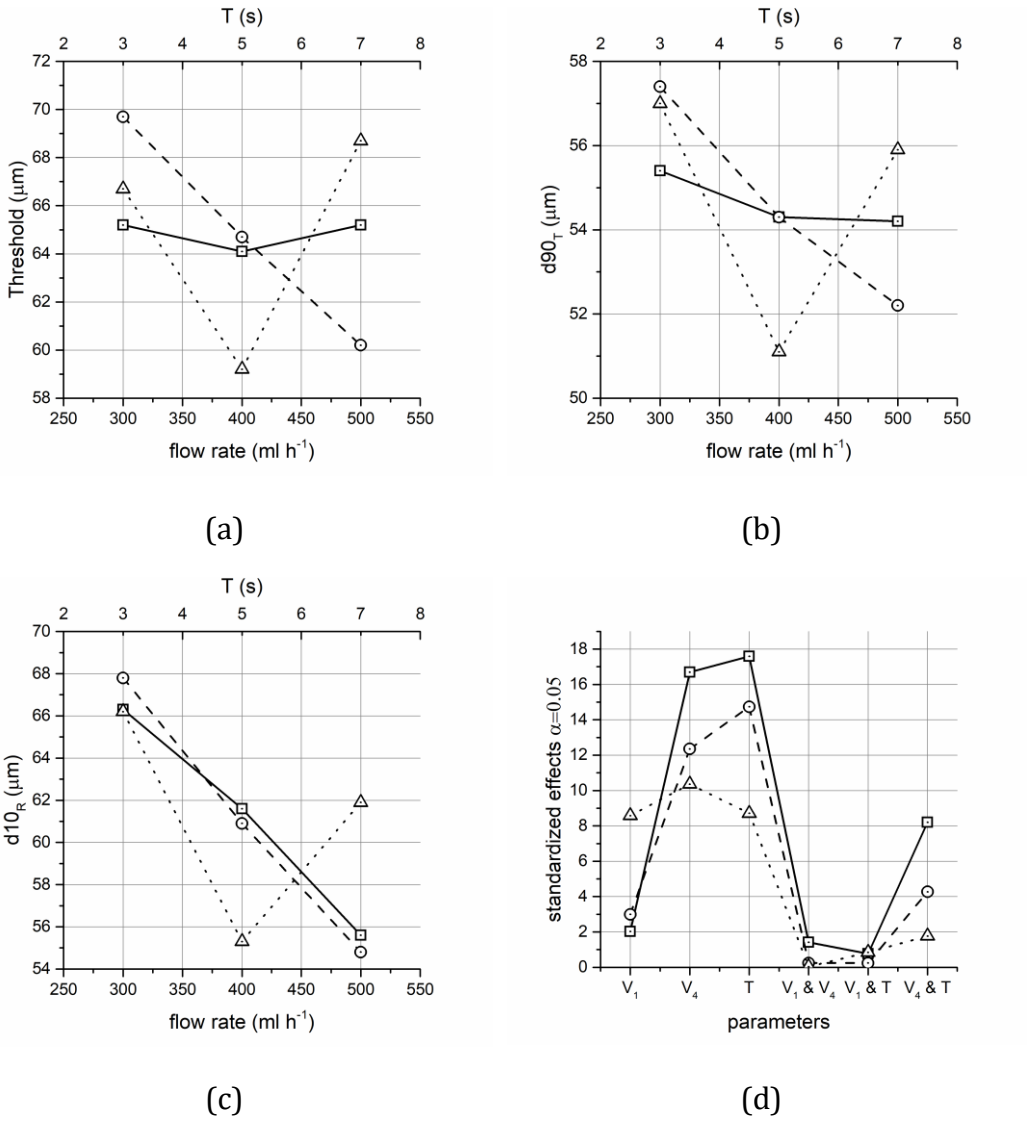

Figure 7.6 - Effects of the flow parameters $\dot{V}_1$ (squares, black line), $\dot{V}_4$ (circles, dashed line), T (triangles, dotted line), after averaging the effect of the other factors, on the threshold (a), $d90_T$ (b) and $d10_R$ (c). Bottom-right panel (d) shows the standardized effects chart based on all 27 simulations, horizontal red line illustrates the level of significance for confidence level of 95% for threshold (squares, black line), $d90_T$ (circles, dashed line), and $d10_R$ (triangles, dotted line).

7.4.4 Periodic two-way application of dual frequency

The fundamental goal of selective particle separation is to put enough distance between different types of particles so that they can be guided to different exits. The dual frequency method can be applied in a way that enhances the distance between particles. First, all particles are pushed in one direction, so that the particle group is squeezed. This requires a higher pressure so that smaller particles are captured as well. Subsequently, particles are selectively pushed in the opposite direction so that distance between particles is increased. Recurrent application of this method can be used to enhance the separation capability. An example is given in Figure 7.7.

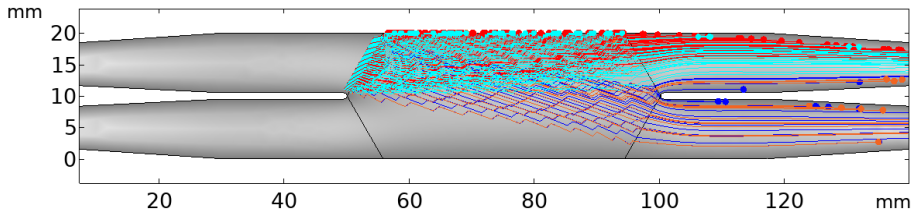

(a)

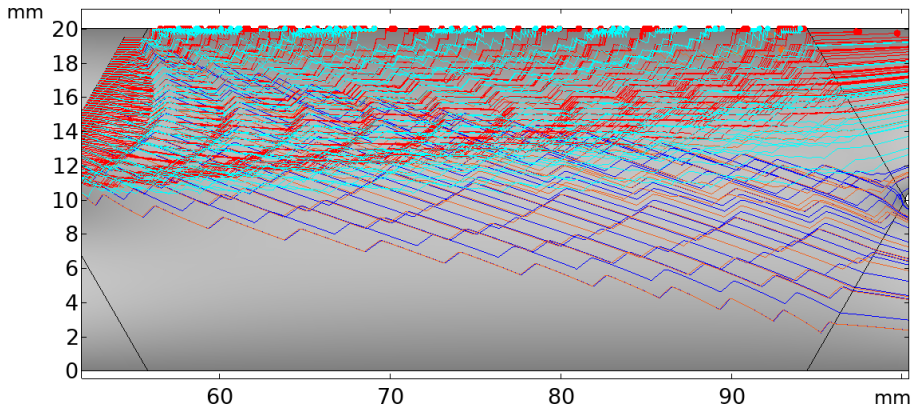

(b)

Figure 7.7 - An example simulation for a two-way application of dual-frequency type acoustic field. The period of application is 10 s. For 8 s the field goes down with Δf = 2 Hz and P_D = 40 kPa. In the next 2 s the field goes up with Δf = -4 Hz and P_D = 200 kPa. Particle properties are the same as in Chapters 5 and 6. Bottom panel provides a zoomed in view. The reflection coefficient R = 0.

In Figure 7.7, when the field goes downwards, the particles were selectively pushed down, in $80\ \%$ of the cycle. In the remaining 20% of the cycle, all particles were pushed up with a higher speed and higher acoustic pressure. As a result, some red ($36\ \mu m$) and cyan ($56\ \mu m$) particles ended up directly at the top edge. All red and cyan particles are forced to the top exit, whereas the majority of orange (19 out of 22) and blue (16 out of 20) particles (larger sizes) is forced to the bottom exit. When run with the full number of particles given in Chapters 5 and 6, The $d90$ value from the top exit for this numerical experiment is equal to $105\ \mu m$ due value from mainly to non-selective pushing of the particles towards the top exit. The $d10$ value from the bottom exit was $79\ \mu m$. Consequently, similar to the application in Chapter 5 with unequal flow rates, this two-way application of dual frequency method can be explored in order to enhance the selectivity capabilities, for this method makes the reactor virtually larger. On the other hand, as the particles are all pushed to one side, the particle-particle interactions may become significant.

7.4.5 Modelling fibers in acoustic field

The simulations and experiments during this research were based on spherical particles. In the literature, behavior of spherical particles in acoustic field is well known. Taking the spherical particles as the starting point, a fiber structure in an acoustic field was modelled as five interconnected spherical particles. Figure 7.8 illustrates the 5-sphere fiber model.

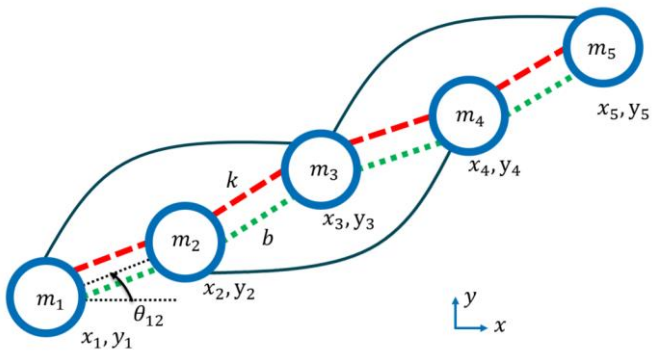

Figure 7.8 - 5-sphere fiber model. Each sphere is connected to the adjacent two spheres by spring and damper elements.

The EOM of the fiber can be expressed as 10 coupled ODEs, where each sphere can move in two directions. The angle and distance between adjacent spheres is given

as $\theta_{ij} = arctan2\left(y_j - y_i, x_j - x_i\right)$ and $s_{ij} = \sqrt{\left(y_j - y_i\right)^2 + \left(x_j - x_i\right)^2}$, respectively. Here, the use of 2-argument arctan function is necessary in order to correctly calculate the angle. Equation (7.1) presents the equations in matrix form.

$$\begin{aligned}[M]\{\ddot{x}\} + [C^x][\dot{x}] + [K^x][x] = [F^x] \\ [M]\{\ddot{y}\} + [C^y][\dot{y}] + [K^y][y] = [F^y]\end{aligned} \tag{7.1}$$

In Equation (7.1), $[M]$, $[C]$ and $[K]$ are the 5×5 mass, damping and stiffness matrices, respectively. Assuming the flow is in x direction and the acoustic force is acting on y direction, the external forces are the acoustic and drag forces on each particle, given by

$$\begin{aligned}F_i^x = C_{d,i}(u_x(y_i) - \dot{x}_i) \\ F_i^y = F_i^{AC} - C_{d,i}\dot{y}_i\end{aligned} \tag{7.2}$$

In Equation (7.2), $u_x(y_i)$ is the flow velocity at the center location of i^{th} sphere and $C_{d,i}$ is the coefficient of drag for each particle. The coupled ODEs were solved in MATLAB by using built-in ODE solvers. The fiber is assumed to be in a dual-frequency type dynamic acoustic field, similar to the field generated in the prototype in Chapters 4 and 6. For the simulations, the fiber parameters used are given in Table 7.3.

The flow and liquid parameters were same as those in Chapter 6, with a total flow rate of $500\ \mathrm{mL\ h^{-1}}$ and channel width of $2\ \mathrm{cm}$. The excitation frequency was set at $f = 2\ \mathrm{MHz}$ with $\Delta f = 0.5\ \mathrm{Hz}$. The reflection coefficient $R = 0.5$ and the acoustic pressure $P_D = 150\ \mathrm{kPa}$. Figure 7.8 illustrates two cases, where the fiber can and cannot follow the nodal movement on the time interval from $t = 0\ \mathrm{s}$ to $t = 15\ \mathrm{s}$. In each case, the fiber started non-stretched, non-bent and perpendicular to the nodal movement.

Figure 7.9 indicates that if the fiber is able to follow the nodal movement, it aligns with the pressure nodes, hence becoming horizontal. This result is in line with other studies demonstrating fiber alignment in acoustic fields [30-32]. In the example of Fig. 7.9, the fiber was smaller than the wavelength at the excitation frequency. Following example illustrates the behavior of the fiber which is larger than the wavelength. Here, $f = 2.5\ \mathrm{MHz}$, $d_i = 81\ \mu\mathrm{m}$ and $s_{ij} = 2d_i$.

Table 7.3 – Fiber parameters used in the simulations

Parameter	Value	Description
d_i	$24\ \mu\text{m}$	Individual sphere diameter
ρ_i	$1050\ \text{kg m}^{-3}$	Density of spheres
c_i	$1720\ \text{m s}^{-1}$	Speed of sound in spheres
k	$1\ \text{N m}^{-1}$	Spring coefficient between adjacent spheres
b	$1 \times 10^{-7}\ \text{N m}^{-1}\text{s}^{-1}$	Damping coefficient between adjacent spheres
s_{eq}	$= \text{d}_\text{i}$	Equilibrium distance between adjacent spheres
k'	$1 \times 10^{-5}\ \text{N m}^{-1}$	Spring coefficient between non-adjacent spheres
b'	$1 \times 10^{-11}\ \text{N m}^{-1}\text{s}^{-1}$	Damping coefficient between non-adjacent spheres
θ_{eq}	$180°$	Equilibrium angle between lines connecting adjacent spheres

Similarly, according to Figure 7.10, when a fiber can follow the nodal movement it is aligned to the pressure nodes. The solutions indicate that the alignment may still be possible for the case in Figure 7.10b, but happening slowly. Simulations for $T = 60\ \text{s}$ confirmed that the fiber does not align with the pressure nodes. This alignment-like behavior is most likely a result of the parabolic flow profile, the spheres closer to the center of the channel move faster in the flow direction, while the spheres close to the edges are retarded.

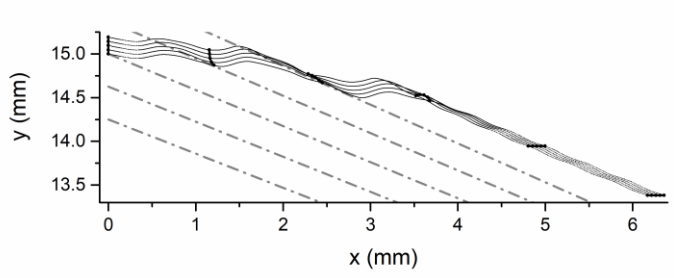

(a)

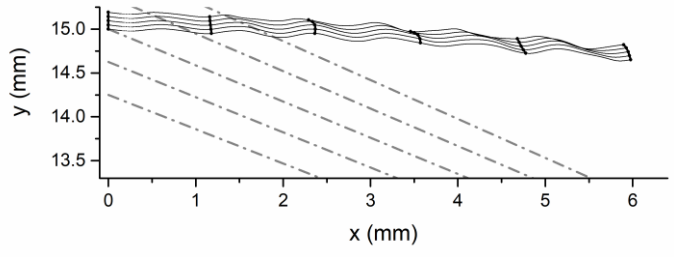

(b)

Figure 7.9 - (a) a fiber that can follow the nodal movement and (b) a fiber that cannot follow the nodal movement when P_D = 120 kPa. The flow is in the positive x direction. Dash-dot lines indicate the nodal movement. Trajectories of the spherical particles are illustrated by dotted lines. The position of fiber is illustrated at every 20% of the total simulation time.

The behavior of the fiber can also be assessed in terms of the K number introduced in Chapter 4. For the case in Figure 7.9, $K = 1.1295$ for each sphere when the fiber can follow and $K = 0.7229$ when the fiber cannot follow. Similarly, for the case in Figure 7.10, the spheres have $K = 2.237$ when the fiber can follow and $K = 0.5584$ when the fiber cannot follow.

Even though the fiber model does not introduce any selectivity possibilities, it can be used as a starting point for follow-up studies. One immediate improvement on the model would be correcting the drag force on the spheres. In the version presented here, the spheres individually experience Stokes drag force and their position does not affect the drag force on the other spheres. A more realistic and accurate drag model can improve the model significantly.

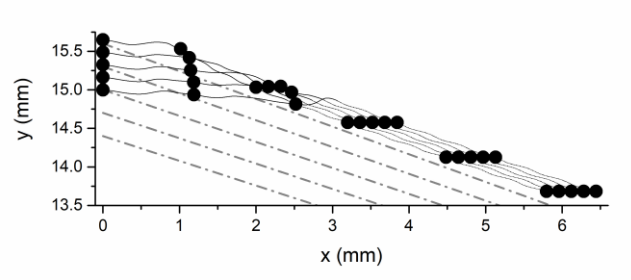

(a)

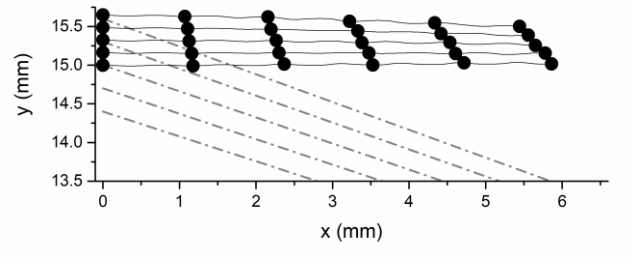

(b)

Figure 7.10 - (a) a fiber that can follow the nodal movement when P_D = 50 kPa and (b) a fiber that cannot follow the nodal movement when P_D = 25 kPa. The flow is in the positive x direction. Dash-dot lines indicate the nodal movement. Trajectories of the spherical particles are illustrated by dotted lines. The position of fiber is illustrated at every 20% of the total solution time.

7.5 Outlook

The results of this research conclude that for selective particle separation multi-wavelength resonators are viable options on centimeter scale. Such a resonator can employ an acoustic standing wave field with a creative flow pattern (Chapter 3), or dynamic acoustic fields with continuous laminar flow (Chapters 4-6). The focus of the study was on development and proof of concept of selective separation. Hence some important aspects like energy consumption and optimization of the design and operation were not addressed here. Possible points that can serve as starting points for future studies and applications are listed as:

- The energy consumption can be lowered by optimizing the geometries such that stronger and closer-to-ideal acoustic fields are obtained.
- In Chapter 3, the inner walls can be replaced by a non-reflecting material and the bottom wall can be replaced by a steel plate. These adjustments will provide a stronger and closer-to-ideal acoustic field.
- Geometry of the dynamic acoustic field devices can be adjusted in a way to improve the separation. A possibility is to make a narrower particle inlet, so that in the beginning of the acoustic field the particles are closer to each other.
- By taking measurements with devices like LDV, the pressure field generated by the transducers can be calculated and fed to the computer simulations. Such an approach will improve the simulations.
- Control systems can be implemented to create more complex flow fields and acoustic fields. With the cost of complexity, such fields may offer better selectivity.
- The 5-sphere fiber model introduced in Chapter 7 can be improved to include a more accurate drag force model. Such a model may lead to future studies on selective fiber removal using acoustics.
- Application-specific devices would not require as versatile equipment as used in the lab experiments in this research. Simplification of electronics may lead to lower energy consumption, at the cost of flexibility of operation.

Instead of further exploration and optimization of selective particle separation using multi-wavelength resonators, future research may also include (i) particle size-specific trapping for sensing and control and (ii) exploration of combinations of acoustical radiation and drag forces with other forces, generated by, for instance, electrical and magnetic fields.

References

[1] Sajeesh, P., Sen, A.K., 2014. Particle separation and sorting in microfluidic devices: a review. Microfluidics and Nanofluidics 17, 1–52. doi:10.1007/s10404-013-1291-9

[2] Lenshof, A., Laurell, T., 2010. Continuous separation of cells and particles in microfluidic systems. Chemical Society Reviews 39, 1203–1217. doi:10.1039/B915999C

[3] Nam, J., Lim, H., Kim, C., Yoon Kang, J., Shin, S., 2012. Density-dependent separation of encapsulated cells in a microfluidic channel by using a standing surface acoustic wave. Biomicrofluidics 6, 024120. doi:10.1063/1.4718719.

[4] Xie, Y., Mao, Z., Bachman, H., Li, P., Zhang, P., Ren, L., Wu, M., Huang, T.J., 2020. Acoustic Cell Separation Based on Density and Mechanical Properties. Journal of Biomechanical Engineering 142. doi:10.1115/1.4046180

[5] Iv, C.W.S., Reyes, C.D., López, G.P., 2015. Microfluidic cell sorting: a review of the advances in the separation of cells from debulking to rare cell isolation. Lab on a Chip 15, 1230–1249. doi:10.1039/C4LC01246A

[6] Nam, J., Lee, Y., Shin, S., 2011. Size-dependent microparticles separation through standing surface acoustic waves. Microfluidics and Nanofluidics 11, 317–326. doi:10.1007/s10404-011-0798-1

[7] Jönsson, H., Holm, C., Nilsson, A., Petersson, F., Johnsson, P., Laurell, T., 2004. Particle Separation Using Ultrasound Can Radically Reduce Embolic Load to Brain After Cardiac Surgery. The Annals of Thoracic Surgery 78, 1572–1577. doi:10.1016/j.athoracsur.2004.04.071.

[8] Huang, T.J., 2019. Acoustofluidics: Merging acoustics and microfluidics for biomedical applications. The Journal of the Acoustical Society of America 145, 1786–1786. doi:10.1121/1.5101531

[9] Wang, K., Zhou, W., Lin, Z., Cai, F., Li, F., Wu, J., Meng, L., Niu, L., Zheng, H., 2018. Sorting of tumour cells in a microfluidic device by multi-stage surface acoustic waves. Sensors and Actuators B: Chemical 258, 1174–1183. doi:10.1016/j.snb.2017.12.013

[10] Gor'kov, L.P., 1962. On the Forces Acting on a Small Particle in an Acoustical Field in an Ideal Fluid. Soviet Physics Doklady 6, 773.

[11] Gröschl, M., 1998. Ultrasonic Separation of Suspended Particles - Part I: Fundamentals. Acta Acustica united with Acustica 84, 432–447.

[12] Bruus, H., 2012. Acoustofluidics 7: The acoustic radiation force on small particles. Lab on a Chip 12, 1014–1021. doi:10.1039/C2LC21068A

[13] Petersson, F., Åberg, L., Swärd-Nilsson, A.-M., Laurell, T., 2007. Free Flow Acoustophoresis: Microfluidic-Based Mode of Particle and Cell Separation. Analytical Chemistry 79, 5117–5123. doi:10.1021/ac070444e

[14] Hawkes, J.J., Radel, S., 2013. Acoustofluidics 22: Multi-wavelength resonators, applications and considerations. Lab on a Chip 13, 610–627. doi:10.1039/C2LC41206C.

[15] Leong, T., Johansson, L., Juliano, P., McArthur, S.L., Manasseh, R., 2013. Ultrasonic Separation of Particulate Fluids in Small and Large Scale Systems: A Review. Industrial & Engineering Chemistry Research 52, 16555–16576. doi:10.1021/ie402295r

[16] Juliano, P., Swiergon, P., Lee, K.H., Gee, P.T., Clarke, P.T., Augustin, M.A., 2013. Effects of Pilot Plant-Scale Ultrasound on Palm Oil Separation and Oil Quality. Journal of the American Oil Chemists' Society 90, 1253–1260. doi:10.1007/s11746-013-2259-3

[17] Juliano, P., Temmel, S., Rout, M., Swiergon, P., Mawson, R., Knoerzer, K., 2013. Creaming enhancement in a liter scale ultrasonic reactor at selected transducer configurations and frequencies. Ultrasonics Sonochemistry 20, 52–62. doi:10.1016/j.ultsonch.2012.07.018

[18] Prest, J.E., Treves Brown, B.J., Fielden, P.R., Wilkinson, S.J., Hawkes, J.J., 2015. Scaling-up ultrasound standing wave enhanced sedimentation filters. Ultrasonics 56, 260–270. doi:10.1016/j.ultras.2014.08.003.

[19] Gorenflo, V.M., Smith, L., Dedinsky, B., Persson, B., Piret, J.M., 2002. Scale-up and optimization of an acoustic filter for 200 L/day perfusion of a CHO cell culture. Biotechnology and Bioengineering 80, 438–444. doi:10.1002/bit.10386.

[20] Radel, S., Gherardini, L., McLoughlin, A.J., Doblhoff-Dier, O., Benes, E., 2000. Breakdown of immobilisation/separation and morphology changes of yeast suspended in water-rich ethanol mixtures exposed to ultrasonic plane standing waves. Bioseparation 9, 369–377. doi:10.1023/A:1011158019835

[21] Cappon, H.J., 2014. Numerical and experimental design of ultrasonic particle filters for water treatment (PhD). Wageningen University, Wageningen.

[22] Böhm, H., Briarty, L.G., Lowe, K.C., Power, J.B., Benes, E., Davey, M.R., 2003. Quantification of a noveL h-shaped ultrasonic resonator for separation of biomaterials under terrestrial gravity and microgravity conditions. Biotechnology and Bioengineering 82, 74–85. doi:10.1002/bit.10546

[23] Mandralis, Z., Feke, D.L., Bolek, W., Burger, W., Benes, E., 1994. Enhanced synchronized ultrasonic and flow-field fractionation of suspensions. Ultrasonics 32, 113–122. doi:10.1016/0041-624X(94)90019-1

[24] Wu, M., Mao, Z., Chen, K., Bachman, H., Chen, Y., Rufo, J., Ren, L., Li, P., Wang, L., Huang, T.J., 2017. Acoustic Separation of Nanoparticles in Continuous Flow. Advanced Functional Materials 27, 1606039. doi:10.1002/adfm.201606039.

[25] Budwig, R.S., Anderson, M.J., Putnam, G., Manning, C., 2010. Ultrasonic particle size fractionation in a moving air stream. Ultrasonics 50, 26–31. doi:10.1016/j.ultras.2009.07.004.

[26] Skotis, G.D., Cumming, D.R.S., Roberts, J.N., Riehle, M.O., Bernassau, A.L., 2015. Dynamic acoustic field activated cell separation (DAFACS). Lab Chip 15, 802–810. doi:10.1039/C4LC01153H

[27] Drinkwater, B.W., 2016. Dynamic-field devices for the ultrasonic manipulation of microparticles. Lab on a Chip 16, 2360–2375. doi:10.1039/C6LC00502K

[28] Wagterveld, R.M., Marijnissen, J.C.M., Gradoń, L., Moskal, A. (Eds.), 2020. Synthetic Nano- and Microfibers. Wetsus. doi:10.20850/9781716632426

[29] Keesman, K.J., 2011. System identification: an introduction. Springer, London.

[30] Schwarz, T., 2013. Rotation of Particles by Ultrasonic Manipulation. ETH Zurich. doi:10.3929/ETHZ-A-010039218

[31] Yamahira, S.Y.S., Hatanaka, S.H.S., Kuwabara, M.K.M., Asai, S.A.S., 2000. Orientation of Fibers in Liquid by Ultrasonic Standing Waves. Japanese Journal of Applied Physics 39, 3683. doi:10.1143/JJAP.39.3683.

[32] Brodeur, P., 1991. Motion of fluid-suspended fibres in a standing wave field. Ultrasonics 29, 302–307. doi:10.1016/0041-624X(91)90026-5.

SUMMARY

Particulate suspensions occur in many different industrial activities, for example in food, biomedical and pharmaceutical industries. These suspensions usually need a treatment step to separate valuable particles from the wet process streams or purify the streams. Such treatments may be needed at any stage during the process. Many technologies exist to perform such treatments. A relatively recent technology is acoustophoresis. Main advantages of the technology are: (i) it does not require any specific particle property (such as electric charge or ferromagnetism) and (ii) an acoustic separation system does not contain internal parts that may get clogged or damaged. Furthermore, by interplay of the acoustic radiation force and other forces, such as drag force, selective particle separation can be realized.

Acoustophoresis is widely and successfully used in biomedical applications on microscale. For biomedical applications, such as blood cell separation for diagnosis, microscale has a size advantage as it reduces the required sample size, typically in the order of mL. For other applications, however, when the volumes to be treated are larger, for instance in the order of $\mathrm{L\,h^{-1}}$, selective particle separation from suspensions on centimeter scale can be a viable option. This thesis investigated and laid down the path towards realizing selective particle separation on centimeter scale

Chapter 2 revisited the equation of motion (EOM) for a particle in a half-wavelength acoustic standing wave field. This EOM is a second-order non-linear ordinary differential equation (ODE). In the literature, a first order non-linear approximation of the EOM is widely used. A different approach was followed in Chapter 2, by representing the particle as a linear single degree-of-freedom (SDOF) vibrating system. This approach resulted in a second-order linear ODE describing the motion of a particle in an acoustic standing wave field. This approximation allows the system behavior to be analytically evaluated in terms of the SDOF parameters, such as damping ratio. The non-linear model assumes that the particle asymptotically converges to the equilibrium position, the pressure node or antinode, whereas the linear model allows the calculation of the damping ratio. Hence, the linear model is able to predict oscillatory behavior, which is also seen in practice for damping ratios smaller than one. Chapter 2 concluded that simply scaling up microscale acoustophoresis to a centimeter scale by increasing the dimensions is not possible; as it requires reduction in frequency and higher damping ratios, where high damping ratios result in unpractically long transit times. Reducing the damping ratio

is possible, for example, by increasing the applied pressure. However, such an increase at lower frequencies also increases the risk of cavitation. Furthermore, the linear model allows the prediction of particle trajectory and transit times between initial and target positions. A one-step linearization on the region of interest was unable to provide satisfactory result. Consequently, a stepwise linearization of the non-linear acoustic radiation force term in the EOM was introduced. A 25-steps solution of the particle trajectory resulted in more accurate approximations compared to the non-linear model, while being computationally more effective than evaluating the complete numerical solution.

In Chapter 3, a 3D-printed multi-wavelength prototype was introduced, where the particle suspension flows in a serpentine channel and a standing wave field is generated by a transducer and a reflector. Given the meandering nature of the flow, the drag force, due to the effect of the surrounding flow on a particle, is changing direction in the hairpins, whereas the acoustic force is always acting in the same direction. Computer simulations confirmed that the interplay was especially enhanced in the hairpins of the serpentine separator, hence selective trapping of the particles in those locations is possible. In this device, the distance between the transducer and the reflector was $4\ \mathrm{cm}$, whereas the maximum flow rate was $400\ \mathrm{mL\ h^{-1}}$. The acoustic force was tuned by changing the input power, whereas the drag force was adjusted by changing the flow rate. The potential of selective separation by using a combination of flow pattern and multi-wavelength acoustic standing wave fields was successfully demonstrated in Chapter 3. In addition, a mixture with flocs (wheat beer) was also filtered, where yeast particles larger than $9\ \mu\mathrm{m}$ were successfully retained in the system when the flow rate was $20\ \mathrm{mL\ h^{-1}}$. By this example, it was confirmed that in a multi-wavelength resonator that utilizes acoustic standing waves, selective separation is possible by adjusting the drag force (through the flow rate) and the acoustic radiation force (through the input power).

In Chapter 4, two types of dynamic acoustic fields were investigated for selective particle separation on centimeter scale. The first type of dynamic acoustic fields is by application of a frequency sweep method, where the excitation frequency is periodically swept from one to another frequency. Such an excitation causes the standing wave pattern to contract towards one side, whereas new nodes are introduced at the other side. As a result, the speed of the pressure nodes are not constant; it is a function of time and position. The speed is faster at the source side and goes to zero at the reflector side. The second type of dynamic acoustic field is generated by a dual frequency method. In this method, the dynamic field is generated by using two separate sound sources operating at slightly different

frequencies. In the resulting dynamic acoustic field, the speed of pressure nodes is constant. While reflection from the reflector generates a pseudo-standing wave in the frequency sweep case, reflections disturb the dynamic acoustic field in the dual frequency case. It was concluded in Chapter 4 that both methods are suitable for size selective particle separation on centimeter scale, both having advantages and disadvantages. The frequency sweep case requires a simpler prototype but the speed of pressure nodes is not constant, whereas in the dual frequency case the constant speed of pressure nodes comes at a cost of increased complexity.

In plain English, for both type of dynamic fields, selectivity is realized between the following conditions: if the pressure nodes move too fast, none of the particles are captured, whereas if the nodes move too slowly, all particles are captured. Keeping the acoustic pressure constant, the selectivity can be adjusted by changing the speed of nodal pattern. Further theoretical investigation and computer simulations on the conditions for capturing a particle resulted in a dimensionless number, K. This dimensionless number can predict the particle behavior without conducting simulations and lab experiments. Furthermore, it can be used to estimate the acoustic pressure in a multi-wavelength acoustophoresis device. Assuming an ideal 1D plane wave field and given the excitation and particle parameters, K can predict whether the particle is captured by the pressure nodes or not. The number is applicable to both type of dynamic fields. For the dual frequency case, reflections can be accommodated in the predictions by K.

The demonstration of the dynamic acoustic fields is presented in Chapters 5 and 6. Each X-shaped prototype has one inlet through which the particle mixture and another inlet through which only water was pumped. The particles were pushed towards the bottom outlet, the samples were taken from the top outlet.

In Chapter 5 size selective separation by a frequency sweep type dynamic acoustic field was demonstrated. The performance of the prototype was evaluated in terms of the largest particle exiting from the top outlet, which defines the separation threshold. The acoustic field was adjusted by changing the sweep period. In addition, while keeping the total flow rate constant at $1000\ \mathrm{mL\ h^{-1}}$, the flow field was adjusted by changing the flow rates of the individual inlets and outlets. A laser Doppler vibrometer was utilized to measure the vibration amplitude of the transducer, in order to provide more insight into the system. An in silico design of experiment study was carried out in order to investigate the effects of the individual flow rates and the sweep periods. Subsequently, lab experiments confirmed the ability of size selective separation, where different combinations of parameters

yielded separation thresholds between $70 - 105$ μm. Similarly to the experiments in Chapter 3, lab experiments with wheat beer were carried out. These resulted in a separation threshold of 11 μm for a flow rate of 100 mL h^{-1}.

In Chapter 6 size selective separation by dual frequency type dynamic acoustic fields was demonstrated. The special geometrical arrangement of the prototype ensured that the reflections were minimized. The performance of the prototype was evaluated by the $d90$ value of the samples from the top outlet. Simulations and lab experiments were carried out for different combinations of frequency differences and total flow rates. The different combinations yielded $d90$ values between $53 - 71$ μm.

Main findings from this research can be listed as follows:

- A particle in a half-wavelength resonator can be modelled as a linear single degree-of-freedom vibrating system. In addition to more or less exponentially decaying particle trajectories this method can be used to predict oscillatory behavior, as well.
- A half-wavelength resonator on centimeter scale is impractical due to reduction in frequency and pressure.
- Multi-wavelength resonators are a viable option for selective particle separation on centimeter scale, as a combination of a creative flow field and an acoustic standing wave.
- Dynamic acoustic fields in multi-wavelength resonators further facilitate selective particle separation on centimeter scale. Versatility of such fields makes it a favorable option over standing wave fields, although more complex devices are required.

As a result, the thesis presented a path for utilizing acoustophoresis for selective particle separation on centimeter scale.

List of Publications by M. H. Kandemir

Kandemir, M. H., Çalışkan, M. (2016). Standing wave acoustic levitation on an annular plate. Journal of Sound and Vibration, 382, 227-237

Kandemir, M. H., Wagterveld, R.M., Yntema, D.R., Keesman, K.J. (2019) Selective particle filtering in a large acoustophoretic serpentine channel. Scientific Reports, 9, 7156

Kandemir, M. H., Beelen, M., Wagterveld, R.M., Yntema, D.R., Keesman, K.J. (2021) Dynamic acoustic fields for size selective particle separation on centimeter scale. Journal of Sound and Vibration, 490, 115723

Kandemir, M. H., Mohan, K., Wagterveld, R.M., Yntema, D.R., Keesman, K.J. (2021) Size selective particle filtering on centimeter scale by frequency sweep type dynamic acoustic field. Separation and Purification Technology, 259, 118188

Kandemir, M. H., Wagterveld, R.M., Yntema, D.R., Keesman, K.J. (2021) Selective Particle Separation on Centimeter Scale using a Dual Frequency Dynamic Acoustic Field. Ultrasonics, 114, 106411

Under review / in preparation

Kandemir, M. H., Wagterveld, R.M., Yntema, D.R., Keesman, K.J. Considerations about a linearized single degree-of-freedom model to predict particle behavior in microscale acoustophoresis. *Status: Under review*. Acta Acoustica.

Bazyar, H., **Kandemir, M. H.**, Peper, J., Schroen, K., Lammertink, Rob G. H. Acoustophoresis of monodisperse oil droplets in water: determining the acoustic energy density. *Status: In preparation.*

Acknowledgements

February 2012: I quit my job at Hidromek and start working at the University. It was just after the first semester of my MS study and I had to determine a dissertation topic. My Professor, Prof. Mehmet Çalışkan told me: “Let’s do something with Acoustic Levitation”. If it wasn’t his vision, and trust in me, the chain of events that lead you reading this piece of text would not even begin.

March 2016: I was in the second year of my PhD (in Turkey), finished the courses, preparing for the PhD qualification exam. One night, I saw an advertisement for a PhD position at Wetsus, and I initially thought “they are looking for me!”. Later I found out that they were indeed looking for me. “They” here, as you read this text became “we” soon (Sept. 2016), and include the most easy-going professor Karel as promotor: full of ideas, fundamental questions, wisdom and support. Any 5-min meeting we had turned into a very long session of discussion, which I enjoyed and will miss a lot. My daily super(1+visors) at Wetsus were very special people: Doekle has his own way of living, a.k.a. *Doeklifying*. What it means can take longer than this book, but one could grasp it after a 1-min talk with him: I guarantee you that your life will not be the same. Martijn’s focus is beyond human: until he points out a solution to me, it was not possible for me to see how easy and obvious it is. By this way, he also taught me how to write an article, you can see his effect in every single chapter in this book. I’m extremely lucky to have worked with this particular group of people. I’m also very thankful to the students that worked with me, Moniek (Anakin), Johan (the package) and Keerthana, for their very rigorous work.

I would like to thank my Wetsus colleagues, the secretaries, financial and HR team for being very helpful and quick when needed. The technical team, both workshop and lab, are very talented, versatile and smart people. I pick Jan(1+nie+ Jurjen+ Willem) from different departments to highlight, and thank them for their support, intelligence, humor and competition in a lot of games.

I feel very lucky to have worked with my office mates, a.k.a. the Champions, they made my time there (very next to the atrium) very bearable and fun. At some point it was a bit too awesome there and they took Fabian from us, for he is the pinnacle of being fun, sarcastic, deep and smart. Raquel is a model professional and very eloquent, I have to thank once again for not going home and inspiring us. Gijs (acanthonus armatus), thanks for all the nijs bike rides, stupid talks, videos, jokes and *censored.* Sandra (dude), thanks for all the random/planned adventures, enjoying the chaos and being able to draw nerdy fun in every single opportunity.

Natascha, thanks for the cakes, sweets, letting me take Angband and bringing the first medal to the office. Yang's students were a very lucky group as they have the best of the champions, and we keep chanting *Forever Yang*, for we know Wetsus wanted that as well. Qingdian is our first official champion, can take a lot of bullets while solving a Rubik's cube (within seconds or something like that) and can still tell you: *That's fine*. Caspar (PC Principal), has a very subtle artistic taste that shines in December, fuels the Dutch Fighter Jets, and compensates for Fabian's absence. Sam (Sauron), shouldn't let orthopedics and other evils keep him away from greatness and should be careful whose jokes he laughs at. Evelyn&Sara, thanks for the joy and fresh spirit you bring to the office.

As paranymphs, I have a very special combination of skills. Shuyana, with her most-friendly-person-ever badge kindly reminded me in every single opportunity that $\sum_{i=1}^{N} 1 = N$, while Maarten would immediately correct such a statement, by "yes, if $N \in \mathbb{Z}^{+}$". Thanks for a lot of good moments I had with Shuyana's *Shuyanating* approach to life, and for my favorite show *Maarten Contra Mundus.*

Towards the end of 2019, we went into a business adventure with Señor Hector and Ilse (golddigger). The long trips to Zeeland were not boring thanks to your ability to keep serious stuff fun: I had very good time with you, while drinking tea, having smart talks, playing stupid games.

I still don't understand why, but at some point I had a fan club, founded by Emad (Priapos) but peaked under the presidency of Adriana supported by Jacinta. I am thankful to all members for their support, which I will always remember.

For my good times at Wetsus, I would like to thank my friends from Wetsus, for being able to make small talk in Turkish super quick to Victor (dostum), for punching my back in every opportunity to Paulina (amigaaa), for being 150% up for a game at any moment to Thomas, for adventures and hard chess games to Sebastian, Prashanth, Chris, Advait, Steffen and Merab, for letting me know what is Christmas spirit to Vania (and her family) and Marianne, for getting me into cycling and not hating me after saving my ass numerous times to Roel (fietsmeester), for initially giving me a safe place to live to Victor (Mr. Beast) and Terica, for making me wait impatiently for every lunch presentation to Carlo (κ), for good times at PV to Ettore, Zexin, Nynke and Emanuel, for very valuable cooperation in terms of pranks to Ragne, Wokke, Jolanda and Ruizhe, for responding to the perturbations with good talk to Gonçalo (amigo), Angel, Diego, Nandini, Antoine, Barbara, Catarina, Rebeca, Xiaoxia, Talie, Rita, and Giulia, for turning borrels into hangovers to Rutger, Mert

and Nick, and for a lot of good moments to Sofia (yenge), (Uncle) Yin, Elias (dingetje), Mariana and Gerwin. Of course, the lovely canteen crew, Gerben, Catharina and Riet, gets a lot of thanks from me, for whatever they prepared was an example of lekker eten.

To the people I've met in Leeuwarden, I'm thankful for keeping me from being homesick to Can&Elvina, Mert&his family and Selen, for very patiently guiding me in archery to Andre, for my inclusion to the order and her silmarilliance to Vasilisa, for a lot of fun games on Sundays/Mondays to Kevin, Maaike, Steven, Mandy, Albert, Erik, Linda, Sjors, Dmitri, Jurre, Ingrid, Fransisca, Daan, Tais, Siewart and numerous other people.

I thank *The Backmarkers*: Oltan, Tunç, Doğan and Çağrı, for keeping me watching every minute battle in F1. Thanks to my friends Hilmi and Çağrı (gülüm), for it was as if I never left METU ME.

Before closing up, I thank Sandra (dude) and Juan for the cover. I'm not really a Star Wars fan at all, somehow most of my prototypes looked like spacescrafts. The prototypes used in Chapters 3-6 became spacecrafts on the cover.

Son olarak aileme ne kadar teşekkür etmem gerektiği konusunda uzun uzun paragraflar yazabilirim, yine de yetmez, hem bizim aile biraz genişçedir. Hepsi ayrı ayrı özel, güzel, sevgi dolu, yaşam dolu insanlar beni hep doğrudan, dolaylı, uzaktan, yakından, bilerek, bilmeyerek destekledi, epeyce şeyi de hep beraber atlattı. Ben öyle çok arayıp soran biri değilim, zaten uzun yıllardır da sizden uzaktayım ama hep aklımdasınız. Her şey için çok sağolun.

About the author

Mehmet Hakan Kandemir was born on November 13, 1989 in Balıkesir, Turkey. He grew up in the same city. In 2003, he started high school in İzmir High School of Science. He already had interest in mechanical engineering, mainly due to having watched F1 for years. In 2006, he started to study mechanical engineering at Middle East Technical University (METU) in Ankara, Turkey. His interests shifted towards acoustics and vibrations during his BSc education. After graduation he started to work at Hidromek as an R&D engineer and was mainly responsible for vibration and acoustics tests, while having started his MSc study at the same university. After some months, he quit his job to start to work as a teaching and research assistant at METU. He started to work on acoustophoresis with his MSc dissertation, titled “design and implementation of an annular acoustic levitation system”. After finishing his MSc, he started PhD at the same department. His dissertation would be about sonoluminescence, but after finishing the course load and passing the PhD qualifier exam, he stopped in order to come to the Netherlands. In 2016, he started his PhD at WUR and Wetsus, and continued working on acoustophoresis, with the project titled “selective particle control in suspensions using acoustics”. The results obtained in his PhD period at WUR and Wetsus are presented in this dissertation.

Netherlands Research School for the
Socio-Economic and Natural Sciences of the Environment

D I P L O M A

for specialised PhD training

The Netherlands research school for the
Socio-Economic and Natural Sciences of the Environment
(SENSE) declares that

Mehmet Hakan Kandemir

born on 13 November 1989 in Balıkesir, Turkey

has successfully fulfilled all requirements of the
educational PhD programme of SENSE.

Leeuwarden, 23 April 2021

Chair of the SENSE board

Prof. dr. Martin Wassen

The SENSE Director

Prof. Philipp Pattberg

The SENSE Research School has been accredited by the Royal Netherlands Academy of Arts and Sciences (KNAW)

KONINKLIJKE NEDERLANDSE
AKADEMIE VAN WETENSCHAPPEN

The SENSE Research School declares that **Mehmet Hakan Kandemir** has successfully fulfilled all requirements of the educational PhD programme of SENSE with a work load of 90.5 EC, including the following activities:

SENSE PhD Courses

- Environmental research in context (2018)
- Research in context activity: 'Organising and teaching a Matlab & Mathcad mini course at Wetsus' (2018)

Other PhD and Advanced MSc Courses

- Introduction to Continuum Mechanics, Middle East Technical University (2015)
- Introduction to Biomechanics, Middle East Technical University (2015)
- Theory of Elasticity, Middle East Technical University (2015)
- Methods for Mathematical Physics II, Middle East Technical University (2015)
- Experimental Analysis of Vibrating Structures, Middle East Technical University (2015)
- Computational Inelasticity, Middle East Technical University (2015)
- Impact Mechanics, Middle East Technical University (2016)
- Starting day, Wetsus (2016)
- Presentation course, Wetsus (2016)
- Communication styles course, Wetsus (2017)
- Supervision course, Wetsus (2017)
- Talents course, Wetsus (2018)
- Leadership course, Wetsus (2019)
- Career development course, Wetsus (2020)

Management and Didactic Skills Training

- Supervising two MSc students with thesis (2018-2020)
- Assisting practicals of the MSc courses 'Computational methods for water technology' and 'Physical modelling' (2018)

Oral Presentations

- *A linear single degree of freedom model for acoustophoresis.* 37th Benelux meeting on systems and control, 27-29 March 2018, Soesterberg, The Netherlands

SENSE coordinator PhD education

Dr. ir. Peter Vermeulen

This work was performed in the cooperation framework of Wetsus, European Centre of Excellence for Sustainable Water Technology (www.wetsus.nl). Wetsus is co-funded by the Dutch Ministry of Economic Affairs and Ministry of Infrastructure and Environment, the European Union Regional Development Fund, the Province of Fryslân and the Northern Netherlands Provinces. This work has also received funding from the European Union's Horizon 2020 research and innovation programme under the Marie Skłodowska-Curie (grant agreement No. 665874).

Cover design by S.M.Drusová

Printed by Proefschriftmaken.nl on FSC-certified paper